Master's thesis

NTNU
Norwegian University of Science and Technology
Faculty of Information Technology and Electrical Engineering
Department of Electronic Systems

Roman Malyshev

A finite element model of plasmonic particle arrays for glucose sensing by surface-enhanced Raman scattering

Master's thesis in Nanotechnology

Supervisor: Astrid Aksnes, Dag Roar Hjelme and Karolina Barbara Milenko

August 2020

NTNU
Norwegian University of Science and Technology

Roman Malyshev

A finite element model of plasmonic particle arrays for glucose sensing by surface-enhanced Raman scattering

Master's thesis in Nanotechnology
Supervisor: Astrid Aksnes, Dag Roar Hjelme and Karolina Barbara Milenko
August 2020

Norwegian University of Science and Technology
Faculty of Information Technology and Electrical Engineering
Department of Electronic Systems

NTNU
Norwegian University of
Science and Technology

Problem description

Motivation

Nanostructures of gold and silver have demonstrated the ability to sense sub-physiological concentrations of glucose and are good candidates for use in platforms for continuous glucose sensing. The collective oscillations of surface electrons, plasmons, when exposed to light of certain wavelengths, amplify the electric field near the structure's surface and make it possible to sense very small concentrations of glucose. One widely studied class of structures is the "metal film over nanospheres" class that includes arrays of gold and silver film over nanosphere structures, AuFONs and AgFONs, respectively. These particles are made up of an insulating core, coated with one of these metals. Silver particles have shown the greatest field enhancement ability. AuFONs are, however, safer to use for sensors meant for *in vivo* measurements, due to the inert nature of gold.

Electromagnetic modeling is one approach used to model plasmonic structures to predict the field enhancement in real-world lab samples. Modeling can reduce the time needed to develop a lab sample by investigating the effects of different structural and material parameters in a computational environment, rather than spending resources on creating a lab sample for every relevant parameter value. As computational methods and hardware become faster and capable of solving larger problems, more advanced structures can be modeled to produce more realistic results and support experimental work. Currently, different approaches have been developed to model single-particle plasmonic structures of arbitrary shapes. Arrays of particles are usually modeled using the coupled-dipole approximation (CDA). This method is simple, but unlike volumetric mesh methods such as the finite element method (FEM), it doesn't allow creating a realistic model, with arbitrary particle shape, ordering, surrounding medium and more.

Goal of this thesis

An FEM model of the AuFON will be developed, to facilitate experimental design of structures with optimal SERS sensing ability. The model will be built bottom-up, based on physical principles behind SERS. An important extension of the model from previous work is the transition from single particle models to particle array models. To support the development, the model will be compared against well-established analytical and numerical methods, such as Mie and CDA. It is not a goal to create a fully realistic model. The final AuFON model will be a platform to support experimental design, that can be further extended as needed to capture effects of adding a substrate, surface roughness, other geometric particle shapes and more. An important goal is that the model should be able to directly estimate the SERS enhancement factor of the modeled structure.

Abstract

Optical biosensors based on surface-enhanced Raman scattering (SERS) have been researched for several decades due to their wide applicability. Continuous blood glucose measurement is an application where such devices have potential to improve management of diabetes treatment and avoid negative side effects from improper insulin dosage. Noble metals have demonstrated the ability to enhance the Raman scattering such that one can measure sub-physiological levels of glucose. This is due to the strong field enhancement from surface oscillations of the metal electron clouds, quantized as surface plasmons, when excited by light.

To find the plasmonic nanostructure that yields optimal field enhancement, computer modeling allows screening different parameter values to see the effects of such changes, rather than produce a lab sample for every parameter value. The finite element method (FEM) used in this thesis allows solving Maxwell's equations directly, without approximations, making it possible to model arbitrary particle shapes and arrangements.

An FEM model is developed in this thesis for a class of nanostructures called *gold film over nanospheres* (AuFON). The AuFON has been much researched due to its relatively simple fabrication process and predictable field enhancement capability. The current state-of-the-art SERS enhancement factor from this structure is $10^6 - 10^8$. The structure consists of a dielectric sphere core, coated with gold film. One can therefore control its performance by changing the core diameter or gold film thickness, along with investigating how the particle shape and spacing affects the enhancement factor.

The model was built bottom-up, each step compared to analytical Mie model or numerical dipole approximation methods, and theory or published results, to verify that its light extinction properties are well-behaved. We first review solid single-particle gold and silver models, showing that larger spheres have redshifted resonances compared to smaller particles and that lower refractive indices of the medium blueshift and dampen extinction. The algorithm for computing the SERS enhancement factor (EF) is then demonstrated on single particles, revealing very modest enhancement factors on the order of 10^2. It was demonstrated that when two or more such particles are coupled via their near-fields, the enhancement factor can approach the theoretical limit of 10^{14} for the electromagnetic contribution. Far-field coupled arrays showed the emergence of lattice resonances, generally agreeing with the coupled oscillator model and the well-established coupled-dipole approximation. The enhancement factors from far-field coupled particles in arrays were on the order of 10^3. Single nanoshells exhibit higher enhancement factors due to the excitation of surface plasmons on both metal-dielectric interfaces, but with larger film thicknesses they behave as solid particles. Finally, close-packed arrays of nanoshells, approximating AuFONs, showed a dependence of SERS EF on film thickness similar to the experimental reference plot, but the SERS EFs, on the order of $10^3 - 10^4$, are much smaller than the state of the art. The top hat structure, an interpretation of the AuFON shape, showed even more modest SERS EFs of 10^3.

Sammendrag

Optiske biosensorer basert på overflate-forsterket Ramanspredning (SERS) har vært forsket på i flere tiår, grunnet deres store applikasjonsområde. Kontinuerlige blodsukkermålinger er en anvendelse der slike innretninger har potensiale for å bedre diabetesbehandling og unngå negative bivirkninger fra feildosering av insulin. Edle metaller har demonstrert en evne til å forsterke Ramanspredning slik at man kan måle selv subfysiologiske mengder sukker. Dette er grunnet i den sterke feltforsterkningen fra overflatesvingninger av metallets elektronsky, kvantisert som overflateplasmoner, når eksitert av lys.

Datamodellering kan hjelpe med å finne plasmoniske nanostrukturer med optimal feltforsterkning ved å utrede hvordan forskjellige parameterverdier påvirker den. Dette heller enn å lage en ny labprøve for hver parameterverdi. Elementmetoden brukt i denne avhandlingen lar oss løse Maxwells likninger direkte, uten å ty til approksimasjoner, som gjør det mulig å modellere vilkårlige partikkelgeometrier og partikkelmatriser.

En elementmetodemodell er utviklet i denne avhandlingen for en type strukturer som heter *gullfilm over nanosfærer* (AuFON). AuFON-er er blitt mye forsket på grunnet relativt enkel fabrikering og deres forutsigbare feltforsterkning. Dagens høyeste rapporterte forsterkningsfaktor fra slike strukturer er $10^6 - 10^8$. Strukturen består av en dielektrisk kuleformet kjerne, dekket med gullfilm. En kan derfor kontrollere dens forsterkningsytelse ved å endre kjernediameter eller filmtykkelse, samtidig som man fortsatt har frihetsgradene i form av partikkelgeometri og partikkelavstand i matrisen.

Modellen er her bygget nedenfra og opp, der man i hvert sted sammenliknet resultatene med analytisk Mie-løsning eller numeriske dipolapproksimasjonsmetoder og teori, eller publiserte resultater. Dette for å forsikre seg om at de optiske egenskapene til modellene er riktige i hvert steg. Vi ser først på homogene enkeltpartikkelmodeller for gull og sølv, som viser at større kuler har rødskiftede resonanser sammenliknet med mindre partikler. Og at en lavere brytningsindeks i mediet gir blåskift av resonanser og demper dem. Algoritmen for å beregne SERS-forsterkningsfaktoren (FF) er så demonstrert på enkeltpartikler, som viser en veldig liten feltforsterkningsevne. En faktor på 10^2. Det ble så demonstrert at når to eller flere slike partikler var koplet sammen via deres nærfelt, kunne FF-en stige mot en teoretisk maksverdi på 10^{14} fra den elektromagnetiske effekten alene. Fjernfelt-koplede partikkelmatriser viste dannelsen av gitterresonanser og oppførte seg generelt i tråd med harmonisk oscillatormodellen og den veletablerte koplete dipolapproksimasjonen. Disse viste en FF på 10^3. Enkeltpartikler av typen nanoskall viste høyere FF grunnet eksitasjon av overflateplasmoner på begge deres metall-dielektrikum grenseflater, men med større skalltykkelse oppførte de seg mer og mer som solide partikler. Til slutt ble tettpakkede nanoskallpartikler, som approksimerer AuFON-er, undersøkt. Disse viste en liknende avhengighet av SERS FF på filmtykkelse som i referanseplottet. Feltforsterkningsfaktorene, på $10^3 - 10^4$, var imidlertid mye mindre enn rapportert i litteraturen. Gullhattstrukturen, en tilnærming til den reelle AuFON-formen, viste en enda mer beskjeden FF på 10^3.

Preface

This work was written as part of the master's degree program in nanotechnology at NTNU, Trondheim. The master thesis presented here is a continuation of the work performed in the project thesis [1].

The field of photonics and plasmonics is fast-evolving. It was exciting to get an insight into how basic physical principles from optics and solid-state physics may be applied to create advanced nanostructures that can be used to get one step closer to a solution of a real-world problem, such as blood glucose monitoring. The work on this thesis introduced me to a lot of new theory and methods, as well as allowing the opportunity to work at the NTNU Nanolab during the thesis work. The latter was, admittedly, halted due to the COVID-19 pandemic, that forced a change of focus towards the computational side of the topic. Thus, the experimental work performed in the project thesis could not be taken further. However, the modeling tasks were just as exciting, allowing to do quite a bit of hands-on programming.

The author would like to thank professors Astrid Aksnes and Dag Roar Hjelme at IES NTNU for invaluable advice and guidance throughout this past year, helping both with steering the work in the right direction as well as helping solve various administrative issues during this pandemic. Dr Karolina Milenko, former postdoc researcher at IES NTNU, is also thanked for her guidance and input. Especially for allowing the use of her results and lab techniques.

Furthermore, a thank you goes to Linus Andersson, application engineer at COMSOL, for help modeling arrays in COMSOL.

Former and current NTNU PhD candidates (in no particular order) Silje S. Fuglerud, Ine J. Larsen, Jens Høvik and Einar Digernes are thanked for helpful discussions and assistance this past year.

A thank you goes to Nanolab senior engineers Svenn Ove Linde and Mark Chiappa for training, and senior engineers Mathilde Barriet and Trine Hjertås, for training and helpful discussions about the chemical processes used during the thesis work.

The Research Council of Norway is acknowledged for the support to the Norwegian Micro- and Nano-Fabrication Facility, NorFab, project number 245963/F50.

Contents

List of abbreviations

AFM	=	Atomic force microscopy
AgFON	=	Ag (Silver) film over nanosphere
AuFON	=	Au (Gold) film over nanosphere
BC	=	Boundary condition
CDA	=	Coupled-dipole approximation
DDA	=	Discrete-dipole approximation
EBL	=	Electron beam lithography
EF	=	Enhancement factor
EM	=	Electromagnetic
FDTD	=	Finite-difference time-domain (method)
FEM	=	Finite-element method
FWHM	=	Full-width at half maximum
HWHM	=	Half-width at half maximum
LD	=	Lorentz-Drude model
LSPR	=	Localized surface-plasmon resonance
IR	=	Infrared
NIR	=	Near-Infrared
PBC	=	Periodic boundary condition
PEC	=	Perfect electric conductor
PMC	=	Perfect magnetic conductor
PML	=	Perfectly matched layer
RI	=	Refractive index
SBC	=	Scattering boundary condition
SEM	=	Scanning electron microscopy
SERS	=	Surface-enhanced Raman Scattering (or, alternatively, spectroscopy)

Chapter 1

Introduction

A lot of research is aimed at developing procedures for continuous monitoring of glucose in diabetics, where optical sensing is widely researched. Optical sensing can be non-invasive and techniques such as microwave spectroscopy, NIR spectroscopy and Raman spectroscopy have been used to measure glucose [2]. Some research groups, e.g. at IES NTNU, are focusing on developing an integrated lab-on-a-chip (LOC) device which can monitor blood sugar levels and administer insulin when needed. A LOC can for instance be implanted, to measure the blood sugar directly, or the measurements can be taken indirectly, e.g. via the saliva, as one non-invasive approach [3]. Raman scattering is normally of very low intensity: The Raman spectrum of a glucose solution with a concentration similar to physiological blood sugar levels is practically impossible to measure without enhancement. However, Raman measurements are non-destructive to the samples, they do not require extensive sample preparation and can be performed in aqueous solutions. Water has a very weak Raman spectrum in the VIS region of the EM spectrum, making it easier to observe the spectrum of glucose in water than in other media [4].

In 1974, Fleischmann discovered that rough silver electrodes, which accidentally fell in contact with pyridine, increased the Raman signal of the substance by several orders of magnitude [5]. This launched research in what has since been called surface-enhanced Raman spectrocopy (SERS), alternatively surface-enhanced Raman scattering. In recent years, SERS has been researched for its application in sensing biologically active molecules, such as DNA, proteins, viruses, glucose and even diagnosis of diseases such as cancer [6], [7]. Gold is also a much used metal in SERS applications, though it has not demonstrated signal enhancement as strong as that of silver. Due to its chemical inertness, however, gold has shown its advantages in *in vivo* applications, such as optical fiber probes patterned with gold nanostructures, for blood glucose measurement [8].

1.1 SERS

As will be explained in more detail in Chapter 3, Raman scattering is inelastic light scattering, where a part of the energy of the incident light can be absorbed by the analyte molecule. The scattered light emitted by the molecule is then of a lower frequency. Raman scattered light can also be of a higher frequency, if the light waves gain energy from the molecule. Surface enhanced Raman scattering is the complex mechanism where the light scattered by the analyte molecule is amplified by the field enhancement on the surface of plasmonic nanostructures. Gold and silver are examples of metals that have conductive

surface electrons that, when excited by incident light, start oscillating with the light waves. These collective electron cloud oscillations are called plasmons.

As a demonstration of SERS enhancement, Figure 1.1 shows first the unenhanced Raman spectrum of a drop of 1000 mM aqueous glucose solution on a microscope slide. The glucose Raman spectrum is completely overshadowed by that of water and the fused silica slide. This demonstrates the shortcomings of the traditional Raman spectroscopy, in that one needs very large concentrations of a substance to be able to find it in the spectrum. Figure 1.1b, however, clearly shows the Raman spectrum of glucose. Here, the slide was coated with a 120 nm thick gold film by evaporation and the spectrum remeasured [1, pp. 55-56].

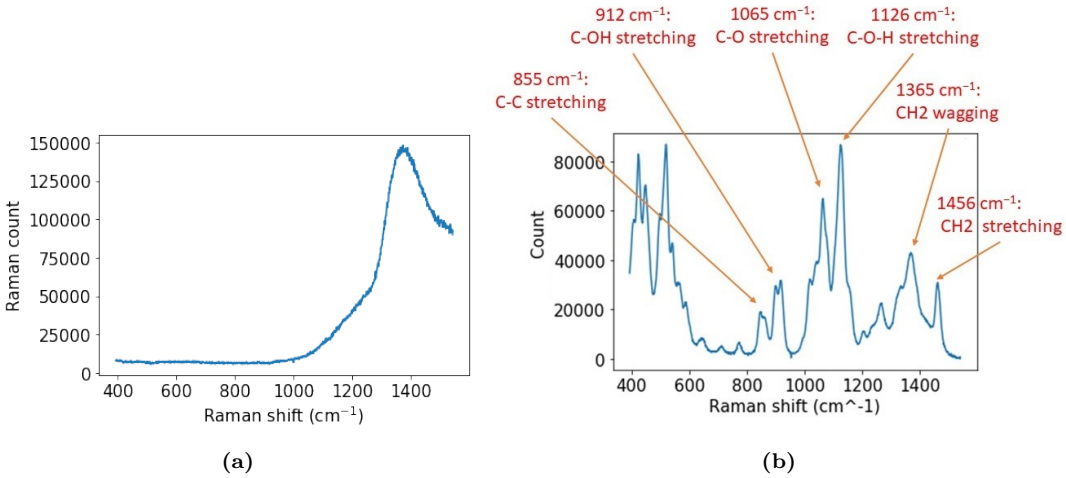

(a) **(b)**

Figure 1.1: Raman spectrum plots of a 1000 mM aqueous glucose solution on a fused silica microscope slide. (a) The unenhanced Raman signal, from a single drop of glucose solution directly on the slide. (b) Enhanced Raman spectrum from the same drop, placed on a slide which had been coated with a 120 nm thick gold film. Image annotated with positions of the vibrational modes of glucose.

The enhanced Raman spectrum has been annotated with wavenumber of the glucose molecule's vibrational modes. These correspond to the energy absorbed by the molecule when the respective bonds are vibrating [9], [10]. The enhancement factor (EF) was estimated as approximately $3.0 \cdot 10^4$ [1, p. 59]. This is however still not a large enhancement and one would not be able to measure low concentrations of glucose, typical of the values measured in human blood. The potential SERS enhancement factors achievable are estimated to be on the order of $10^{12} - 10^{14}$ from electromagnetic contribution, and an additional $10^2 - 10^3$ from a chemical contribution. So far, EFs of $10^6 - 10^8$ have been reported in experiments [11], [12], [13]. However, authors such as Sooraj *et al.* [9], have reported measurements of glucose levels lower than those typically found in blood using SERS.

1.2 Diabetes and blood sugar levels

As the primary motivation for the project was to build a modeling platform for the design of SERS sensors for continuous measurements of blood glucose, a short review of diabetes and healthy versus unhealthy blood sugar levels is needed.

Diabetes mellitus is a disease where not enough insulin is produced, or the insulin is not used properly by the body [14]. The blood sugar then may stay at a dangerously high level for prolonged periods of time. Without enough insulin to help cells take up glucose, cells start dying of nutrient deprivation. Glucose can attach itself to the red blood cells, leading to

glycation of the hemoglobin, and impairs their ability to bring nutrients and oxygen to other cells. Left untreated, the condition may lead to ketoacedosis as cells do not get glucose and oxygen are forced to use other sources of energy, producing ketones as a byproduct, which gradually poisons them. Loss of eyesight or numbness are common serious first symptoms.

Diabetes types

Clinically, diabetes is diagnosed by a test measuring the concentration of glycated hemoglobin, HbA1c, in a blood sample [15]. This gives information about the average blood sugar level over the last 4-12 weeks. If the average value was 48 millimoles per mole hemoglobin, then the person is diagnosed as diabetic, after which one tests for antibodies of pancreatic beta cells to find out if the type is I or II.

Type I diabetics are dependent on externally administered insulin. This condition is seen in about 5-10 % of all diabetes cases. Type II diabetes is seen in 90-95 % of all diabetics [16]. Initially, Type II diabetics do not have to inject themselves with insulin for survival, but may become more dependent on externally supplied insulin at severe stages of the affliction as their body develops resistance to its own insulin. Figure 1.2 shows the differences between these two main types of diabetes in terms of dependence on insulin. There are also other types of diabetes, that are either not permanent or that affect only specific groups of patients. Gestational diabetes during pregnancy is the most common example of the latter [16].

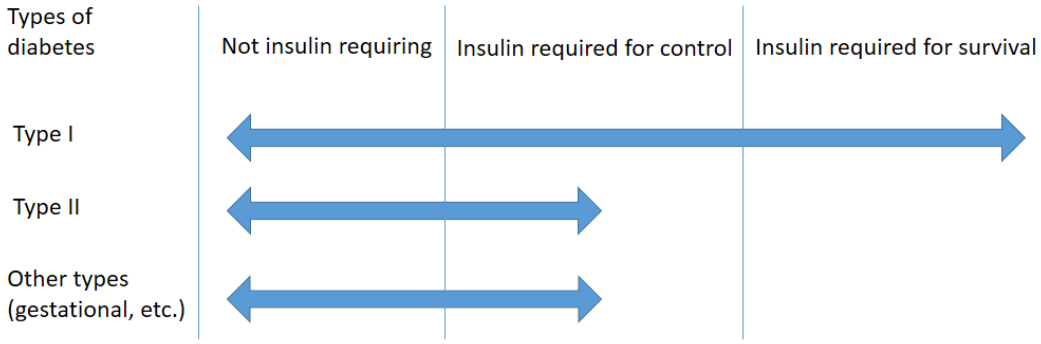

Figure 1.2: Diabetes types and the dependence on insulin of each type.

In 2014, about 420 million people were afflicted by diabetes of either Type I or Type II [17].

Blood sugar levels

The Fasting Plasma Glucose Test can be used to define high and low blood sugar levels. If the blood sugar level before breakfast or after at least 8 hours of fasting is at least 7.0 mM or higher, the blood sugar is defined as high. The condition is called hyperglycemia [14]. An alternative convention defines the level as high if there is 126 mg glucose per dL of blood or higher. An other test, Oral Glucose Tolerance test, is performed by having a person drink 75 g of glucose in aqueous solution and then measuring the glucose level in his or her blood two hours later. If the concentration is at least 11.0 mM then the blood sugar is high. This translates into 200 mg/dL. After three hours, the limit is set to 7.8 mM [16]. On the lower end, low blood sugar, hypoglycemia, is defined as when blood sugar is below 3.9 mM, or 70 mg/dL. The symptoms of hypoglycemia include dizziness, headaches and shakiness. At low blood sugar levels, hypoglycemic shock can occur, where the person may experience seizures or loses consciousness [18]. In rare cases, it can lead to death. The blood sugar limits presented here translate into a healthy blood sugar level range between

about 4.0 mM and 8.0 mM when at least three hours have passed since the last meal. This is illustrated in Figure 1.3.

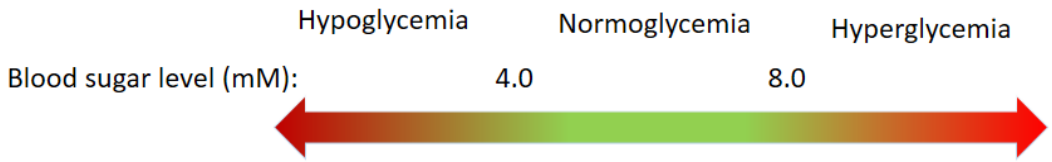

Figure 1.3: Blood sugar levels. Red indicates dangerous levels. Green indicates safe levels.

1.3 Nanostructures in SERS-based sensors. State of the art

Many types of nanostructures have demonstrated large SERS enhancement factors. Examples are metallic thin films, nanowires and arrays of metallic nanoparticles in various arrangements [4], [11], [19]. Coating dielectric or semiconducting particles with noble metals is a technique used to tune the resonances of the structure to e.g. the incident light wavelength [20], [21]. Additionally, these particles can be ordered into self-assembled monolayers by colloidal chemistry techniques which facilitates fabrication. A surface covered by a plasmonic monolayer is called a SERS substrate. Moreover, it has been demonstrated that surface roughness is a strong contributor to SERS [22]. Periodic arrays of self-assembled particles exhibit periodic surface roughness, which produces reliable enhancement factor measurements. Conversely, on randomly rough surfaces, the EF would depend strongly on where on the surface one places the drop with analyte molecules. Finally, the benefit of close-packed particles is that placing two or more plasmonic particles closely, they are coupled by their near fields, which can greatly enhance the EFs in small gaps between the particles. One widely researched class of periodic, metal coated particles, is the *gold film over nanospheres*, AuFON [8], [12], [23]. The EFs achieved with these structures are on the order of $10^6 - 10^8$.

Both periodic and disordered arrays of dielectric particles can be used for producing masks for hole-mask, or colloidal, lithography. Depositing gold or silver over the mask and subsequently removing it, can be used to pattern large areas [24]. These masks can be used to create 2D structures [11] and 3D structures [19]. The latter allows plasmon excitation along a third dimension and can potentially produce greater EFs.

Ion and electron beam lithography can also be used to produce nanoscale SERS substrates [25]. Currently, however, these techniques are too time-consuming and expensive to cover entire substrate areas.

1.4 Simulating the SERS EF in AuFONs

The goal of this thesis is to use physical principles to build an AuFON model using the finite element method (FEM). The finite element method allows solving Maxwell's equations directly by discretizing the simulation space and particles into a volumetric mesh. This allows solving for arbitrary particle shapes and arrangements, unlike the dipole approximation methods commonly referenced in literature.

The model will be able to predict how the resonances change when the dielectric core diameter is changed, when the gold film thickness changes, as well as a change in surrounding

medium or substrate. While the literature most often presents Raman intensity plots, such as the ones in Figure 1.1, the model calculates the SERS EF directly from electromagnetic computations. The value is estimated using an approximation, based on the structure's surface field. Due to the many complexities of a real-world AuFON sample, it can therefore be difficult to verify that a model, with the necessary simplifications that come from the time limitations of a master's level thesis, matches the few available explicit SERS values found in the literature.

The modeling process uses a bottom-up approach, where the single homogeneous gold particle model presented in the project thesis [1] is reviewed and extended to estimate the SERS EF. The model is compared against analytical Mie calculations, as well as the numerical discrete-dipole approximation, which is also widely used. The criteria for comparison are the resonances seen in the extinction spectrum of the sphere. Emphasis is put on comparing how these resonances match with the analytical Mie solution, how they change with different particle sizes, composition – i.e. replacing gold with silver – and a change of surrounding medium from air to water. The model is also compared with the discrete-dipole approximation, to investigate these models early on and be sure they can be used for comparison on more advanced stages, when Mie is no longer valid and published results are not available. These two numerical models also allow comparing the surface field enhancement and SERS EF estimation.

This model is then extended to particle dimers and arrays, to verify that the model performs as expected both in the near and far field. The dimer is used as an approximation of the properties seen in arrays during strong near-field coupling. The gold model, with several diameters, is benchmarked on what maximum SERS EFs it can achieve.

The array models are also studied thoroughly for their far-field properties, to ensure that they behave physically in both near-field and far-field. 1D and 2D arrays of gold and silver are investigated, how new lattice resonances emerge and couple with the plasmon resonances seen in single-particle models. These narrow lattice resonances have important implications for resonance tuning, but it is shown that they do not demonstrate the SERS enhancement potential seen in state-of-the-art results in literature. Here, the coupled-dipole approximation is a useful tool for comparing with the FEM. Because of the easier comparability of silver models to published results, the emphasis is on silver arrays, but gold arrays are also investigated.

Going further, the homogeneous gold particle model is then replaced with a nanoshell model, with a dielectric particle core and a thin metal film around it. These particles are simulated for various film thicknesses, revealing that they allow tuning resonances much more than the solid metal particles and may exhibit stronger surface fields. However, they lose these properties as the film becomes thicker.

The final periodic structure consisting of such gold nanoshells is an approximation of an AuFON structure. The model is further fitted to an actual AuFON shape by implementing a "top hat" structure, where the gold film does not fully envelop the core, but only its upper half. SERS EFs from both periodic nanoshells and top hats are estimated for different film thicknesses and particle spacings, as well as compared against available experimental data.

1.5 Thesis structure

Chapter 2 will review how an AuFON is fabricated, based on the procedure used in the project thesis. Chapter 3 will present the theoretical foundation for the model, from basic electromagnetic principles and a solid state physics model for metals, to a model for the scattering of light and a description of surface plasmons.

As the FEM modeling is performed in COMSOL, Chapter 4 presents the details of implementing the model in COMSOL, as well as an introduction to the reference DDA and CDA methods used. The chapter also presents an outline of the modeling process.

Chapter 5 finally presents the calculations performed with the model and how it compares to theory, the reference methods, analytical solutions and published results.

The appendices contain a mathematical description of the FEM, with a discussion of some computational issues. A description of the practical aspects of using DDSCAT, the DDA implementation used in this thesis, and a listing of all the codes written for this thesis. This listing contains the CDA and Mie implementations. There is also section with secondary simulation results, which explore larger sphere models.

Chapter 2

A review of the fabrication of AuFON SERS substrates.

Before introducing the physical models used in this thesis and how they were implemented numerically, in COMSOL or Python code, it is instrumental to review how AuFONs are fabricated and characterized in a laboratory environment. This is not meant to be an in-depth review of fabrication techniques, but merely an overview of the different steps, with illustrations, to get the reader familiar with what an AuFON structure is. To better understand the description of the modeling approach that follows in the next chapters.

It was already mentioned that there are currently many techniques for producing plasmonic structures for use as SERS substrates. Common lithographic techniques that have been demonstrated in the last two decades are electron beam and colloidal (hole mask) lithography [4], [11], [13], [25] along with more simple techniques such as drop coating, spin coating or Langmuir-Blodgett deposition [13], [26].

In this review of AuFON fabrication, we take a quick look at drop coating, following the approach previously presented in the project thesis [1, Ch. 4]. For detailed reviews on fabrication using Langmuir-Blodgett, see e.g. Zhang *et al.* [27] or Braathen [28]. Zhang *et al.* also present a detailed approach for spin coating, which was used for demonstrating a colloidal crystal in Figure 2.3a below, due to the lack of a good image of a colloidal crystal produced by drop coating. All these methods have the same goal: produce a close-packed crystalline monolayer of dielectric nano- or microspheres, typically made of polystyrene, on a substrate, for the subsequent coating of the sphere layer with gold.

Figure 2.1 is an scanning electron microscope (SEM) image of the resulting hexagonal close-packed AuFON array, consisting of 500 nm polystyrene spheres coated with 120 nm gold film by evaporation [1].

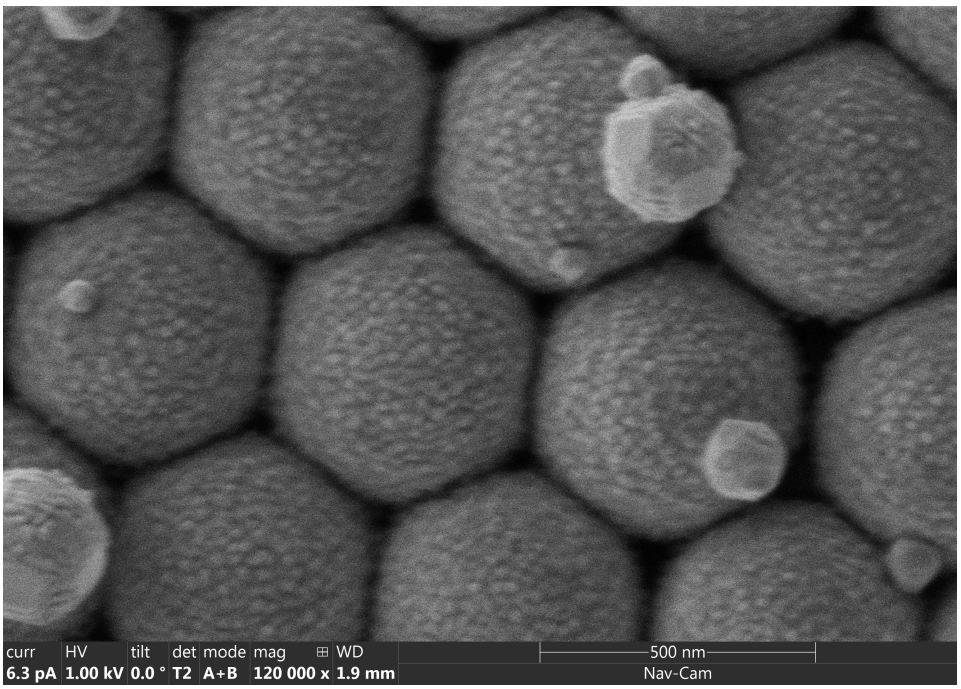

Figure 2.1: (a) SEM image, magnified 120 000 times, of an AuFON array consisting of particles with a 500 nm polystyrene core and 120 nm gold film. Reproduced from previous work [1].

A substrate, such as a microscope slide, is cleaned using a standard piranha cleaning process [27], and then one deposits a polystyrene sphere suspension, diluted with ethanol and/or DI water to obtain a self-assembled monolayer of spheres on the substrate. The optimal weight percent to achieve good area coverage, but at the same time avoid multilayered patches, depends on the physical size of the spheres in suspension, as well as the initial concentration.

The suspension is left to air dry, whence the spheres are drawn close to one another by the capillary forces during the evaporation of solvent and arrange themselves in a hexagonal close-packed crystalline lattice. Figure 2.2 illustrates this conceptually. Macroscopically, it creates a colloidal crystal with an iridescent surface that diffracts light.

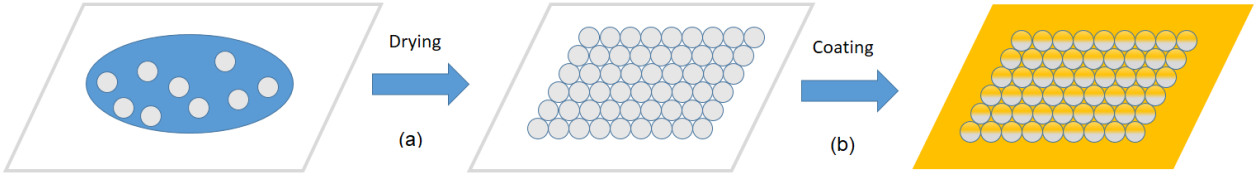

Figure 2.2: (a) Illustration of the AuFON fabrication process. Part (a) shows the suspension being dropped onto a substrate. During solvent evaporation, the spheres are drawn together and form a colloidal crystal. Part (b) shows the coating of spheres with metal by evaporation. Note that the spheres are coated only at the top, as the vapor doesn't reach the spheres' underside due to the tight packing. Image modified from previous work [1].

A photoimage of such a colloidal crystal is shown in Figure 2.3a. This sample was produced by spin coating a silicon substrate with 500 nm polystyrene spheres, but the result is similar to a drop cast monolayer of spheres.

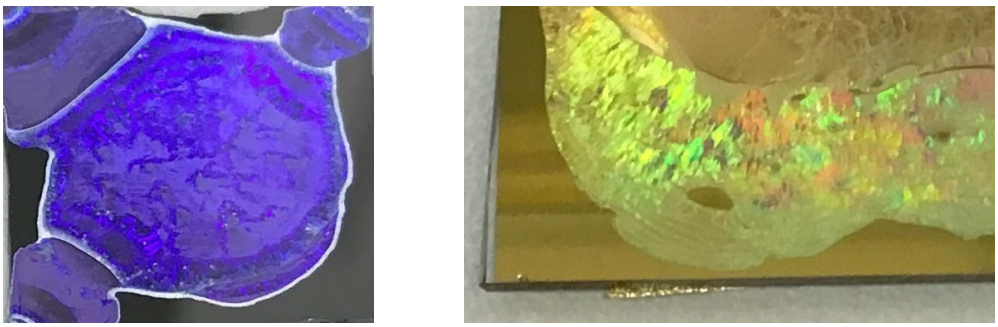

(a) **(b)**

Figure 2.3: Macroscopic view of the results of each fabrication step. (a) The colloidal crystal formed after depositing the spheres on a substrate. This specific image shows a silicon substrate spin coated with 500 nm polystyrene spheres, but drop cast samples would look similar, with the characteristic iridescence because of light diffracted by the periodic structure. (b) The AuFON after the colloidal crystal has had gold evaporated onto it. This is a real drop cast sample on a fused silica microscope slide.

Next, the sample is coated with metal using an evaporation process, to the desired thickness. This is shown in Figure 2.2, part (b). Note that the spheres are coated only at the top, as the vapor doesn't reach the spheres' underside due to the tight packing. This will be clearly seen in a SEM image, Figure 4.13, of real coated particles in Chapter 4. Figure 2.3b shows the final structure macroscopically. The image shows the actual result of drop coating on a microscope slide, coated with gold.

After this step, the sample is characterized using tools such as the SEM or atomic force microscopy (AFM). The Raman spectroscopy may damage the sample, if the colloidal crystal has many defects and one is not careful, and so all the non-invasive characterization techniques must be performed before it.

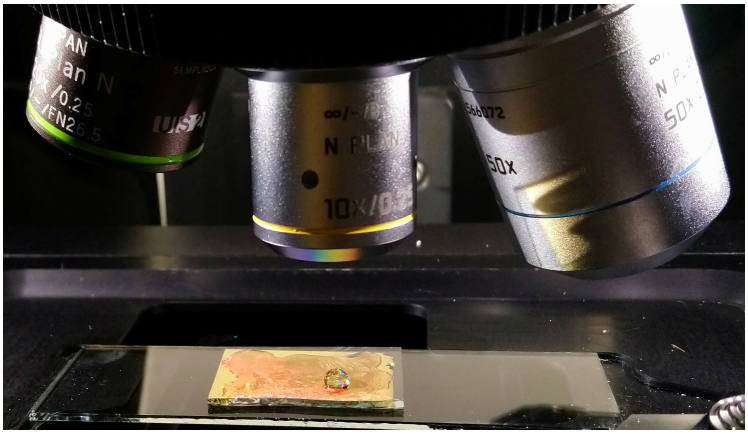

Figure 2.4: Illustration of the Raman spectroscopy setup, showing the substrate with the AuFON structure on its surface, placed under the microscope objective of a Raman spectrometer. There is a droplet with aqueous glucose solution placed on top of the AuFON structure and the microscope is focused on this drop [1].

Finally, the sample can be inserted into a Raman spectrometer to measure the intensity peaks. In the case of an aqueous glucose solution, this can be performed by simply placing a drop of the solution on top of the SERS substrate and then focus the spectrometer on the drop, as in Figure 2.4. From the Raman spectroscopy, one can calculate the SERS enhancement factor using Equation (3.52), which will be presented in the next chapter. The

Raman measurements may be performed using both VIS and NIR wavelengths, but there are advantages of using NIR wavelengths, to avoid the effects of fluorescence in glucose measurements [29]. We will assume throughout the thesis that the wavelength is 785 nm, as used in previous work at IES NTNU [8], [28] and in the experimental part of the project thesis [1].

Chapter 3

Theory

Surface-enhanced Raman scattering is explained by solid-state physics and electromagnetics. A review of relevant topics is presented here.

First, a short review of electromagnetism leading to the wave equation is presented. Then, central expressions from the Lorentz-Drude of metals are derived, with a short discussion on the polarization of dipoles and local fields. An extensive derivation of Mie theory, based on Mie coefficients, follows. The expressions for scattering and absorption cross sections, originally derived by Gustav Mie [30], are directly used for verifying the single particle FEM model.

Raman scattering is briefly reviewed from a quantum mechanical perspective. Surface plasmons (SP) and the mechanism of SERS, as it is currently understood, is discussed, including a short section on surface roughness. Localized field enhancement by plasmonic structures is one of the most important mechanisms that leads to enhancement of the Raman spectrum in SERS [4] and so attention is devoted to near-field coupling. However, to make the model complete, far-field coupling in periodic structures that gives rise to Fano resonances is also explained using a model with coupled harmonic oscillators.

3.1 Electromagnetism

Electromagnetic (EM) waves are electric and magnetic fields that oscillate together, governed by Maxwell's equations in their harmonic form [31, p. 58] with angular frequency ω,

$$\nabla \times \mathbf{E} = -i\omega\mu\mathbf{H} \tag{3.1}$$

$$\nabla \times \mathbf{H} = \mathbf{J} + i\omega\epsilon\mathbf{E} \tag{3.2}$$

$$\nabla \cdot \mathbf{E} = \frac{\rho}{\epsilon} \tag{3.3}$$

$$\nabla \cdot \mathbf{H} = 0, \tag{3.4}$$

where $\mathbf{E}$ and $\mathbf{H}$ are the electric and magnetic field vectors, $\mathbf{J}$ is the current density vector, $\epsilon = \epsilon_r\epsilon_0$ is the electric permittivity of the medium, as the product of the dielectric function and the permittivity of free space, $\mu = \mu_r\mu_0$ is the magnetic permeability of the medium. ρ is the charge density. i is the imaginary unit Throughout this thesis, EM waves propagate through a dielectric medium. That is, setting $\mathbf{J} = 0$ and charge density $\rho = 0$.

The complex dielectric function is defined [31, p. 230] as

$$\epsilon_r(\omega) = \epsilon'(\omega) + i\epsilon''(\omega) = 1 + \chi(\omega), \tag{3.5}$$

ϵ' represents the real part and ϵ'' its imaginary part. χ is the electric susceptibility and is a complex value. The parentheses indicating frequency dependence in (3.5) were omitted before for conciseness of the notation. This will be continued throughout this text. The refractive index is defined, for non-magnetic materials ($\mu_r = 1$), as $n_r = \sqrt{\epsilon_r}$ [32, p. xii]. Similarly to the dielectric function, it can also be represented as a sum of a real, n, and an imaginary part, k [31, p. 27],

$$n_r = n + ik. \tag{3.6}$$

The electric and magnetic fields are defined as time-dependent plane waves,

$$\mathbf{E}(\mathbf{r}) = \mathbf{E}_0 \exp\left(i\mathrm{k}\mathbf{r} - i\omega t\right) \tag{3.7}$$

$$\mathbf{H}(\mathbf{r}) = \mathbf{H}_0 \exp\left(i\mathrm{k}\mathbf{r} - i\omega t\right). \tag{3.8}$$

$\mathrm{k} = n_r \mathrm{k}_0 = \omega\sqrt{\mu_0\epsilon_0}$ is the wavenumber in the medium, expressed using the wavenumber in vacuum, k_0. To distinguish the wavenumber from the extinction coefficient, it is in Roman font type, not italic, following Bohren and Huffman [31, p.27]. Solving (3.1) for the magnetic field and inserting it into (3.2), yields

$$-\frac{1}{i\omega\mu_0}\nabla \times \left(\frac{1}{\mu_r}\nabla \times \mathbf{E}(\mathbf{r})\right) = i\omega\epsilon\mathbf{E}(\mathbf{r}). \tag{3.9}$$

Multiplying the whole expression by the negative fraction on the left-hand side produces the wave equation in inhomogeneous media,

$$\nabla \times \left(\frac{1}{\mu_r}\nabla \times \mathbf{E}(\mathbf{r})\right) - \mathrm{k}_0^2\epsilon_r\mathbf{E}(\mathbf{r}) = 0. \tag{3.10}$$

For a non-magnetic medium the curl expression can be evaluated as

$$\nabla^2\mathbf{E}(\mathbf{r}) - \mathrm{k}_0^2\epsilon_r\mathbf{E}(\mathbf{r}) = 0. \tag{3.11}$$

The models will be simulated using a planar wave polarized along a plane, e.g. along the y axis, and propagating in another direction, such as the x-direction, i.e. transverse waves. For particles arranged in arrays, polarization of light along the array axis – assume for now a 1D array, a "string" of particles – is called p (parallel) polarization. Orthogonal to the array, it is called s polarization.

We assume for simplicity that the propagating medium is homogeneous. The wave equation becomes a homogeneous scalar wave equation.

$$\frac{\partial^2 E_y}{\partial x^2} - \mathrm{k}_0^2\epsilon_r E_y = 0. \tag{3.12}$$

3.2 Material properties

The metal particles and electron oscillations on their surface, called plasmons, which are the physical basis of SERS, depend on the particles' material properties. This section presents the Lorentz-Drude metal model used to simulate the metal particles in this thesis and how

metal particles act in the presence of external EM fields.

3.2.1 Lorentz-Drude model of metals

In metals, the electrons at Fermi level can be excited to higher intraband energy states with little photon energy and described using the free electron model. The dielectric function, previously denoted ϵ_r, is now ϵ. Unless otherwise noted, variable definitions from the preceding sections are used.

The dielectric function can be expressed in terms of the plasma frequency ω_p and EM field frequency ω,

$$\epsilon(\omega) = 1 - \frac{\omega_p^2}{\omega^2}. \tag{3.13}$$

ω_p is the frequency above which the electron cloud can no longer oscillate in phase with the field and the metal starts behaving as a dielectric [33, pp. 396-397].

However, in a metal not all electrons are behaving as free electrons, but rather as bound oscillators which resonate when excited by incident radiation. Lorentz oscillators are modeled [31, Ch. 9.1] as homogeneous masses on springs with stiffness constant K. The resulting dielectric function from the Lorentz model is

$$\epsilon = 1 + \chi = 1 + \frac{\omega_p^2}{\omega_0^2 - \omega^2 - i\gamma\omega}, \tag{3.14}$$

where ω_0 is the resonance frequency and γ a damping constant. The oscillator model has the optical characteristic that around ω_0, there's high absorbance.

Setting the constant $K = 0$, which implies $\omega_0 = 0$ [31, Ch. 9.4], the dielectric function is

$$\epsilon = 1 + \chi = 1 - \frac{\omega_p^2}{\omega^2 + i\gamma\omega}, \tag{3.15}$$

which constitutes the Drude model of a free electron *metal*. Since the scattering of electrons in a metal at ambient temperatures is mostly with phonons, γ is normally much smaller than ω_p. At visible and UV light frequencies, the real part of ϵ is therefore approximately equal to that of a free electron,

$$\begin{aligned} \epsilon' &\approx 1 - \frac{\omega_p^2}{\omega^2} \\ \epsilon'' &\approx \frac{\omega_p^2\gamma}{\omega^3}. \end{aligned} \tag{3.16}$$

In the low frequency limit, the oscillator properties are more pronounced.

Using that susceptibilities are additive, one can add multiple Lorentz oscillator susceptibilities in Eqn. (3.14) to the Drude model, (3.15), each with its respective resonance frequency ω_j, to account for multiple resonances. The dielectric function is then expressed as a sum of the intraband (Drude model) ϵ_f, and interband (Lorentz oscillators) effects ϵ_b,

$$\epsilon(\omega) = \epsilon_f(\omega) + \epsilon_b(\omega) \tag{3.17}$$

$$\epsilon_f(\omega) = 1 - \frac{f_0\omega_p^2}{\omega(\omega - i\gamma_0)} \tag{3.18}$$

$$\epsilon_b(\omega) = \sum_{j=1}^{k} \frac{f_j\omega_p^2}{(\omega_j^2 - \omega^2) + i\omega\gamma_j}. \tag{3.19}$$

The notation here is borrowed from Rakic *et al.* [34], where a quantum-mechanical (QM) formulation is used: k is the number of oscillators with resonance frequencies ω_j (in QM, the energy difference between excited state j and ground state), oscillator strength – probability of excitation to state j from ground state – f_j, and γ_j is the damping constant. Essentially, the QM formulation represents a weighted-average of Lorentz oscillators as the bound electron term.

3.2.2 Polarization of particles

When a metal particle is placed in an electric field, the free electrons move against the field, separating the charges on the particle surface, as shown in Figure 3.1a. This creates a dipole moment $\mathbf{p} = ve\mathbf{r}$, in the direction $\mathbf{r}$ of charge separation [33, p. 455]. v is here the number of charges per volume and e is the elementary electron charge. For every atom, ion or molecule j, the local field contribution from the total dipole moment in j, p_j, is

$$\mathbf{E_j}(\mathbf{r_j}) = \frac{3(\mathbf{p_j} \cdot \mathbf{r_j}) \cdot \mathbf{r_j} - \mathbf{r_j}^2 \mathbf{p_j}}{4\pi\epsilon_0 \mathbf{r_j}^5}. \tag{3.20}$$

With the net dipole moment as polarization $\mathbf{P}$, and displacement field $\mathbf{D} = \epsilon_0\mathbf{E} + \mathbf{P}$, one arrives at the depolarization field

$$\mathbf{E_{depol}} = -\frac{\mathbf{P}}{\epsilon_0} \tag{3.21}$$

in the longitudinal wave limit (for $\epsilon(\omega) = 0$). This is the restoring force that pushes the separated charges back together, as seen from Figure 3.1.

Suppose that the dipole is located inside an ellipsoidal crystal with principal axes x, y, z. The axes give rise to depolarization factors N_j which satisfy $N_x + N_y + N_z = 1$ and $\epsilon_0 E_{depol} = -N_x P_x - N_y P_y - N_z P_z$. Their values are derived from the ratios between the principal axes. For a sphere, all $N_j = 1/3$ and the depolarization field is equal to $-P/3\epsilon_0$ [33, pp. 456-458].

Now, imagine that a sphere was cut out from the crystal ellipsoid, as in Figure 3.1b, but is then inserted back in. The discontinuity gives rise to a surface charge that cancels the depolarization field by inducing a Lorentz field. In a spherical cavity, this field is $\mathbf{E_L} = P/3\epsilon_0$ [33, p. 462]. The local field ([33, pp. 460-462]) in the cut out sphere is then the sum of the depolarization field, Lorentz field and dipole contributions from atoms inside that sphere, as well as the externally applied field E_0,

$$\mathbf{E_{local}} = \mathbf{E_0} + \mathbf{E_L} + \mathbf{E_{depol}} + \mathbf{E_{dipole}}. \tag{3.22}$$

$\mathbf{E_{dipole}}$ is dependent on crystal structure. In a reference atomic site in a sphere, in cubic crystal lattices, it can be shown that $\mathbf{E_{dipole}} = 0$ [33, p. 460] if all the atoms are replaced with point dipoles and arranged parallel to one another. Defining the macroscopic field $\mathbf{E}$ as the sum of external and depolarization fields, the local field is given by the Lorentz relation,

$$\mathbf{E_{local}} = \mathbf{E} + \frac{\mathbf{P}}{3\epsilon_0}. \tag{3.23}$$

Moreover, in a sphere in a cubic environment, the depolarization and Lorentz fields cancel, leaving the local field equal to the external field,

$$\mathbf{E_{local}} = \mathbf{E_0}. \tag{3.24}$$

The polarizability of an atom or molecule is the factor α that expresses the dipole moment as

$$\mathbf{p} = \alpha \mathbf{E}_{\mathbf{local}}. \tag{3.25}$$

For a molecule or larger particle, one has to sum over all atoms j and their concentrations N_j to get net polarization,

$$P = \sum_j N_j \alpha_j E_{local}. \tag{3.26}$$

Inserting Eqn. (3.23) into (3.26) and using Eqn. (3.5) we obtain

$$\frac{\epsilon - 1}{\epsilon + 2} = \frac{1}{3\epsilon_0} \sum N_j \alpha_j, \tag{3.27}$$

the Clausius-Mossotti equation that relates the dielectric function to polarizability [33, p. 464].

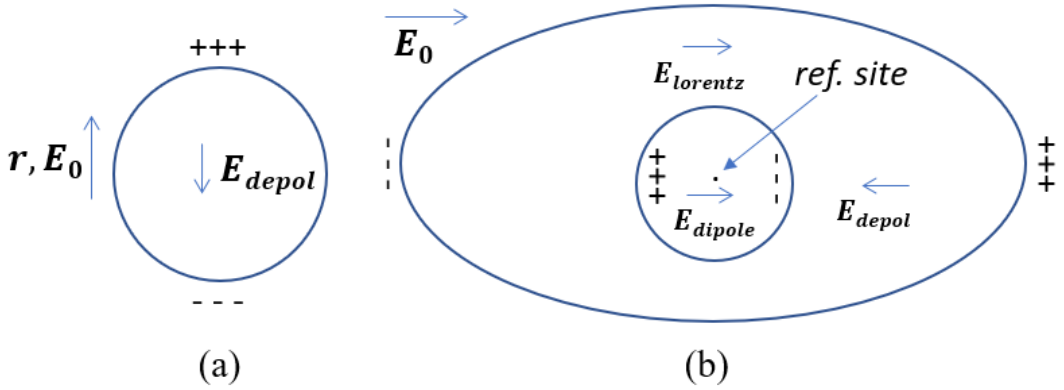

Figure 3.1: (a) Dipole moment emerging under the influence of an external field **E**. Directions of charge separation r and depolarization field are also shown. The depolarization field is due to the surface charge. (b) Ellipsoidal crystal subjected to an external field. The depolarization field, Lorentz field and dipole contributions to the local field are shown. The local field is the sum of all fields in the plot.

3.3 Scattering and absorption from particles

The following presentation is based on Chapters 3 and 4 of Bohren and Huffman [31]. When a plane wave interacts with a particle in its path, some of the non-transmitted energy is absorbed by the particle and some is scattered in different directions. The sum of these two effects is the extinction caused by the particle: Suppose a detector was placed behind the particle and the light intensity received was I. Then, if there was no particle in its path, the light received by the detector would be $I_0 > I$, where I_0 is the initial intensity of light, as seen in Figure 3.2.

An imaginary integrating sphere of radius r is placed around a particle of radius a, to "collect" the flux lines scattered by its surface, allowing us to express the rate at which the electromagnetic energy crosses that sphere [31, p. 69] as

$$W_a = -\int_A \mathbf{S} \cdot \hat{\mathbf{e}} dA, \tag{3.28}$$

where $\mathbf{S}$ is the Poynting vector, $\mathbf{S} = \mathbf{E} \times \mathbf{H}^*$, which defines the direction of power flow [32, p. 40]. A is the surface area of the imaginary sphere and $\hat{\mathbf{e}}$ defines the normal vector to A.

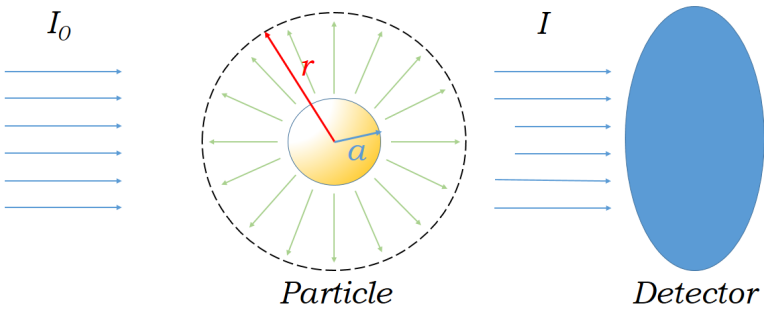

Figure 3.2: Light of intensity I_0 is partially extinct by a scattering and absorbing particle in its path, allowing an intensity $I < I_0$ to reach the detector. An imaginary integrating sphere (black, dotted line) is "collecting" the scattered flux lines. r is the radius of the integrating sphere. a is the radius of the particle. Some of the field lines going into the detector are a bit shorter, to illustrate that transmission and forward scattering may be lower in intensity than that of incident light due to absorption. The detector in the figure is a simplified representation.

Using that the total Poynting vector of a scattering problem is the sum of vectors for the incident and scattered radiation, as well as extinction [31, p. 63],

$$\mathbf{S} = \mathbf{S_i} + \mathbf{S_s} + \mathbf{S_{ext}}. \tag{3.29}$$

The extinction vector here represents the interaction between scattered and incident fields. Provided that the medium within the integrating sphere is non-absorbing, the particle is the only absorbing body withing the imaginary sphere. $W_a = W_i - W_s + W_{ext} = -\int_A \mathbf{S_i} \cdot \hat{\mathbf{e}}\, dA + \int_A \mathbf{S_s} \cdot \hat{\mathbf{e}}\, dA - \int_A \mathbf{S_{ext}} \cdot \hat{\mathbf{e}}\, dA$ is then the particle's absorption rate. In a non-absorbing medium W_i vanishes [31, p. 70], allowing the expression of the extinction rate as the sum of scattering and absorption rates

$$W_{ext} = W_a + W_s. \tag{3.30}$$

Dividing these by the incident radiation intensity I_0 yields the scattering, absorption and extinction cross-sectional areas, from hereon called *cross sections*,

$$\sigma_s = \frac{W_s}{I_0} \quad \sigma_a = \frac{W_a}{I_0} \quad \sigma_{ext} = \frac{W_{ext}}{I_0}. \tag{3.31}$$

The extinction cross section can be understood intuitively as the shadow that the particle is casting on a detector placed some distance behind it. A part of the detector's area is obscured by the shadow of the particle. The area covered by the shadow can be higher than the particle's geometrical cross section, G. G is the projection of the particle's surface area onto a plane perpendicular to the light's direction of propagation. Figure 3.3 illustrates this.

Dividing the cross sections above by the geometric cross section G of the scattering particle, produces the efficiency factors

$$Q_s = \frac{\sigma_s}{G}, \quad Q_a = \frac{\sigma_a}{G} \quad \text{and} \quad Q_{ext} = \frac{\sigma_{ext}}{G}. \tag{3.32}$$

These dimensionless factors will be called *efficiencies*. Eqn. 3.32 lists the scattering, ab-

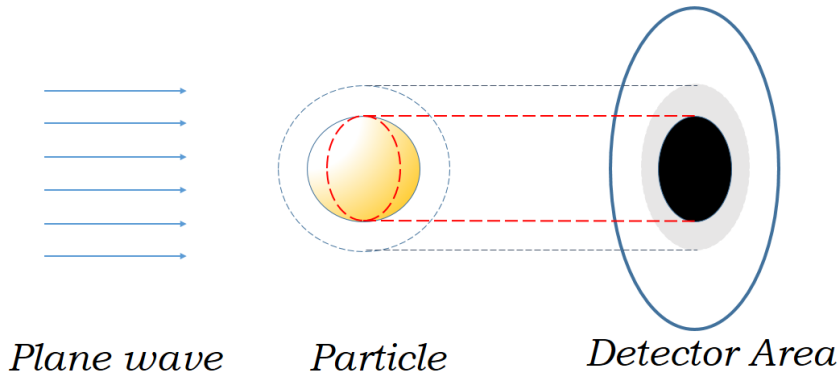

Figure 3.3: Extinction cross section intuitively illustrated as the shadow of a particle, in the path of the incident light, on the surface of a detector. The area of the shadow is in this case equal to the particle's geometric cross section.

sorption and extinction efficiencies, respectively. These are normalized values that allow for a comparison of e.g. the scattering of light by particles of different sizes. In Figure 3.3, the extinction cross section is equal to the particle's geometric cross section (red dashed ellipse within the particle's bounds) and the extinction efficiency is therefore exactly equal to unity. However, the efficiencies can be higher than unity (or lower) [31, p. 72]. A metal particle can have a scattering cross section larger than its geometric cross section G. In this case, as extinction is the sum of absorption and scattering, both positive, it will also be larger than G. Figure 3.3 illustrates this by imagining as if a highly efficient scattering body casts a larger shadow (light grey) than its geometric cross section (black) on the detector. The illustration is based on Bohren and Huffmann's interpretation of the extinction cross section [31, p. 75]. In practice, extinction is measured as described in the beginning of this section, with the accompanying illustration in Figure 3.2.

Using the vectors in Figure 3.2, we follow Sarid and Challener [32, p. 203] in defining the near-field scattering by evaluating the integral (3.28) at $r = a$. That is, integrating the electric field at the particle surface. Far-field scattering is then defined for all $r >> a$. Formally, scattering is defined in the forward direction, with backscattering quantifying scattering in the other direction. However, extinction accounts for scattering in all directions [31, p. 75].

3.3.1 Mie coefficients

The qualitative presentation of optical cross-section and efficiencies above is now followed by a derivation of analytical expressions for these using Mie theory, so as to calculate the scattering of light from a homogeneous gold sphere.

As the electric field polarizes the particle, it excites multipole resonant modes on its surface. Smaller particles are polarized as dipoles and Mie theory can be simplified according to the quasi-static approximation in Section 3.3.2 below.

For large spheres, the field is not able to homogeneously polarize the sphere as a dipole, due to phase retardation [35], [36, pp. 73-74], and we need full Mie theory to model these. The polarization is now defined as $\mathbf{P} = \epsilon_0 \epsilon_m \alpha \mathbf{E_0}$ [36, p. 68], with ϵ_m being the surrounding medium's dielectric constant.

This leads to the excitation of higher-order multipole modes. Using size parameter $x = \frac{2\pi a}{\lambda}$, where λ is the excitation wavelength in the medium, the polarizability can be expressed [36,

p. 74] as

$$\alpha = \frac{1 - \frac{1}{10}(\epsilon + \epsilon_m)x^2 + O(x^4)}{(\frac{1}{3} + \frac{\epsilon_m}{\epsilon - \epsilon_m}) - \frac{1}{30}(\epsilon + 10\epsilon_m)x^2 - i\frac{4V\pi^2\epsilon_m^{3/2}}{3\lambda_0^3} + O(x^4)}. \tag{3.33}$$

V is the volume of the particle and λ_0 is the excitation wavelength in free space. This expression can be split into several parts. $O(x^4)$ represents the higher-order multipolar excitation modes, the second-order terms account for retardation and the depolarization field inside the sphere and the imaginary term in the denominator – radiation damping. The first term in the denominator accounts for the lowest-order, dipolar, mode.

The scattering cross section in the previous section can be shown to exhibit a quadratic dependency, $\sigma_{sca} \propto |\alpha|^2$, on polarizability. Absorption is linearly dependent on the imaginary part of polarizability α'', $\sigma_{abs} \propto |\alpha''|$, [32, pp. 213-214]. These relationship are used in deriving the dipole approximation in Section 3.3.2.

However, it is possible to calculate the optical cross sections by encapsulating the physics into Mie coefficients. The expressions for the scattering and extinction coefficients are then expressed as

[31, p. 103]

$$\sigma_{sca} = \frac{2}{x^2}\sum_{j=1}^{\infty}(2j+1)(|a_j|^2 + |b_j|^2) \tag{3.34}$$

$$\sigma_{ext} = \frac{2}{x^2}\sum_{j=1}^{\infty}(2j+1)\mathrm{Re}(a_j + b_j), \tag{3.35}$$

where j is an index denoting the order of the multi-pole modes. The coefficients a_j and b_j are two of the four Mie coefficients. The extinction cross section is obtained as the sum of scattering and absorption, as seen in Eqn. (3.30). In calculations, the infinite sums in (3.34) are approximated as a finite sum of N terms, where N can be expressed [31, p. 477] as

$$N = 2 + x + 4x^{1/3} \tag{3.36}$$

and rounded to the nearest integer. As an example, for a size parameter $x \approx 1$, corresponding to a particle of radius $a = 100$ nm and an excitation wavelength of 630 nm, N is equal to 7.

Since absorption can be found as the difference between extinction and scattering, we'll only focus on the first two coefficients. In the non-magnetic particle case, these assume the form

$$\begin{aligned} a_j &= \frac{m\psi_j(mx)\psi_j'(x) - \psi_j(x)\psi_j'(mx)}{m\psi_j(mx)\xi_j'(x) - \xi_j(x)\psi_n'(mx)} \\ b_j &= \frac{\psi_j(mx)\psi_j'(x) - m\psi_j(x)\psi_j'(mx)}{\psi_j(mx)\xi_j'(x) - m\xi_j(x)\psi_n'(mx)}. \end{aligned} \tag{3.37}$$

m is the relative refractive index of the scattering sphere to that of the surrounding medium. ψ_j and ξ_j are the Riccati-Bessel functions of order n, defined as

$$\psi_j(x) = xj_j(x) \qquad \xi_j(x) = xh_j(x), \tag{3.38}$$

with $j_j(x)$ being the spherical Bessel function of the first kind and $h_j(x) = j_j(x) + iy_j(x)$ the spherical Hankel function. y_j is the spherical Bessel functions of the second kind. The derivatives of $\xi_j(x)$ and $\psi_j(x)$ in Eqn. 3.37 are of the form $z_j'(x) = z_{j-1}(x) - \frac{j}{x}z_j(x)$, with z_j representing any of the functions $j_j(x), y_j(x), h_j(x), \psi_j(x)$ or $\xi_j(x)$. Spherical Bessel

functions of the first and second kind have the form [31, pp. 86-87]

$$j_j(x) = \sqrt{\frac{\pi}{2x}} J_{j+1/2}(x) \quad \text{and} \quad y_j(x) = \sqrt{\frac{\pi}{2x}} Y_{j+1/2}(x). \tag{3.39}$$

J and Y are the ordinary Bessel functions of the first and second kind, respectively. For $n = 0$ and $n = 1$, these are expressed as

$$\begin{aligned} j_0(x) &= \frac{sin(x)}{x} & y_0(x) &= -\frac{cos(x)}{x}, \\ j_1(x) &= \frac{sin(x)}{x^2} - \frac{cos(x)}{x} & y_1(x) &= -\frac{cos(x)}{x^2} - \frac{sin(x)}{x}. \end{aligned} \tag{3.40}$$

The difference relation $z_{j-1}(x) + z_{j+1}(x) = \frac{2j+1}{x} z_j(x)$, can be used to find higher-order functions.

The expressions in this section are implemented in Python in Appendix E.2. Furthermore, the code was tested against the values provided by Bohren and Huffman [31, Appendix A] to make sure the formulas were implemented correctly. Figure 3.4 demonstrates the extinction efficiencies, obtained from using this code, of a single silver sphere of various diameters. Extinction efficiencies are extinction cross sections normalized with the particle's geometric cross section, as previously shown in Eqn. (3.32).

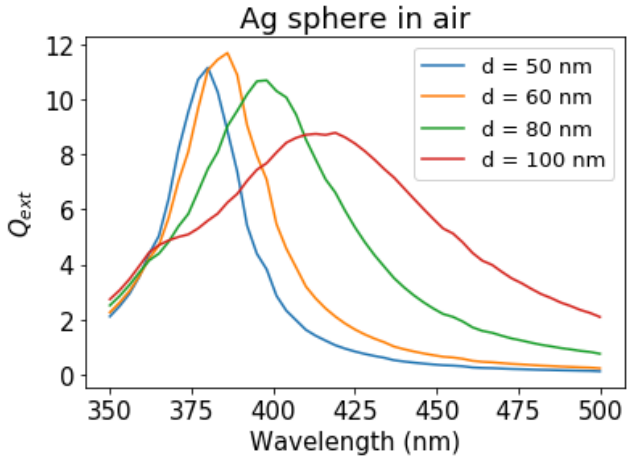

Figure 3.4: Extinction efficiencies of single silver spheres of various diameters from 50 nm to 100 nm. Note the emerging quadrupole in the 100 nm plot – the kink between $\lambda = 350$ nm and 375 nm.

3.3.2 The quasi-static approximation.

When the radius of the sphere is much smaller than the wavelength of the incident light, we can neglect the phase retardation effects and excitation of higher-order modes. The main feature of the quasi-static method is that one assumes that, for particles where the diameter is a lot smaller than the incident wavelength, $d << \lambda$, the phase of the field is approximately constant over the entire particle surface. A suggested region of validity for this approximation is $d < 50$ nm [21]. One can therefore simplify the problem to one with an electrostatic field [36, p. 66], [32, p. 211]. Because the incident field is assumed constant it can only excite the lowest-order dipole mode on the surface of the particle, but not the higher-order multipolar modes. This is therefore also referred to as the dipole approximation, as the particle is assumed to act as a dipole. The complete derivation of optical properties under this approximation is demonstrated by Sarid and Challener [32, pp. 211-215] or Maier [36, pp. 66-71].

The polarizability in Eqn. (3.33) can be simplified to

$$\alpha = 4\pi a^3 \frac{\epsilon - \epsilon_m}{\epsilon + 2\epsilon_m}, \tag{3.41}$$

which contains only the dipole term. Hence, this formulation neglects retardation effects and dampening.

The scattering and absorption cross sections can be expressed as

$$\begin{aligned} \sigma_{sca} &= \frac{8\pi}{3} \mathrm{k}^4 a^6 \left| \frac{\epsilon - \epsilon_m}{\epsilon + 2\epsilon_m} \right|^2 \\ \sigma_{abs} &= 4\pi \mathrm{k} a^3 \mathrm{Im}\left(\frac{\epsilon - \epsilon_m}{\epsilon + 2\epsilon_m} \right). \end{aligned} \tag{3.42}$$

As particle radius increases, the scattering cross section increases as $\sigma_{ext} \sim a^6$, while the absorption cross section increases as $\sigma_{abs} \sim a^3$. It will be seen that for small particles with radii $a << \lambda$, the extinction cross section, $\sigma_{ext} = \sigma_{sca} + \sigma_{abs}$ is dominated by the absorption term. However, as the particle radius increases, the scattering term eventually becomes larger than absorption.

Note that as the optical cross sections are Lorentzian lineshapes they are subject to lineshape-broadening with increasing sphere diameter. This holds true for the full Mie solution as well, as seen in Figure 3.4 and have been noted by e.g. Averitt et al. [21]. Eqn. (3.42) reveals that the condition for resonance ([32, p. 212]) is

$$\epsilon' \approx -2\epsilon_m. \tag{3.43}$$

Note that as the dielectric function is size-independent, Eqn. (3.43) predicts resonance at the same wavelength, independent of particle size. This makes the approximation different from the full Mie solution.

3.4 Raman scattering

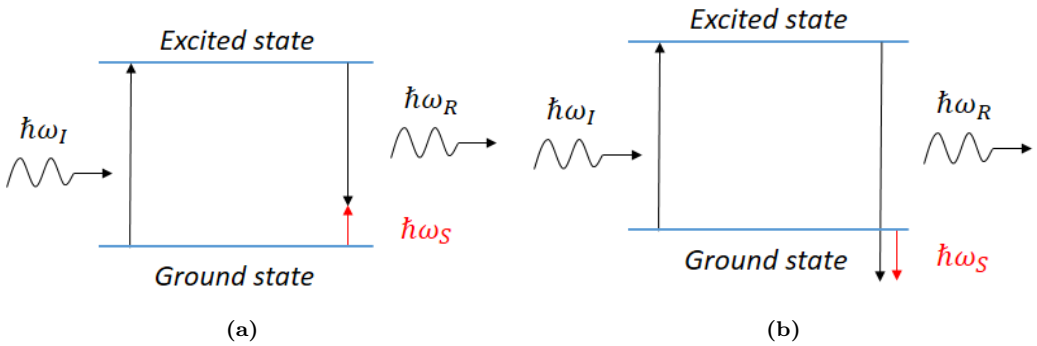

Figure 3.5: Raman scattering illustrated in terms of photon energies. (a) Stokes scattering, where the scattered photon has less energy than the incident and (b) anti-Stokes – scattered photon has absorbed energy from phonons in the material and has more energy.

When illuminating a material, most of the light is elastically scattered. A small fraction is inelastically, Raman, scattered. The Raman spectrum can be used to identify a material, due to the resonance peaks at frequencies where the material's vibrational modes, such as stretching and rotational modes, quantized as phonons, resonate. Unlike elastic scattering,

where the incident and scattered photon have the same energy, Raman scattering is inelastic and is defined by

$$\hbar(\omega_I \pm \omega_R) = h\omega_S. \tag{3.44}$$

$\hbar\omega_I$ is the energy of the incident photon, $\hbar\omega_R$ is that lost or gained by interaction with the vibrational modes of a material and $\hbar\omega_S$ is the energy of the scattered photon. If the loss $\hbar\omega_R$ is positive, then we have Stokes scattering. When the loss is negative and the photon scattered has higher energy than the one absorbed – anti-Stokes. [37, p. 527] See Figure 3.5. It's worth noting that the scattered photon isn't the same one that was incident on the material, but a new photon created in the collision with a phonon. The intensity ratio between Stokes and anti-Stokes scattering is

$$\frac{I_{Stokes}}{I_{anti-Stokes}} = \exp\frac{\hbar\omega_R}{k_B T}, \tag{3.45}$$

where $k_B T$ is thermal energy. The intensity ratio is generally larger than unity, implying that most of the inelastically scattered photons are Stokes scattered.

The following mechanism is specific to the case when an incident photon collides with a phonon in the material studied [38, pp. 3-6]. The incident photon has a wave vector $\mathrm{k}_I(\omega_I)$ and the scattered photon has $\mathrm{k}_S(\omega_S)$. The phonon representing e.g. a lattice vibrational mode has wave vector q, which is the crystal's momentum. From the definition of Raman scattering above and the requirement that energy is conserved in the collision, the phonon's scattering frequency is the difference $\omega = \omega_I - \omega_S$. Momentum conservation also requires that $q = \mathrm{k}_I - \mathrm{k}_S$, as it is in the case of one lattice excitation participating in the scattering process. However, for non-crystalline materials, where a single q isn't representative for all the lattice excitations, and especially in the case of complex refractive indices in absorptive materials, the condition breaks down and must be approximated as

$$\Delta q \approx Im(\mathrm{k}_I) + Im(\mathrm{k}_S), \tag{3.46}$$

which gives a range of phonon wave vectors, such that the Raman spectrum peaks stretch over a continuous band of frequencies. Amorphous materials with no or little crystalline order, such as glass, have wide bands due to absorption.

The dipole mode set up by the incident light and the elementary excitations of the analyte material emits has a small chance of emitting Stokes and anti-Stokes shifted on [13]. Merlin et al. state that "... The effect may be understood as that from an induced polarization **P** (the dipole moment per unit volume) that oscillates at the frequency ω_S." [38, p. 6]. They represent the polarization by a modulated electric susceptibility of the medium χ^m induced by the elementary excitations of frequency ω_q. We omit the tensor notation used by Merlin et al. [38, p. 6] and express element i of the analyte's polarization vector simply as

$$P_i(\omega_S) = \chi_i^m E(\omega_L) \tag{3.47}$$

The notion that the analyte molecule is polarized by incident light is used when explaining the mechanism of SERS.

3.5 Surface plasmons and SERS

This section defines the elementary excitations on the surface of a metal more closely. The field-enhancement in SERS is attributed to oscillation of surface electrons in metals, when

excited by incident light. The quantization of these oscillations of the electron gas is called a plasmon [33, p. 401]. A qualitative introduction to surface plasmon polaritons on single and double metal-dielectric interfaces is given first, before localized surface plasmons will be presented as the excitation contributing to SERS in the nanostructures modeled in Chapter 4. Finally, surface roughness is discussed as a way to excite surface plasmons and to localize them.

3.5.1 Single- and double-interface surface plasmon polaritons

Surface plasmon polaritons (SPP) are surface waves, obtained from the coupling of photons from incident light to the electric oscillations. Such surface waves can propagate along a single metal-dielectric interface, such as the surface of a metal particle in a dielectric medium, or along two such interfaces. The latter is the case for nanoshells, particles that consist of a dielectric core, coated with a metal film, also with a dielectric surrounding medium. Figures 3.6a and 3.6b show simple outlines of a single and double interface.

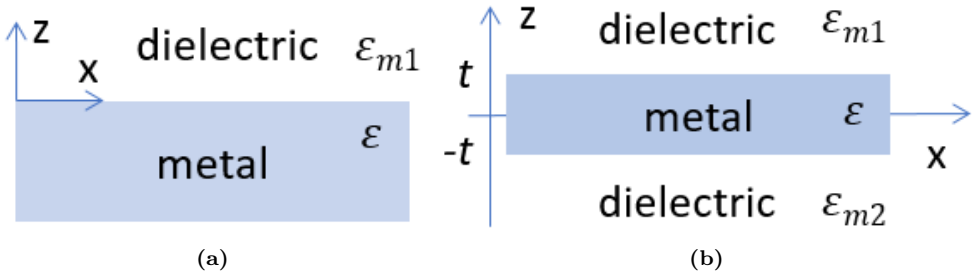

Figure 3.6: (a) Single dielectric-metal interface, between a dielectric medium, with constant ϵ_{m1} and metal with dielectric function of wavelength ϵ. The direction of SPP propagation is in x. (b) Double dielectric-metal interface, with the metal layer wedged in-between two dielectrics with constants ϵ_{m1} and ϵ_{m2}, respectively.

Single-interface SPPs

The main feature of SPPs that will be used in this thesis is the property of confinement, or localization, of the surface wave to such dielectric-metal interfaces, where the evanescent fields in the direction normal to the interface, along the z axis in Figure 3.6a, have a decay length $\hat{z} = 1/k_z$. k_z is the z component of the EM wave in each respective medium i, dielectric and metal. Recall, however that metals are transparent to fields only when the frequency is higher than the metal's plasma frequency, introduced in Section 3.2. Thus, the evanescent fields penetrate into the dielectric. Confinement to the surface requires that the EM wave in both media has $\mathrm{Re}(k) > 0$ [36, p. 27]. Maier [36] further concludes that to ensure continuity of the electric and magnetic field components E_y and H_x at the interface, while satisfying confinement, SPPs can only exist for TM polarization.

From the dispersion relation of SPPs, the propagation constant equals

$$\beta = \mathrm{k}_0 \sqrt{\frac{\epsilon \cdot \epsilon_{m1}}{\epsilon + \epsilon_{m1}}}. \tag{3.48}$$

To excite SPPs, the incident photon's wavevector needs to match the propagation constant, which is the component of the surface wave's wavevector along x. However, plotting the dispersion relation together with the photon's light line, $\omega = c\mathrm{k}$, reveals that normally $\beta > \mathrm{k}$ [36, Figure 2.3, p. 27]. Coupling SPPs with light on smooth metal surfaces is therefore only possible in the small wavelength interval, where the phases match, for small wavevectors.

There are, however, several phase-matching techniques for exciting SPPs, such as using gratings, prisms, near-field and end-fire coupling [36, Ch. 3], [32, Ch. 10]. Rough surfaces facilitate SPP excitation and will be discussed below, as it is the method implicitly used when performing Raman measurements on SERS substrates, such as AuFONs.

Confinement of the SPPs results in faster decay of the evanescent fields in z direction, but also localizes the surface waves in the plane of the interface. There is, therefore, a trade-off between confinement and damping. At small wavevectors, where one can couple light to SPPs of a smooth metal surface, the evanescent fields penetrate deep into the dielectric. However, as $\beta \to \infty$, the SPP frequency approaches the surface plasmon frequency ω_{sp},

$$\omega_{sp} = \frac{\omega_p}{\sqrt{1+\epsilon_{m1}}}. \tag{3.49}$$

Then, the propagation length along the interface, as well as the decay length $\hat{z}$ into the dielectric, decreases due to intra- and interband electron damping. Sensing applications benefit from confined SPPs, as SPP localization results in stronger surface field enhancement, but the losses are also larger than for smaller wavevectors [36, p. 29].

Double-interface SPPs

Double-interface SPPs, as on the geometry pictured in Figure 3.6b, have the added property of coupling with one another when the separation distance decreases such that $t < \hat{z}$. Conversely, as the metal layer becomes thicker, the SPPs on both sides of the metal layer act as single-interface SPPs described above. Figure 3.8b further below will demonstrate how a thick, shell-like film around a dielectric core does not allow the SPPs on the inner, core-shell, interface to be measurably excited at all.

In the case of a decreasing film thickness, the coupling gives rise to odd and even modes, ω_+ and ω_-. Maier presents a simplified derivation, with equal dielectric constants on both sides of the metal layer [36, pp. 30-33], $\epsilon_{m1} = \epsilon_{m2} = \epsilon_m$. The odd and even modes are then

$$\begin{aligned} \omega_+ &= \omega_{sp}\sqrt{1+\frac{2\epsilon_m e^{-2\beta t}}{1+\epsilon_m}} \\ \omega_- &= \omega_{sp}\sqrt{1-\frac{2\epsilon_m e^{-2\beta t}}{1+\epsilon_m}}. \end{aligned} \tag{3.50}$$

From these relations we can see that as $t \to 0$, both modes approach the surface plasmon frequency and the coupling between them get stronger. For odd modes, decreasing metal thickness means less confinement of SPPs and emergence of plane waves on the metal-dielectric surface, long-ranging SPPs. For even modes, it is the opposite, where decreasing thickness increases confinement and decreases propagation length, essentially localizing the SPPs. In this thesis, we will focus on the properties of localized surface plasmons (LSP). These are also referred to as simply surface plasmons (SP).

3.5.2 Localized surface plasmons

When the interface area between a metallic particle and a dielectric is small, only non-propagating localized surface plasmons modes can exist [32, p. 201]. The same is true for quasi zero-dimensional nanoparticles, the dimensions of which are much smaller than the excitation wavelength. An alternative formulation is that their dimensions are smaller than

the conduction electrons' mean free path. Figure 3.7 shows the LSPs, where the electron cloud of the metallic nanoparticle is moving in sync with the external electric field [13]. The LSP resonances (LSPRs) determine the optical properties of metal nanoparticles. Some research argues that the plasmon resonance for noble metals, which has been generally believed to be determined purely from the metal's dielectric properties (recall e.g. Eqn. (3.43)), is actually better determined by the polarizability [39]. The extinction peak can be predicted from the wavelength where the polarizability peaks, as will be seen later, in Chapter 5.

For spherical particles, their curved surface makes it possible to excite the plasmons with direct light illumination [36, p. 65]. Metal deposition by vacuum evaporation creates a rough metal film surface, which has also proved to be a method to both localize and excite the SPPs [32, pp. 275-276].

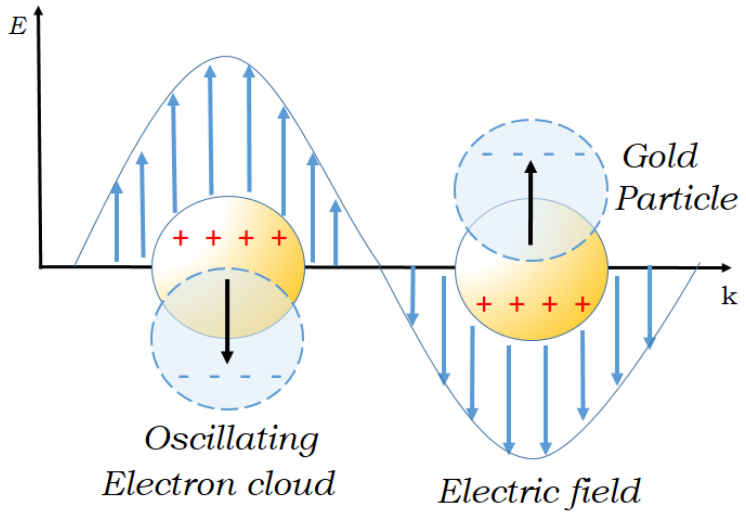

Figure 3.7: Illustration of localized surface plasmons, showing how the electron cloud is oscillating as the electric field is acting upon it. The axes show the magnitude and propagation direction of the field.

Coupling of LSPs is achieved by placing the nanoparticles close enough to one another for near-field interactions [36, p. 81]. High degree of field localization in the gaps between particles is achieved this way, due to the suppression of far-field scattering. The more localized the field becomes, the stronger the enhanced field relative to the average field outside of the hot spot [40, p. 359]. In small particles, the decay of plasmons is mainly due to absorption. In large particles, the dominant decay mechanism is by photon emission, i.e. light scattering [36, pp. 74-75]. In the case of near-field coupling, the plasmons are predominantly excited near the interparticle axis and, thus, the density of plasmons which can emit photons, on the remaining surface of the nanoparticle, is greatly reduced. SPs are in this case excited predominantly along the interparticle axis, leading to the emergence of *hot spots* of high local field enhancement [4, pp. 21-22]. The local field norm can be many times larger than the average field norm around the particle. Such an effect is seen in Figure 3.8a, showing a field enhancement by a factor of 50. These hot spots depend on the length l of separation between the two particles. For large field enhancements, the separation distance is much smaller than the particle diameters. Maier [36, p. 82] shows a l^{-3} dependency, stating that at $l > 150$ nm the particles interactions are no longer noticeable. However, the exact extent of coupling effects depends on particle composition and size. The near-field interactions lead to a shift in the resonance wavelengths, depending on the polarizations of

the adjacent particles [36, p. 82].

3.5.3 SERS

Surface-enhanced Raman scattering has multiple origins. Researchers are still unsure of its exact mechanism [4]. The enhancement is believed to be due to an EM component and a chemical component. The former contributes the most, due to the electric field enhancement produced when light impinges on the surface of metallic structures. Figure 3.8b shows the simulated local field enhancement of the electric field when an 80 nm gold thin film over a 500 nm polystyrene sphere is excited by an external electric field at 785 nm wavelength. When an analyte molecule is exposed to the local field enhancement, it is polarized, emitting photons at its characteristic Raman frequencies. This assumes that the molecule's resonance frequencies encompass both the incident and scattered light waves.

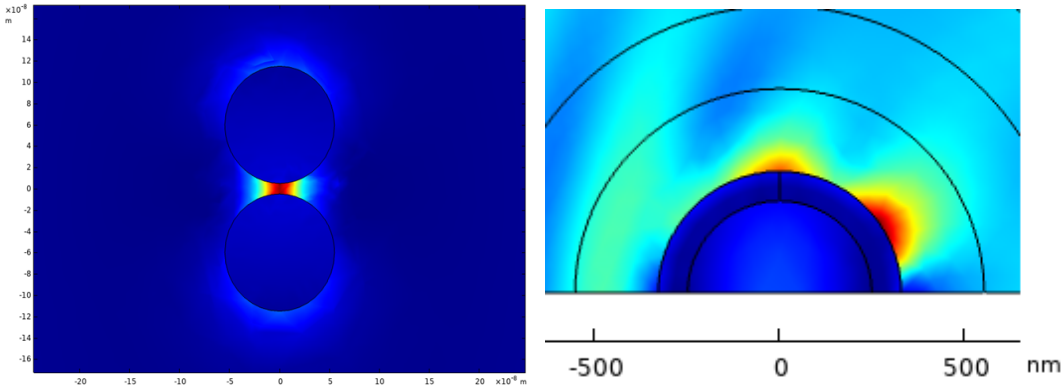

(a) (b)

Figure 3.8: (a) COMSOL simulation of two 100 nm diameter gold metal discs separated by 10 nm, showing the hot spot in the gap between the two. The external field is 1mV/m in magnitude, polarized along the interparticle axis, while the maximum field norm is 50 times larger. (b) COMSOL simulation of a 500 nm polystyrene sphere coated with 80 nm Au film, excited by 785 nm light, showing the electric field enhancement. The maximum field norm (in the red patches) near the metal surface is about 3 times larger than the incident field.

The hot spots give rise to the electromagnetic component of SERS that is due to re-radiation enhancement [4, p. 7]. The analyte molecule sets up a self-radiating field. Radiated power diffuses into space following a dipole diffusion pattern. If interfaces with particles, such as metallic nanostructures, are present around the molecule, the EM field irradiated by the dipole is scattered at these interfaces. It is partially reflected backwards at the dipole position. This process depends on the medium as well as the nanostructured substrate, as the medium can absorb and diminish these effects. The field enhancement in hot spots diminishes exponentially and its contribution is dominant only when the separation distance l is 10 nm or less.

Each of the two EM contributions contribute with a factor of $|E/E_0|^2$, where E is the enhanced surface-field amplitude. The total SERS enhancement factor (EF) due to field enhancement can be estimated from the "E^4" approximation [13, Eqn. 6]

$$g_{SERS} \approx \left|\frac{E}{E_0}\right|^4. \tag{3.51}$$

A field enhancement by a factor of 50, illustrated in Figure 3.8a, yields a SERS EF of $6.25 \cdot 10^6$, using (3.51). The maximum achievable EF from the EM field enhancement alone

is believed to be on the order of 10^{12}-10^{14} [4]. However, there is also the chemical component of SERS enhancement, which acts over an even shorter distance than the electromagnetic component. The chemical enhancement is believed to come from the electron orbitals of the analyte molecule overlapping with the plasmon oscillations near the surface, typically a few nanometers, or less, from the metallic surface. It contributes an additional 10^2-10^4 to the total SERS enhancement factor.

Experimentally, the SERS enhancement factor is expressed as

$$g_{SERS} = \frac{I_{SERS}/N_{surf}}{I_{Ref}/N_{vol}}. \tag{3.52}$$

I_{SERS} is the enhanced Raman spectrum intensity, I_{Ref} is the unenhanced reference Raman spectrum, N_{surf} is the number of analyte molecules bound to the metallic surface and N_{vol} is the number of molecules in the measured analyte volume [13].

Thin film thickness and roughness as a factor in SERS

A presented in Chapter 1, SERS enhancement was first discovered on a rough silver electrode surface [5]. Lee *et al.* [22] demonstrate empirically that the ability of thin silver films to enhance the Raman spectrum comes, to a large extent, from the roughness of the metal surface. For thin films, the enhancement comes primarily from localized surface plasmons. The rough features act as sub-wavelength nanoparticles, accomodating LSPs. The rough surface also functions as a random grating, which facilitates phase-matching between the light and the various SPP modes that can be excited. Sarid and Challener [32, pp. 274-275] suggest similarly that rough surfaces act similar to diffraction gratings, allowing light of many different wave vectors, incident over a range of angles θ, to couple to many SPPs. The localization of SPPs on rough surfaces comes from interference effects of waves scattered at random. Expressing the light photon's in-plane momentum along the dielectric-metal interface as $\mathrm{k}_x = \mathrm{k}\ \sin\theta$, the phase-matching condition

$$\beta = \mathrm{k}_x \pm \Delta\mathrm{k}_x \tag{3.53}$$

is fulfilled with the aid of momentum components $\Delta\mathrm{k}_x$ from scattering [36, p. 47].

However, the enhancement gains of surface roughness are off-set by the thickness of the film. With increasing thickness, more of the excited SPPs are propagating, which results in decreased field enhancement.

Zhao *et al.* [41] suggest that the enhancement increase from surface defects comes from the many hot spots formed between them. An example of a grainy gold film surface is the image of AuFONs in Figure 2.1. Even plain metal films are left with disordered arrays of bumps and wrinkles after metal deposition. The project thesis [1] used near-field coupling between solid gold half-spheres, or domes, to model these bumps and surface roughness, and some of the model results will be reviewed in Chapter 5.2.1. However, surface roughness is introduced here only for completeness, as it is an extensive topic, which complicates the models significantly and must be left for future work.

3.6 Nanoshells

The previous section presented models for solid particles, with only one metal-dielectric interface. AuFON arrays, however, are made up of particles with a dielectric core, coated

with a metal film. These nanoshells particles exhibit two metal-dielectric interfaces and the ability to excite and localize surface plasmons inside the metal shell, at the inner interface with the metal, is an important difference between solid particles and nanoshell. There are extensions to Mie theory for nanoshells, as investigated by e.g. Aden and Kerker [42], Sarkar [43, Ch. 4] or Oldenburg [44]. We will however only present a simple analytical model, to guide the AuFON modeling process.

In our model of such particles, we will use the convention outlined in Figure 3.9, where the core and shell have two different dielectric functions, ϵ_1 and ϵ_2, respectively.The outer radius of the shell, r_2 is the particle's total radius, while the shells thickness is the difference between r_2 and the core radius r_1, i.e. $r_2 - r_1$. The medium outside is assumed characterized by a wavelength-independent dielectric constant ϵ_m, as before.

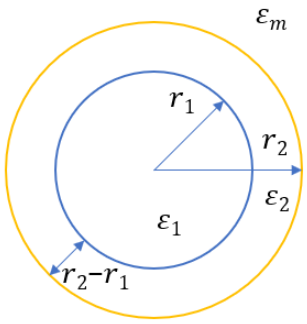

Figure 3.9: Nanoshell structure outline. The core is made of a material with dielectric function ϵ_1 and has radius r_1, while the shell is made of a material with a different dielectric function ϵ_2 and thickness $r_2 - r_1$. The total radius of the nanoshell is r_2. The surrounding medium is described by the dielectric constant ϵ_m.

3.6.1 Quasistatic approximation for nanoshells

Similarly to solid plasmonic particles, for particles much smaller than the incident wavelength, the optical properties of nanoshells can be approximated as if the electric field is static, or slowly-varying. Averitt *et al.* [21] have suggested that for diameters $d < 50$ nm, i.e. same as for solid spheres, the quasistatic approximation produces results similar to the Mie theory extensions for nanoshells.

Averitt *et al.* express the polarizability and optical cross sections using artificial dielectric functions, made up of the physical ones, ϵ_1 and ϵ_2, weighted by a ratio of the shell volume to total particle volume. In their notation, this ratio is expressed as

$$P = 1 - (r_1/r_2)^3. \tag{3.54}$$

Don't confuse this with polarization scalar value P. The additional dielectric functions are

$$\begin{aligned} \epsilon_a &= \epsilon_1(3 - 2P) + 2\epsilon_2 P \\ \epsilon_b &= \epsilon_1 P + \epsilon_2(3 - P) \end{aligned} \tag{3.55}$$

The dipole moment is the same as in the case of solid particles, $\mathbf{p} = \epsilon_0 \epsilon_m \alpha \mathbf{E}_{local}$.

Polarizability α is then, using equations (3.55),

$$\alpha = 4\pi\epsilon_0 r_2^3 \frac{\epsilon_2\epsilon_a - \epsilon_m\epsilon_b}{\epsilon_2\epsilon_a + 2\epsilon_m\epsilon_b}. \tag{3.56}$$

The scattering and absorption cross sections are finally

$$\begin{aligned} \sigma_{sca} &= \frac{\mathrm{k}^4|\alpha|^2}{6\pi\epsilon_0^2} \\ \sigma_{abs} &= \frac{\mathrm{k}}{\epsilon_0}\mathrm{Im}(\alpha). \end{aligned} \tag{3.57}$$

The resonance condition for nanoshells is expressed as the ratio of core radius to total radius, required for achieving resonance at a given wavelength λ,

$$\frac{r_1}{r_2} = \left(1 + \frac{3}{2}\frac{\epsilon_2'(\lambda)(\epsilon_1 + 2\epsilon_m)}{(\epsilon_2')^2 - \epsilon_2'(\lambda)(\epsilon_1 + \epsilon_m) + (\epsilon_1\epsilon_m - (\epsilon_2''(\lambda))^2)}\right)^{1/3}. \tag{3.58}$$

To understand the main insight of this model for nanoshells, we can use the Au_2S core, Inserting the parameters for a Au_2S core, Au film nanoshell, given by Averitt *et al.* and the dielectric function values for gold, results in the plot in Figure 3.10. It indicates that the resonance wavelength is redshifted when the core radius increases relative to the total radius.

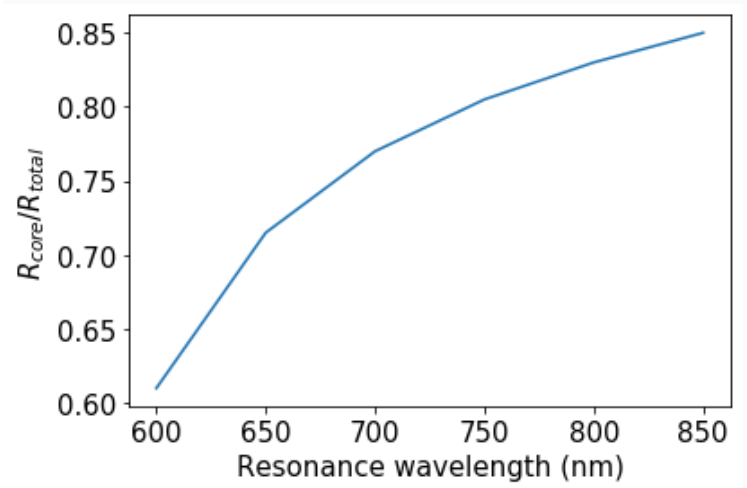

Figure 3.10: Nanoshell resonance condition in the quasistatic approximation. The plot line shows a trend where the plasmon resonance wavelength is redshifted as the core radius is increased relative to the total radius.

3.7 Particle arrays

The models in this thesis are extended from single particles, as in the project thesis [1], to arrays of particles. This section presents some common lattices and the optical effects that lattices introduce.

3.7.1 Lattice structures

Large periodic particle arrays are represented using primitive lattice cells repeated infinitely many times in the x direction (1D array), both x and y directions (2D square array) or along the a_1, a_2 primitive vectors of a hexagonal lattice (2D hexagonal close-packed array). In an atomic lattice, a primitive cell contains one lattice point. A Wigner-Seitz cell is a primitive cell of the least possible volume that can be repeated infinitely to obtain the lattice structure. In a square lattice, $a_1 = a_2 = a$ and the angle between them is 90°. In a hexagonal lattice, the angle is 120°, as illustrated in Figure 3.11. For 3D hexagonal close-packed structures

based on the hexagonal lattice, the vector **c** between vertical lattice point planes has length $c = 1.633a$ [33, pp. 6, 8-10, 15-16].

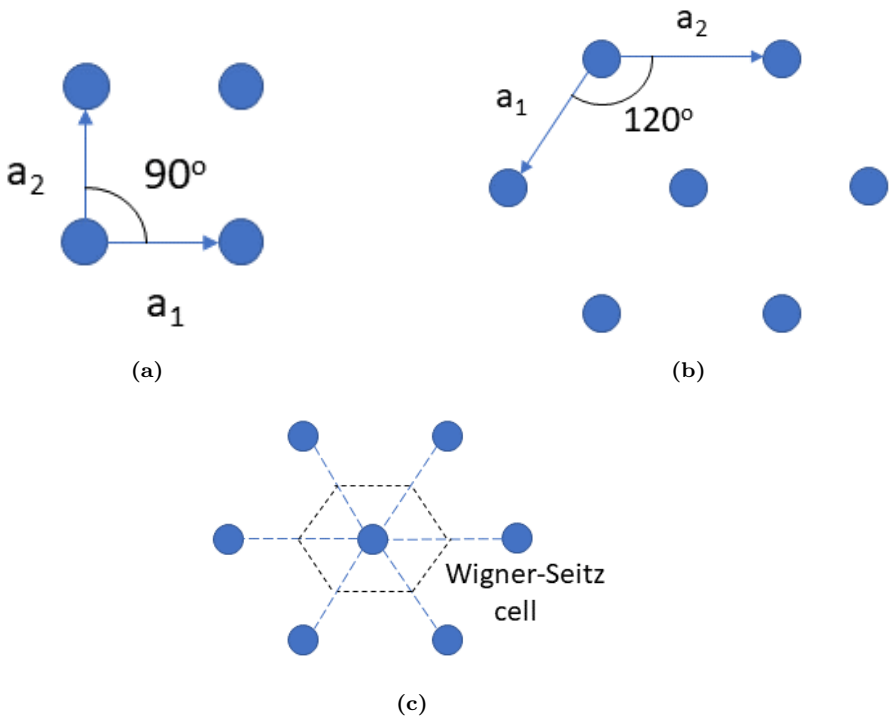

Figure 3.11: Top row: 2D lattices showing their primitive vectors and angles between them. (a) Square lattice. (b) Hexagonal lattice. Bottom row: (c) A Wigner-Seitz primitive unit cell in a hexagonal lattice.

The arrangement of particles in an array bears significance for their plasmonic properties. In square arrays, the polarization of particles is highest when the incident light's polarization is parallel with the rows or columns of the array. For close-packed square arrays, the effect is similar to the near-field coupling between two particles demonstrated in Figure 3.8a. Hexagonal arrays offer more directions along which the particles can couple, as well as a closer packing order, but the coupling is weaker than for square arrays. Figure 3.12 shows the electric field amplitudes over several particles arranged in a close-packed hexagonal array. The first subfigure shows the polarization of particles when the light is linearly polarized in y direction. We see coupling between the center particle and all other particles. However, the coupling is strongest along the y axis. In the second subfigure, the light polarization is changed to x direction. The coupling in y direction now fully disappears. The diagonal directions from the center particle contain an x component. Thus, the coupling along these is now stronger.

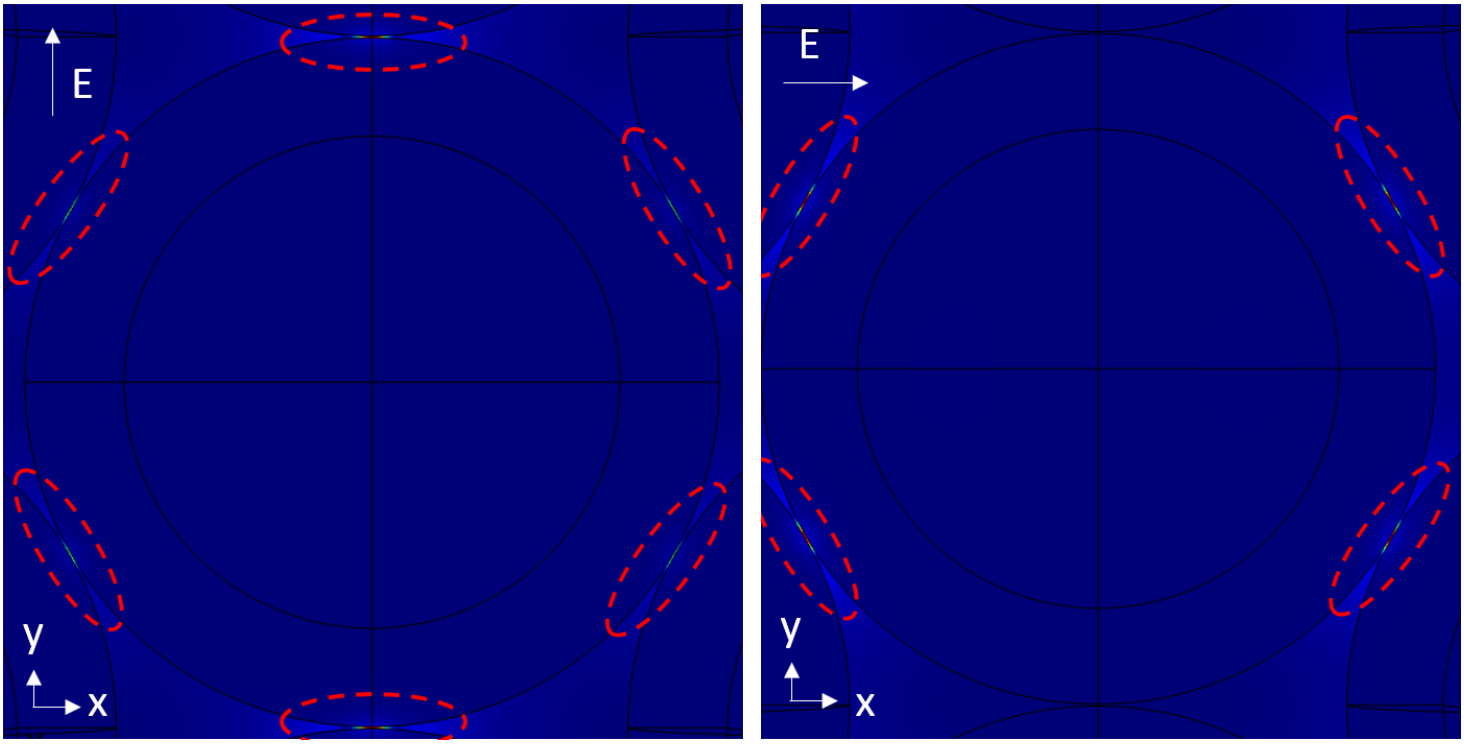

(a) (b)

Figure 3.12: Close-packed hexagonal lattices of particles and different incident light polarization directions. The particle couplings are marked with the red dashed rings. (a) Linearly polarized in y direction. There is coupling to all particles from the center one, with the coupling being strongest along the y axis (the faintly-visible red patches of extremely high field enhancement between the center sphere and the two over and under it). (b) Linearly polarized in x direction. Note that the coupling in y direction is no longer visible. The coupling to the spheres on the left and right of the center one is now stronger than in (a).

Note that the lattices in this figure are rotated 90° compared to the hex arrays in Figure 3.11b-c.

3.7.2 Surface lattice resonances

In addition to the near-field coupling that leads to formation of hotspots, there is also far-field coupling between the fields scattered by the particles. Periodic lattices act as diffraction gratings. The incident light excites LSPs in the particles that make up the grating. When the array's period or lattice constant is approximately equal to the wavelength of incident light, the LSPs interact with one another through the far-field radiation caused by their decay and interfere with the diffracted incident light. The constructive interference causes coupled resonances, known as Fano resonances [39], [45], [46], [47, pp. 4-10]. Figure 3.13a presents a sketch of this process. The resulting far-field extinction cross section has LSPR peaks as in single-particle optical cross sections, but also at least one more peak, the surface lattice resonance (SLR) or lattice plasmon, located at a wavelength roughly corresponding to the lattice constant. There are both classical and quantum mechanical approaches to explain the phenomenon.

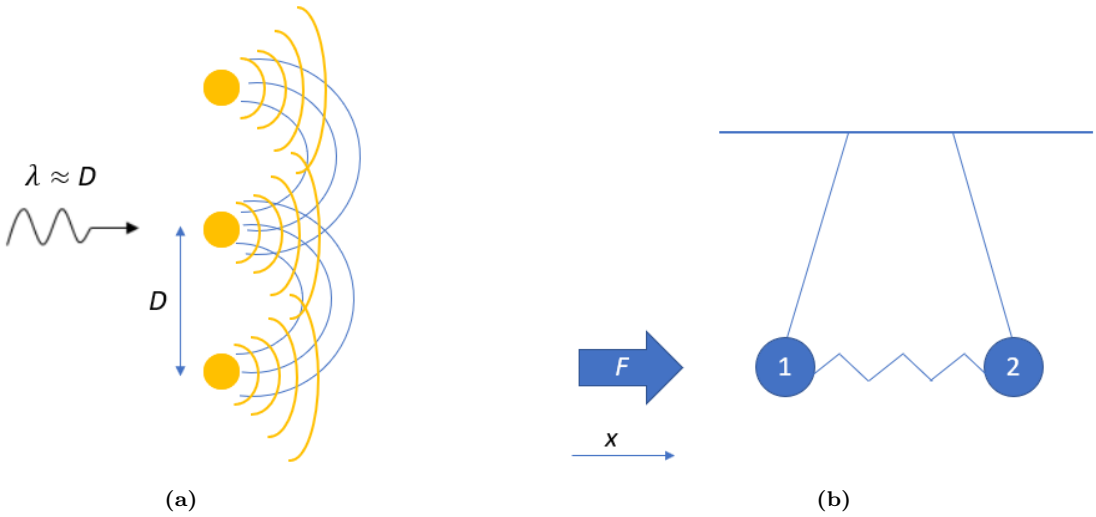

Figure 3.13: (a) Incident light of wavelengths close to a particle array's lattice constant D lattice is diffracted by the particle grating and interferes with the LSPs it has excited. This results in a coupling between the LSPs' collective far-field radiation and the diffracted light, that produces lattice plasmons, or surface lattice resonances. (b) Harmonic oscillator model of SLRs. An external force F does work on the system. Oscillator 1 models the dipole mode of the LSP, which is coupled with a spring to oscillator 2, the lattice resonance.

In this thesis, we'll review the classical coupled harmonic oscillators model by Joe *et al.* [48]. We can think of the LSP and SLR resonances as oscillators. If we assume that the particles are not large enough to support modes higher than dipolar and that there is only one SLR resonance, the model has two oscillators, as in Figure 3.13b. The external force F, with amplitude a_F and frequency ω_F, drives oscillator 1, which oscillates with eigenfrequency ω_1. Oscillator 2 is acted upon by oscillator 1 through the spring and has eigenfrequency ω_2. Each oscillator can be modeled with its own damping coefficient γ_j. The oscillators' equations of motion are then

$$\begin{aligned} \frac{\partial^2 x_1}{\partial t^2} + \gamma_1 \frac{\partial x_1}{\partial t} + \omega_1^2 x_1 + \xi_{12} x_2 &= a_F e^{i\omega_F t} \\ \frac{\partial^2 x_2}{\partial t^2} + \gamma_2 \frac{\partial x_2}{\partial t} + \omega_2^2 x_2 + \xi_{12} x_1 &= 0 \end{aligned} \tag{3.59}$$

When there is no external force acting upon the system, the coupling coefficient ξ_{12} is zero and the oscillators move only according to their eigenfrequencies ω_i, as becomes apparent from the following relation:

The interaction term modifies the oscillator's eigenfrequencies, such that the coupled eigenmodes are

$$\begin{aligned} \hat{\omega}_1^2 &\approx \omega_1^2 - \frac{\xi_{12}^2}{\omega_2^2 - \omega_1^2} \\ \hat{\omega}_2^2 &\approx \omega_2^2 + \frac{\xi_{12}^2}{\omega_2^2 - \omega_1^2}. \end{aligned} \tag{3.60}$$

The second term in both of these expressions is positive, so the interaction term red-shifts the wavelength of oscillator 1 and blue-shifts that of oscillator 2.

The oscillator amplitudes are solved as

$$c_1 = \frac{\omega_2^2 - \omega^2 + i\gamma_2\omega}{(\omega_1^2 - \omega^2 + i\gamma_1\omega)(\omega_2^2 - \omega^2 + i\gamma_2\omega) - \xi_{12}^2} a_F \tag{3.61}$$

$$c_2 = \frac{\xi_{12}}{(\omega_1^2 - \omega^2 + i\gamma_1\omega)(\omega_2^2 - \omega^2 + i\gamma_2\omega) - \xi_{12}^2} a_F. \tag{3.62}$$

In the case where the damping constants are zero and the external force makes the oscillators oscillate with approximately the same frequency, c_1 becomes zero. At that frequency, one would see an asymmetric profile or a small dip [48]. This matches experimental observations, where the SLR is seen as a drop in absorbance [45] or a large asymmetric peak at the wavelength close to the lattice constant D, as will be seen in Chapter 5. This wavelength is, according to the relations in Eqn. (3.60), redshifted compared to D, depending on the coupling strength.

Chapter 4

Modeling

In plasmonic structures for SERS, it is important to find the resonances of the plasmonic excitations, as well as calculating an estimate for the SERS enhancement [49]. This chapter describes a computational method developed to estimate the SERS enhancement from a model of the AuFON structure.

4.1 Simulation approach

Although the end goal is to arrive at a model for SERS enhancement in AuFONs, the focus is on making sure that the model behaves correctly for single solid particles and arrays, both in the near- and far-field. This is because extinction efficiency spectra for AuFONs were not found in the literature. Raman intensity plots vary widely in published results, with reference intensities, as required to estimate g_{SERS} by Eqn. (3.52), not specified. Thus, it is difficult to convert these to SERS enhancement factors. There is, however, one set of measurements, in Figure 4.1, that relates gold film thickness to SERS enhancement factor for AuFONs, for a set of polystyrene core sizes used in research at the IES department at NTNU. This plot was produced by Dr. Milenko [50] from experimental measurements. It will be used for comparing with the final AuFON model. However, it is not a goal to produce a highly realistic model, with surface roughness, a substrate, etc. Rather, the model will be a platform for adding these more complex features, to facilitate SERS substrate design, and it is therefore important that the model is physically well-behaved throughout. Even if the model doesn't fully match Figure 4.1, due to some missing features.

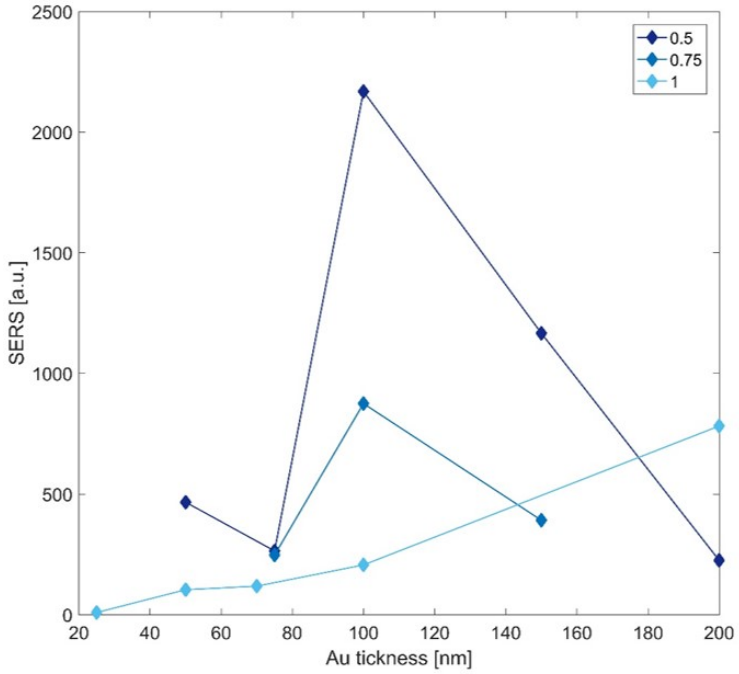

Figure 4.1: SERS enhancement factor versus gold film thickness in 500 nm, 750 nm and 1000 nm polystyrene core AuFON samples. Experimental values. Reproduced with permission [50].

The model is built via a bottom-up approach, starting with solid single particles and extending the model gradually to arrays and eventually replacing the solid particles by nanoshells, before finally building the AuFON structure. This allows verifying each step using theory and analytical Mie solutions and well-established, numerical methods such as the discrete-dipole approximation (DDA) and the coupled-dipole approximation (CDA).

Extinction efficiency spectra are used to ensure that the model behaves physically correct and to compare extinction spectra with published results. The spectra help visualize how the localized surface plasmon resonances (LSPRs) and Fano resonances shift with changes in the properties of particles and arrays of these, as well as estimating the resonance wavelengths. When it is found that the models in each modeling step behave well, the SERS enhancement factor (EF) is estimated.

4.2 Modeling methods and software

Analytical solutions to light scattering problems expressed using Maxwell's equations are known only for simple geometries. More specifically, the Mie coefficient method of finding optical cross sections, presented in chapter 3, is based on a solution of Maxwell's equations in spherical coordinates and with boundary conditions appropriate for spheres [21]. Also nanoshell models are sometimes possible to solve using Mie theory, but are limited to very small sizes and certain constraints on the refractive indices of the layers [31, Appendix B], although modern extensions to Mie theory for these particles do exist [44] and will be used for comparison against the nanoshell FEM models.

Numerical methods are needed to solve for geometries with other shapes than spheres, or when one wishes to solve for the scattering efficiencies and surface-fields of structures consisting of arrays of coated or inhomogeneous spheres, such as AuFONs. The main method

chosen for this thesis is the finite-element method (FEM), as it allows solving the wave equation for the electric field using an arbitrary geometry, by discretizing the geometry volume into a finite-element mesh. The advantage of this method is that it allows solving the problem as if the electromagnetic waves were standing waves and not propagating in space, thus eliminating the time domain and the complexity that comes with it. This makes FEM well-suited for simulations of antenna-like structures that emit or scatter radiation.

This thesis uses the FEM implementation in COMSOL Multiphysics 5.4 (COMSOL), with the Wave Optics module installed. COMSOL makes it relatively easy to define a model, offering a graphical user interface with a 3D geometry builder and viewer. However, to the author's knowledge, there are not many FEM simulations published for plasmonic nanostructures. Specifically for AuFONs, none were found in the literature.

As mentioned in the section above, the results produced in COMSOL are compared against other modeling methods. In the project thesis [1], the COMSOL models of single homogeneous Lorentz-Drude gold spheres were compared to analytical Mie solutions. In this thesis, the DDA is also used for comparison. In its most basic form, DDA is equal to the quasi-static approximation in Chapter 3.3.2. The strength of the DDA, compared to the quasi-static method, is that it can take into account phase retardation effects neglected by the quasi-static approximation and permit modeling structures comparable to the wavelength of incident light: The volume of the structure is partitioned into a 3D array of dipoles, each much smaller than the incident wavelength. Mie solutions are still used to verify the single-particle models.

DDSCAT by Draine and Flatau [51], [52], [53] is a popular implementation of the DDA, due to its accuracy [49] and the fact that it is freely available. This makes DDSCAT the most widely used DDA implementation, with an active user-base that has contributed several tools which facilitate the creation of models. There are however numerous DDA implementations that try to improve on DDSCAT and incorporate either simpler modeling processes or improve the actual solver algorithms. They do, however, often lack proper documentation and support. The greatest improvement in more recent implementations of the DDA is use of multiprocessor computations. In DDSCAT this is not well-implemented. When solving the DDA models for each wavelength in a pre-defined range of values, each subproblem is independent of the others. Thus, such *embarrassingly parallel* problems can easily benefit from parallel computations. Other DDA implementations, such as ADDA, have this feature [54] and there are algorithms that try to improve on the original DDSCAT codebase [55] to enable this in DDSCAT. These are however not distributed with the DDSCAT code and for this thesis it was chosen, instead, to create a trivial parallelization method by dividing the main model into several submodels, which are then each run on their own CPU core. This method is described in Appendix D.

The coupled-dipole approximation (CDA) is a much-used extension of the DDA to particle arrays. It was originally developed to understand the far-field coupling in arrays of dipoles [45] and is the tool referenced in most literature on surface lattice resonances. It's accuracy predicting the localized surface plasmon resonances does, however, depend on the dipole polarizability function implemented in the model. The lattice resonances are more independent from the polarizability form. The CDA, although an approximation, has shown good agreement with the physics of far-field coupling and a rigorous mathematical foundation has been developed for it in recent decades [56]. This thesis uses CDA to verify that the particle array FEM model behaves physically correct and a simple implementation, based on Zou *et al.* [57], [58], was written for this thesis.

4.3 The finite element method

The finite element method is used for solving the simulated models in this thesis. Appendix A presents a thorough description of the method, based on Polycarpou [59], solving the Poisson equation in one dimension as an example application. This section simply introduces the main features.

The foundation of the method is the discretization of a simulation domain into discrete finite elements that are bounded by a set of nodes, as shown in Figure 4.2 for a one-dimensional domain. In these nodes, one evaluates the unknown function values. In a scattering problem, it is the electric field. Interpolation functions are used to evaluate the function at any point in the element between the nodes. Higher-order interpolation functions approximate the solutions between nodes more accurately, but at the cost of higher computational complexity. Examples of linear interpolation functions are presented in figures A.2a and A.2b in Appendix A.

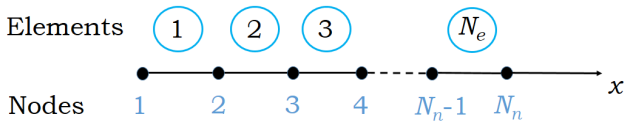

Figure 4.2: 1D domain discretization into N_e elements and N_n nodes.

In accordance with the Galerkin approach, weighted residuals are constructed for each node in an element and arranged into a matrix equation

$$K^e \mathbf{V^e} = \mathbf{f^e} + \mathbf{D^e}, \tag{4.1}$$

where K^e contains the integrated weights of the residuals in Eqn. (A.5), while $\mathbf{V^e}$, $\mathbf{f^e}$ and $\mathbf{D^e}$ are the vectors of node potentials, weighted charges and electric displacement fields. These element equations have to be assembled into a global matrix equation containing all elements in the domain,

$$K\mathbf{V} = \mathbf{f} + \mathbf{D}, \tag{4.2}$$

summing the last node of element e_n with the first node of element e_{n+1}. For a large enough number of finite elements in the domain, the displacement fields in adjacent nodes cancel each other, such that the D vector only contains non-zero values for the *first* and *last* nodes in the 1D domain in Figure 4.2. The boundary conditions are then applied. The most common is the Dirichlet condition, which defines the unknown function values at the domain boundaries, as well as the absorbing scattering condition, which absorbs the field flux at the domain boundaries. Figure A.4 in Appendix A illustrates how the electric field calculated using 1D FEM with linear elements compares with the analytical solution.

2D and 3D FEM methods discretize the domain into finite areas and volumes. 2D elements such as triangles can, similarly to 1D elements, also be linear, quadratic or of higher order. Similarly for 3D elements. Figure 4.3a shows an example 2D linear triangle mesh of the domain outside of a spherical scattering particle. Figure 4.3b illustrates a fine-mesh solution to the 2D scattering problem with a spherical scattering particle. Figure A.6 in Appendix A demonstrates how a fine or coarse mesh influences the accuracy of the solution.

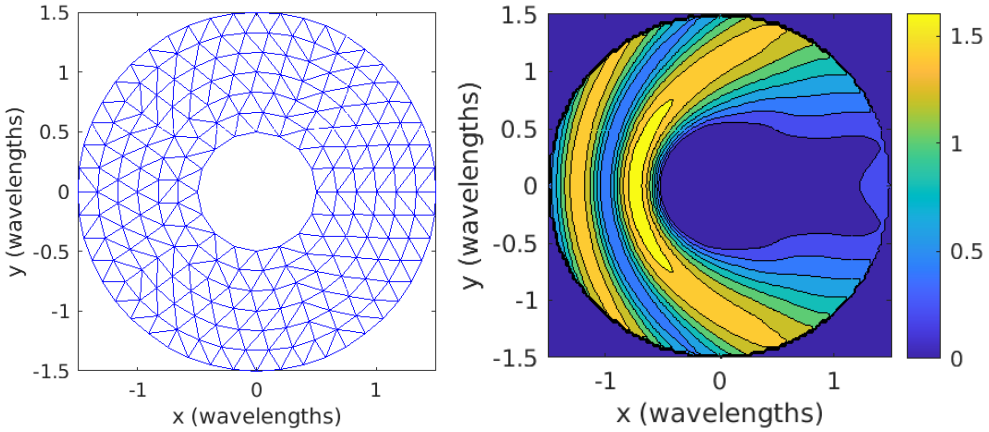

Figure 4.3: FEM solution of a 2D problem with a perfectly-conducting spherical scattering particle in the middle of the domain. (a) Example mesh and (b) fine-mesh solution to the wave equation showing the field amplitude distribution. The incident field has unity amplitude, is y polarized and propagates in x direction.

4.4 The discrete-dipole approximation

The discrete-dipole approximation (DDA) is another technique used to calculate the light scattering and absorption properties of a particle. Also computing the near-field. However, instead of solving the wave equation, it solves for the polarization. This is achieved by discretizing the target particle's volume into an array of sub-wavelength dipoles, each with its own polarization. The Claussius-Mossotti relation, Eqn. 3.27, was seen as a relation of the polarizability of the atoms in a material and the bulk dielectric response of the material [60]. For infinite atomic arrays. In the DDA, the atomic lattice is replaced by an array of dipoles and one can thus use the relation $P_i = \alpha E_{local,i}$ in matrix form to solve for the polarization of each dipole i.

The drawback of the quasi-static approximation in Ch. 3.3.2 is that in order to justify the neglect of retardation effects, the target diameter has to be very small compared to the incident light wavelength for the results to be valid. Pennypacker and Purcell [61] introduced retardation effects by expressing $E_{local,i}$ acting on dipole i as a sum of the external field and the contributions from all the other dipoles j, as derived in Chapter 3.2.2 with their polarizations P_j. Thus, the DDA can be used on target geometries comparable to the wavelength of incident light.

4.4.1 Formulation

A simple formulation of the scattering problem in DDA, following Draine [52], follows here.

The dipole moment of each dipole j is written as

$$\mathbf{p}_j = \alpha_j(\mathbf{E}_{inc,j} - \sum_{k \neq j} \mathbf{A}_{jk}\mathbf{p}_k). \tag{4.3}$$

$E_{inc,j}$ is the incident field at dipole j, expressed as a plane wave, Eqn. (3.7), with amplitude E_0 as before. $-\mathbf{A}_{jk}\mathbf{p}_k$ is the contribution to the field from a dipole k. We'll omit the underlying expression here, as it is a somewhat rewritten form of Eqn. (3.20) (see [52, Eqn. 2.06]).

The scattering problem can then be compactly formulated, using $\mathbf{A}_{jj} = \alpha^{-1}$, as

$$\sum_{k=1}^{N} \mathbf{A}_{jk}\mathbf{p}_k = E_{inc,j}, \tag{4.4}$$

for a system of N dipoles. Note that $\mathbf{A}_{jk}$ is symmetric, $(\mathbf{A}_{jk})_{lm} = (\mathbf{A}_{jk})_{ml}$.

Defining $3N$-dimensional vectors $\tilde{p} = (\mathbf{p}_1, \mathbf{p}_2, .., \mathbf{p}_N)$ and $\tilde{E}_{inc} = (\mathbf{E}_{inc,1}, \mathbf{E}_{inc,2}, .., \mathbf{E}_{inc,N})$ and the $3N \times 3N$ matrix $\tilde{\mathbf{A}}$, satisfying $\tilde{A}_{3j-l,3k-m} = (A_{jk})_{3-l,3-m}$, the problem is expressed as matrix equation

$$\tilde{\mathbf{A}}\tilde{\mathbf{p}} = \tilde{\mathbf{E}}_{inc}. \tag{4.5}$$

The method used for solving this equation in this thesis, using the software package DDSCAT, will be discussed in Section 4.6. The fact that matrices $\mathbf{A}_{jk}$ and $\tilde{\mathbf{A}}$ are symmetric is important not only for the formulation, but also when choosing a solver.

4.4.2 Applicability and limitations

The quasi-static approximation requires that the size of the dipole is a lot smaller than the wavelength of incident light. Ideally, the dipole should be a point dipole. Discretizing the target geometry into an infinite array of point dipoles would be impossible for practical computations. In DDA, one needs to set a non-zero distance between the dipole making up the geometry, the dipole spacing d. The rule of thumb [54] is that d should be at least an order of magnitude smaller than the wavelength of incident light inside the target material,

$$d = \frac{\lambda}{10|n_r|}. \tag{4.6}$$

$|n_r|$ is the absolute value of the target material's refractive index. Adhering to this rule should produce a solution, deviating not more than 10 % from the Mie solution. The dipole spacing can be computed as the extent of the geometry in any given direction, divided by the number of dipoles in that direction. In DDSCAT, the number of dipoles along each of the three axes in a Cartesian coordinate system, is represented as *shape parameters*, SHPAR1, SHPAR2 and SHPAR3. For a sphere, these are all equal, represented by SHPAR. The following equation relates the shape parameter to the interdipole spacing:

$$\text{SHPAR} = \frac{diam}{d}, \tag{4.7}$$

where *diam* is the sphere diameter. That is, SHPAR represents the number of dipoles the diameter is divided into. Figure 4.4 illustrates the discretization of a 100 nm sphere into a three-dimensional array of dipoles with SHPAR = 21. Note that the figure shows the dipoles as spheres with a non-zero volume, rather than point dipoles, for illustration purposes.

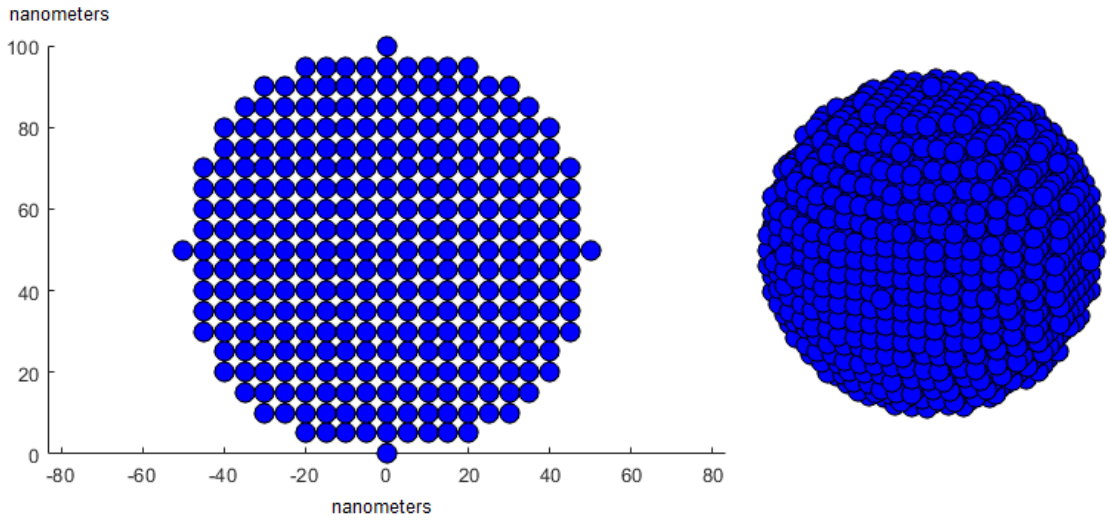

Figure 4.4: 100 nm diameter sphere, discretized into 4369 dipoles (shown as small spheres rather than as point dipoles), with the diameter partitioned into 21 dipoles, i.e. SHPAR = 21. Produced using *Shape Generator for the DDscat Software* [62]. (a) 2D view, clearly demonstrating the partitioning of the diameter into a string of dipoles, (b) 3D view.

When setting up a model in DDSCAT, d is set implicitly from the target geometry, described with SHPARs in the *.par* file. For more complex models, such as nanoshells, the *Shape Generator for the DDscat software* [62] is used and allows setting an explicit d.

Figure 4.5 demonstrates how the DDA performs compared to Mie for SHPAR = 30 and 50. The plot shows scattering efficiency as a function of sphere radius. With increasing radius, the dipole spacing d, kept constant due to the constant SHPAR values, increases and accuracy falls. The DDA solution with SHPAR equal 30 starts deviating by more than 10 % at a radius of 92 nm, while the SHPAR = 50 solution stays within the 10 % error limit until a radius value of 213 nm.

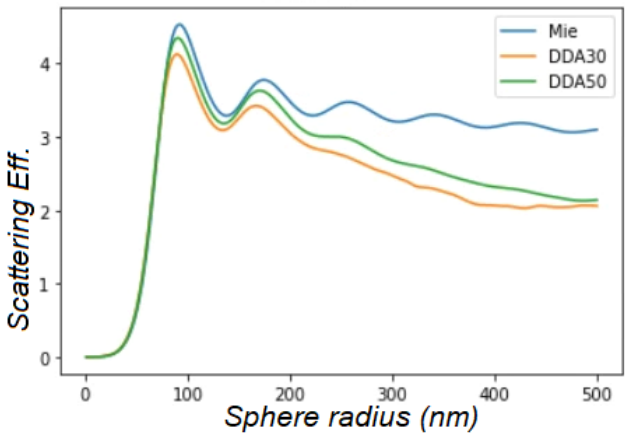

Figure 4.5: Scattering efficiency of a sphere as a function of its radius. Comparison of DDA solutions, SHPAR=30 and 50, with a Mie solution.

In this thesis, the DDA is used to compare with the FEM, in developing an AuFON model, only for single solid and nanoshell particles. An tutorial on how to set up a DDA model in DDSCAT is included in Appendix D. Of all the methods used in this thesis, it is the only one that could be used to calculate the surface field, for comparison with the trends seen in

the FEM. The DDA was, however, not capable of reproducing the SLRs in far-field coupled arrays. Thus, the coupled-dipole approximation was employed for this purpose.

4.5 Coupled-dipole approximation (CDA)

The CDA was the method that initially helped researchers predict and understand surface lattice resonances [45]. A rigorous mathematical treatment of it was given by Markel [56]. Most of the literature on the topic still employs variations on that formulation. The CDA is also based on Purcell and Pennypacker's discrete-dipole approximation [61] and there is in fact some ambiguity in references to CDA and DDA in the literature. Although initially being two different names for the same methodology, the literature on lattice resonances frequently refers to the application or extension of the DDA to periodic structures as the CDA.

There are many formulations for the polarizability employed in the CDA in the literature. DeJarnette [63] demonstrates the use of several different polarizability functions based on Mie, long wavelength corrected quasistatic approximation, dipole polarizabilities with an added quadrupole term and others, that correct for e.g. radiative emissions. For the purposes of this thesis, the CDA method is most valuable for its ability to demonstrate the trends in how SLRs change with type of array and array periodicity, for comparison with the FEM models, as the goal is to build a FEM model of the AuFON in COMSOL. Thus a more simple polarizability function was chosen with only the dipole contribution to the LSPR. Figure 4.6, plotting the extinction spectrum of a 1D array of 100 nm silver spheres, demonstrates this. The LSPR, to the left of the sharp SLR, starting at $\lambda_0 = 450$ nm, has a wide dipole resonance, but no quadrupole peak. However, the Mie solution of a single 100 nm silver sphere would clearly demonstrate the quadrupole (see the 100 nm plot ine in Figure 3.4). An approach to include a quadrupole term into the polarizability is presented in e.g. [39]. Another approach is also to use the DDA to solve for a single particle of arbitrary shape and size, and then use the polarization data with the CDA to solve for lattice effects [64]. However, DeJarnette *et al.* [39] argue that although well-researched, the CDA can only be used to investigate the general behavior of particle arrays. Numerical methods based on direct solving of Maxwell's equations, such as the FEM or FDTD, must be used for larger particles that exhibit higher-order extinction peaks, or, in general, more complex structures. The reason is simply that such structures might require very complex polarizability formulations to capture all the effects exhibited by the particles.

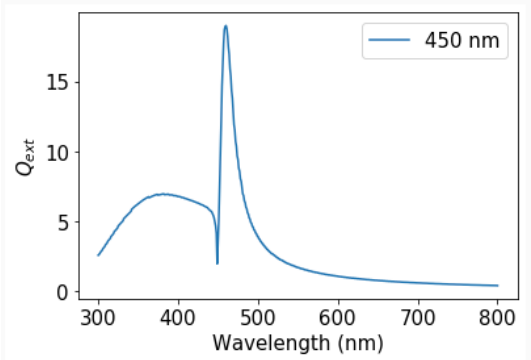

Figure 4.6: The LSPR and SLR peaks for a 1D array consisting of 100 nm silver spheres. A single-particle solution would reveal that the LSPR should have a dipole and a quadrupole resonance at this silver sphere size. This illustrates the limitation of the CDA approach employed in this thesis.

4.5.1 Formulation

In this thesis, a CDA formulation based on Zou *et al.* [57], [58] and Zhao *et al.* [65] is used. It is simplified from the authors' in the way that for the LSPR, only the dipole peak is included. Additionally, the authors use a Drude metal, with only the free electron (Drude model, Eqn. (3.13)) contributions, while in this thesis, a Lorentz-Drude metal model is used. This difference in approaches produces narrower LSPRs with higher peak values than those demonstrated by Zou *et al.* when the periodicity increases.

In a sufficiently large array of N particles, the particles in the middle of it will be acted upon by the dipole fields of all the surrounding particles. Letting N go to infinity, one can approximate that every particle will act as the central particle in the array. Thus, the polarization of each particle is assumed equal,

$$P = \alpha E_{local}. \tag{4.8}$$

E_{local} is the amplitude of the sum of the incident electric field and the retarded fields from all the surrounding dipoles. For a single small particle near resonance, polarizability is expressed as

$$\alpha = \frac{-A}{\omega - \omega_p + i\gamma + AS}, \tag{4.9}$$

where $A = \frac{1}{2}\omega_p R^3$ and S the retarded dipole sum. ω_p is the plasmon resonance frequency (electron volts) in the Drude model and R is the particle radius. w is the incident wave frequency in electron volts. γ is the half-width at half maximum from the Drude model, also expressed in eVs.

The polarization, with the expression for α inserted, is

$$P = \frac{-AE_{local}}{\omega - \omega_p + i\gamma + AS}. \tag{4.10}$$

Zou *et al.* further specify P for clusters or arrays of particles as

$$P = \frac{\alpha_s E_{local}}{1 - \alpha_s S}, \tag{4.11}$$

When the wavevector is perpendicular to the plane – or axis, in the case of 1D – the retarded dipole sum S is specified as

$$S = \sum_{j \neq 0} \left(\frac{(1 - ikr_{0j})(3\cos^2\theta_{0j} - 1)e^{ikr_{0j}}}{r_{0j}^3} + \frac{k^2 \sin^2\theta_{0j} e^{ikr_{0j}}}{r_{0j}} \right). \tag{4.12}$$

Assuming that particle 0 is the central particle in the array, r_{0j} is the distance between particle j in the array and the central one. The angle θ_{0j} is between the polarization direction and r_{0j}. See Figure 4.7. The accuracy of the dipole sum depends on whether N particles is enough for the sum to converge. In this thesis, it was experimented with array sizes between 1001x1001 and 5001x5001, the results of which will be discussed in Chapter 5.

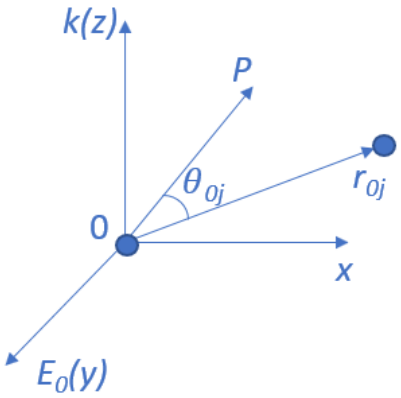

Figure 4.7: Illustration of the coordinate system used in the CDA. The axis labels show the direction of the propagation vector $\mathbf{k}$ and the incident field $\mathbf{E_0}$. In the simple case of a 1D array, the x axis would coincide with the array axis, as it is orthogonal to both $\mathbf{k}$ and $\mathbf{E_0}$. An arbitrary polarization vector $\mathbf{P}$ is used to define the observation point, with the angle θ_{0j} between $\mathbf{P}$ and the position vector of particle j, $\mathbf{r_{0j}}$. Figure adapted from [65].

In arrays with many particles, approximating an infinite system, optical cross sections can be expressed relative to a single particle [56]. The extinction cross section can be expressed as in [45],

$$C_{ext} = 4\pi k \mathrm{Im}\left(\frac{\alpha_s}{1-\alpha_s S}\right). \tag{4.13}$$

4.5.2 Applications of the CDA to finite 1D and 2D particle arrays

Zuo *et al.* [57], [58] suggest that having the polarization of light orthogonal to the array axis, results in more narrow resonances due to a positive contribution from the $1/r_{0j}$ term to the dipole sum. Conversely, for p polarization, $\theta_{ij} = \pi n, n = 0, \pm 1, \pm 2, ...$ and thus the sine term is zero. This is expected as dipoles radiate orthogonally to their axis of oscillation [39], [46]. This example was specific for 1D arrays, but does however demonstrate how the direction of polarization affects the dipole sum.

The following sections demonstrate how the CDA results for 1D, 2D square and 2D hexagonal arrays in this thesis were derived. The resulting derivations were implemented in Python and can be found in appendices E.3 - E.5.

1D arrays

From the argument above, let the incident light be s polarized light and each particle's induced polarization be directed parallel with the incident field. Next, the array axis is positioned such that the array axis is orthogonal to the polarization. See Figure 4.8. The position vectors $\mathbf{r_{0j}}$, which lie along the array axis, are also orthogonal to the polarization and hence the angle θ_{0j} is a constant value for all particles. Note that r_{0j} can be expressed as jr, $j = \pm 1, \pm 2, ...$, where the lattice constant $D = r$. This lattice constant will be used throughout Section 4.5 to keep a similar notation to Zou *et al.* Furthermore, it is realized that the distances r_{0j} from particle 0 to each particle j are the same on both sides of the symmetry axis for each j. This means that instead of summing over $j = \pm 1, \pm 2, ...$, it is enough to sum over $j = 1, 2, ...$ and multiply the resulting dipole sum by a factor of 2. This allows the simplification of Eqn. (4.12) as

$$S = 2\sum_{j>0} e^{ikjr}\left(\frac{ikjr-1}{(jr)^3} + \frac{k^2}{jr}\right). \tag{4.14}$$

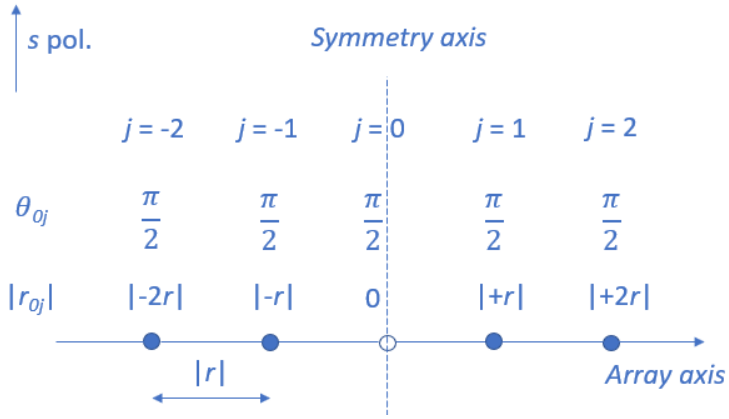

Figure 4.8: 1D array schematic showing the particle array, with the polarization of incident light and the derived angles θ_{0j} and distances r_{0j} from the center particle to each particle j. The distances are denoted as an integer number of r, the norm of vector $\mathbf{r}$. Note that the absolute distances are mirrored about the symmetry axis, allowing a reduction of the number of summations of particle contributions by a factor of two.

Such computational optimizations, utilizing array symmetry, in the implementation of the CDA method, result in the rapid semi-analytical CDA, rsa-CDA [39]. The rsa-CDA code is copyrighted and not openly published, but the approach described in this thesis emulates it by utilizing array symmetry.

2D square arrays

The expression for S in Eqn. (4.12) assumes that the direction of propagation is always orthogonal to the plane (2D) or axis (1D) of the particle array. For a 2D array, the polarization of a transverse wave will therefore always be in the plane of the array. The implication of this is that the polarization direction can be chosen freely in the plane of the array. For 2D arrays, we can set it parallel with the x axis, to simplify expressions.

Similarly to the 1D array, and in line with the rsa-CDA, we utilize symmetry to focus only on the first quadrant. The coordinates of particle j are $(m_j, n_j) = m_j\hat{x} + n_j\hat{y}$, where the real scalars $m_j, n_j > 0$. In the following, the subscripts j will be omitted and the coordinate pair of particle j will be expressed as (m, n). This allows us to express the distance from particle 0 to an arbitrary particle j as

$$r_{m,n} = \sqrt{(m\hat{x})^2 + (n\hat{y})^2}. \tag{4.15}$$

and the angle between $\mathbf{r_{m,n}}$ and polarization as

$$\theta_{m,n} = \arctan\left(\frac{n}{m}\right). \tag{4.16}$$

Figure 4.9 illustrates how the angles and distances can be mapped onto a 2D array.

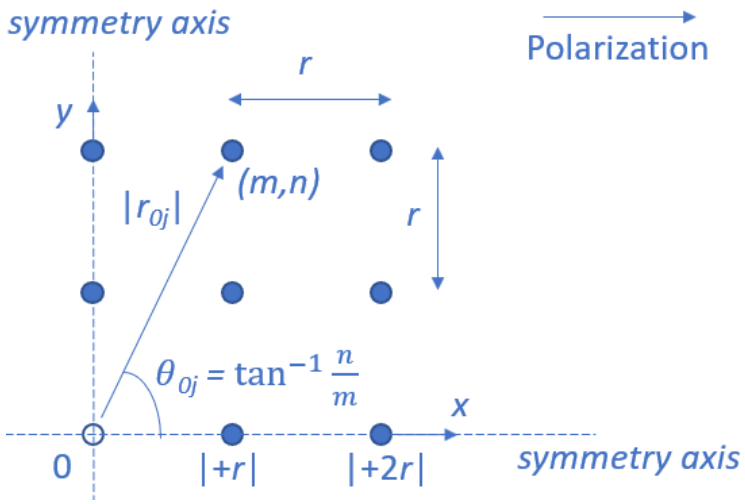

Figure 4.9: 2D square lattice array, with the key parameters illustrated. The horizontal and vertical periodicity is still r. The two symmetry axes allow restricting the dipole sum to the particles in the first quadrant, the angles of which can be found as shown in the figure. The expression for the angle uses the coordinates of particle j, (m, n).

The square 2D lattice has periodicity r horizontally and vertically. There is now also a periodicity along the half-diagonal, $r\sqrt{2}/2$, even though the diagonal spacing is $r\sqrt{2}$. In fact, the array is periodic along any off-axis or off-diagonal line through particles distanced

$$r\sqrt{(m^2+n^2)} \tag{4.17}$$

from one another [39]. The lattice resonances from these periods are, however, dominated by those resulting from coupling over distances r and $r\sqrt{2}$, due to the much higher number of particles satisfying these periods.

The dipole sum of the particles in the first quadrant, multiplied by four to obtain the dipole sum for all particles that do not lie on the symmetry axes, can then be expressed as

$$S = 4\sum_{m,n>0} e^{ikr_{m,n}}\left(\frac{(1-ikr_{m,n})(3\cos^2(\theta_{m,n})-1)}{r_{m,n}^3} + \frac{k^2\sin^2(\theta_{m,n})}{r_{m,n}}\right). \tag{4.18}$$

The contribution of the particles that lie on the axes can be found by assuming that the particles along each axis make up a 1D array, either orthogonal to the polarization or parallel to it. The same approach as for the 1D array in the section above can then be used. However, it's important to note that with the light polarization direction indicated in Figure 4.9, the contribution from particles on the x-axis is zero.

2D hexagonal arrays

The procedure to extend the 2D square lattice model to a hexagonal lattice, necessitates the introduction of new lattice vectors. Recall from Chapter 3.7.1 that the hexagonal lattice has lattice vectors $\mathbf{a_1}, \mathbf{a_2}$. It can be shown, using the 60° angle of the diagonal in the first quadrant of such lattices, that these vectors may take the form

$$\mathbf{a_1} = \frac{r}{2}\hat{x} - \frac{r\sqrt{3}}{2}\hat{y} \tag{4.19}$$

$$\mathbf{a_2} = \frac{r}{2}\hat{x} + \frac{r\sqrt{3}}{2}\hat{y}. \tag{4.20}$$

The approach to derive the position vectors and angles of each particle for the dipole sum is similar to the one used for the square lattice. The symmetry axes formed by drawing lines through the central particle, parallel to each lattice vector, respectively, form the coordinate system. Each particle j now has a coordinate $(m, n) = m\hat{a}_1 + n\hat{a}_2$, using the lattice vectors as the basis. See Figure 4.10. The position vector, from particle 0 to j, is now denoted $\mathbf{r_{m,n}} = m\mathbf{a_1} + n\mathbf{a_2}$ and its norm is $|r_{m,n}|$. The basis vectors are no longer orthogonal, such that one cannot use a simple method such as *Pythagoras' rule* to compute the norm. Likewise, the angle between the polarization vector and each particle's position vector, $\theta_{m,n}$ can no longer be calculated using a simple trigonometric relation. Both values are computed using Python's vector calculus functions in Appendix E.5.

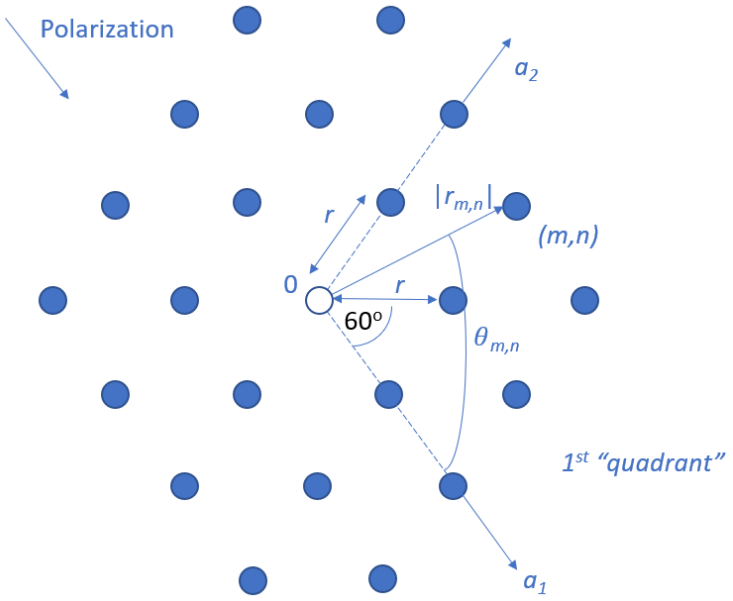

Figure 4.10: 2D hexagonal array. The periodicity is r. The coordinate system is in terms of the lattice vectors $\mathbf{a_1}, \mathbf{a_2}$. The symmetry axes from the central particle, parallel with the lattice vectors, allow restricting the problem to the first "quadrant", delimited by the a_1 and a_2 axes. The position vector from the center particle to particle j, with coordinates (m, n), is denoted $\mathbf{r_{m,n}}$ and has scalar value $|r_{m,n}|$.

The contribution from the particles along the axes, with either the m or n coordinate set to zero, the dipole sum is found the same way as in the 1D array case.

The symmetry axes through the central particle again allow restricting our attention to only the particles located in the first quadrant (as defined by the a_1, a_2 axes), then multiplying the resulting dipole sum by a factor of four. The contribution of these particles to the dipole sum is then

$$S = 4 \sum_{m,n>0} e^{ikr_{m,n}} \left(\frac{(1 - ikr_{m,n})(3\cos^2(\theta_{m,n}) - 1)}{r_{m,n}^3} + \frac{k^2 \sin^2(\theta_{m,n})}{r_{m,n}} \right) \tag{4.21}$$

The complete procedure for computing the dipole sum, with contributions from all particles and utilizing symmetry, is implemented in Appendix E.5.

4.6 Numerical solvers

Numerical solvers of systems of equations can be divided into two main categories, direct and iterative. Simple examples of such methods are the methods of Gauss' elimination (direct), where one manipulates the system matrix using row operations, and Gauss-Seidel' iterative method, where the system converges to a solution by using intermediate solutions from previous iterations. Problems that reformulate a large set of partial differential equations into a linear system often result in sparse matrices, matrices that have many zero off-diagonal elements. The FEM method is a good example, as seen from the derivations in Appendix B. This section describes the main sparse matrix solvers used in COMSOL and DDSCAT, and their strengths and weaknesses.

4.6.1 Solvers in COMSOL

COMSOL offers several direct solvers. These solvers are robust, but do require a lot of memory and computation time. Another drawback is that the resource usage grows fast with larger problem complexity [66]. The fastest of these, though at the expense of somewhat higher memory usage, is the free MUMPS solver, developed as part of the European project PARASOL to make use of parallel computers, and specifically for use with the FEM [67]. It is a multifrontal solver, specifically for solving large sparse systems of equations. The benefit of this solver is its universality. It can be used regardless of the boundary conditions applied and even if the mesh is so fine in certain domains that the iterative solvers will not converge. COMSOL makes it possible to save memory usage by solving the model *out of core*. That is, the intermediate matrix factorizations are stored on the hard drive. This may, however, require large amounts of storage space, which can cause a system crash – if the system runs out of space to operate normally – or simply slow down the computations significantly, as the hard drive is much slower than the RAM.

Iterative solvers are faster and less memory-intensive. A model with one million degrees of freedom can normally be solved on a computer with 8 GB RAM using an iterative solver. The same model using MUMPS could require more than 70 GB RAM when out-of-core mode is disabled and storing all parameter solutions in memory. It was, however, experienced that iterative solvers fail to converge when using periodic boundary conditions, presented in Section 4.9.4. This was also confirmed by COMSOL Support. Domains with extremely fine meshes can also cause the solver to converge very slowly. The latter can, however, be combated by relaxing the error tolerance or increasing the number of iterations the solver will perform before giving up finding a solution that satisfies the set error tolerance. The iterative solvers offered in COMSOL are based on the conjugate-gradient (CG) method. In their general form, these solvers require that the matrix A, in a general system of the form

$$A\mathbf{x} = \mathbf{b}, \tag{4.22}$$

is positive definite and symmetric. However, COMSOL sets the biconjugate gradient stabilized method (BiCGSTAB) as the default iterative solver. This solver is more robust, as it can be used for non-symmetrical matrices as well [68]. The trade-off is that a standard CG implementation, while not as robust, is faster for the special case of symmetric matrices.

4.6.2 Solvers in DDSCAT

DDSCAT implements only iterative CG-based solvers. In the DDA section, it was shown that the physical accuracy of the method depends on the dipole spacing. The numerical

accuracy of the solution, given a set dipole spacing, is evaluated by Draine and Flatau [52], [51] as

$$\frac{|\mathbf{A}^\dagger\mathbf{A}\mathbf{P} - \mathbf{A}^\dagger\mathbf{E}|}{|\mathbf{A}^\dagger\mathbf{E}|} < h. \tag{4.23}$$

h is the error tolerance value. DDSCAT doesn't produce any error messages when the iterations fail to converge to a solution. It simply moves on to the next parameter value after the maximum number of iterations defined in the parameters file *ddscat.par* (see Appendix D) are tried. Making the model produce a solution for all parameter values might require experimenting with different values for the error tolerance, also defined in the parameter file.

Recent versions (7.1 and above) of DDSCAT implement the BiCGSTAB solver. As the goal of using DDSCAT was initially to support the modeling process in COMSOL, it was chosen to use a solver that is available in both software packages. Therefore, the BiCGSTAB was chosen for use in DDSCAT as well. A comparison of solvers available in DDSCAT has been performed by Flatau [69]. Though this was published before the implementation of the current BiCGSTAB solver, the comparison did, however, show that an earlier third-party implementation of the biconjugate stabilized gradient method performed well compared to other iterative solver algorithms.

4.7 Materials

Chapter 3 presented the dielectric response function and showed that it depends on wavelength. The Raman spectrometer used for the measurements in the experimental part of this thesis was operated at 785 nm, so the wavelength range of the models was set to an interval that captured the behavior at this wavelength. Refractive indices (RI) for the particle material and surrounding medium are needed for a complete specification of the wave equation, as seen in Chapter 3.1. The Mie and DDA models also need material RIs. The CDA model requires only electronvolt values corresponding to the resonance frequency and the half width at half maximum. In this thesis, these are based on the Mie solution of Lorentz-Drude gold and silver metals.

4.7.1 Gold and silver

Gold and silver nanoparticle scattering resonances typically occur in the VIS region of the EM spectrum [36, p. 65]. Thus a simulation range of about 450 nm - 850 nm wavelengths was chosen for gold, to capture some of the behavior at NIR wavelengths. The models for silver use 350 nm as the lower limit.

The optical materials library in COMSOL is based on published experimental results and models of refractive indices of materials. The gold and silver films used in this text were modeled using the calculations based on the Lorentz-Drude model presented in Chapter 3.2, using parameters from Rakic et al. [34]. COMSOL version 5.4 has a materials library that contains these parameters for both metal models, though the tabulated values are limited to VIS and IR regions. However, as already mentioned, the particles' properties are most promiment in the VIS and NIR regions of the spectrum. It should also be mentioned that COMSOL interpolates between the tabulated values, by piece-wise cubic interpolation. For Mie calculations, the Python code in Appendix E.1 was used to calculate the refractive indices for both metals.

4.7.2 Polystyrene

The model for polystyrene is based on experimental measurements from Sultanova *et al.* [70]. Experimental measurements of polystyrene's refractive index (RI) in the VIS region result in very uncertain values for the imaginary part of the RI. The data by Sultanova *et al.* are for wavelengths 436 nm - 1052 nm, effectively limiting the model to this range, and contain only the real part of the refractive index (RI). The polystyrene then acts as an ideal dielectric with no absorption of incident light.

4.7.3 Surrounding medium

The simulations were done using air and water as the surrounding medium. Air has an average refractive index (RI) of about 1.0003 in the VIS region. In this text, the real part of the RI is rounded to exactly unity for simplicity. It is assumed that air exhibits almost no absorption at ambient temperature and thus the imaginary part of its RI is set to zero [71]. For water, the RI at 20 °C is in the 1.33-1.35 range in the VIS region. At the wavelength used for measurements in this text, 785 nm, the water's RI is approximately 1.33 [72]. The high absorption caused by the O-H stretching modes occurs at higher wavelengths, well into the IR region [31, p. 278]. In the wavelength range 400 nm to 800 nm, used in the models, absorption in water is negligible and the complex part of its RI is ignored.

In non-saturated solutions, glucose has a refractive index very similar to that of water, about 1.34 in aqueous solution with less than 10 % glucose concentration [73]. However, the relevant concentrations are between the physiological level (4-8 mM) and 1 M [28]. The concentrations in the higher end of that range are mostly useful for calibration of sensing devices. In the results discussing models with water as surrounding medium, one can therefore assume that these approximate the results one would have for a non-saturated glucose solution. The reason is that even at 1 M, glucose molecules only make up less than 2 % of the solution, as it can be shown that pure water has a molar concentration of 55 M. The average RI of a 0.004 M - 1 M glucose solution would therefore be about 1.33.

4.8 Modeling process

Figure 4.11 presents an overview of the modeling process. The main simulation process was developing the FEM model, but the supporting models were used simultaneously. The arrows going both ways between two adjacent boxes illustrate a process where one went back between the boxes and changes parameters or improved the model.

First, the single gold particle model from the project thesis [1] was reviewed and modified to find extinction efficiencies from both gold and silver. Then extended to calculate surface area-averaged SERS enhancement factor G_{SERS}, as described in Section 4.9.6 further below. The model was verified against theory and analytical Mie solutions, as well as a comparison with DDA. Then the model was extended to near-field coupled dimers and 1D arrays to estimate the maximum SERS achievable for select sphere diameters, if the values references in the literature could be obtained.

The model was then extended to far-field coupled solid particle arrays and the lattice resonances were investigated to see whether these could produce SERS EFs comparable to those seen in near-field coupled particles. Both 1D and 2D arrays were investigated. The CDA model was used to verify these results, as well as for comparison against published CDA results. Silver spheres are used here predominantly, as there are published results available

for silver. This is also why single particle silver models were developed, and not just gold. To enable a direct comparison of single particle resonances and far-field coupled particle resonances.

Not all results were included in this thesis, as e.g. the results of changing medium in a 2D array were similar to doing so in a 1D array.

Then, going back to single particles, nanoshells were simulated to see how they differ from solid particles. These results were compared with Mie theory for nanoshells by Oldenburg [44], as implemented by Nanocomposix, the quasistatic approximation for nanoshells in Chapter 3.6.1 and DDA. Finally, solid particles were replaced by nanoshells in the hexagonal array model to produce AuFONs. As the model was already checked for correct behavior in the far-field, the AuFON model was created only for a close-packed hexagonal lattice, as it was introduced in Chapter 2. All aspects of the nanoshell and AuFON models could not be investigated, but it is believed that since the solid particle models behave correctly, for both single particles and arrays, and both for near- and far-field coupling – the nanoshell and AuFON models should therefore also be well-behaved within the range of wavelengths supported by the material models. The resulting AuFON model is then a platform that more complex features, such as surface roughness, can be added to.

A few simulations with close-packed nanoshell arrays and top hat arrays were performed to test the final model and compare against available experimental data.

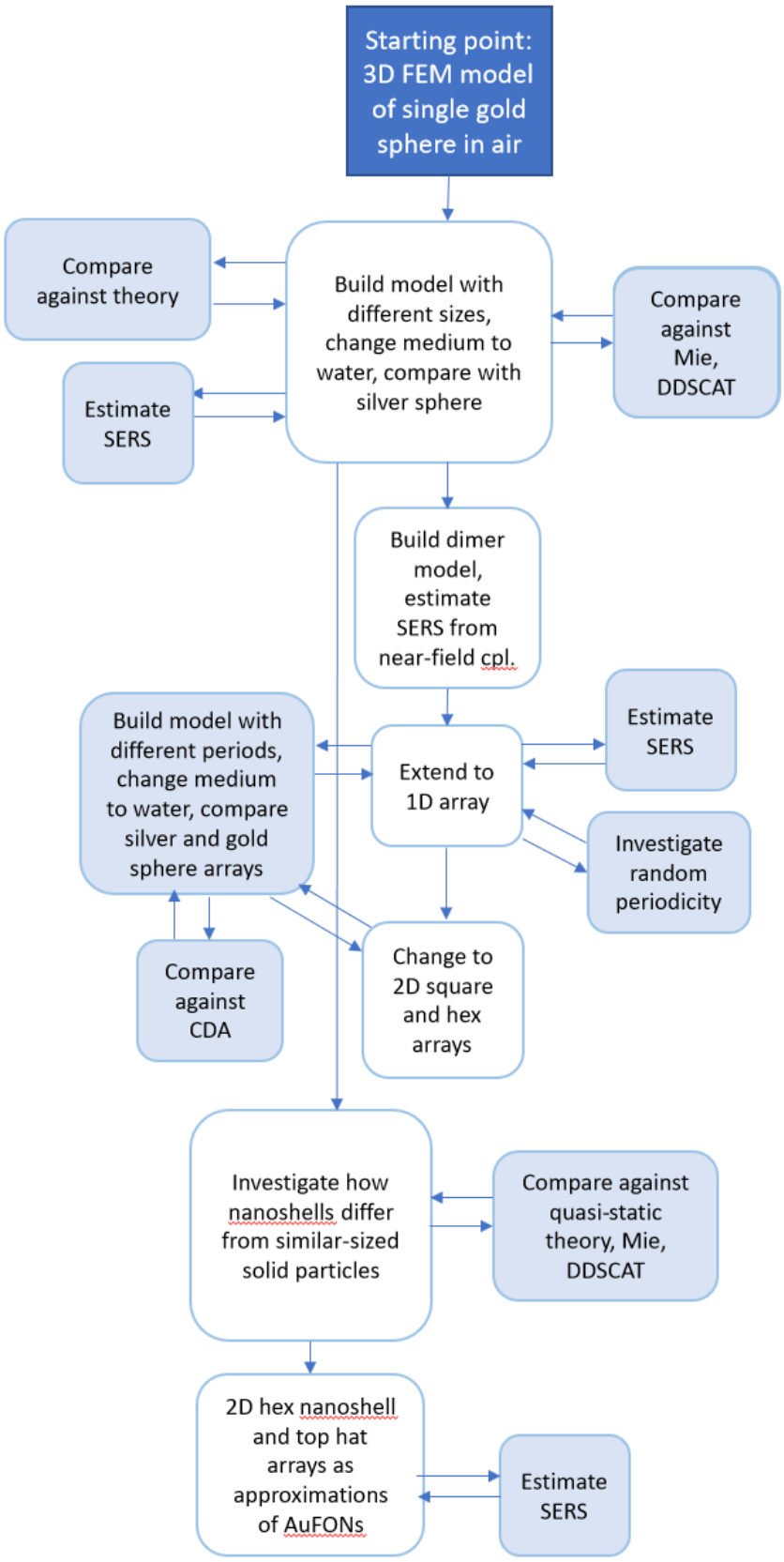

Figure 4.11: Illustration of the modeling process, showing the different computational steps performed sequentially.

4.9 Models in COMSOL

The COMSOL model calculates optical cross sections in the *scattered field* formulation from the scattered field using the *relative* Poynting vector, defined in terms of the *relative* electric and magnetic fields, $\frac{1}{2}E_{rel} \times H^*_{rel}$ (this can be seen by activating *Equation View* in COMSOL's model builder view. See Appendix B for details.). The relative fields are the total field minus the incident field. For the electric field, this is $E_{rel} = E - E_i$, which is, outside a particle, just the scattered field. Inserting the relative Poynting vector into (3.28), instead of the total field Poynting, and dividing by the incident light intensity I_0, as in (3.31), produces the scattering cross section. The absorption cross section is determined from the heat losses inside the particle volume, rather than using the surface integral of the Poynting vector. This is the recommended way in COMSOL [74], as it eliminates any contribution to the absorption cross section in the case of an other absorbing material or medium around the relevant particle volume.

Initially it was attempted to build a two-step model for solving the electric field in and around the particles, where the background field is calculated in the first step, using the *total field* formulation. The solution from this step is then inserted as the background field in the *scattered field* formulation in step two. However, this effectively doubles the degrees of freedom in the total problem, doubling the memory demands, and more than doubles the computation time. Instead, the background field is set manually using the relation

$$E_0 = \sqrt{2I_0\eta}, \tag{4.24}$$

where $\eta = \eta_0/n_r$ is the impedance of the medium. $\eta_0 \approx 377\,\Omega$ is the impedance of free space [37, pp. 165-166]. The intensity I_0 is calculated from an incident power of 150 mW. This power is achieved when running the 785 nm laser at 50 % power in the Renishaw InVia Reflex Raman Spectrometer [75], previously used in the lab section of the project thesis [1]. Thus, the model gets one step closer to the lab setup one would use with the structures modeled. It should also be pointed out that the background field can simply be normalized to 1 [V/m], as for SERS enhancement factor estimation, we are primarily interested in the relative field enhancement and not the nominal amplitude of the scattered field.

The models are set up with the background field in the form of a plane wave, Eqn. (3.7), linearly polarized in y direction and propagating in $-z$ direction. To make the results comparable to those from using CDA, where the propagation direction is orthogonal to 1D and 2D particle arrays, array periodicities are in the xy-plane.

4.9.1 Single sphere models

The single particle models used as reference, to examine the effects of changing the medium, particle composition, size, as well as the effect of extending the model to particle arrays, are a gold and a silver sphere with a diameter of 100 nm. In the project thesis [1], this particle size was interesting as the scattering cross section of a 100 nm *gold* sphere is much larger than its absorption cross section and thus the extinction cross section as a function of wavelength has a similar lineshape to scattering, with the same peak location. In the literature, this result can be found in e.g. Ref. [76]. This made it possible to examine the single sphere model using only the scattering cross section or efficiency. Additionally, gold spheres of this size are not large enough to support a quadrupole resonance mode. This particle size is therefore carried over into this thesis to connect it with previous work.

The modeling approach for single sphere models is based on Ref. [74], where symmetry is used to limit the geometry to a quarter-sphere, using perfect electric conductor boundary conditions (BC) in COMSOL, in conjunction with the perfect magnetic conductor (PMC) BC. This technique is described in Section 4.9.4 below.

To make the model easily extendable to an array model, periodic in either one or two dimensions, the simulation space of this model was modified from spherical, as in Refs. [1], [74], to cubic, as shown in Figure 4.12. This comes at a slightly higher computational cost, as there are more degrees of freedom in a cubic model with the same width and mesh resolution. This is offset by the employment of PMCs, though, as will be illustrated in Figure 4.17b. The base model is very simple, with a single metal sphere inside the cubic simulation space, which is itself enveloped in a perfectly matching layer (PML) to absorb scattered radiation. The PML is described in Section 4.9.7 below. In the base model, the medium that fills the simulation space has the refractive index set to 1, to indicate free space or an approximation for ambient atmosphere [71].

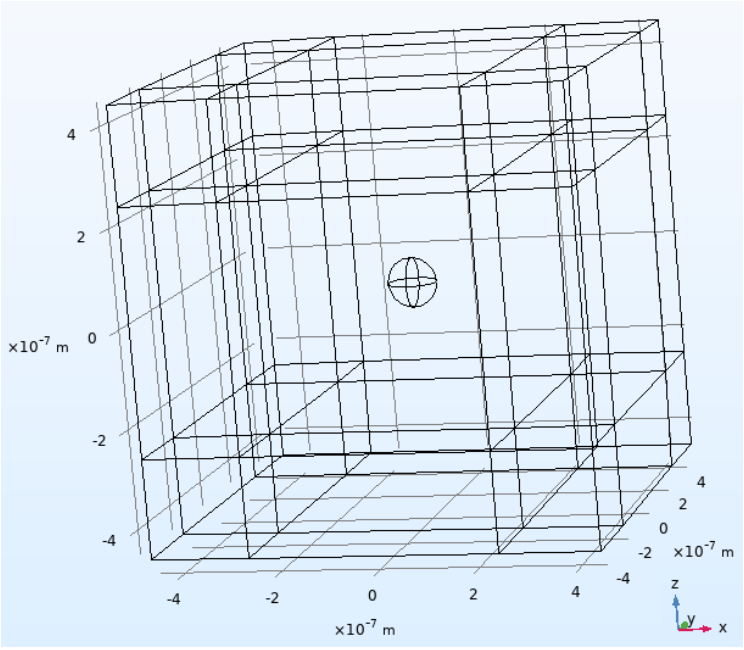

Figure 4.12: Wireframe sketch of a single-sphere model, showing a cubic simulation space, particularly apt for extending it into a periodic array. The simulation space contains a single metal sphere and is enveloped in a perfectly matching layer (PML) that prevents scattered radiation from reflecting back. The medium around the sphere can have an arbitrary refractive index n_m, which is initially set to 1, for free space.

4.9.2 Nanoshell particles

Nanoshells are approximations for the individual particles in an AuFON structure. These are modeled as two concentric spheres, with the core sphere having a radius r_1 and the film around it having a thickness $r_2 - r_1$, such that the total particle radius is r_2. Figure 3.9 already presented such structures. Both COMSOL and DDSCAT are used to calculate the light scattering properties of such particles and estimate their surface field, by replacing the solid metal particle in the model in Section 4.9.1 above with a dielectric polystyrene core and a metal film. The calculations for these structures were only performed with gold as the metal and the results compared with solid gold particles.

A closer approximation of the AuFON shape is the "top hat" structure. This was inspired

by the particles pictured in Figure 4.13. It can be clearly seen that only the top half of the dielectric core is covered by gold film. The result resembles a glazed muffin top, or similar.

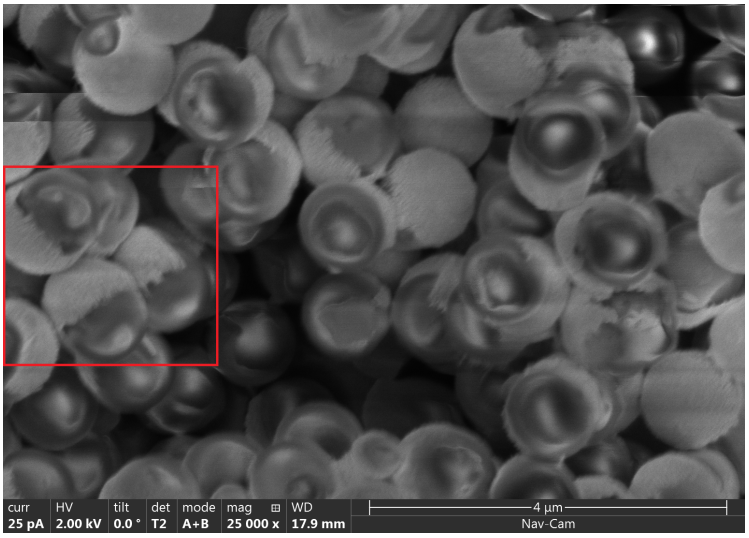

Figure 4.13: SEM image of disordered 1 µm polystyrene particles coated with 200 nm thick gold film magnified 25 000 times. Note the shape of the gold cap which covers only the top half of the polystyrene core. This fact was previously used for illustrating the AuFON fabrication process in Figure 2.2.

The top hat structure in the model looks as imaged in Figure 4.14. The hat is an ellipsoid-half, with a vertical major axis and a horizontal minor axis. The core still has radius r_1, while the gold hat has thickness $r_2 - r_1$ where it is thickest, on the very top. The hat is modeled as an ellipsoid, with the major axis along the vertical. The horizontal extent of the hat, the minor axis, is set to extend a third of the vertical thickness beyond the core radius. That is, the horizontal radius of the particle is $r_1 + (r_2 - r_1)/3$. This parameter, alternatively the major-minor axis ratio, is another degree of freedom in the model, that can be optimized. There is research on how ellipsoids acts optical versus spheres, e.g. Ref. [77]. This thesis does, however, not try to arrive at the most optimal top hat structure, as that will be too extensive in addition to verifying all the build steps in the model. It but merely presents it as the final stage in the AuFON model and demonstrates some trial simulation results, which are compared to the simpler nanoshell model.

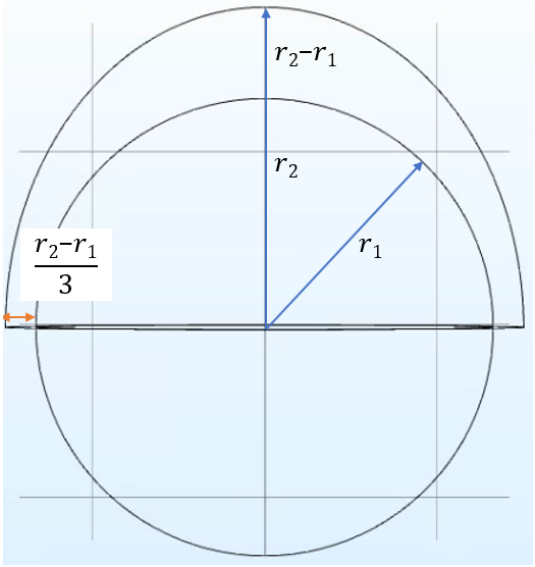

Figure 4.14: Wireframe model of the top hat structure in COMSOL. The core is spherical and dielectric, with a radius r_1, while the gold hat is a half-ellipsoid, with thickness $r_2 - r_1$ along the major axis and $(r_2 - r_1)/3$ along the minor axis.

4.9.3 Array models

The single-sphere model is extended in one or more directions in the XY plane using periodic boundary conditions. In this thesis, the simplest, 1D arrays, are first investigated to see how the resonances shift compared to an isolated single homogeneous particle. Then 2D square lattice and 2D hexagonal lattice arrays are built and investigated.

4.9.4 Modeling periodicity in COMSOL

Two methods for extending a COMSOL single-particle model into a particle array were examined in this thesis. They both produce the same results, but there are some trade-offs. Periodic boundary conditions (PBCs) can be applied on a wider range of problems. They do, however, not support the use of iterative solvers. Additionally, PBCs do not allow exploiting symmetry to the same extent as the method based on the use of perfect magnetic conductor (PMC) boundary conditions. Models using the PMC can therefore be solved several times faster due to both a significant reduction in degrees of freedom, using symmetry, and using a faster and less-memory intensive iterative solver.

Periodic Boundary Conditions (PBCs)

COMSOL employs a few different types of PBCs. The most common PBC in COMSOL models is the Floquet PBC [78]. It is defined as

$$E_{dst} = E_{src} e^{-ik_F(r_{dst} - r_{src})}. \tag{4.25}$$

The source and destination (periodic) boundaries, as defined in an orthorhombic unit cell, are pictured in Figure 4.15. The Floquet wavevector k_F introduces a phase difference between the boundaries. The component that is tangential to the periodic boundaries has to be set to a value, based on the refractive index of the surrounding medium in the unit cell. When using excitation ports in a COMSOL model, this vector can be set automatically by the software. $r_{dst} - r_{src}$ is the norm of the vector describing the distance between boundaries. For the purposes of this thesis, the Floquet wavevector is set to zero, such that the field on

the source boundary is equal to that on the destination boundary. This assumption matches COMSOL's automatic assessment quite well: Early on in the work process, before setting the background field manually, the model was initially set up in two steps, with excitation ports to provide the background radiation. COMSOL's feature of setting k_F automatically was employed (though this value is not output by the software explicitly). It was found that the result matches the assumption of no phase change for the periodic arrays modeled,

$$E_{dst} = E_{src}. \tag{4.26}$$

This reduces the Floquet PBC to a continuity PBC. It should be noted that PBCs can only be applied on plane boundaries, and the source and destination boundaries must be parallel.

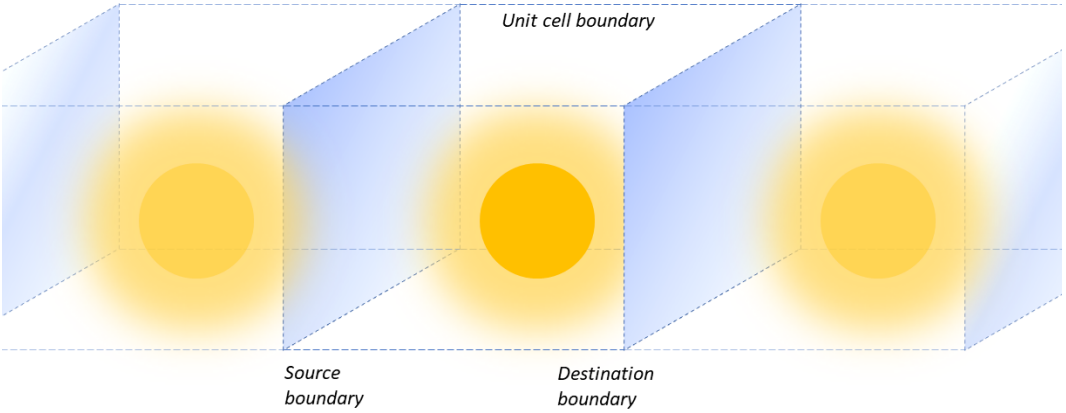

Figure 4.15: A 1D array of unit cells, with an irradiating particle in each, modeled as a single unit cell with two of its boundaries set as the source and destination periodic boundaries, translating the wave equation solution between the boundaries along the array axis. This is a mathematical representation of the coupling of radiation between cells in the array.

Figure B.1 in Appendix B illustrates how the PBCs were implemented in the final hex lattice nanoshell model.

Perfect Magnetic Conductor (PMC)

The PMC boundary condition is used alongside the default perfect electric conductor (PEC) boundary condition to exploit the symmetry in a problem. Assuming the unit cell is cubic, with the particle placed in the middle of it, one can reduce the number of degrees of freedom by a factor of four, or even by a factor of eight, by employing perfect magnetic conductor boundaries. The added benefit is that one can also use iterative solvers, which are faster and use less computational resources. The PMC is defined as

$$\mathbf{n} \times \mathbf{H} = 0, \tag{4.27}$$

where $\mathbf{n}$ is the normal vector to the symmetry plane considered and $\mathbf{H}$ the magnetic field. This condition implies that the tangential magnetic field is equal to zero at the boundary. The second implication is that the current vector will be mirrored on both sides of the plane and has no normal component [79]. Figure 4.16 illustrates this.

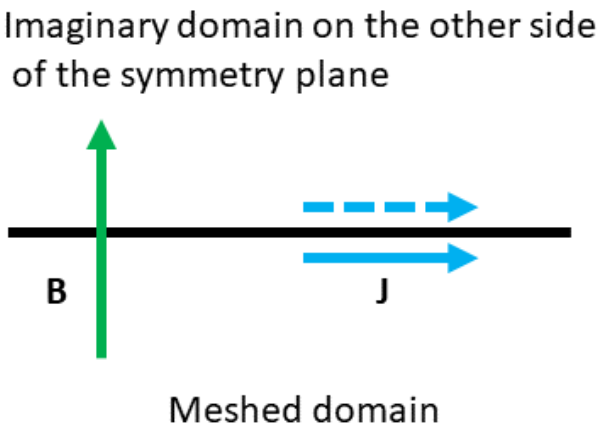

Figure 4.16: The PMC boundary condition represented by a symmetry plane. The boundary condition allows the magnetic flux ($\mathbf{B} = \mu\mathbf{H}$) to have a normal component and the current $\mathbf{J}$ to flow tangentially to the boundary.

The perfect electric conductor (PEC) is a similar boundary condition that COMSOL automatically applies to all external boundaries. It is similarly defined as

$$\mathbf{n} \times \mathbf{E} = 0. \tag{4.28}$$

This, similarly, imposes symmetry across the boundary for tangential magnetic fields and currents, while restricting the electric field to its normal component.

Figure 4.17a shows a cubic unit cell, with PML layers over and under it. The software auto-applies the PEC to all outer boundaries. The extinction cross section calculated over the particle's surface area will be the same, only reduced by a factor of four, if the model is cut along the YZ and XZ planes to extract only the first quadrant (in the XY plane). Applying the PMC along the incident light's polarization plane, in this model the YZ plane (the light is linearly y polarized), results in the model shown in Figure 4.17b.

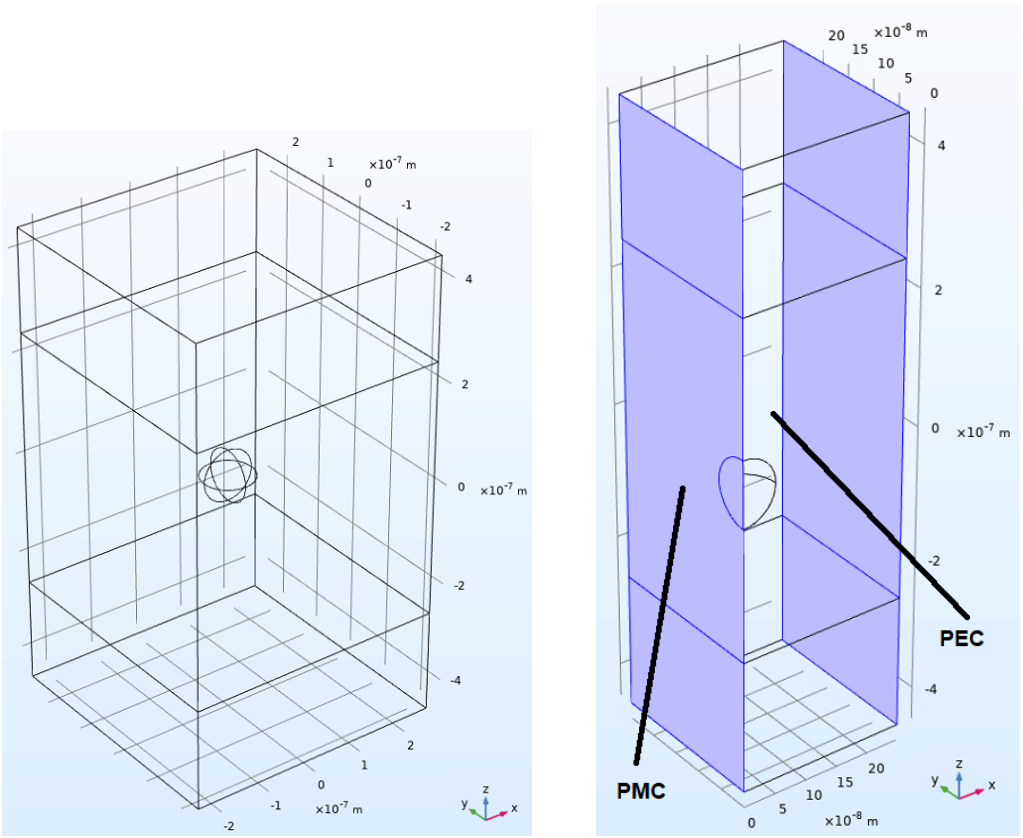

(a) (b)

Figure 4.17: (a) Cubic unit cell with PML layers over and under it. Model delimited by PEC boundary conditions on all outer boundaries. (b) Model reduced to the first quadrant (in the XY plane), with PMCs applied to the highlighted planes parallel with the polarization of the incident light, along the y axis. The remaining outer boundaries still have PECs applied.

In the model in Figure 4.17b the electric field is allowed to flow tangentially to the PMC and normal to the PEC, making it continuous along the y axis. Similarly, the magnetic field is continuous along the x axis. The result of using these boundary conditions is identical to that of imposing PBCs in the x and y directions, but saves memory and time. The drawback of this method of introducing periodicity into the model is that the boundaries where one applies the PMC need to be parallel with the polarization of the incident electric field, while the boundaries where PECs are applied must be tangential. Thus, this approach cannot be used to study periodic structures with a hexagonal lattice. Note that the model can be reduced to a single particle model, without periodicity, by applying PMLs on the outer boundaries where $x, y > 0$ and removing the PMC from the boundary where $x > 0$. Then the model still exploits the geometric symmetry, reducing the number of degrees of freedom by a factor of four.

4.9.5 Evaluating the optical cross sections and efficiencies

The models are set up to calculate the extinction, scattering and absorption cross sections as well as efficiencies. Formally, scattering is calculated by integrating the scalar flux over the surface area of the integrating sphere and dividing by the incident field intensity I_0. In other words, integrating the scattered field's Poynting vector, discussed in Section 4.9 above, over the integrating sphere surface and dividing by I_0. Absorption is calculated by integrating heat losses inside the particle over its volume. The extinction cross section is, as in Eqn. (3.30), the sum of the two. The efficiencies are found by dividing cross section by

the particle's geometric cross section, as in Eqn. (3.32). Tables B.1 and B.2 in Appendix B present the expressions used in COMSOL.

4.9.6 Estimating the SERS enhancement factor

Eqn. (3.51) presented the $|E/E_0|^4$ approximation for SERS EF. The important issue is exactly where this enhancement factor should be sampled. Sampling this at the point where field enhancement is maximal would not be representative for the whole structure or particle. An average of the surface-field enhancement over a particle's surface area would be more appropriate. The surface area-averaged enhancement factor for a single particle can then be expressed as in [80],

$$G_{SERS} = \frac{1}{A_0} \int \left(\left| \frac{E}{E_0} \right| \right)^4 dA. \tag{4.29}$$

A is the surface area of the particle and A_0 its geometric cross section. Similar approaches have also been reviewed by Pilot *et al.* [4, pp. 8-9]. Formulations similar to Eqn. (4.29) were also proposed by Zhao *et al.* [41] and Schedin *et al.* [81], but the present formulation was selected due to its ease of implementation in a volumetric mesh model, such as the 3D FEM model developed in this thesis.

Due to the volume discretizations employed in numerical methods, the surface field in the near-field region, directly on the particle surface, is not a reliable measure of the surface-field enhancement. See Figure 4.18a. The particle surface serves as a domain boundary, separating the mesh elements inside the particle where the internal field is calculated, and the elements in the surrounding medium with the external field values computed at their nodes. The surface field measurement is therefore performed by placing an integrating sphere around the particle, a small distance δ from the particle's surface, as seen in Figure 4.18b. The shorter this distance, the more accurate the field measurement.

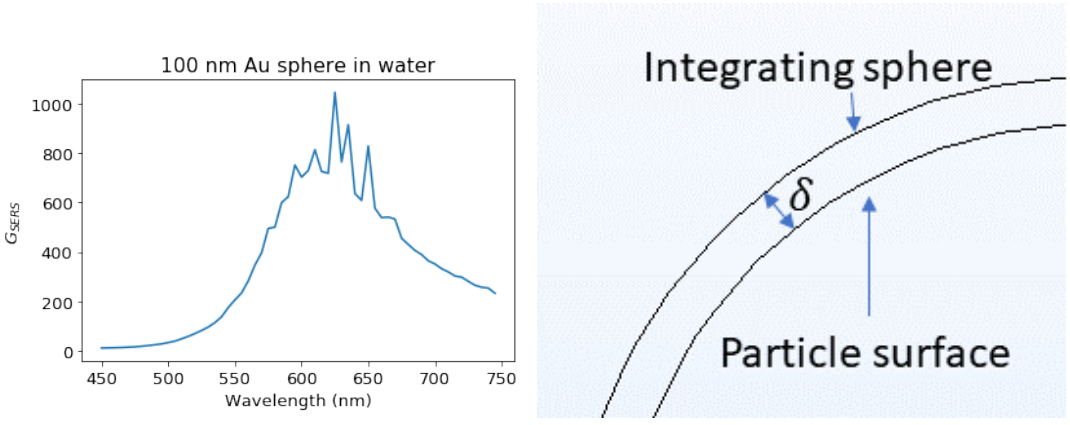

(a) **(b)**

Figure 4.18: (a) SERS enhancement factor estimate measured directly on a particle's surface, showing a distorted lineshape. (b) Illustration of an integrating sphere placed a distance δ from the particle's surface to combat the issue demonstrated in (a).

There is a trade-off between accuracy in estimating the surface field and computational complexity, since a smaller δ would result in a much finer mesh between the particle's surface and the integrating sphere boundary. A distance of 1.5 nm was found to be a good value and used in single-particle SERS estimations, or in arrays with periodicities $>>$ 1.5

nm. Smaller δ values do not result in significantly increased accuracy, but considerably increase the number of degrees of freedom and computational complexity.

As demonstrated in Chapter 3.5.3, the field enhancement between two or more closely-spaced particles is highly localized. For a particle in a close-packed lattice structure, the integrating spheres of each particle would intersect each other and possibly even merge with the particles. In models of close-packed arrays, to avoid the integrating sphere from intersecting the Wigner-Seitz cell boundaries, the cell boundaries themselves are used as integrating surfaces as illustrated in Figure 4.19. In such arrays, the field is highly localized between the cell boundaries and the part of the particle surface whose outward normal vector is parallel to that of the closest cell boundary. This was seen in Figure 3.12. Thus, most of the field flux would be captured by the cell boundaries. Surface area A in Eqn. (4.29) is then replaced by the surface area of the cell boundaries. Flux lines coming from directions other than those along the highly localized field lines are assumed to be much weaker. Thus, the normalization cross section A_0 is still assumed to be equal to the particle's geometric cross section.

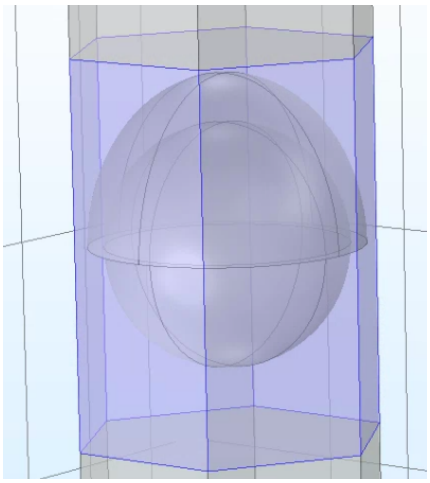

Figure 4.19: The cell boundaries in a hex lattice top hat model used as integrating surfaces for SERS EF estimation. The image shows the COMSOL implementation.

4.9.7 Perfectly matched layer (PML)

As the FEM is a volumetric mesh method, it needs a boundary condition to terminate the mesh. The problem with a simple absorbing boundary condition (ABC), such as the one presented in Appendix A, is that it creates nonphysical reflections. The scattering boundary condition (SBC) in COMSOL is an improved version of the ABC that is designed to let out the scattered waves. It can be formulated to match the shape of the scattered wave, such as plane, spherical or cylindrical. However, there are still considerable reflections when the incident wave is not perfectly orthogonal to the boundary. In this thesis work, the SBC was demonstrated to slightly misplace resonance peaks and make them appear wider. The PML was therefore chosen for the final models.

The PML is a spatial domain that wraps around the simulation space and absorbs the scattered waves [82]. The layer's properties can be adjusted to the curvature of the simulation space by adjusting the scaling and curvature factors of the PML. The rule of thumb is that the PML thickness should be at least half the wavelength of the incident wave. An advantage of PMLs over SBCs is that one does not need to know the shape of the scattered wave. In simple cases, such as the 1D array, one can assume the scattered wave is cylindrical [56],

but in more complex arrays, this is more difficult to assert.

4.9.8 Meshing

One of the most important aspects of modeling in COMSOL is setting an appropriate mesh. The distribution of the finite elements in various regions of the geometry not only has a drastic effect on memory requirements, but also on whether the computations will converge to a solution. Figure A.6 in Appendix A shows the most important reason for setting an appropriate mesh, i.e. the accuracy of the solution at various points in the simulation domain.

The mesh size should be governed by the excitation wavelength used in the simulation. It should be at least an order of magnitude lower than the wavelength to adequately resolve the electric field. For a nanoscale structure and VIS region wavelengths, this still gives a lot of freedom in setting minimal and maximal mesh size parameters. In the near-field domain by the nanoparticle's surface, we would want the FEM solution of the electric field to be highly resolved, and thus have a finer mesh there. Further away, the mesh can be coarser, although COMSOL does set limitations on how fast the element size may grow, since adjacent elements need to have equally large side facets, as explained in Appendix A on the FEM.

A technique to minimize the number of mesh elements in domains where the solution is of little interest, such as the PML, is that of swept meshes, which creates a layered mesh where the layers have equal distributions of mesh elements. This reduces the number of elements, compared to tetrahedral or tetragonal elements, and thus memory usage.

4.10 Random periodicity in arrays

Besides fabrication techniques such as colloidal mask-hole lithography or drop-casting, other lithographic techniques are also employed to create periodic arrays. Modern electron beam lithography (EBL) techniques have progressed from allowing minimum periodicities in the range of 160-220 nm in the mid-1990s, with linewidths permitting feature sizes of about 10 nm, to modern setups permitting feature sizes of just a few nm and periodicities of less than 50 nm [83], [84]. Thus, there is always some inaccuracy in fabrication and exact periodicities of arbitrary size cannot be obtained, making it worthwhile to investigate models with deviations from perfect periodicity.

The surface lattice resonances (SLR) in periodic arrays arise due to constructive interference between the dipole fields of the particles that emerges on a wavelength at, or close to, the wavelength corresponding to the exact periodicity D. We disregard, for the sake of argument, the fact that SLRs are not always located at a wavelength $\lambda = D$, as was discussed in the harmonic oscillator model with coupling between diffracted light and the LSPRs (recall from Chapter 3.7.2). When the distances between the radiating dipoles deviate from D randomly, due to fabrication errors or similar, by a value $0 < \tilde{\epsilon} < \epsilon$, the interference between the LSPR of any given dipole with the far-field dipole irradiation of surrounding dipoles may occur at a wavelength $D \pm \tilde{\epsilon} \neq D$. This means there is a positive probability that they do no longer contribute to constructive interference at the wavelength corresponding to D. Additionally, they create destructive interference at that wavelength, which further decreases the SLRs that are observed with non-random periodicities. Some literature, employing both models and experiments, investigates disordered arrays. It has been demonstrated in lab experiments with discs that random generation of gold discs on a substrate using colloidal

lithography, with no crystalline order, produces extinction similar to that calculated for single discs [24], [32, Ch. 9.4.1], [85]. That is, if the deviation from periodicity is large enough, one can eliminate the constructive interference that gives rise to SLRs completely.

An approach that can make computational models a bit closer to real lab extinction measurements is by adding random deviations from perfect period. Modeling disorder with stochastic period is the method chosen for this thesis to investigate this: If the CDA or FEM model employs a period D, one can introduce a stochastic period

$$\tilde{D} = D \pm \tilde{\epsilon}. \tag{4.30}$$

$\tilde{\epsilon}$ is here a stochastic variable having some probability distribution. As a simple approach, one can assume that it is uniformly distributed, $\tilde{\epsilon} \sim \mathcal{U}(0, \epsilon)$, with ϵ being a predefined constant upper limit [86, pp. 171-172]. $\tilde{D}$ is then also uniformly distributed,

$$\tilde{D} \sim \mathcal{U}(D - \epsilon, D + \epsilon), \tag{4.31}$$

as shown in Figure 4.20. The distribution is centered on the intended periodicity D, the mean of the distribution, and the probability of each value in the support $\tilde{D} \in [D - \epsilon, D + \epsilon]$ is a constant value

$$f(\tilde{D}) = \frac{1}{2\epsilon}. \tag{4.32}$$

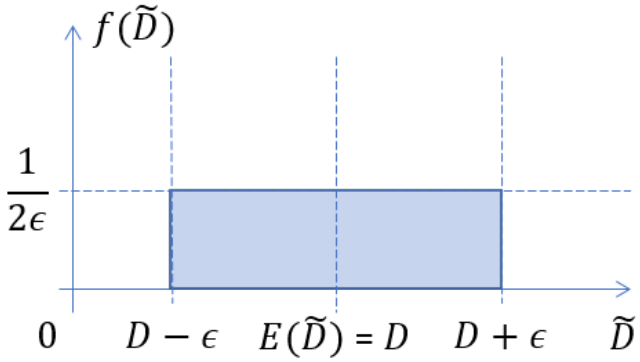

Figure 4.20: Uniform distribution model of the stochastic array periodicity $\tilde{D}$. The mean value is the intended exact period D, while ϵ is the maximum deviation in either direction.

A Gaussian distribution may also be used, because it puts greater weight on outcomes close to the mean, than a uniform distribution. With modern fabrication techniques, such as colloidal lithography which produces tightly-packed crystals, large deviations from periodicity are unlikely. However, the tails in a Gaussian distribution may have a significant weight, increasing the chance of occurrence for high values. For simplicity, we'll use a uniform distribution, as formulated above.

Appendix E contains a code snippet that modifies the CDA 1D array model to include the proposed modeling approach for random periods. In COMSOL, it is also possible to modify the model to include random periods. However, to see the effects of this, one needs to include at least 100 particles in the model. In COMSOL, this demands too much memory and would require a supercomputer to implement. Another complication is that in FEM, one meshes also the space between the particles, so the memory demand grows with larger lattice constants, even if the number of particles is kept constant. Random periodicities will therefore only be demonstrated briefly using results from CDA computations and it is

implied that the behavior noted there is also valid for FEM models, as the effects are largely determined by statistics.

4.10.1 Simulation methods summary

Simulating much more than a few particles is not possible in COMSOL due to memory constraints. Thus, CDA is more suited to demonstrate the effects of variation in periodicity or how the SLRs emerge with less or more particles in the array. In COMSOL, one has to restrict oneself to simulating an infinite array and, thus, look at the fully developed lattice effects only. The CDA, on the other hand, lacks the possibility to simulate realistic particles as it uses the dipole approximation. It ignores all higher-order modes and effects such as non-homogeneous surface polarization and phase retardation. It is possible to include more complex polarizability functions into the CDA to include e.g. quadrupole effects into the model. However, some researchers have adopted a simulation methodology where they use DDSCAT to simulate a single particle of arbitrary shape and composition [64]. Then they use the computed single particle results in the CDA model to predict the plasmon-lattice interactions. This approach was not explored in this thesis, as the main goal was to develop a COMSOL model, and use the alternative methods to compare the results. Still, COMSOL offers more flexibility in both designing arbitrarily-shaped particles and arranging them in an arbitrary fashion within the primitive cell. Furthermore, COMSOL allows more flexibility in estimating the SERS EF by using integrating spheres and other surfaces. The only one of the alternative method that allows computing the surface field is DDSCAT, but it does not offer any options of integrating the values over a surface. One can only sample it at a specific coordinate.

The analytical Mie model is obviously only applicable for spherical geometries, but is invaluable when building the model and making sure it behaves well for simple spheres, or concentric nanoshells, as in the Mie extension from NanoComposix.

Table 4.1 presents a summary of the simulation methods, with their strengths and weaknesses. Note that the limitations of the CDA pertain only to the implementation in this thesis. As discussed before, more complex formulations can be found with extended capabilities.

Table 4.1: Comparison of numerical simulation methods used in this thesis.

Parameter	**COMSOL (FEM)**	**DDSCAT (DDA)**	**CDA**
Computation time	Slowest (depends on desired accuracy)	Slow (dep. on desired acc.)	Fast (though also depends on accuracy)
Memory usage	High	Moderate	Low
Parallel computations	Limited support, but enough for 10-20 CPU core workstations	Limited, but can easily be mitigated (Appendix D)	Not in the present implementation
Applicability	Any particle shape/-composition, any periodicity, multiparticle structures, etc.	Single particles, arbitrary shape and composition	Single-material particle arrays, particles modeled as dipoles
Based on approximation method	No, solves wave equation directly	DDA	DDA
Type of discretization	Volumetric mesh	dipole array	Dipole array
Computes optical cross sections by	Integrating Poynting vector	Solving for polarization of each dipole	Solving for polarization of each dipole
Computes field in/outside partice	Yes	Yes	No (this implementation)
Calculates SERS enhancement directly	Yes	No	No

Chapter 5

Results and discussion

Simulation results obtained using the models and tools presented in Chapter 4 are presented and discussed here. First, single-particle results from Mie, FEM and dipole approximation methods are summarized here for noble metal spheres, with a quick summary on how the resonances change with medium RI and particle size. This is, to some extent, a summary of the main results presented in [1], with DDA and a comparison between silver and gold particles added, along with the introduction of SERS enhancement factor (EF) estimation.

This chapter focuses on the light scattering and absorption, that is, extinction, properties of particles, along with the SERS EF. Recall that extinction cross sections, normalized by particle cross-sectional area, as in Eqn. (3.32), are unit-less extinction efficiencies. The extinction efficiency spectrum allows seeing at which wavelengths particles exhibit resonances and how wide or narrow these are, as discussed in Chapter 3.3.1. Apart from an analysis of how the resonances of extinction and the SERS EF are related, the extinction efficiency will be the main way of comparing the models. Whether they have similar resonances. The analytical Mie solution serves as the benchmark and it will be discussed how the numerical models deviate from it.

Data found in the literature for single particles was available for both scattering and extinction efficiencies, but mostly from calculations. Empirical data for spherical particles is difficult to obtain. For particle arrays, the published calculations mainly present extinction efficiencies. As a consequence, the results previously presented in [1] for single particles have been recalculated as extinction efficiencies, such that the shifts in resonances, when extending the model from a single particle to an array, are directly comparable with published extinction efficiencies. Furthermore, results from applying the SERS EF estimation approach in Chapter 4.9.6 are also presented here.

The model is built upon, until we finally arrive at the AuFON model in Section 5.3.1, where the computed SERS EF is compared to published results and the reference plot in Figure 4.1.

5.1 Single sphere

The optical of single spheres are first presented, to demonstrate the behavior of single spheres before the model is extended to arrays. This section will focus on the behavior of surface plasmons in gold particles, as that is the metal used in the final AuFON structure. A short comparison with silver, which is used much more in the literature, will be made at the end.

5.1.1 Comparison of single particle model results

First, the extinction efficiency is estimated using the DDA, FEM and Mie models and compared. The plots for a single 100 nm (diameter) gold sphere in air as a function of wavelength, using these models are fitted to Lorentzians and plotted in Figure 5.1b. The full width at half maximum (FWHM) data was computed by fitting the spectra to Lorentzians of the form

$$\gamma = \frac{a(\Delta/2)^2}{(\Delta/2)^2 + (\lambda - \lambda_0)^2}. \tag{5.1}$$

$\Delta/2$ denotes the half linewidth at half maximum (HWHM), a is the amplitude and λ_0 is the resonance frequency. Figure 5.1a shows the close fit achieved between a Lorentzian and the extinction efficiency of a 100 nm Au sphere computed using FEM.

Table 5.1 lists the main parameters of these single particle models, illustrating the differences between the different computational methods.

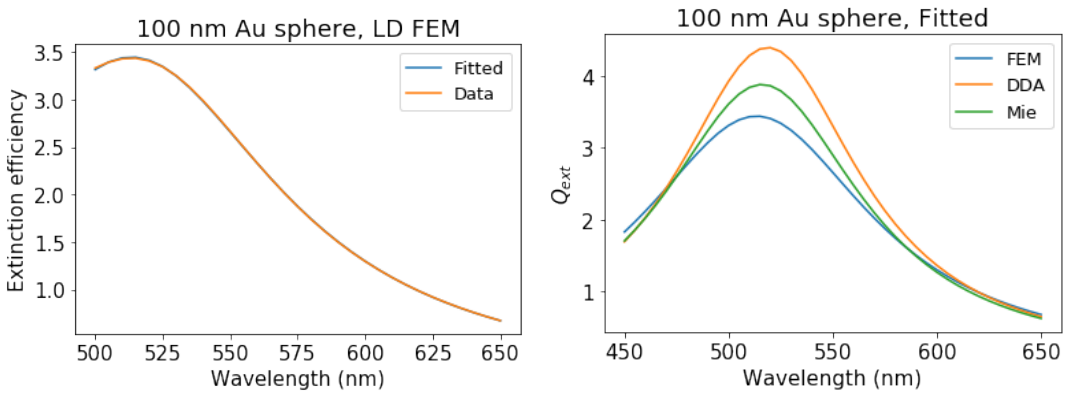

(a) **(b)**

Figure 5.1: Extinction efficiencies of numerical and analytical solutions for a 100 nm Au sphere fitted to Lorentzian lineshapes. (a) FEM solution data vs. the fitted function (b) Fitted lineshapes superimposed on one another.

The justification of the present line fitting approach is that the resonance peaks in the Lorentz-Drude model are explicitly defined using Lorentzian oscillators. Furthermore, the extinction cross section itself was, in Section 3.3.2, expressed as a Lorentzian. One can then model the extinction cross section or efficiency as a superposition of Lorentzians from the underlying models. In the case of a particle not large enough to support modes other than the dipolar one, such as the 100 nm gold sphere model, the lineshape can be represented using a single Lorentzian, as a dipole has a single resonance.

Similarly to the fitted FEM data in Figure 5.1a, the Mie and DDA model results were well-fitted to a Lorentzian. As the dipole resonance lineshape is not symmetrical, the fit was performed on one side only.

Table 5.1: The peak extinction efficiencies, resonance wavelengths and FWHM of the single particle LSPRs solved for with Mie (based on Bohren and Huffman), DDA and FEM. For comparison, the Mie solution from NanoComposix is also included. The model solved using these methods is a single Au 100 nm sphere in air or free space.

Model	Max Q_{ext}	$\lambda_{resonance}$ (nm)	FWHM (nm)
FEM	3.4	513	155
Mie	3.9	516	125
DDA	4.4	519	110
NanoComposix	3.95	520	95

The table shows that the Mie values are in the middle of the intervals delimited by the numerical models. Both the max values of extinction, as well as the resonance wavelengths. The FEM method underestimates the maximal extinction compared to Mie, while the DDA overestimates it. This pattern is seen for other sphere diameters as well, before the particle becomes large enough to support a quadrupole mode. However, it does not mean that this holds for all particles/materials, all surrounding media etc. Recall from Chapter 4.7.1 that COMSOL uses interpolated RI values from its material library, while the Mie code uses the code in Appendix E.1 that generates a value for every nanometer in the wavelength range. Furthermore, this inference is based on the current Mie implementation, based on Bohren and Huffman [31, pp. 479-482]. While the results of this code were checked against the examples given in [31], an alternative Matlab implementation [87], where absorption is computed using the internal field inside the sphere, and additionally, compared against the Mie solutions by Jain *et al.* [88], errors cannot be ruled out.

Table 5.1 also includes the analytical solution from NanoComposix[1], based on a Mie model extensions for nanoshells [44]. This solution was also fit to a Lorentzian for comparing with the others. NanoComposix values present an extinction maximum value and resonance wavelength similar to the Mie solution based on Bohren and Huffman. NanoComposix's solution has a much narrower lineshape, though. Note that the NanoComposix data uses gold metal data of unknown origin. It is likely that it is experimental bulk metal data by Johnson and Christy [89], as most literature refers to them. Thus the NanoComposix values are not directly comparable, but proved very useful for guiding simulation work, as one can estimate from them where one should find a resonance. The resonance wavelengths between the Lorentz-Drude and Johnson and Christy gold data are not that different, as seen from the table.

The accuracy of FEM and DDA methods is subject to a trade-off with computational cost. In DDA, one can use more dipoles to represent a particle, which may improve solution accuracy, but increases the computation time significantly. For the models in this thesis, at least 10^5 dipoles were used, in agreement with the benchmark in Table D.1, Appendix C. In FEM, one can also improve the resolution of the mesh, which will lead to greater computation time, as well as much higher memory usage. The resolution was therefore fitted to the smallest dimension of a given model, which required a minimum element size of at most 5 nm.

Concluding this section, we see that the discrepancy between maximum extinction values, predicted from Mie and the numerical model, is somewhat more than 10 %. It was noted in Chapter 4.4 that, at least for the DDA, a deviation of up to 10 % from Mie is considered a good match. The present results are considered adequate, as the models, in general, follow

[1] (`https://nanocomposix.com/pages/mie-theory-calculator`)

the Mie solutions, when compared across several particle sizes.

5.1.2 Single-particle plasmonic properties

As the numerical models are benchmarked against the Mie model, the remainder of this section will use Mie extinction efficiencies to demonstrate a few important properties of the single particle model.

The dependence of the extinction peak value, resonance wavelength and width of the peak on sphere diameter is illustrated in Figure 5.2a. The plot demonstrates the characteristic traits of the extinction efficiency's diameter dependence. The retardation and dampening effects manifest themselves with a redshift in the resonance wavelength. This results in a characteristic *volcano* or cascade pattern when going from one sphere size to the next, as noted by e.g. Shafiqa *et al.* [76]. This cascade would not be seen when using the quasistatic approximation, as it doesn't include these effects. Another effect that is seen in the model, when going from smaller to larger sphere diameters is that the scattering efficiency starts to contribute increasingly more to total extinction. Recall from Eqn. (3.30) that extinction is the sum of scattering and absorption. As Figure 5.2b shows, the presented sphere diameters are not large enough to see scattering dominate over absorption, but it will be seen when changing the medium from air to water. As was described in Section 3.5.2, for smaller particles the decay of surface plasmons is by absorption. For larger spheres the mechanism changes towards emission of light, scattering, which explains the modeled behavior. It is noted also in e.g. Ref. [76].

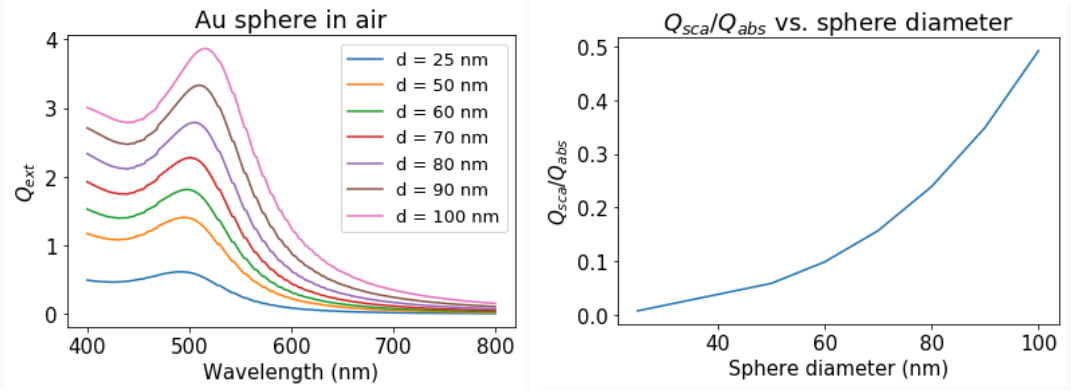

(a) **(b)**

Figure 5.2: (a) Extinction efficiencies (Q_{ext}) of single gold spheres of various diameters (in legend) in air. (b) Scattering versus absorption efficiency ratio as a function of sphere diameter.

It is also important to note that for the sphere sizes included in the plot, gold spheres act as dipoles, with only the dipole peak clearly visible. Examining a surface plot depicting the electric field's amplitude distribution in an area in the XY-plane around the particle, one can predict the emergence of a quadrupole by the rotation of the poles about the z axis (out of plane). Figure 5.3 below illustrates the difference in the radiation pattern between 50 nm and 100 nm diameter gold spheres. The 50 nm sphere has perfectly symmetrical poles. The dipole pattern outside of the 100 nm sphere is clearly unsymmetrical, with the poles rotated closer together. This is an indication of an emerging quadrupole [77], even though it is not yet visible in the extinction spectrum in Figure 5.2a. The reader is referred to Appendix C for a demonstration of the emergence of higher-order multipoles in large gold particles.

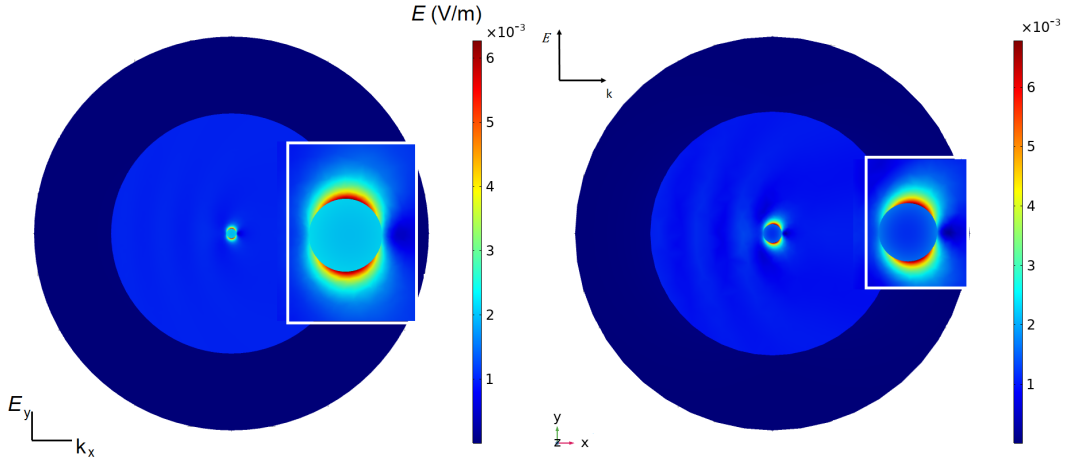

Figure 5.3: Electric field norm distribution in XY-plane for gold spheres. The incident field was 10^{-3} V/m. The inset shows the spheres magnified and incident light polarization and propagation directions are indicated. (a) 50 nm sphere. (b) 100 nm sphere, showing the poles rotated closer together.

The final property worth noting in Figure 5.2a is that there is a lineshape broadening with larger diameter. This was expected from the quasistatic optical cross sections in Eqn. (3.42). In the full Mie solution, as shown here in Figure 5.2a, there is also a gradual broadening of the dipole resonance as the higher-order modes start to emerge with higher particle size. This reduces the dipole oscillator strength [32, pp. 206-207] in addition to redshifting resonances.

5.1.3 Change of medium

The final effect presented in this summary of single sphere model extinction properties is that of changing the RI of the medium. In the previous subsections the medium was air, or free space, with RI ≈ 1. Lower medium RIs dampen the radiation, lowering all optical efficiencies [32, pp. 208-209]. Thus, changing the medium to water, RI ≈ 1.33 as discussed in Chapter 4, increases the extinction efficiency as shown in Figure 5.4a. The wavelengths on the abscissa still refer to free space wavelengths, λ_0, and will do so for the remainder of this thesis.

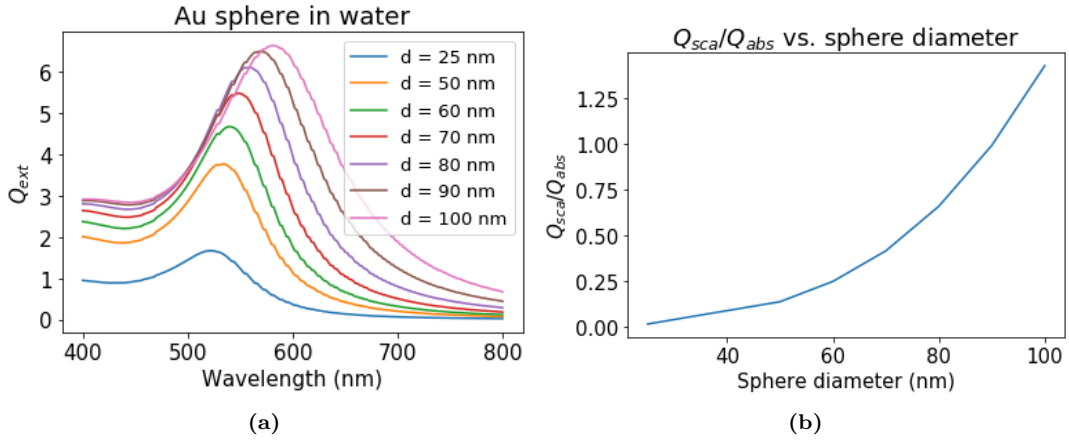

Figure 5.4: (a) Extinction efficiencies of single gold particles in water, with different diameters, as shown in the legend. In water the peaks are redshifted and peak efficiency values are increased compared to air. (b) Scattering versus absorption ratios for several sphere diameters in water.

As mentioned in the previous section, when discussing how scattering increases with sphere size, Figure 5.4b illustrates that in water, the presented sizes are already large enough for scattering to contribute more to extinction than does absorption.

Change of medium also shifts the resonance wavelengths. Sarid and Challener [32, p. 313] note that for every unit change in the medium's real RI, the extinction peaks are redshifted by 200 nm. Comparing figures 5.2a and 5.4a, we observe a redshift of the extinction peak for the 100 nm gold particle from 516 nm to 580 nm. This corresponds well with Sarid and Challener's rule of thumb. The peak extinction efficiency for the 100 nm sphere has increased from 3.9 to 6.6, which indicates decreased dampening in a higher-index medium, as mentioned above.

5.1.4 SERS Enhancement factor estimation

In this section, all sphere models were calculated using the FEM model. Figure 5.5 plots the surface area-averaged SERS enhancement factor as a function of wavelength for a single 100 nm diameter (a) gold particle and (b) silver particle, respectively, alongside the extinction efficiency. Both particles in air.

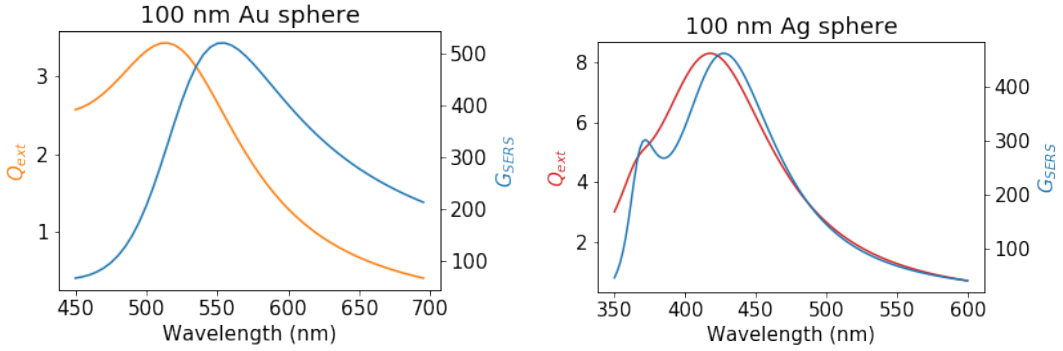

(a) **(b)**

Figure 5.5: Extinction efficiencies (Q_{ext}) and SERS enhancement factors (G_{SERS}) as functions of wavelength, for an isolated 100 nm (a) gold and (b) silver particle, respectively, in air.

The plots let us compare the properties of single gold and silver particles. Silver particles exhibit higher extinction efficiency than gold for equal sphere sizes. Figures 3.4 and 5.2a can be used to compare gold and silver sphere Mie solutions for a few additional diameters. From the extinction plot for silver, we see that at a diameter of 100 nm, the particle already has an emerging quadrupole peak at about 370 nm, which broadens the dipole resonance and decreases its peak value. These strong plasmonic properties in silver are due to the significantly higher imaginary part of its RI [2], which yields stronger polarization. The SERS EF plot line in Figure 5.5b demonstrates the superior polarization of silver more prominently. For the particle size shown here, the quadrupole peak at 370 nm is clearly evident in the SERS EF plot for silver. Due to the sharing of energy between the two oscillators in the silver plot, rather than just the one strong dipolar oscillator in a similar-sized gold sphere, the SERS enhancement factor for silver has a lower peak value. Typically, the literature on SERS focuses on silver, as it exhibits larger enhancement factors than gold at particle sizes where the LSP modes are only dipolar. Sarid and Challener demonstrate this for 60 nm particles [32, p. 206]. Here, the 100 nm silver sphere is already large enough

[2] This can be readily compared using e.g. `https://refractiveindex.info/?shelf=main&book=Au&page=Rakic-LD` and `https://refractiveindex.info/?shelf=main&book=Ag&page=Rakic-LD`

to support a quadrupolar mode and thus it exhibits lower peak values than a 100 nm gold sphere, which is still not large enough to support quadrupoles.

Both plots exhibit the same tendency of the SERS EF peak to be redshifted relative to the extinction efficiency resonances. Similar results were also seen from the DDA model. The SERS peak for gold is wider and more redshifted than that of silver. This comes from a redshift of the maximal surface field amplitude relative to extinction maximum efficiency. This redshift, much like the extinction resonance redshift with increasing particle size discussed before, is due to the dampening effects from spontaneous radiation emission, which increase with particle size [77]. Ignoring these effects, as done in the quasistatic model, would result in the maximum field amplitude occurring at the same wavelength as the dipole peak.

The SERS EF follows the same pattern as the extinction efficiencies, when simulated for different sphere sizes. One sees the same cascading volcano profile, with redshifts of the SERS EF peaks as the diameter increases. It is instrumental to look at the maximum surface field amplitudes for a few gold particle diameters, and estimate the maximal SERS EF that can be achieved on the surface of a single particle. Table 5.2 summarizes this for a few select diameters in the 50 nm – 100 nm interval. The maximum surface-field is measured on the surface of the particle at the poles – an average of the values at the two poles.

Table 5.2: Surface-field enhancement factors (EF), maximum SERS EF estimated using the $(E/E0)^4$ approximation, the wavelengths at which the surface-field is maximal and the wavelengths of peak extinction efficiencies for spheres of diameters 50 nm, 60 nm, 80 nm and 100 nm.

Sphere diameter (nm)	Max surface-field EF	Est. Max SERS EF	λ_{max}^{EF} (nm)	λ_{max}^{ext} (nm)
50	4.5	410	522	494
60	4.9	576	525	496
80	5.1	676	531	503
100	6.4	1678	556	515

The table demonstrates that for particle sizes considered here, the surface field intensity increases with size. With increasing diameter, so does the surface area, which becomes increasingly more polarized until the particle reaches a size where the surface area is too large to be homogeneously polarized. At this point, secondary, quadrupole and higher oscillators emerge, decreasing the maximal surface field. Note that the peak in average SERS EF seen in Figure 5.5a is a lot smaller than the theoretical maximum at the poles of a 100 nm particle, as shown in the last row in Table 5.2.

This concludes the review of relevant single particle optical and plasmonic effects and the comparison of single particle computational models. It was seen how particle size and medium permit tuning the resonances. These are only some of the properties which allow tuning the nanostructure to a specific resonance wavelength. Particle shape, although not considered here (see e.g. [32, Ch. 9]) also greatly affects the resonance wavelengths and achievable surface field enhancement factors.

Putting together several particles, or ordering them in an array, also affects the localized surface plasmon resonance wavelengths, as well as giving rise to new resonances, as will be seen next.

5.2 Near-field and far-field coupling in arrays

Extending the homogeneous single particle model to an array results in near-field coupling when the array is close-packed and far-field coupling when the lattice constant is on the order of several particle radii. Near-field coupling is only between nearest neighbors, as it was seen in Section 3.5.2 that the coupling weakens at a rate l^{-3} as particle separation l increases. It can therefore be modeled using as little as two particles. This will be presented first.

Far-field coupling produces SLRs. This will be investigated in the 1D array case, as it is simple, yet exhibits most of the coupling effects observed in more complex arrays. 2D arrays will also be considered, as the final AuFON structure is a 2D hexagonal lattice array. The difference between a single particle's far field radiation and a periodic array is that the array is essentially a diffraction grating. As presented in Section 3.7.2, lattice peaks occur as the result of constructive interference between the diffracted incident and scattered light. When the light wavelength approximately matches the array periodicity, the diffracted waves from the slits in the grating are in phase with one another.

5.2.1 Near-field coupling

The values of the SERS EF peaks for both metal particles in Figure 5.5 demonstrate that without near-field coupling, that results in *hotspots* of local field enhancements (introduced in Section 3.5.2), the field enhancement on the surface of a single particle yields rather modest SERS enhancement factors. Both noble metal particles produce SERS peaks with a magnitude on the order of 10^2, which is several orders of magnitude below the enhancement factors reported for colloidal crystals. Recall that these are $10^6 - 10^8$, as reviewed in Chapter 1).

For the 100 nm diameter gold particle considered, the dipolar oscillator mode still dominates and we consider these particles as dipoles. Dipoles radiate in the far-field in directions perpendicular to the dipole axis [39], [46]. They do however couple in the near-field along their dipolar axis. To see the near-field coupling the incident light must be polarized along the dipole axis, parallel with the particle chain. To avoid confusion, it is useful to use particle separation distance l, rather than the lattice constant D. These quantities relate as $l = D - d$. Here, diameter $d = 100$ nm. Figure 5.6a plots the extinction efficiencies of gold spheres in an array with various distances l. The plot next to it shows the average SERS enhancement factors. From the extinction plot, one can see that with smaller lattice constants, the extinction efficiency is decreasing. As discussed in Section 3.5.2, near-field coupling suppresses far-field scattering with decreasing l, so this tendency agrees with theory. Additionally, the extinction peaks are redshifted with decreasing l. The discussion in Maier [36], reviewed in Section 3.5.2, does not specify exactly in which direction the extinction peak shifts from near-field interactions. We can, however, use the CDA, presented in Section 4.5. The polarization expression in Eqn. (4.10) includes a term AS. Zou *et al.* [65] argue that this term can be used to predict the shift. For polarization parallel with the array, the term is positive and for particle separations of less than 100 nm, the peaks are redshifted due to near-field coupling. The CDA is only valid dipoles, but it was already argued above that the spherical 100 nm gold particles behave very much as dipoles. Le Ru and Etchegoin [40] demonstrate a similar behavior for 25 nm gold spheres, as will be shown below. The SERS plot in Figure 5.6b demonstrates how the average and peak enhancement factors drastically increase with smaller l. As presented in Section 3.5.2, the near-field coupling weakens as l^{-3}. Conversely, it increases as l^3 for very small values of l. This is seen well for l values

less than 10 nm in the figure below. Ru and Etchegoin [40, p. 356] note that the l^{-3} rule is observed for separation distances around $l = 1$ nm. Figure 5.7a further below shows that at $l < 1$ nm, the field EF is almost doubled for every 0.2 nm decrease in l.

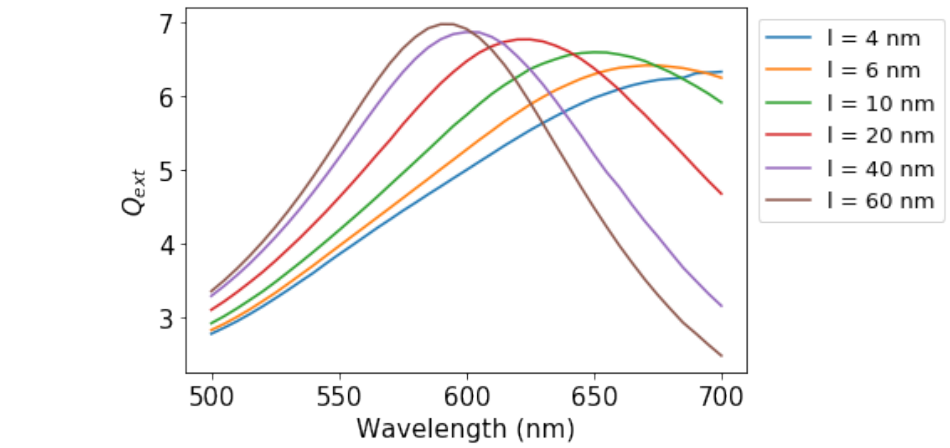

(a)

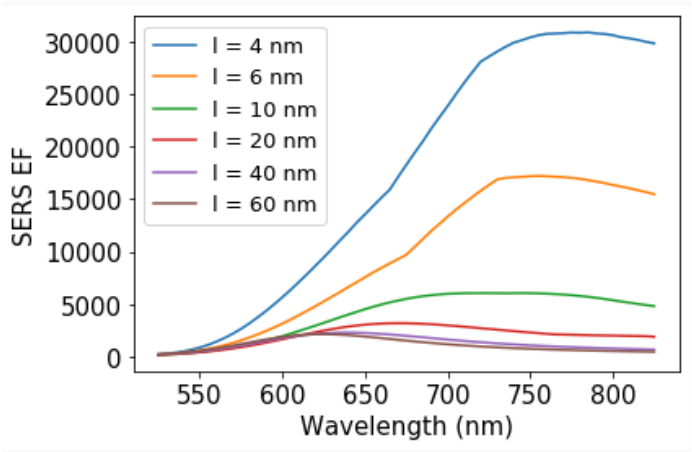

(b)

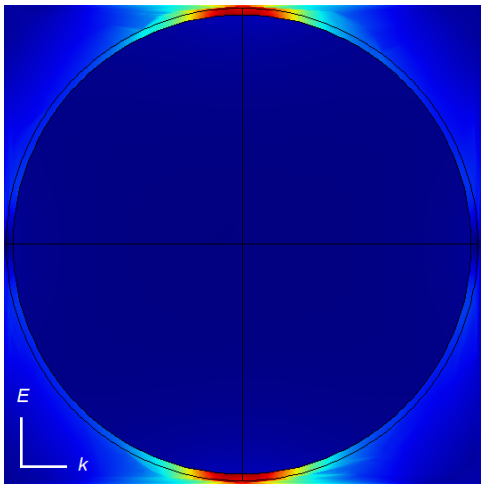

(c)

Figure 5.6: Arrays of 100 nm gold particles with particle spacing l. (a) Extinction efficiencies. (b) SERS enhancement factors. (c) Field norm distribution in the XY-plane, showing a unit cell in the array with $l = 4$ nm. The field is highly localized at the poles, as seen from the dimensions of the hotspot (the bright red spots on the axis along the field polarization). The circle around the particle is the integration sphere.

All near-field calculations in this section were made with FEM. Note from Figure 5.6c that the field is highly localized into hotspots at the poles, as previously seen in Figure 3.8a in Section 3.5.3.

The tendency of sharply increasing field enhancement with decreasing l was demonstrated in the project thesis [1] for 180 nm spheres. It was demonstrated in that work that this gold sphere size gave the largest field enhancement at the 785 nm wavelength used for SERS glucose measurements, when modeling particle interactions in a sphere dimer. Figure 5.7a illustrates the trend. The EF when $l < 1$ nm is well above 10^3. Applying the SERS EF approximation rule $|E/E_0|^4$, Eqn. (3.52), yields SERS EFs approaching the theoretical limit of 10^{14} for the EM contribution. The highest calculated field enhancement factor is 3420, for a separation distance of 0.2 nm. The corresponding SERS enhancement factor is $1.37 \cdot 10^{14}$. It would of course not be realistic to have a sub-nanometer spacing between the spheres, due

to fabrication challenges and because the analyte molecule has to fit inside the hotspot. The realistic maximum EF in such dimer structures is likely around 10^2, which yields a SERS EF of 10^8, agreeing well with the SERS EFs in the range $10^6 - 10^8$ reported in the literature [13], [26], [12]). Note also that the plots here show SERS EF estimation based on *maximal* surface field EF, not surface area-averaged SERS EF, as computed previously for the single particle. This is to investigate the absolute maximum achievable.

It can also be noted from Figure 5.7a that at separation distances of about $l = 15$ nm or more, the surface field EF is on par with single particles. Near-field coupling effects are still present until the separation distance is increased to about 150-200 nm, for sphere sizes considered here, or about three radii [36, p. 82]. Figure 5.7b shows the field norm plot for the 180 nm gold sphere dimer, with $l = 10$ nm. The measurements were taken in the middle of the bright red hotspot and calculated from an incident field $E_0 = 10^{-3}$ V/m.

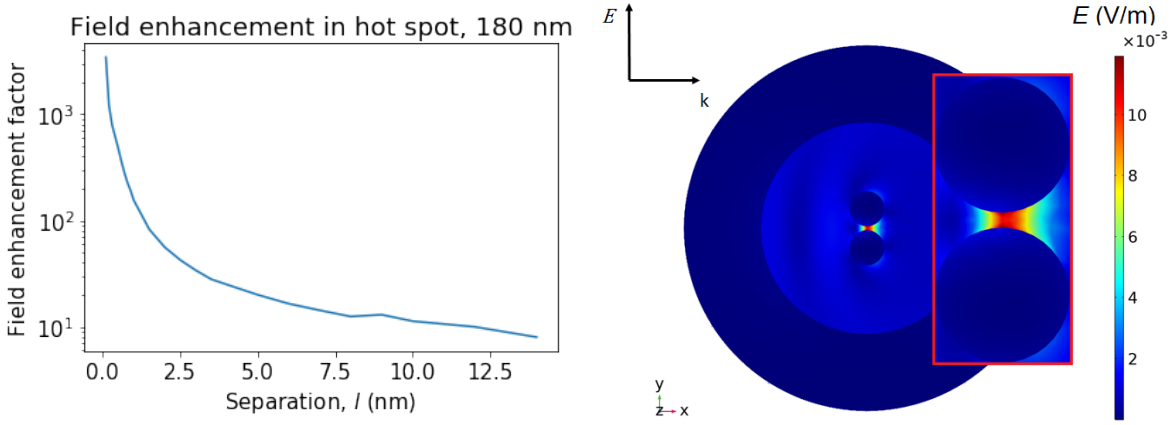

(a) **(b)**

Figure 5.7: (a) Surface field enhancement ($|E/E_0|$) as a function of particle separation distance in a dimer consisting of 180 nm gold spheres. SERS EF can be approximated as $|E/E_0|^4$. Thus, for $l < 1$ nm, the EF approaches the theoretical limit $\sim 10^{15}$ predicted for SERS. (b) Field norm distribution in the XY plane, showing the 180 nm gold spheres in the dimer separated by 10 nm. The field enhancement was calculated from the bright red hotspot between the spheres. The incident field amplitude was $E_0 = 10^{-3}$ V/m [1, p. 46].

Concluding this section, we take a look at a comparison of enhancement values for gold dimers of 50 nm and 180 nm diameters in water. The 50 nm spheres were simulated using FEM and compared with the plot in Figure 6.19 in Ru and Etchegoin [40, p. 356]. Table 5.3 illustrates the difference in attainable EF for the two diameters, both at resonance (for the smaller diameter) and at the target 785 nm wavelength.

The table data demonstrates that while the larger spheres have higher EF at the target 785 nm wavelength, the smaller spheres consistently achieve a higher EF at their resonance wavelength. This is consistent with research showing that smaller particles can have larger surface field intensities than larger ones, due to lower retardation and dampening in smaller particle volumes and higher polarizability of smaller surface areas (see e.g. [32, p. 207]). The 180 nm sphere exhibits a strong quadrupole mode, decreasing its dipole oscillator strength. The table demonstrates for 50 nm sphere dimers the pattern already seen in Figure 5.6, for the 100 nm sphere array, where the resonance was redshifted with decreasing l. The 180 nm dimer data is for 785 nm wavelength only, as a reference. Because of the resonance redshift caused by the dimer structure, the dipole peak has been shifted too far into the IR region and out of the relevant wavelength range. The conclusion drawn from this is that

Table 5.3: Comparison of 50 nm and 180 nm gold sphere dimers in water at different separation distances l. SERS EF at 785 nm wavelength, SERS EF maximum at resonance and resonance wavelengths are presented. For the larger diameter, all data are for the 785 nm wavelength, as reference.

Model	$EF_{\lambda = 785\ nm}$	Max EF	λ_{max}^{EF} (nm)
l = 1 nm:			
50 nm gold dimer	$2.0 \cdot 10^8$	$1.1 \cdot 10^{11}$	660
180 nm gold dimer	$5.1 \cdot 10^{10}$	$5.1 \cdot 10^{10}$	785
l = 2 nm:			
50 nm	$2.0 \cdot 10^6$	$2.0 \cdot 10^9$	630
180 nm	$5.8 \cdot 10^8$	$5.8 \cdot 10^8$	785
l = 3 nm:			
50 nm	$4.0 \cdot 10^5$	$2.0 \cdot 10^8$	610
180 nm	$4.5 \cdot 10^7$	$4.5 \cdot 10^7$	785
l = 5 nm:			
50 nm	$7.0 \cdot 10^4$	$1.0 \cdot 10^7$	590
180 nm	$3.1 \cdot 10^6$	$3.1 \cdot 10^6$	785

for a given structure or arrangement of particles, the particle size is a relevant parameter for tuning the EF maximum to the relevant excitation wavelength. Although the smaller spheres are capable of higher EFs at their LSP resonance, larger particles are needed to achieve maximum EFs at the 785 nm wavelength.

5.2.2 Far-field coupling

Although near-field coupling is believed to be the main contributor to SERS enhancement factors due to the close packing in colloid films used in SERS substrates, there is also a far-field coupling contribution that comes from long-range order. The model would not be complete without a discussion of how it behaves when the particles have larger spacing between them, such that near-field coupling is no longer present. The main periodic structure considered here is the 1D array, because it is the simplest one and captures most of the periodic lattice effects. As the AuFON structure is a 2D hex lattice array, we will extend the 1D array after reviewing its most important features. The polarization is now orthogonal to the array axis, as opposed to the setup used for investigating near-field coupling. This section will explore arrays using predominantly silver particles, as that is easier to compare with published results, but important differences between gold and silver are noted where appropriate.

1D arrays of homogeneous noble metal particles in vacuum

Figure 5.8 demonstrates how the SLRs emerge at different periods D when the number of particles N in the array increases. The results are from the CDA model of one-dimensional arrays of 100 nm silver particles in air, except for the last subfigure which shows gold particles.

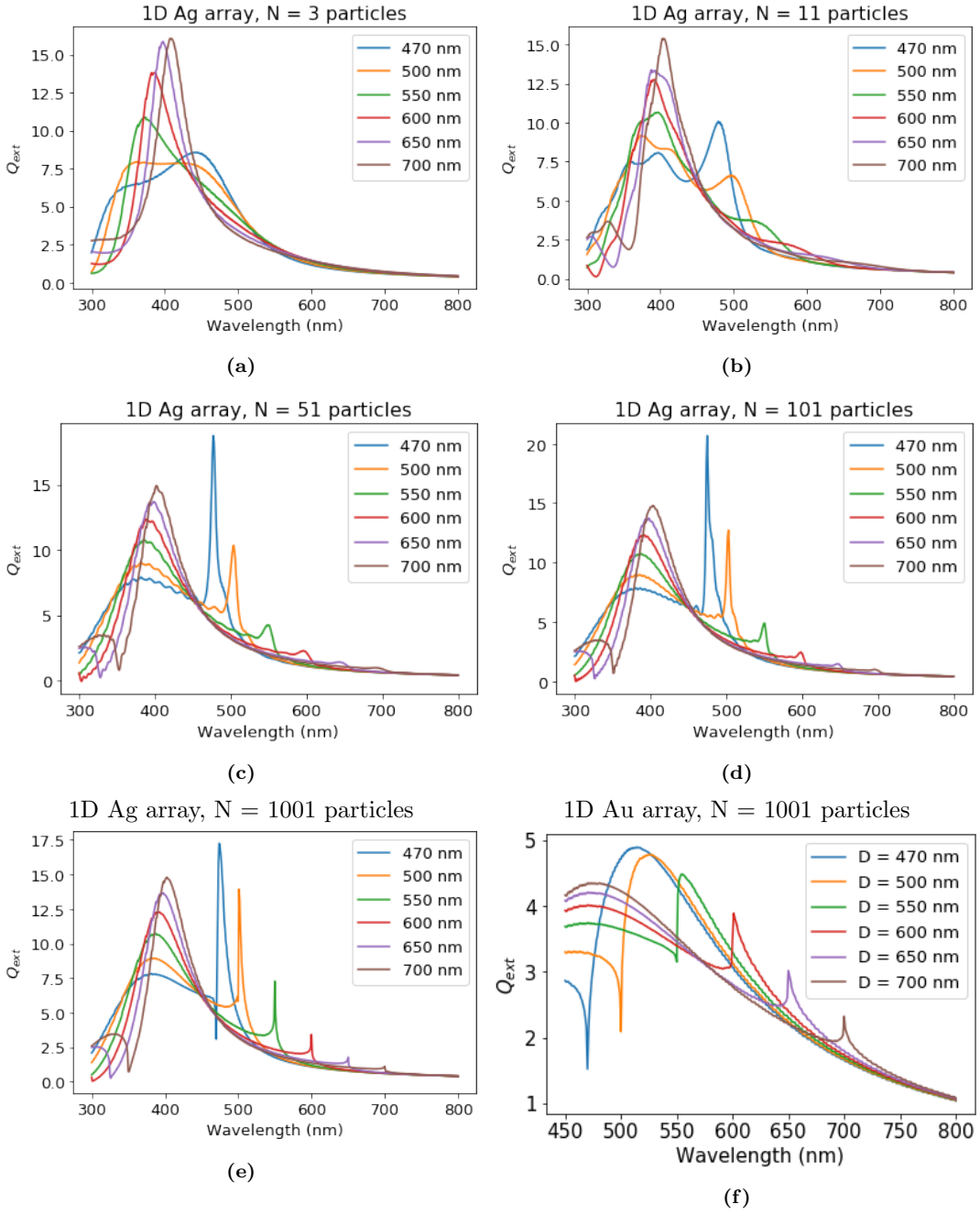

Figure 5.8: Plots showing how lattice surface resonances start to emerge and become narrower with increasing array length. CDA model of 1D arrays for various periods consisting of N silver spheres, 100 nm in diameter, in vacuum. (a) $N = 3$, (b) $N = 11$, (c) $N = 51$, (d) $N = 101$ and $N = 1001$. (f) CDA model of 100 nm gold particles ordered in a 1D array, for comparison with silver.

Figure 5.8a shows that for a lattice constant of 470 nm, an array of only three particles is enough to see a lattice resonance emerge. However, one needs to increase the array size to 11 particles to locate the SLR peak, for the 470 nm plot line, at a wavelength around $D = 470$ nm. Increasing the array size to 51 particles is enough to see lattice resonances for all periods presented here. However, while the lattice peaks for shorter periods are already quite narrow at $N = 51$, with $Q \sim 20$, the lattice resonances for the longest periods presented are much wider. An array size of 101 particles is needed to see a peak emerging in the 700 nm plot line. Increasing the array size further, to $N = 1001$, makes the resonances narrower and the plot lines smoother. This results in a plot quite close to the 1D array results in Zou *et*

al. [57] [58], which were based on 400 particles. Both the LSPR and SLR peak values are similar and located at the same wavelengths. Zou *et al.* do, however, achieve much sharper resonances for lattice constants in the 450 nm - 500 nm range.

The resonance peaks in Figure 5.8 were produced using the CDA code in thesis, Appendix E.3, and the good agreement with literature means it can be used for comparison with the FEM results further below. It was however already mentioned in Section 4.5 that the LSPR in the present CDA model only includes the dipole contribution. Furthermore, it should be noted that this CDA implementation overestimates the LSPR peaks by a factor of as much as 1.5 for the largest lattice constants demonstrated here. For completeness, it should be noted that the literature often uses other dielectric constants than those used in this thesis. Zou *et al.* [57], [58] use silver metal data by Hunter and Lynch [90]. However, as seen in Table 5.1 comparing single particle models, the LSPR peaks shift only a few nanometers between datasets. The linewidth may, however, change significantly. It is believed that this is not of great relevance in this discussion, as the main interest is in the LSPR and SLR shifts due to lattice effects. These are more significant than the small resonance wavelength differences between datasets.

The FEM model is better suited to demonstrate the effect of an infinite array, due to its periodic conditions defined in Section 4.9.4. Compared with CDA, the FEM demonstrates the effects of going beyond the dipole approximation. Figure 5.9 shows the extinction efficiencies of infinite one-dimensional arrays of silver and gold particles, respectively. Each subfigure presents the lattice resonances for various lattice constants. The particles are still in air and have a diameter of 100 nm each.

Zou *et al.* [57] analyze the polarization expression (4.10) in their CDA implementation further, suggesting that the real part of the AS term in the denominator is typically positive for array periodicities below 100 nm. This produces a red-shift in the LSPR when the periodicity is further decreased, as previously seen for near-field coupling. For larger array lattice periodicities, there is a blue-shift when the particle spacing is reduced. This was seen in the CDA models in this section, but similar results are also seen from the FEM model in Figure 5.9.

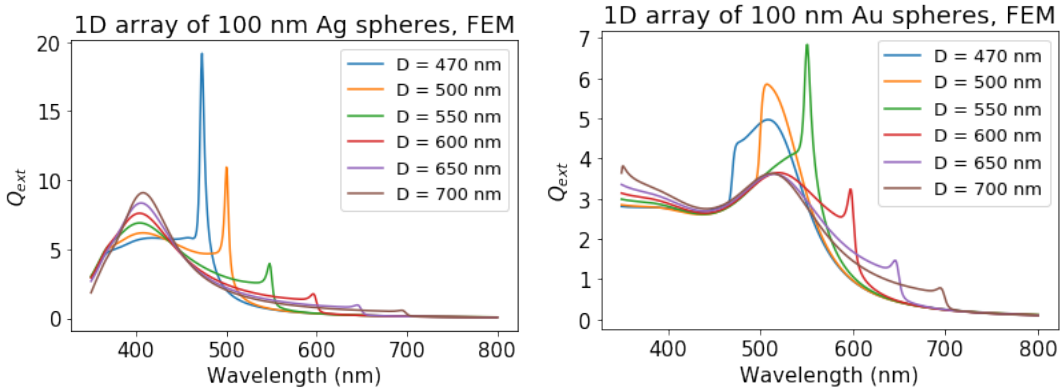

(a) **(b)**

Figure 5.9: Infinite 1D arrays of (a) silver and (b) gold particles in vacuum simulated using FEM. Each plot line corresponds to a model with one of the lattice constants in the legend.

Both gold and silver metals demonstrate similar lattice effects. Initially, the lattice resonances are at a slightly red-shifted wavelength compared to the wavelengths corresponding to the lattice constants: E.g. the Fano resonance in the silver particle array with a 470

nm lattice constant is located at 473 nm. This agrees with the harmonic oscillator model in Section 3.7.2. The interaction between LSPs and the diffracted light red-shifts the SLR from $\lambda = D$. We will henceforth call this wavelength λ_D. There is also a blue-shift of the LSPR from the position seen for single particles in Section 5.1. However, the FEM model does deviate from this as the lattice constant becomes larger – the SLRs become blueshifted relative to λ_D! For the 600 nm and 700 nm lattice constants, the SLR is at 596 nm and 694 nm respectively. Both gold and silver FEM models show this behavior. The deviation might not be large, but it is definitely a trend. The dipole LSPR peaks for $D = 600$ nm and 700 nm are at 401 nm and 367 nm, respectively. That is, blue-shifted from the LSPR wavelength of 375 nm for an isolated 100 nm silver sphere. Thus, the LSPRs in the FEM model behave as predicted by the harmonic oscillator model, even though the SLRs do not.

Figure 5.10 illustrates the mismatch between the FEM and CDA models. The CDA results seem to be more in agreement with the oscillator model for smaller lattice constants, but for higher array periods, the SLR peak locations eventually converge to λ_D. That would correspond to a zero interaction term in Eqn. (3.60) in the oscillator model. This behavior is seen for both gold and silver and is due to the simplifying assumptions made in the CDA model's polarizability in this thesis. The rsa-CDA model by DeJarnette *et al.* [39], in contrast, does not converge to $\lambda_{SLR} = \lambda_D$, indicated by the red dotted lines in Figure 5.10, but rather to an asymptote parallel to these lines. However, they do only demonstrate results for a 2D square lattice of gold particles. In defense of the FEM results, it does seem likely that as interactions between the LSPs at adjacent particles grow weaker, with larger particle separation, that the interaction term in Eqn. (3.60) vanishes. This is seen in Figures 5.8 and 5.9 from the decreasing SLRs in the extinction plots for both metals, and both CDA and FEM, as the lattice constant increases. Then it is sensible that the LSPR goes back to the position predicted by the single particle models, while the SLR simply vanishes. One could also use this to explain the trend for the CDA models implemented in this thesis, seen in Figure 5.10. As far field interactions are weakened, the interaction term in the oscillator model, Eqn. (3.60), disappears, and the SLRs gradually shift to the wavelength λ_D as they decrease in strength. The fact that this does not happen in the FEM model, is likely due to dampening, retardation and inhomogeneous surface polarization in the plasmonic particles. This might shift the resonances differently than predicted by the simple oscillator model. It is important to remember that the particles in the FEM model are not point-dipoles.

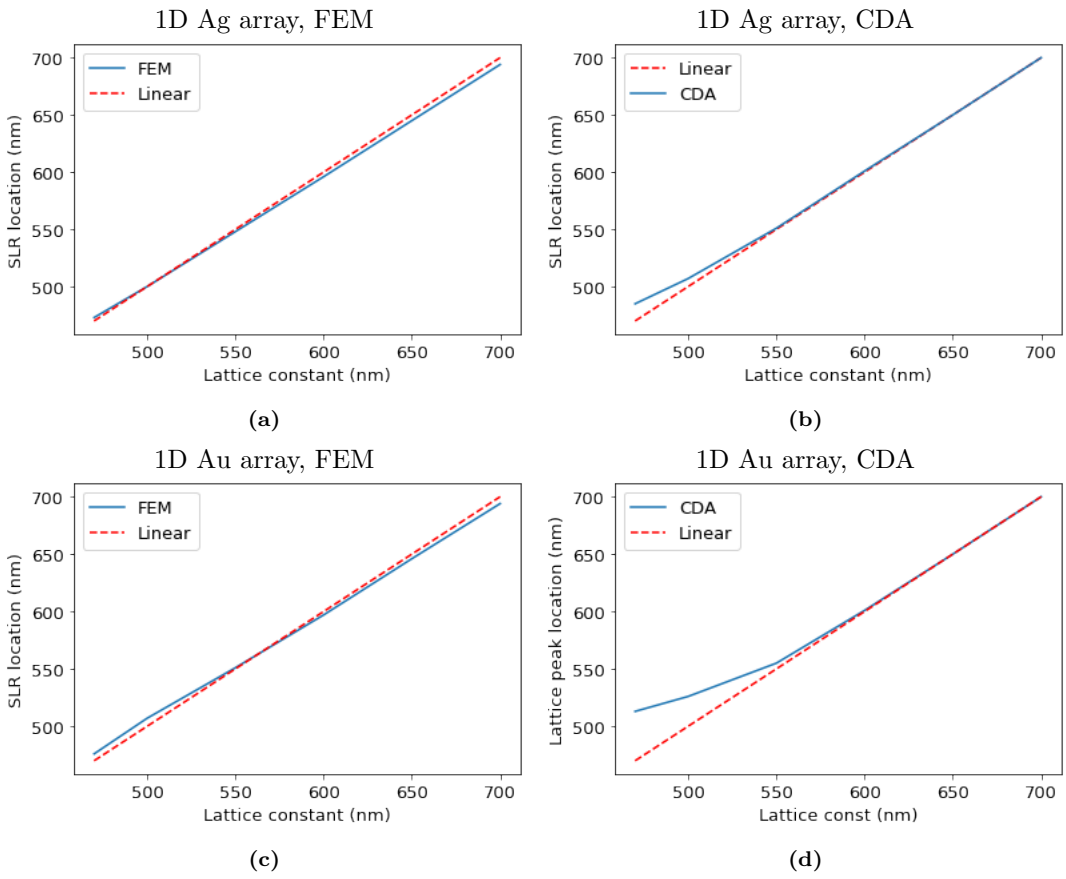

Figure 5.10: Lattice peak positions versus constants for 1D arrays. Red dotted lines indicate the trend when all SLR peaks are located strictly at the wavelength which equals the lattice constant, $\lambda_{SLR} = \lambda_D$. Top row: silver particle arrays simulated using (a) FEM and (b) CDA. Bottom row: gold arrays, using (c) FEM and (d) CDA.

The gold array in Figure 5.9b shows the same properties as the silver array. However, for the smallest lattice constants, the SLR and LSPR are very close – they almost coincide in the plot where the lattice constant is 500 nm, producing a very wide resonance peak. The CDA result for 1D gold arrays in Figure 5.8f shows the same, only the LSPR and SLR peaks for $D = 470$ nm and 500 nm are completely merged into wide resonances. The gold SLRs exhibit the same disagreement with the oscillator model at larger lattice constants, for both CDA and FEM. The SLR position versus λ_D plot for the CDA gold model in Figure 5.10d shows a larger deviation from the $\lambda_{SLR} = \lambda_D$ line for the smallest lattice constants D, before it also converges to that line. At these lattice constants, the LSPRs and SLRs in gold are much closer and there is likely stronger coupling between them than in silver.

Effects of changing the medium's refractive index

As the final AuFON model is intended to have a glucose solution as surrounding medium, this section presents the results of changing the medium's refractive index to that of water. Recall the arguments for approximating the RI of a glucose solution with concentrations up to 1 M using the RI of water in Section 4.7.3. The extinction efficiencies for 1D arrays of 100 nm silver spheres in water are shown in Figure 5.11a. Comparing these plots to those in Figure 5.9a, the SLR peaks are shifted to wavelengths predicted by computing the optical distance, $\lambda_D \times n_{medium}$ [85]. The small redshift from surface plasmon-lattice interactions, as predicted by the oscillator model, also carry over: E.g. for the 470 nm lattice constant, the optical distance relation suggests that the surface lattice resonance in water should be

located at $470 \times 1.33 = 625$ nm. However, due to the plasmon-lattice interactions, the plot in Figure 5.11a places this SLR at 628 nm, with a small redshift, as expected.

Note that in the single particle models the LSPRs were simply shifted, following a change in medium RI, but any substantial broadening was not seen. Here the LSPRs are either significantly broadened, or the medium's contribution to scattering, on the lower wavelengths, is dominating the LSPRs and thus what we see at ca. 400 nm, is actually not the silver sphere LSPR anymore.

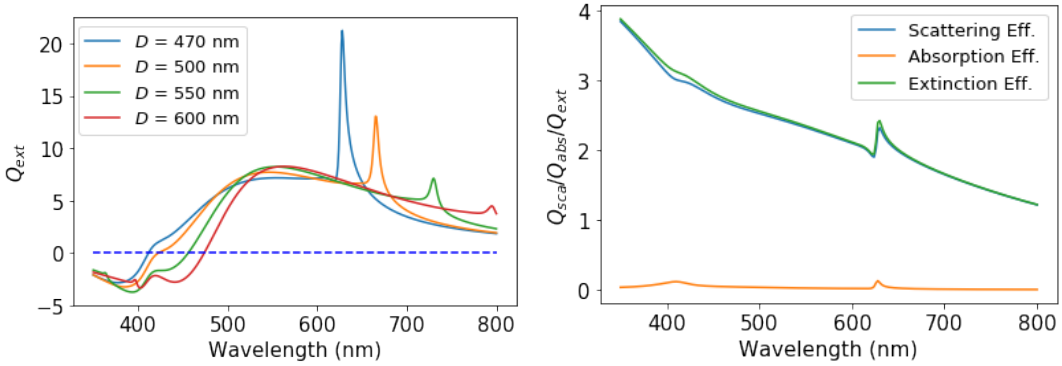

(a) (b)

Figure 5.11: Extinction efficiencies of 1D arrays of 100 nm silver spheres in water. (a) Plotted for several lattice constants, simulated with an integrating sphere on the surface of the particle. The dotted blue line helps identify where the plots turn negative. (b) Scattering, absorption and extinction efficiencies plotted only for $D = 470$ nm. Simulated by integrating the relative Poynting vector over the whole simulation space, including the medium.

For some wavelengths, the extinction efficiency is negative. There are computational studies for particle arrays that have shown that at wavelengths where the particle's refractive index is smaller than that of the medium, extinction efficiencies can be negative due to interference effects [91]. This is attributed to absorbing media, but the refractive index of water in this thesis is strictly real, only causing phase retardation. This interference might be caused by the medium close to the particle's surface, at wavelengths where the particle's RI is smaller than that of the medium. As a result, integrating along the particle's surface produces a negative scattering and, therefore, extinction cross section. As the medium is not absorbing, this has no effect on the absorption cross section. Figure 5.11b demonstrates a possible workaround the problem. When the medium is also included within the integral, the scattering cross section is positive. The insight from this is that, with a high-index medium, where one places the integrating sphere is no longer arbitrary. This effect was, however, only observed in far-field coupled arrays and not in single particles, when changing medium to water.

The plot in Figure 5.11b was normalized with the geometric cross section of the whole simulation space, not just the particle, which has resulted in decreased efficiency values along the whole spectrum. The resonances are still on the same wavelengths, although the broad dipole resonance peak is no longer clearly seen. Going forward, we will still integrate close to the particle's surface, but be aware of the potential negative efficiency values. We can justify this by the fact that a lab setup for measuring SERS enhancements will uses a NIR wavelength, such as 785 nm [8], [28], at which the models in Figure 5.11a demonstrate positive extinction values.

The gold model in water behaves similarly and is omitted here for brevity. The difference from gold arrays in vacuum is that as the medium redshifts the SLR, there is no longer an

overlap between the gold sphere LSPR and SLR, producing narrow SLRs, just like the silver model.

2D square lattice particle arrays

Most of the relevant far-field coupling and SLR properties were already discussed in the 1D array case. Ordering the particles in 2D arrays introduces new SLRs. It was shown in Chapter 4.5.2, that such arrays are periodic in more than one direction. The periods along the vertical and horizontal axes in the array plane are equal. In a generalized rectilinear case, they could be different, giving rise to two SLRs rather than one main SLR peak. There are also periods $D\sqrt{(m^2+n^2)}$ for every combination of m, n, as was seen from Eqn. (4.17). Some of these give rise to destructive interference [47, p. 6] or produce weak resonances, such that only the half-diagonal, for $(m, n) = (1, 1)$ produces a strong SLR resonance besides the main SLR due to periodicity along the axes.

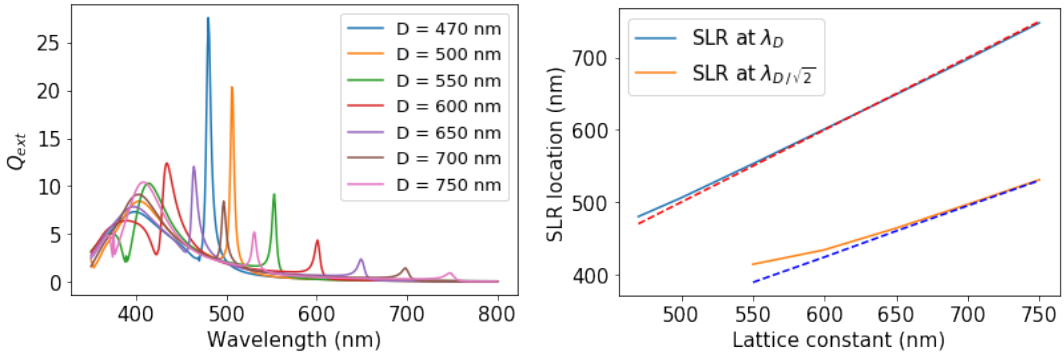

(a) **(b)**

Figure 5.12: (a) Extinction efficiencies of 2D square lattice arrays of 100 nm silver spheres in vacuum. Plotted for several lattice constants. (b) SLR peak wavelengths, for periods D along the axes and $D\sqrt{2}$, the half-diagonal. These are plotted against dotted lines indicating the positions of these SLR if there were no redshifts or blueshifts (i.e. plotting the relations $\lambda_D = \lambda_{SLR}$ and $\lambda_{D\sqrt{2}} = \lambda_{SLR,\,half-diag}$).

In addition to the SLRs at approximately λ_D, which were already discussed in the 1D case, there are now smaller SLRs, corresponding to the half-diagonal period, $\lambda_{D/\sqrt{2}}$. Note that the latter is due to the diagonal distance $D\sqrt{2}$, not $D/\sqrt{2}$! See Figure 5.12a. There is now far-field coupling in two dimensions, which increases the extinction efficiencies by about 25 % and makes them narrower, compared to the 1D extinction spectrum in Figure 5.9a. The second subplot demonstrates the redshift in the SLRs compared to λ_D, for the main period, and $\lambda_{D/\sqrt{2}}$ for the half-diagonal. Compared to the 1D array, the redshift at smaller values of D is higher, but then the SLRs converge to a constant blueshift of about 2 nm at larger D. We can also see that the half-diagonal SLRs are initially strongly redshifted, but then they converge to the linear asymptote. There is stronger coupling with LSPRs at smaller periods, which might explain this.

2D hexagonal lattice particle arrays

Concluding the investigation on how the FEM model performs in the case of far-field coupled particles in arrays, Figure 5.13 presents the results for the 2D hexagonal lattice particle array, with 100 nm silver spheres.

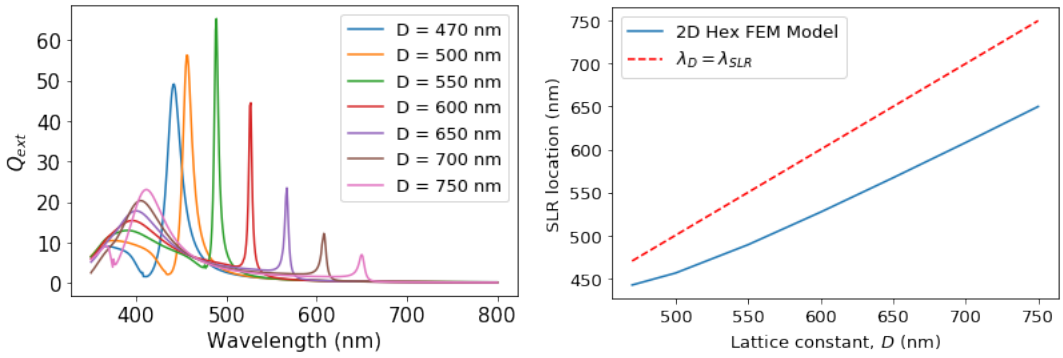

(a) **(b)**

Figure 5.13: (a) Extinction efficiencies of 2D hexagonal lattice arrays of 100 nm silver spheres in vacuum. Plotted for several lattice constants (see plot legend). (b) SLR peak wavelengths in the hex model, for array periods D, plotted against the trend line where the SLR peaks are exactly at each corresponding λ_D.

The first subfigure plots the extinction efficiencies, which resemble the pattern seen in the 1D array case, Figure 5.9a. There is again only one strong SLR peak, due to period D in all directions along the hexagonal lattice. The peaks are not as narrow as in the 1D case, due to coupling between LSPs in two dimensions, rather than just one. The same occurred in the 2D square lattice case seen previously. The model seems to overestimate the maximum extinction efficiencies by a factor of about two, compared to the hex lattice CDA results in Zou *et al.* [65]. The 2D hex lattice CDA implementation in this thesis is in good agreement with Zou *et al*, but is omitted here to focus on the FEM.

The SLR peak wavelengths in FEM seem to follow the same trend as in the CDA models. The $D = 500$ nm peak is located approximately at 450 nm, and for the larger lattice constants, the $D = 700$ nm peak is centered on a wavelength of about 600 nm. The trend is that with larger values of D, the SLR peaks are more and more blue-shifted, compared to λ_D. This is clearly visible from the plot line in Figure 5.13b, as it diverges with higher lattice constant, D, from the linear trend line where $\lambda_D = \lambda_{SLR}$. This blueshift is clearly a deviation from the oscillator model in Chapter 3.7.2. However, the 2D hexagonal lattice is a more complex system than the simple 1D array and demands a more complex model. It is encouraging that the 2D hex FEM model and CDA models place the resonances at approximately the same wavelegths. The final AuFON structure is, after all, a tightly-packed hexagonal lattice particle array.

The fact that the FEM model's near and far field properties follow close to theory and are comparable to other models indicates that it is a viable modeling approach.

SERS estimation in an array with far-field coupling

SERS enhancement from near-field coupling, due to field localization in hotspots, was demonstrated in Section 5.2.1. In arrays with periods larger than the distance where near-field coupling is effective, there is an additional surface field enhancement maximum at virtually the same wavelength as the SLR peak in the extinction spectrum, which can be one or several orders of magnitude higher than the field enhancement peak corresponding to the LSPR [92]. Figure 5.14 demonstrates the average SERS enhancement factors in 1D, 2D square lattice and 2D hexagonal lattice infinite arrays of both gold and silver particles. Figure 5.14a plots the LSPRs and SLRs in silver arrays with period $D = 500$ nm, while Figure 5.14b plots these resonance peaks for gold particles with period $D = 600$ nm. These

choices were based on observations made in the previous sections, showing that the SLR peaks for array periods of 500 nm, in silver, gave the tallest extinction resonance peaks. Given that the 100 nm gold spheres have LSP resonances at slightly above 500 nm, the LSPR and SLR peaks coincided, forming wide resonances. Thus, for gold a period of 600 nm was selected, as it produced tall and narrow peaks. The figures use logarithmic y axes, which make the resonances look much wider than in a linear scale.

Table 5.4 contains the maximal SERS EF values for each one of the array types, ordered by metal. The enhancement factor at SLR, for the 1D silver array is 8767, versus a factor of 463 at LSPR previously seen in Figure 5.5b for the single particle model. It is worth noting that the SLR peaks in the enhancement factor plots are located at virtually the same wavelength as the SLR peaks in the extinction efficiency plots. For the 1D silver array, the SERS EF SLR peak is 502 nm, while the extinction SLR maximum in the same model, seen in Figure 5.9a, was at 500 nm. Thus there is a very small redshift, but for higher lattice constants it becomes immeasurable. This is in stark contrast to the significant redshifts in LSPR, between the extinction and SERS EF peaks, seen in e.g. Figure 5.5. However, the virtually no redshift in the case of SLR is reasonable because the retardation and radiative emissions that redshift the surface field maximum compared to the extinction maximum in plasmon resonances are not an issue in the case of lattice resonances. The SLR is a diffraction effect and the resonance wavelength is controlled by the array period.

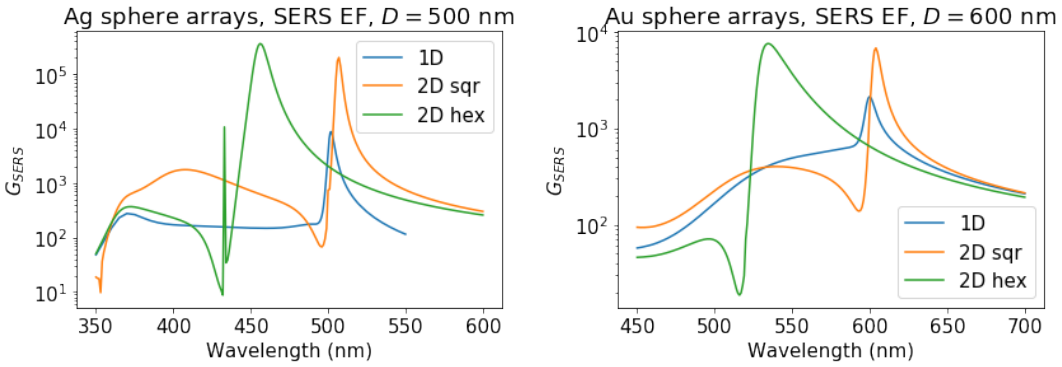

(a) **(b)**

Figure 5.14: SERS enhancement factors in infinite 1D, 2D square lattice and 2D hexagonal lattice arrays of silver and gold 100 nm spheres in vacuum. (a) Silver arrays, period $D = 500$ nm. (b) Gold arrays, period $D = 600$ nm.

The tall and narrow SERS enhancement peaks, located at the same wavelength as the extinction SLR, suggest that one can easily tune sensors to desired excitation wavelengths to achieve high sensitivities. According to Zuo and Schatz [92], single molecule SERS enhancement factors on the order of $10^{12} - 10^{14}$ have been demonstrated in calculations. This is close to the theoretical maximum enhancement factor. The tabulated values below show that the gold arrays perform several orders of magnitude worse than what is currently achieved for gold structures in experiments, which produce EFs of $10^6 - 10^8$ [12], [13]. As mentioned in Chapter 3.7.2, at this moment, the practical applications of SLRs are mostly limited to lasing, as SERS substrates are mostly fabricated using techniques such as colloidal lithography, where the near-field coupling is dominating and suppresses far-field scattering.

Table 5.4: SERS enhancement factor (EF) values of infinite 1D, 2D square lattice and 2D hex lattice arrays of silver and gold spheres in vacuum. The tabulated SERS EFs are for the EF peak corresponding to the SLR peak in the extinction spectrum plots for each respective array class. The period is 500 nm and 600 nm for silver and gold, respectively.

Array class	Silver, Max SERS EF, $D = 500$ nm	Gold, Max SERS EF, $D = 600$ nm
1D	$8.8 \cdot 10^3$	$2.1 \cdot 10^3$
2D, sqr lattice	$2.0 \cdot 10^5$	$6.8 \cdot 10^3$
2D, hex lattice	$3.6 \cdot 10^5$	$7.5 \cdot 10^3$

5.2.3 Random deviations from exact periodicity

Applying random periodicity reveals behavior similar to that seen in experiments and models of disordered gold disc arrays [24], [93]. The deviation from crystalline order and exact periodicity cancels the constructive interference that produces the SLRs at λ_D. Hence, with larger deviation from the exact intended periodicity D, the one sharp SLR at D becomes smaller. Lesser SLR peaks might emerge due to constructive interference at other, random wavelengths, as seen in Figure 5.15, with increasing ϵ. The SLRs completely vanish and the particle array acts as a single particle, with a similar extinction spectrum, albeit more distorted.

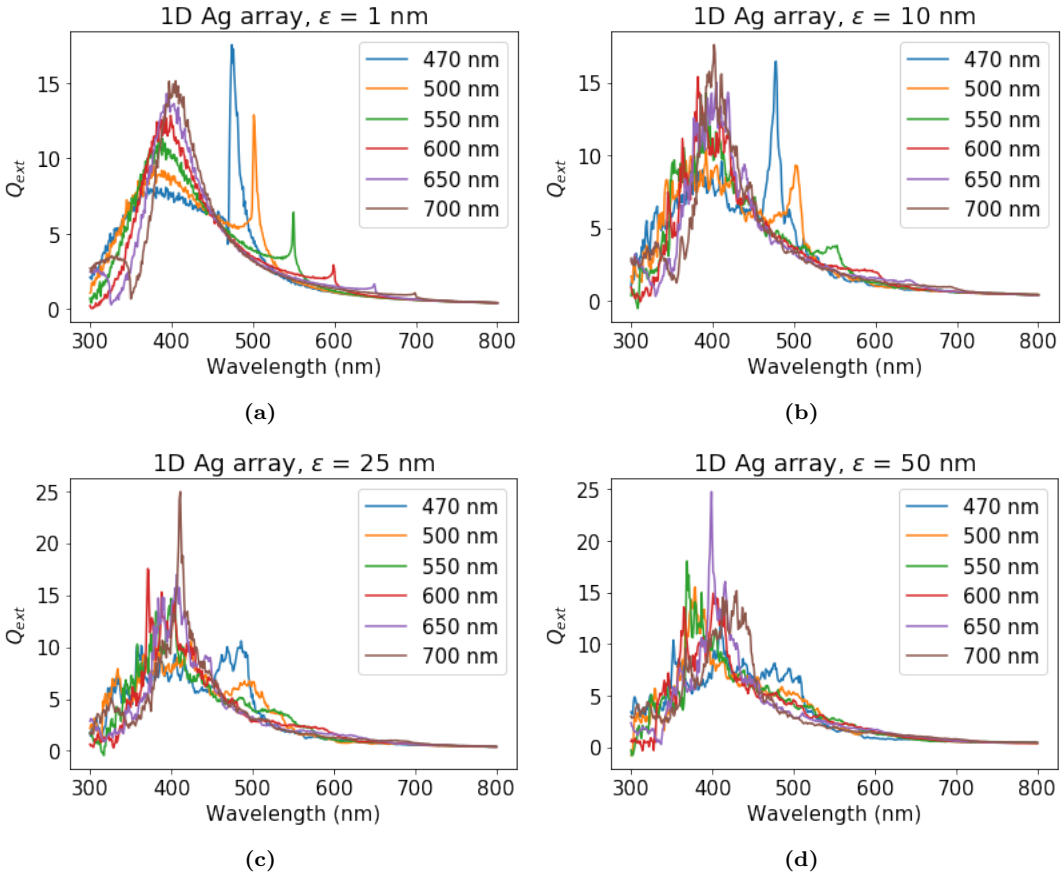

Figure 5.15: 1D array of silver 100 nm spheres with the periods specified in the legend. Each subplot has the exact periodicity P modified with a random part ϵ, such that the resulting $\tilde{P} = P \pm \tilde{\epsilon}$, $\tilde{\epsilon} \sim \mathcal{U}(0, \epsilon)$. The maximum deviation in a given subplot is indicated in its title.

The figure demonstrates how the SLRs corresponding to each D first become smaller and less defined, before finally disappearing completely. This is due to the cancelling of the

constructive interference that caused the SLRs in the first place. The lineshapes produced with $\epsilon = 50$ nm are not exactly what was seen in Section 5.1, but the overall spectrum is similar, if not as smooth. The LSPR resonances are centered on about 400 nm, with a FWHM of 80-100 nm, which is similar to the single particle model. It can also be noted that the LSPRs around 400 nm become stronger when the SLRs disappear, due to more energy available to the Lorentzian oscillators representing the LSPRs. The maximum LSPR peak values are 2-3 times larger than that observed for single particles. However, that is due to a general overestimation of LSPRs in the current implementation of the CDA. The polarizability function used in this thesis was chosen for its simple, but explicitly Lorentzian, lineshape. One can see e.g. DeJarnette [63] for a comparison of different specifications of polarizability functions that might match single particle results more closely, i.e. match the peak LSPR values.

5.3 Nanoshells

Covering all the optical properties of nanoshells would be too extensive for the purposes of this thesis. It is, however, instrumental to show the basic properties of such particles.

Figure 5.16 plots the extinction efficiencies of a single nanoshell in air, consisting of a dielectric polystyrene 50 nm diameter core, coated with a concentric layer of Lorentz-Drude gold of various thicknesses t. In the first subplot, by varying t from 1 nm to 5 nm while keeping the core diameter constant, the extinction peak blueshifts by up to several hundred nanometers for an increment of 1 nm. Note that this fits well with the quasistatic theory for nanoshells in Chapter 3.6.1, specifically the plot in Figure 3.10 which showed a redshift in resonance wavelength as the core takes up an increasingly larger fraction of the total particle radius. The particle size considered in this section, Figure 5.16b does not satisfy $d < 50$ nm, but does not deviate from the trend seen in the quasistatic approximation.

Furthermore, whereas solid gold nanospheres in air, e.g. with diameters up to 100 nm, have dipole resonances at wavelengths up to 516 nm (Recall from Table 5.1, Figure 3.4), we can see there that nanoshells allow tuning resonances across a much wider wavelength range without a significant increase in particle size. Larger solid spheres can also have resonances in the infrared region, but at sizes large enough to support these, they are multipoles, with the dipole resonance significantly weakened and widened. See Appendix C.

Modern sputtering methods allow depositing sub-nanometer thicknesses and can therefore tune the resonance to an even higher wavelength than those shown in Figure 5.16b, keeping the core diameter the same. However, varying the core size, as well as the film thickness, allows easier tunability, even when using simpler vapor deposition methods that do not permit precise sub-nanometer film thicknesses. Oldenburg *et al.* have performed extensive modeling studies on the resonance tuning properties of nanoshells [44], [20].

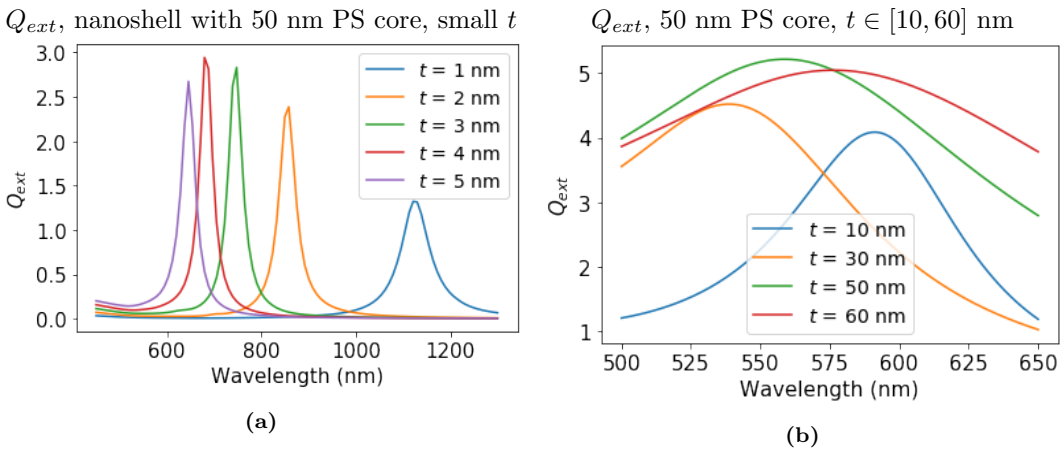

Figure 5.16: Single-nanoshell models, consisting of a 50 nm polystyrene core and a gold film of thickness $t \in [10, 60]$ nm. (a) Extinction efficiencies. Note that for $t = 60$ nm, the extinction spectrum matches that of a solid gold nanosphere of same total diameter, 170 nm. (b) Field enhancement factors of the two extremes in the selected thickness interval.

The second subplot shows more modest shifts for larger t increments, before the extinction efficiency peak finally moves for $t = 60$ nm to nearly the same wavelength as where one would find the dipole peak of a 170 nm solid gold sphere, 576 nm and 574 nm respectively. 170 nm is the total diameter of the nanoshell with a 50 nm polystyrene core and a uniform gold film thickness of 60 nm. This indicates that for large enough film thicknesses, when it is larger than the decay length of the evancescent fields discussed in Chapter 3.5.1, the surface plasmons on both sides of the metal-dielectric interfaces can no longer couple with one another. The nanoshell then behaves as a solid gold nanosphere.

Figure 5.17a shows how the peak field enhancement on the nanoshell surface changes when going from film thickness $t = 10$ nm to 60 nm. Note that the peak surface field enhancement for $t = 60$ nm is the same as for a 170 nm solid gold sphere, a factor of 4.9. The cut line in the plot is defined as in Figure B.3. For smaller film thicknesses, the surface field is stronger, most likely due to the excitation of surface plasmons on both sides of the metal film and the superposition of their scattered fields. Figures 5.17b and 5.17c illustrate the field distribution inside the $t = 10$ nm and 60 nm nanoshells. It is clearly seen that the thinner film allows the incident field excite surface plasmons on both sides, while the thicker film shows no such behavior.

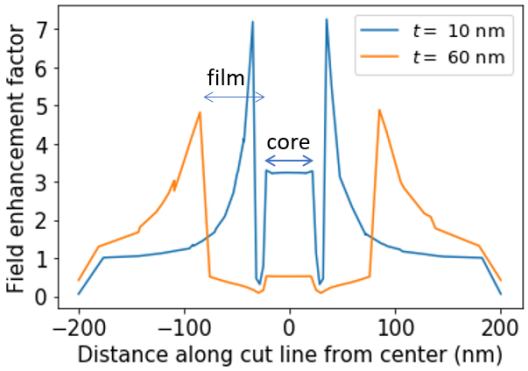

(a)

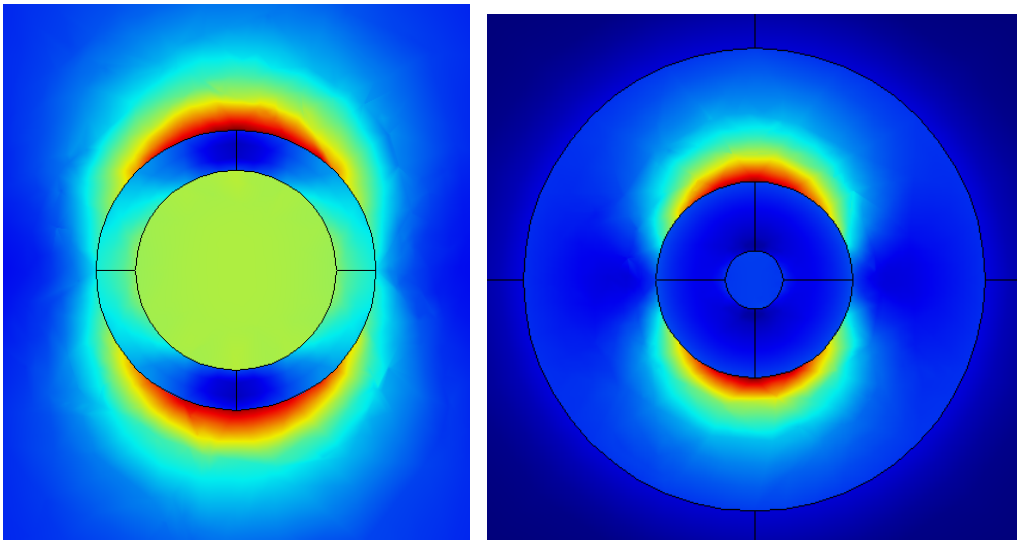

(b) **(c)**

Figure 5.17: Single-nanoshell models, consisting of a 50 nm polystyrene core and gold film thicknesses t 10 and 60 nm, in air (a) Peak surface field enhancements: the $t = 10$ nm model reaches an EF of about 7, at 611 nm excitation wavelength. The $t = 60$ model – an EF of 4.9, at 650 nm. The field enhancement norm inside the $t = 10$ nanoshell is also clearly larger, at about 3.5, versus 0.5. The cut line is defined in Figure B.3. Bottom row: Field norm distributions in the XY plane at resonance. (b) $t = 10$ nm, (c) $t = 60$ nm. The nanoshells are not to scale, as the $t = 60$ model has a larger total diameter.

It is now interesting to investigate how the FEM model performs compared to other models and to the model presented by Averitt *et al.* [21]. Figure 5.18a plots several lines, modeling the extinction efficiency of a nanoshell consisting of a Au_2S core, 4 nm in diameter, wrapped in a 2 nm thick Au film. The parameters for this model were taken from Averitt *et al.*. The dielectric constant of the Au_2S core is estimated, using bandgap calculations [94], to 2.33. The surrounding medium is described with $\epsilon_m = 1.78$, which corresponds to a real refractive index of 1.33 – water. The gold model used in the calculations in this thesis is still Lorentz-Drude, while Averitt *et al.* use Johnson & Christy [89].

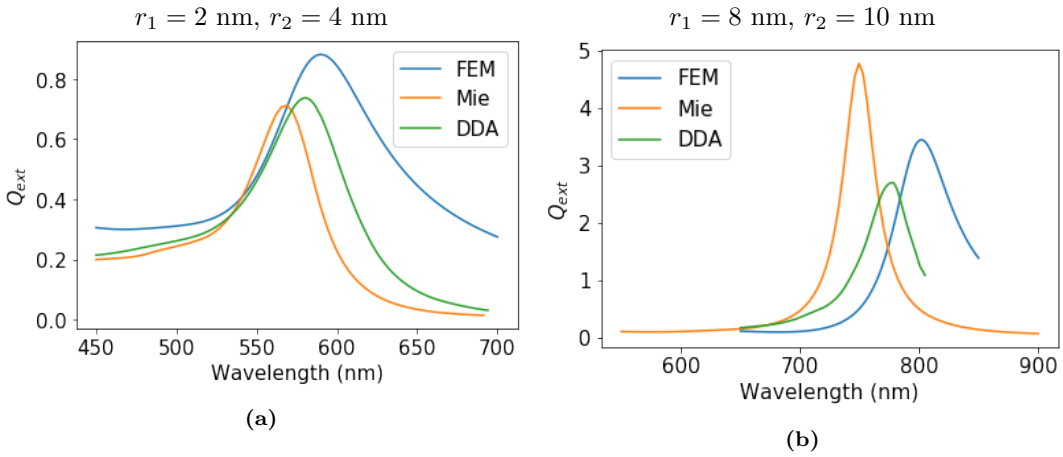

Figure 5.18: Extinction efficiencies of Au_2S/Au nanoshells in water with shell thickness 2 nm, calculated using the FEM, NanoComposix Mie model and DDA. (a) Core radius $r_1 = 2$ nm, total radius $r_2 = 4$ nm. (b) Core radius $r_1 = 8$ nm, total radius $r_2 = 10$ nm. The QS model is only included in the first figure.

The resonance wavelengths and peak extinction efficiencies are summarized in Table 5.5. The values from Averitt *et al.* are estimated from their plot and are only approximate values. They plot both a Mie solution based on Aden and Kerker [42] and Sarkar [43] and values from their quasistatic approximation, based on Eqn. (3.57), [21].

The FEM model deviates the most from the authors' values, while the Mie model by Nanocomposix (from hereon, simply Mie) matches their values well. The FEM resonance wavelength, however, does not deviate a lot from Averitt *et al.* or the Mie model. The DDA model also estimates a maximum extinction efficiency close to Mie and Averitt *et al.*. Due to fact that Averitt *et al.* data are estimated from a plot, the values are approximated. Under these circumstances, the match between the models is believed to be close. The deviation between the FEM and Mie models is large, but at least some of it can be attributed to the different gold models used.

Table 5.5: Peak extinction efficiencies and extinction resonance wavelengths for the nanoshells with $r_2 = 4$ nm and $r_2 = 10$ nm. The values are compared between the FEM, Mie (Nanocomposix) and DDA models. Estimates of max extinction and resonance wavelength values from plots by Averitt *et al.* [21] are also included for comparison.

	$r_2 = 4$ nm		$r_2 = 10$ nm	
Model	$\lambda_{max}^{Q_{ext}}$ (nm)	Max Q_{ext}	$\lambda_{max}^{Q_{ext}}$ (nm)	Max Q_{ext}
FEM	590	0.88	802	3.45
Mie	569	0.71	750	4.78
DDA	580	0.74	777	2.70
Averitt *et al.*	567	0.75	750	4.77

We showed in this section that for single nanoshells with increasing film thickness, the SPP coupling across the two interfaces weakens. That could be used to approximate that for thicknesses relevant for AuFONs, 20 nm – 200 nm, the nanoshell effects become increasingly negligible. However, it should be noted that this assumption might not be true for periodic arrays of AuFONs in the next section. It has been observed that the periodic lattice improves light transmission through the film, yielding extraordinary optical transmittion [95]. The periodic array acts as a perforated metal film.

5.3.1 AuFON model

Finally, this section presents some simulation results for AuFONs. First, we will approximate AuFON arrays with a hexagonal lattice array of nanoshells of the sizes previously used in the project thesis [1], and from previous work by the research group at IES NTNU [8], [28]. The polystyrene core diameters investigated in these works were 500 nm, 750 nm and 1000 nm. Due to diameter variability in the polystyrene particles used to fabricate the AuFONs, one cannot easily estimate the nanometric particle spacing in the array from a SEM image, such as that previously seen in Figure 2.1. We must therefore make some assumptions of particle spacing and investigate the SERS enhancement factor with these. The surrounding medium is water, or, as it was discussed in Chapter 4.7.3, one can think of it as a non-saturated aqueous glucose solution. The excitation wavelength is kept at 785 nm, as in experimental Raman measurements in the referenced works.

Figure 5.19 plots the area-averaged SERS enhancement factor from close-packed nanoshells in a hexagonal lattice. The first subfigure samples the enhancement factors of spheres with 500 nm, 750 nm and 1000 nm polystyrene cores over different gold film thicknesses. The particles are spaced 10 nm apart in these arrays. The second subfigure focuses on the 500 nm core particles. comparing the enhancement factors over film thicknesses when the spacing varies. That is, the array is gradually becoming more close-packed.

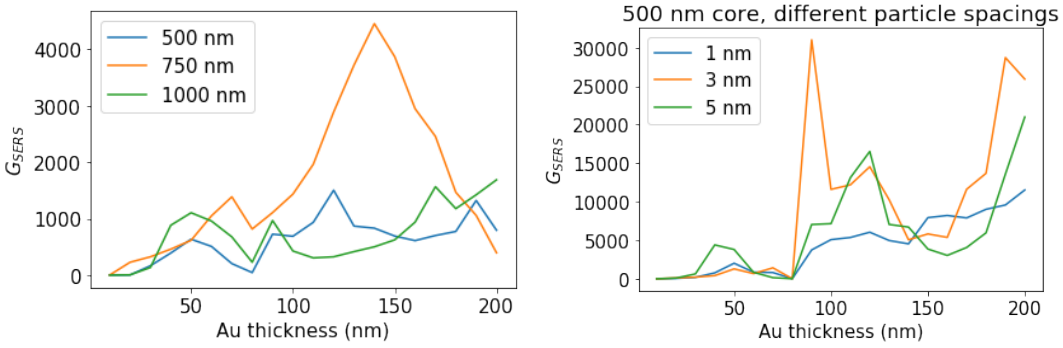

(a) (b)

Figure 5.19: SERS EFs of close-packed gold nanoshells with polystyrene cores in water. The plots shows the dependence of SERS EFs on gold film thickness. (a) Core diameters of 500 nm, 750 nm and 1000 nm. Particle spacing 10 nm. (b) Core diameter 500 nm. Spacings 1, 3, 5 nm.

The comparison of core diameters in Figure 5.19a is meant to mirror the plot of experimental values seen in Figure 4.1, the reference plot. Looking at each plot line separately, there are some similarities. For instance, the 1000 nm core AuFON exhibits maximum SERS EF at the highest film thickness, 200 nm. The two other core diameters shows maxima somewhere in the range 100-150 nm. At first glance, this deviates from the experimental reference plot, but then that plot does not have many data points in that region. Neither is it known what spacing the particles were at in the experimental measurements. The next subfigure shows that the spacing may shift resonances, as was investigated in Section 5.2.1. The actual SERS EF values are of the same orders of magnitude as in the reference plot, $10^2 - 10^3$, although the 750 nm nanoshells seem to exhibit the highest EF.

Figure 5.19b shows the spacing-dependence of SERS EF, over the same set of film thicknesses. The core diameter is held constant at 500 nm. Although this core size might not be the best-performing in the adjacent subfigure, it was used extensively in the referenced work and the reference plot, Figure 4.1. Other works have also suggested this size as optimal,

from a fabricational point of view (e.g. [27]). We see that the smaller spacing, going from 10 nm in Figure 5.19b, yields stronger near-field coupling and therefore higher SERS EF – though the 1 nm results fall out of this trend. We do not achieve the high EFs seen in Figure 5.7a and Table 5.3. Note that the values seen there were not surface-area averaged, but estimated from the maximum observed field enhancement in the hotspot between two spheres. We can compare the values to the reference plot, where all results are of orders $10^2 - 10^3$, or the experimental measurements in a previous master thesis [28] at the research group, also using the 500 nm core particles. These were on the order of 10^4, which fits well with film thicknesses of around 100 nm in the present 500 nm model. Note also that the SERS EF in these close-packed arrays was estimated using the Wigner-Seitz cell boundaries as the "integrating sphere", as the integrating sphere in single-particle or far-field coupled arrays was placed two nanometers from the particle surface. Here, the spacing is not large enough to allow that. The cell boundary approach is computationally simpler, as it does not introduce domains with a high density of degrees of freedom, such as the domain formed between the particle and the integrating sphere. Bearing in mind that the surface field strength decreases exponentially with distance from the particle surface, the cell boundary method favors low spacings. This might also explain the very low SERS EF values in Figure 5.19a, where the spacing is 10 nm.

These model results are, however, only a demonstration of the final AuFON model, as one would have to optimize the parameters in the model. Figure 5.20a demonstrates another potential error in using the calculated values to evaluate an AuFON structure. It plots surface area-averaged SERS EF as a function of wavelength. The model is a nanoshell with a 500 nm core and a 100 nm concentric gold film. Note that the 785 nm wavelength is not the location of any SERS maximum. Recall the effects of changing the film thickness in nanoshells, Section 5.3, and the particle spacing, Section 5.2.1. These must be optimized simultaneously to engineer a structure where the required wavelength is at a SERS EF maximum.

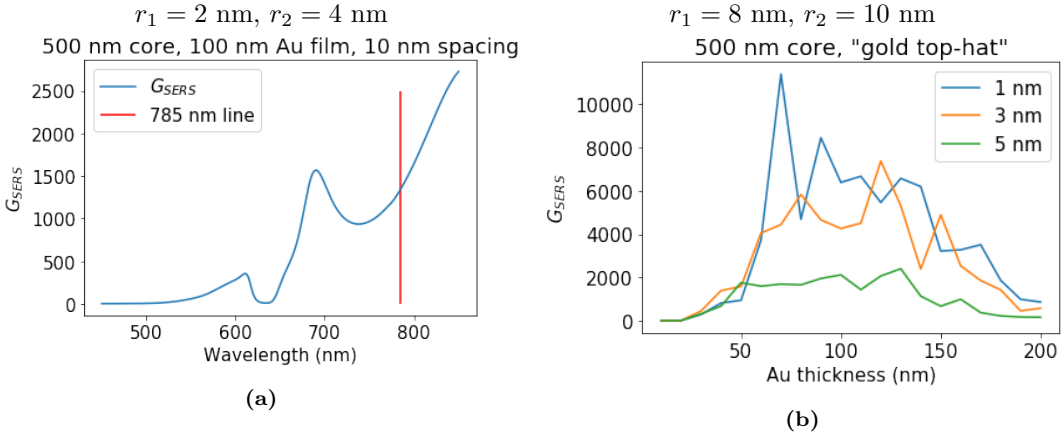

Figure 5.20: (a) SERS EF of a 500 nm polystyrene core 100 nm Au film nanoshell hex lattice array, with 10 nm spacing. (b) Top hat structure with a 500 nm polystyrene core and a variable film ('hat') thickness. Hex lattice with spacings 1, 3, 5 nm.

Finally, Figure 5.20b is a demonstration of replacing the 500 nm polystyrene core nanoshell with a similar-sized top hat structure, as discussed in Chapter 4.9.2, in a close-packed hex lattice array. This emulates the shape of an actual AuFON particle. The figure again shows the SERS EF as a function of film thickness, at the thickest point of the "hat", and for several spacings. The plots again demonstrate that maximum EF is achieved for film

thicknesses in the range 100-150 nm. For the smallest spacing, however, the EF maximum shifts to a thickness of 70 nm. Though not directly comparable, due to a different core size, at least one result was reviewed where a thickness of 60 nm showed a SERS EF of 10^6 [12]. However, comparing the top hat model with the nanoshell plots above, the top hat produces smaller surface area-averaged SERS EFs, compared to the 500 nm nanoshell. 10^4 vs $3 \cdot 10^4$ at the maxima, respectively. This is most likely due to different resonance peak locations in the top hat model. We will not explore this structure in more detail here, but as its "hat" was modeled as an ellipsoid, it is likely that its resonance peaks are shifted in accordance with the major-minor axis ratio. Resonance shifts in ellipoids has been reviewed by e.g. Kelly *et al.* [77].

The conclusion in this section is that the AuFON model derived shows some similar trends with available experimental data, but more work needs to be done to investigate the AuFON properties more thoroughly and optimize model parameters. It should also be noted that the model used smooth metal surfaces with no surface roughness which is seen in real-world samples (recall Figure 2.1). The foundation of the model, developed throughout this thesis, is based on well-behaved models that agree with research.

Chapter 6

Conclusion

This thesis developed a FEM model to simulate the AuFON structure, using a bottom-up approach, with the capability to predict its surface area-averaged SERS enhancement factor. An emphasis was placed on ensuring that the model behaves physically correct in every step, before adding more complexity. This was verified by studying how extinction resonance peaks emerge, are shifted and become wider or narrower, when changing parameters such as particle size and surrounding medium RI. The model was compared to analytical Mie solutions, numerical results from dipole approximation methods (CDA, DDA) and published results, when available.

The single-particle models for gold and silver spheres showed good consistency with theory and analytical Mie solutions. They also compare well with the DDA, showing similar resonance peak wavelengths and linewidths also when changing particle size or medium. As expected from theory, larger particles had their resonance peaks redshifted. Their SERS enhancement capability is not very high, producing surface area-averaged enhancement factors on the order of 10^2. With near-field coupling of two or more particles very closely, one can achieve a theoretically maximal SERS enhancement factor of 10^{14} at sub-nanometer spacings. An EF of 10^8 at a spacing of about 1 nm is, however, more reasonable and matches the SERS EFs reported in literature. The models demonstrate resonance tuning by altering the particle size. Larger spheres generally have resonances at higher wavelengths, and exhibit larger enhancement factors at NIR wavelengths, typically used for Raman spectroscopy.

The far-field coupled array models act in accordance with theory for all investigated array types, both 1D and 2D. There is some disagreement with the simple oscillator model and some divergence from the CDA, due to the fact that the particles in the FEM are not point dipoles. For gold, they peak at 10^3. From the extinction plots, it is generally seen that the model otherwise behaves correctly with changes in the lattice constant, with slightly redshifted SLRs and blueshifted LSPRs due to coupling. The 2D square model exhibits the half-diagonal SLRs predicted from theory. These were also reproduced with the CDA and showed a good match. The SLRs do not exhibit the large SERS EFs found in the near-field.

Single nanoshells demonstrate larger surface field enhancements than similar-sized solid particles. Nanoshells exhibit a greater capability for resonance tuning. This behavior compares well to the quasi-static model at the particle sizes presented. Larger shell thicknesses do, however, eventually make the nanoshells behave as solid particles. Though agreering with theory, nanoshell FEM models deviate somewhat from the quantitative Mie results, but as the metal dataset in the NanoComposix Mie implementation is not known and that there

currently are several Mie extensions for nanoshells in the literature, it can not be concluded that the Mie result is more correct. The DDA model results place somewhere between Mie and FEM and make it difficult to conclude which model they support more.

Nanoshells in close-packed hex lattice arrays, as an approximation of AuFONs, exhibit SERS EFs of $10^3 - 10^4$, depending on particle spacing. This generally fits with the reference plot and previous work, but is several orders of magnitude smaller than the current state of the art, $10^6 - 10^8$. The relation between film thickness and SERS EF is generally in agreement with the reference plot, with the highest SERS EF for 500 nm and 750 nm core diameters at film thicknesses in the 100 nm - 150 nm range.

The top hat structure shows similar results, although the EFs are generally lower at the same spacing than demonstrated by plain nanoshells. The top hat structure modeled is, however, just one interpretation of the AuFON shape. In general, one needs more experimental measurements with more data points to verify the final AuFON model and the model parameters need optimization. The current model also lacks features such as surface roughness, which is believed to contribute greatly to SERS EF.

The surface-averaged SERS estimation algorithm based on the E^4 approximation is relatively easy to implement in single particles or far-field coupled arrays, but cannot be applied in close-packed arrays where the integrating sphere cannot fit. Replacing the integrating sphere with Wigner-Seitz cell boundaries to estimate the EF in such arrays, however, favors very small particle spacings and becomes increasingly inaccurate at larger spacings. It is therefore difficult to conclude if the values produced by this method are accurate.

One identified short-coming of the FEM is modeling particle arrays at wavelengths when the medium RI is higher than the particle RI. This causes interference and makes it difficult to know where to place the integrating sphere such that the scattering cross section will be modeled correctly. Placing it too far out makes the medium's scattering properties dominate the system's scattering cross section. Placing it too close to the particle produces a negative extinction cross section at wavelengths where the medium's RI is higher than that of the particle. Note, however, that as glucose measurements using Raman spectroscopy use NIR wavelengths, and noble metals' RIs become increasingly larger with longer wavelengths, this does not pose a problem for modeling AuFONs at the relevant wavelengths.

Comparing all the modeling methods used in this thesis, the FEM is more flexible with particle geometry and allows potentially highly realistic models, though at a higher computational resource cost than the simpler numerical models offered by dipole approximation-based methods.

6.1 Suggestions for future work

The model used smooth particles. However, Chapter 3 does review literature that state that surface roughness is a significant contributor to SERS. There are ways to implement randomly rough surfaces in COMSOL and so the FEM model can be extended with surface roughness. This would also make it easier to compare against published results, as the model will be more realistic. Adding a substrate can also be considered, as the refractive index of a glass substrate, a fused silica microscope slide, might affect the resonance locations. Furthermore, during metalization of real-world AuFON samples, some metal falls into the gaps between the spheres. When the spheres are lifted off, such as during a colloidal lithography process, structures resembling triangles (see e.g. van Duyne and Hayes [11]). These

triangles alone have shown SERS EFs on the order of 10^8, as demonstrated by van Duyne and Hayes. It might be of value to inspect how these triangles affect the overall SERS EF of the model, when both the spheres and triangles are present. Some optimization of the EF measurement approach, i.e. adapt the surface integral to capture the contribution from the triangles.

Some work should be devoted to optimize the top hat structure, to achieve a shape closer to actual AuFONs and making sure that the SERS estimation algorithm captures the localized field enhancement where particle coupling occurs.

In the end, one should perform measurements on a fabricated sample and compare more closely with the model. Even if more data was found in the literature, it is difficult to model their values due to unknown parameters in the geometry and such.

Bibliography

[1] R. Malyshev. Plasmonic Nanostructures for SERS Glucose Sensors, 2020. Project Thesis, NTNU. Submitted 10.01.2020.

[2] N. Li, H. Zang, H. Sun, X. Jiao, K. Wang, T. Cheng-Yi Liu, and Y. Meng. A Non-invasive Accurate Measurement of Blood Glucose Levels with Raman Spectroscopy of Blood in Microvessels. *molecules*, 24, 2019.

[3] D. G. Jung, D. Jung, and S. H. Kong. A Lab-on-a-Chip-Based Non-Invasive Optical Sensor for Measuring Glucose in Saliva. *Sensors (Basel)*, 17:2607, 2017.

[4] R. Pilot, R. Signorini, C. Durante, L. Orian, M. Bhamidipati, and L. Fabris. A review on Surface-Enhanced Raman Scattering. *Biosensors*, 9(57), April 2019.

[5] M. Fleischmann, P. J. Hendra, and A. J. McQuillan. Raman spectra of pyridine adsorbed at a silver electrode. *Chemical Physics Letters*, 26:163–166, 1974.

[6] T. Joshua Moore, A. S. Moody, T. D. Payne, G. M. Sarabia, A. R. Daniel, and B. Sharma. In Vitro and In Vivo SERS Biosensing for Disease Diagnosis. *biosensors*, 8, 2018.

[7] Kyle C. Bantz, Audrey F. Meyer, Nathan J. Wittenberg, Hyungsoon Im, Özge Kurtuluş, Si Hoon Lee, N. C. Lindquist, S.-H. Oh, and C. L. Haynes. Recent progress in SERS biosensing. *Phys. Chem. Chem. Phys.*, 13:11551–11567, 2011.

[8] K. Milenko, S. S. Fuglerud, S. B. Kjeldby, R. Ellingsen, A. Aksnes, and D. R. Hjelme. Micro-lensed optical fibers for a surfaceenhanced Raman scattering sensing probe. *Optics Letters*, 43(24):6029–6032, November 2018.

[9] K.P. Sooraj, M. Ranjan, R. Rao, and S. Mukherjee. SERS based detection of glucose with lower concentration than blood glucose level using plasmonic nanoparticle arrays. *Applied Surface Science*, 447:576 – 581, 2018.

[10] D. R. Parachalil, C. Bruno, F. Bonnier, H. Blasco, I. Chourpa, M. J. Baker, J. McIntyrea, and H. J. Byrne. Analysis of bodily fluids using vibrational spectroscopy: a direct comparison of Raman scattering and infrared absorption techniques for the case of glucose in blood serum. *Analyst*, 144:3334–3346, 2019.

[11] C. L. Haynes and R. P. Van Duyne. Plasmon-Sampled Surface-Enhanced Raman Excitation Spectroscopy. *J. Phys. Chem. B*, 107:7426–7433, 2003.

[12] L. Baia, M. Baia, J. Popp, and S. Astilean. Gold Films Deposited over Regular Arrays of Polystyrene Nanospheres as Highly Effective SER Substrates from Visible to NIR. *J. Phys. Chem. B*, 110:23982–23986, 2006.

[13] P. L. Stiles, J. A. Dieringer, N. C. Shah, and R. P. van Duyne. Surface-Enhanced Raman Spectroscopy. *Annual Review of Analytical Chemistry*, 1:601–626, 2008.

[14] B. O. Åsvold. Diabetes. `https://sml.snl.no/diabetes`, October 2019. A part of NTNU's contribution to Store Norske Leksikon. Last accessed 24.11.2019.

[15] K. Miedema. Standardization of HbA1c and Optimal Range of Monitoring. *Scandinavian Journal of Clinical and Laboratory Investigation*, 65(sup240):61–72, 2005.

[16] American Diabetes Association. Diagnosis and Classification of Diabetes Mellitus. *Diabetes Care*, 33 suppl 1:S62–S69, 2010.

[17] WHO. Diabetes. `https://www.who.int/en/news-room/fact-sheets/detail/diabetes`, 2014. Last accessed 24.11.2019.

[18] Mayo Clinic. Diabetic hypoglycemia - Symptoms and Causes. `https://www.mayoclinic.org/diseases-conditions/diabetic-hypoglycemia/symptoms-causes/syc-20371525`, 2019. Last accessed 22.12.2019.

[19] E. Cara, L. Mandrile, F. Ferrarese Lupi, A. M. Giovannozzi, M. Dialameh, C. Portesi, K. Sparnacci, N. De Leo, A. M. Rossi, and L. Boarino. Influence of the long-range ordering of gold-coated Si nanowires on SERS. *Scientific Reports (Nature)*, page 11305, 2018.

[20] S. J. Oldenburg, R. D. Averitt, S. L. Westcott, and N. J. Halas. Nanoengineering of optical resonances. *Chemical Physics Letters*, 288:243–247, 1998.

[21] R. D. Averitt, S. L. Westcott, and N. J. Halas. Linear optical properties of gold nanoshells. *Journal of the Optical Society of America B*, 16:1824–1832, 1999.

[22] C. Lee, C. S. Robertson, A. H. Nguyen, M. Kahraman, and S. Wachsmann-Hogiu. Thickness of a metallic film, in addition to its roughness, plays a significant role in SERS activity. *Scientific reports*, 2015.

[23] K. Kouba, J. Proška, and M. Procházka. Gold Film over SiO2 Nanospheres—New Thermally Resistant Substrates for Surface-Enhanced Raman Scattering (SERS) Spectroscopy. *nanomaterials*, 2019.

[24] C. Langhammer, B. Kasemo, and I. Zorić. Absorption and scattering of light by Pt, Pd, Ag, and Au nanodisks: Absolute cross sections and branching ratios. *Journal of Chemical Physics*, 126(194702), March 2007.

[25] L. Petti, R. Capasso, M. Rippa, M. Pannico, P. La Manna, G. Peluso, A. Calarco, E. Bobeico, and P. Musto. A plasmonic nanostructure fabricated by electron beam lithography as a sensitive and highly homogeneous SERS substrate for bio-sensing applications. *Vibrational Spectroscopy*, 82:22–30, 2016.

[26] A. D. McFarland, M. A. Young, J. A. Dieringer, and R. P. Van Duyne. Wavelength-Scanned Surface-Enhanced Raman Excitation Spectroscopy. *J. Phys. Chem. B*, pages pp. 11279–11285, 2005.

[27] C. Zhang, S. Cvetanovic, and J. M. Pearce. Fabricating ordered 2-D nano-structured arrays using nanosphere lithography. *MethodsX*, 4:229–242, 2017.

[28] S. K. Braathen. Surface-Enhanced Raman Scattering for Biosensor Probes. Master's thesis, NTNU, 2018. `https://ntnuopen.ntnu.no/ntnu-xmlui/handle/11250/2569679`. Last accessed 24.11.2019.

[29] J. Šugar and P. Bouř. Quantitative analysis of sugar composition in honey using 532-nm excitation Raman and Raman optical activity spectra. *Journal of Raman Spectroscopy*, 2016.

[30] G. Mie. Beiträge zur Optik trüber Medien, speziell kolloidaler Metallösungen. *Annalen der Physik*, 25, 1908.

[31] C. F. Bohren and D. R. Huffman. *Absorption and scattering of light by small particles*. Wiley, 1983.

[32] D. Sarid and W. Challener. *Modern Introduction to Surface Plasmons*. Cambridge University Press, 2010.

[33] C. Kittel. *Introduction to Solid State Physics*. John Wiley & Sons, Inc., 8th edition, 2004.

[34] A. D. Rakić, A. B. Djurišić, J. M. Elazar, and M. L. Majewski. Optical properties of metallic films for vertical-cavity optoelectronic devices. *Applied Optics*, 37(22): 5271–5283, Aug 1998.

[35] J. Olson, S. Dominguez-Medina, A. Hoggard, L. Wang, W. Chang, and S. Link. Optical Characterization of Single Plasmonic Nanoparticles. *Chem. Soc. Rev.*, 44(1):40–57, 2015.

[36] S. A. Maier. *Plasmonics: Fundamentals and Applications*. Springer, 2007.

[37] Bahaa E.A. Saleh and M.C. Teich. *Fundamentals of Photonics*. Wiley, 2nd edition, 2007.

[38] R. Merlin, A. Pinczuk, and W. H. Weber. *Raman Scattering in Materials Science*. Springer, 2000.

[39] D. DeJarnette, D. K. Roper, and B. Harbin. Geometric Effects on Far-Field Coupling Between Multipoles of Nanoparticles in Square Arrays. *Journal of the Optical Society of America B*, 29:88–100, 2012.

[40] E. Le Ru and P. Etchegoin. *Principles of surface-enhanced Raman spectroscopy*. Elsevier, 2009.

[41] Y. Zhao, X. Liu, D. Y. Lei, and Y. Chai. Effects of surface roughness of Ag thin films on surface-enhanced Raman spectroscopy of graphene: spatial nonlocality and physisorption strain. *Nanoscale*, 6:1311 – 1317, 2014.

[42] A. L. Aden and M. Kerker. Scattering of Electromagnetic Waves from Two Concentric Spheres. *Journal of Applied Physics*, 22:1242, 1951.

[43] D. Sarkar. *Vector basis function solution of Maxwell's equations*. PhD thesis, Rice University, 1996. `https://scholarship.rice.edu/handle/1911/19204`. Last accessed 13.08.20.

[44] S.J. Oldenburg. *Light Scattering from Gold Nanoshells*. PhD thesis, Rice University, 2000. `https://scholarship.rice.edu/handle/1911/19543`. Last accessed 29.07.20.

[45] V. G. Kravets, A. V. Kabashin, W. L. Barnes, and A. N. Grigorenko. Plasmonic Surface Lattice Resonances: A Review of Properties and Applications. *Chemical Reviews*, 118:5912–5951, 2018.

[46] C. Cherqui, M. R. Bourgeois, D. Wang, and G. C. Schatz. Plasmonic Surface Lattice Resonances: Theory and Computation. *Accounts of Chemical Research*, 52:2548–2558, 2019.

[47] V. Bejugam. *Opto-Thermal Characterization of Plasmon and Coupled Lattice Resonances in 2-D Metamaterial Arrays*. PhD thesis, University of Arkansas, Fayetteville, 2018. h8ps://scholarworks.uark.edu/etd/2868. Accessed 02.06.20.

[48] Y. S. Joe, A. M. Satanin, and C. S. Kim. Classical analogy of Fano resonances. *Physica Scripta*, 74:259–266, 2006.

[49] M. A. Yurkin, D. de Kanter, and A. G. Hoekstra. Accuracy of the discrete dipole approximation for simulation of optical properties of gold nanoparticles. *Journal of Nanophotonics*, 4, 2010.

[50] K. B. Milenko. Film thickness comparison plot. Unpublished.

[51] B. T Draine and P. J. Flatau. Discrete-dipole approximation for scattering calculations. *J. Opt. Soc. Am.*, 11:1491–1499, 1994.

[52] B. T Draine. The discrete-dipole approximation and its application to interstellar graphite grains. *The Astrophysical Journal*, 33:848–872, 1988.

[53] B. T Draine and P. J. Flatau. Fast near-field calculations in the discrete dipole approximation for regular rectilinear grids. *Optics Express*, 20:1247–1252, 2012.

[54] M. A. Yurkin and A. G. Hoekstra. The discrete-dipole-approximation code ADDA: Capabilities and known limitations. *Journal of Quantitative Spectroscopy & Radiative Transfer*, 112:2234–2247, 2011.

[55] R. W. Numrich, T. L. Clune, and K.-S. Kuo. A New Parallel Version of the DDSCAT Code for Electromagnetic Scattering from Big Targets. *PIERS Proceedings, Taipei, March 25-28*, 2013.

[56] V. A. Markel. Coupled-dipole Approach to Scattering of Light from a One-dimensional Periodic Dipole Structure. *Journal of Modern Optics*, 40:2281–2291, 1993.

[57] S. Zou, N. Janel, and G. C. Schatz. Silver nanoparticle array structures that produce remarkably narrow plasmon lineshapes. *J. Chem. Phys.*, 120:10871 – 10875, 2004.

[58] S. Zou and G. C. Schatz. Narrow plasmonic/photonic extinction and scattering line shapes for one and two dimensional silver nanoparticle arrays. *J. Chem. Phys.*, 121: 12606 – 12612, 2004.

[59] A. C. Polycarpou. *Introduction to the finite element method in electromagnetics*. Morgan & Claypool Publishers, 2006.

[60] H. A. Lorentz. Theory of Electrons. *Teubner, Leipzig*, 1909.

[61] E. M. Purcell and C. R. Pennypacker. Scattering and Absorption of Light by Nonspherical Dielectric Grains. *The Astrophysical Journal*, 186:705–714, 1973.

[62] M. V. Seeram, G. T. Forcherio, and D. K. Roper. Shape Generator for the DDSCAT software. https://nanohub.org/resources/ddscatshapegene, 2016. Last accessed 01.04.20.

[63] D. Dejarnette. An Extension to Particle Polarizability to Predict Coupling Behavior in Periodic Nanoplasmonic Arrays. Master's thesis, University of Arkansas, Fayetteville, 2012. http://scholarworks.uark.edu/etd/540. Accessed 02.06.20.

[64] K. R. Berry Jr., R. L. Romo, M. Mitchell, V. Bejugam, and D. K. Roper. Controlled Gold Nanoparticle Placement into Patterned Polydimethylsiloxane Thin Films via Directed Self-Assembly. *Journal of Nanomaterials*, pages 1–11, 2019.

[65] L. Zhao, K. Lance Kelly, and G. C. Schatz. The Extinction Spectra of Silver Nanoparticle Arrays: Influence of Array Structure on Plasmon Resonance Wavelength and Width. *J. Chem. Phys. B*, 107:7343–7350, 2003.

[66] COMSOL Inc. Understanding the Fully Coupled vs. Segregated approach and Direct vs. Iterative linear solvers. `https://www.comsol.no/support/knowledgebase/1258`, 2020. Last accessed 02.07.20.

[67] P.R. Amestoy, I. S. Duff, J. Koster, and J.-Y. L'Excellent. A fully asynchronous multifrontal solver using distributed dynamic scheduling. *SIAM Journal on Matrix Analysis and Applications*, 23(1):15–41, 2001.

[68] H. A. Van der Vorst. Bi-CGSTAB: A Fast and Smoothly Converging Variant of Bi-CG for the Solution of Nonsymmetric Linear Systems. *SIAM Journal on Scientific Computing*, 13:631–644, 1992.

[69] P. J. Flatau. Improvements in the discrete-dipole approximation method of computing scattering and absorption. *Optics Letters*, 22:1205–1207, 1997.

[70] N. Sultanova, S. Kasarova, and I. Nikolov. Dispersion Properties of Optical Polymers. *ACTA PHYSICA POLONICA A*, 116, 2009.

[71] P. E. Ciddor. Refractive index of air: new equations for the visible and near infrared. *Appl. Opt.*, 35(9):1566–1573, Mar 1996.

[72] P. Laven. Refractive index of water. `http://www.philiplaven.com/p20.html`, 2019. Last accessed 26.10.2019.

[73] D. R. Lide. *CRC handbook of chemistry and physics*. CRC Press, London, 82nd edition, 2001.

[74] COMSOL Inc. Optical Scattering off a Gold Nanosphere. `https://www.comsol.com/model/optical-scattering-off-a-gold-nanosphere-14697`, 2020. Last accessed 29.06.20.

[75] NTNU Nanolab. Micro-Raman Spectroscopy. `http://ntnu.norfab.no/WebForms/Equipment/EquipmentView.aspx?toolId=82#description-accordion`, 2014. Last accessed 02.07.20.

[76] A. R. Shafiqa, A. A. Aziz, and B. Mehrdel. Nanoparticle Optical Properties: Size Dependence of a Single Gold Spherical Nanoparticle. *Journal of Phys., Conference Series*, 2018.

[77] K. Lance Kelly, E. Coronado, L. L. Zhao, and G. C. Schatz. The Optical Properties of Metal Nanoparticles: The Influence of Size, Shape, and Dielectric Environment. *J. Phys. Chem. B*, 107:668–677, 2003.

[78] C. Hakoda, J. Rose, P. Shokouchi, and C. Lissenden. Using Floquet periodicity to easily calculate dispersion curves and wave structures of homogeneous waveguides. *AIP Conference Proceedings*, 1949:020016, 2018.

[79] W. Frei. Exploiting Symmetry to Simplify Magnetic Field Modeling. `https://www.comsol.com/blogs/exploiting-symmetry-to-simplify-magnetic-field-modeling/`, 2014. Last accessed 18.06.20.

[80] I. Knorr, K. Christou, J. Meinertz, A. Selle, J. Ihlemann, and G. Marowsky. Prediction and Optimization of Surface-Enhanced Raman Scattering Geometries using

COMSOL Multiphysics. `https://www.comsol.com/paper/download/37320/Knorr.pdf`, 2008. Last accessed 27.01.20. Excerpt from the Proceedings of the COMSOL Conference 2008 Hannover.

[81] F. Schedin, E. Lidorikis, A. Lombardo, V. G. Kravets, A. K. Geim, A. N. Grigorenko, K. S. Novoselov, and A. C. Ferrari. Surface-Enhanced Raman Spectroscopy of Graphene. *ACS NANO*, 4:5617–5626, 2010.

[82] J.-P. Berenger. A Perfectly Matched Layer for the Absorption of Electromagnetic Waves. *Journal of Computational Physics*, 114:185–200, 1994.

[83] E.-B. Kley and B. Schnabel. E-beam lithography: a suitable technology for fabrication of high-accuracy 2D and 3D surface profiles. *Proceedings of SPIE, Austin, Texas, USA*, 2640:71 – 75, 1995. Microlithography and Metrology in Micromachining.

[84] STS-ELIONIX. ELS-F150. `https://www.sts-elionix.com/product/els-f150/`, 2020. Last accessed 28.06.20.

[85] Y. Chu, E. Schonbrun, T. Yang, and K. B. Crozier. Experimental observation of narrow surface plasmon resonances in gold nanoparticle arrays. *Appl. Phys. Lett.*, 93: 181108, 2008.

[86] R. E. Walpole, R. H. Myers, S. L. Myers, and K. Ye. *Probability & Statistics for Engineers & Scientists*. Pearson, 9th edition, 2012.

[87] C. Mätzler. MATLAB Functions for Mie Scattering and Absorption, 2002. Research Report No. 2002-08, University of Bern.

[88] P. K. Jain, K. S. Lee, I. H. El-Sayed, and M. A. El-Sayed. Calculated Absorption and Scattering Properties of Gold Nanoparticles of Different Size, Shape, and Composition: Applications in Biological Imaging and Biomedicine. *J. Phys. Chem.*, 110:7238–7248, 2006.

[89] P. B. Johnson and R. W. Christy. Optical Constants of the Noble Metals. *Phys. Rev. B*, 6:4370, 1972.

[90] E. D. Palik. *Handbook of Optical Constants of Solids*. Academic, New York, 1985.

[91] M. I. Mishchenko and J. M. Dlugach. Scattering and extinction by spherical particles immersed in an absorbing host medium. *J. Quant. Spectrosc. Radiat. Transfer*, 211: 179–187, 2018.

[92] S. Zou and G. C. Schatz. Silver nanoparticle array structures that produce giant enhancements in electromagnetic fields. *Chemical Physics Letters*, 403:62 – 67, 2005.

[93] B. Auguié and W. L. Barnes. Diffractive coupling in gold nanoparticle arrays and the effect of disorder. *Optics Letters*, 34:401–403, 2009.

[94] J. I. Pankove. *Optical Processes in Semiconductors*. Dover, 1975. Referenced by Averitt et al., *Linear optical properties of gold nanoshells*.

[95] C. Farcau, M. Giloan, E. Vinteler, and S. Astilean. Understanding plasmon resonances of metal-coated colloidal crystal monolayers. *Applied Physics B*, 106:849–856, 2012.

[96] C. Johnson. *Numerical solution of partial differential equations by the finite element method*. Cambridge University Press, 1987.

[97] M. Herlihy and N. Shavit. *The Art of Multiprocessor Programming*. Elsevier, 2012. Revised ed.

[98] A. Arbouet and G. Agez. ETPMSE2016: Numerical Simulations for Plasmonics. https://etpmse2016.sciencesconf.org/conference/etpmse2016/pages/Introduction_Simulations_Plasmonics.pdf, 2016. Ecole Thématique Plasmonique Moléculaire et Spectroscopies Exaltées, June 20-24, 2016, Toulouse (France). Last accessed 28.03.2020.

[99] J. Armstrong. OpenMP on Ubuntu. https://medium.com/swlh/openmp-on-ubuntu-1145355eeb2, 2018. Last accessed 28.03.20.

[100] M. V. Seeram. Acceleration of DDSCAT Computation by Parallelization on a Supercomputer. Chemical Engineering Undergraduate Honors Theses Retrieved from https://scholarworks.uark.edu/cheguht/88, 2016. Last accessed 01.04.20.

[101] COMSOL and Multithreading. https://www.comsol.com/support/knowledgebase/1096, 2019. Last accessed 20.04.20.

[102] COMSOL. Optical Scattering Off of a Gold Nanosphere. https://www.comsol.com/model/download/563181/models.woptics.scattering_nanosphere.pdf, 2019. Last accessed 31.10.2019.

Appendices

Appendix A

The Finite Element Method

The models simulated in this text were solved using the finite element method (FEM). It is a numerical method for solving large sets of partial differential equations (PDEs) by splitting the simulation domain into smaller domains, finite elements, and solving for the unknown variable. In this case, the electric field. This splitting of the domain into many elements makes it easier to solve for the electric field, finding the field in each one of these elements, rather than in the whole domain at once. The FEM is used when simulations in the time domain, such as those of wave propagation, are not required. Otherwise, the finite-difference time-domain method is used. However, for the scattering problem, it is assumed that the scattered field is constant in time. A general variational formulation of the FEM for some common problems is given in Johnson [96, Ch. 1].

A.1 Solving the Poisson equation.

This appendix presents the FEM following Polycarpou [59, Ch.1-2], as this reference is written specifically with electromagnetic applications in mind and uses the weighted-residual, Galerkin, method. The Galerkin method doesn't require us to construct a functional for the boundary-value problem, but starts directly from the governing PDE.

For the purposes of this thesis, the FEM solution of the wave equation with boundary conditions was computed using COMSOL Multiphysics. However, as a demonstration of the steps involved, this chapter shows how to solve the Poisson equation, as it is simpler to follow than a solution of the wave equation. It is demonstrated how to apply it to the Poisson equation in one dimension first, as it makes it easier to understand all the steps, and then expand it to 2D. The 1D problem is that of solving the Poisson equation for the potential between two parallel infinite conducting plates separated by distance d, where one plate is held at a fixed potential $V = V_0$ and the other is grounded, $V = 0$.

$$\begin{aligned} \nabla(\epsilon_r \nabla V) &= -\frac{\rho_v}{\epsilon_0} \\ V &= V_0 \\ V &= 0, \end{aligned} \tag{A.1}$$

where volume charge density $\rho_v = -\rho_0$. ϵ_r is the dielectric constant. The two boundary

conditions in (A.1) are the Dirichlet conditions. The analytical solution is

$$V(x) = \frac{\rho_0}{2\epsilon}x^2 - \left(\frac{\rho_0 d}{2\epsilon} + \frac{V_0}{d}\right)x + V_0, \tag{A.2}$$

where $\epsilon = \epsilon_0\epsilon_r$. The electric field is defined as $\mathbf{E}(x) = -\nabla V$ and can be solved for after finding V.

Meshing

The method starts by discretizing the domain. Here, the domain is the distance between the two plates, which is divided into N_e lengths – elements – of equal lengths. This results in $N_n = N_e + 1$ nodes, as shown in Figure A.1. For now, we only use the end-points as nodes, making the elements linear.

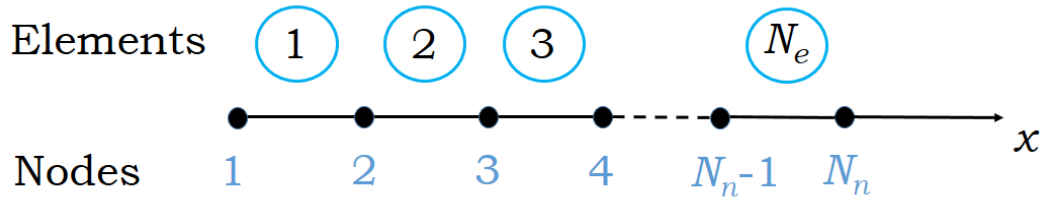

Figure A.1: 1D domain discretization into N_e elements and N_n nodes.

The solved function will later be evaluated at arbitrary points x inside an element, as $V(x) = V_1^e N_1(x) + V_2^e N_2(x)$, where $N_i(x)$ are interpolation functions corresponding to node i of an element e. V_i^e is V evaluated in element e, node i. For now the interpolation functions will also be linear.

To simplify the computations, it is convenient to introduce coordinates along an element as natural coordinates, $-1 \leq \xi \leq 1$, such that the first node of an element, at $x = x_1^e$ corresponds to $\xi = -1$ and $x = x_2^e$ to $\xi = 1$. Thus, every node will have the same *local* coordinates along the ξ-axis, while the global x-coordinate is ever-changing. The coordinate transformation follows the form

$$\xi = \frac{2(x - x_1^e}{x_2^e - x_1^e} - 1. \tag{A.3}$$

Figures A.2 and A.3 show the interpolation functions and the resulting value of V at the nodes and at any point inside element e.

The number of interpolation functions used to evaluate V is equal to the degrees of freedom, or nodes, per element. For linear elements, two interpolation functions are used. For quadratic – three, etc.

The weighted-residual approach

The Galerkin method is based on constructing a weighted residual on a single element e by moving all terms of the PDE to the left-hand side, multiplying by a weighing function w and integrating over the element coordinates:

$$r^e = \int_{x_1^e}^{x_2^e} w\left[\frac{d}{dx}\left(\epsilon^e \frac{dV}{dx}\right)\rho_v\right]dx = 0. \tag{A.4}$$

In addition, the method requires only once-differentiable weight and interpolation functions in the weak formulation, rather than twice-differentiable (the PDE is a second-order one),

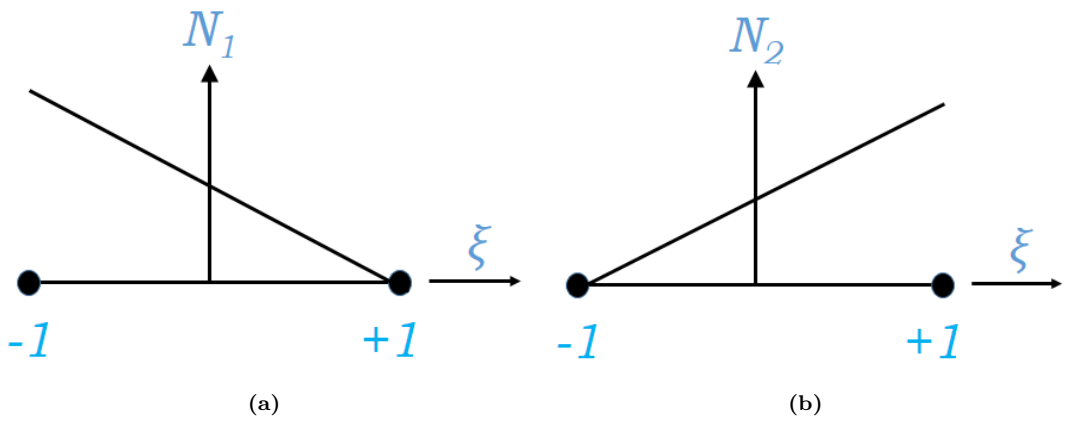

Figure A.2: Interpolation functions (a) $N_1(\xi)$ and (b) $N_2(\xi)$, used to weigh the electric potentials V_1^e and V_2^e in the nodes to find the potential $V(\xi)$ at a point ξ in an element.

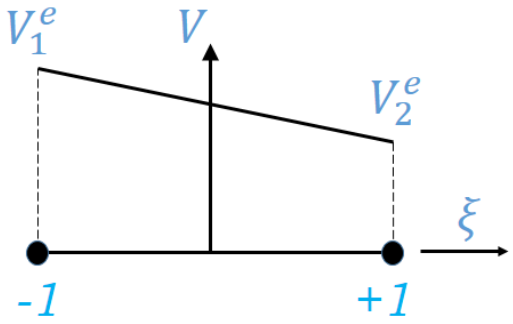

Figure A.3: Evaluation of V in an element, using the node values.

meaning that we can use the linear interpolation functions $N_i(x)$ as weight functions. Integrating (A.4) by parts, setting $D_x^e = -\epsilon^e \frac{dV}{dx}$ and replacing V by $\sum_{j=1}^{n} V_j^e N_j$, the weighted residuals for the two nodes of element e are

$$\int_{x_1^e}^{x_2^e} \frac{dN_1}{dx} \epsilon^e \left(\sum_{j=1}^{2} V_j^e \frac{dN_j}{dx} \right) = \int_{x_1^e}^{x_2^e} N_1 \rho_v dx + N_1(x_1^e) D_x^e(x_1^e) - N_1(x_2^e) D_x^e(x_2^e) \tag{A.5}$$

$$\int_{x_1^e}^{x_2^e} \frac{dN_2}{dx} \epsilon^e \left(\sum_{j=1}^{2} V_j^e \frac{dN_j}{dx} \right) = \int_{x_1^e}^{x_2^e} N_2 \rho_v dx + N_2(x_1^e) D_x^e(x_1^e) - N_2(x_2^e) D_x^e(x_2^e) \tag{A.6}$$

Using the definition of the interpolation functions above, $N_1(x_1^e) = N_2(x_2^e) = 1$ and $N_2(x_1^e) = N_1(x_2^e) = 0$, the equations above can be further reduced to

$$\int_{x_1^e}^{x_2^e} \frac{dN_1}{dx} \epsilon^e \left(\sum_{j=1}^{2} V_j^e \frac{dN_j}{dx} \right) = \int_{x_1^e}^{x_2^e} N_1 \rho_v dx + N_1(x_1^e) D_x^e(x_1^e) \tag{A.7}$$

$$\int_{x_1^e}^{x_2^e} \frac{dN_2}{dx} \epsilon^e \left(\sum_{j=1}^{2} V_j^e \frac{dN_j}{dx} \right) = \int_{x_1^e}^{x_2^e} N_2 \rho_v dx - N_2(x_2^e) D_x^e(x_2^e) \tag{A.8}$$

and written in matrix form as

$$\begin{bmatrix} K_{11}^e & K_{12}^e \\ K_{21}^e & K_{22}^e \end{bmatrix} \begin{bmatrix} V_1^e \\ V_2^e \end{bmatrix} = \begin{bmatrix} f_1^e \\ f_2^e \end{bmatrix} + \begin{bmatrix} D_1^e \\ -D_2^e \end{bmatrix}, \tag{A.9}$$

where $K_{ij}^e = \int_{x_1^e}^{x_2^e} \frac{dN_i}{dx} \epsilon^e \frac{dN_j}{dx} dx$ and $f_i^e = \int_{x_1^e}^{x_2^e} N_i \rho_v dx$ for $i, j = 1, 2$. Converting this to the natural coordinate from x,

$$d\xi = \frac{2}{x_2^e - x_1^e} dx = \frac{2}{l^e} dx \tag{A.10}$$

and rewriting

$$\frac{dN_i}{dx} = \frac{dN_i}{d\xi} \frac{d\xi}{dx} = \frac{2}{l^e} \frac{dN_i}{d\xi}. \tag{A.11}$$

The interpolation functions, in local coordinates, were defined as $N_1(\xi) = \frac{1-\xi}{2}$ and $N_2(\xi) = \frac{1+\xi}{2}$, which, differentiated w.r.t. ξ, simplifies to

$$\frac{\epsilon^e}{l^e} \begin{bmatrix} 1 & -1 \\ -1 & 1 \end{bmatrix} \begin{bmatrix} V_1^e \\ V_2^e \end{bmatrix} = -\frac{l^e \rho_0}{2} \begin{bmatrix} 1 \\ 1 \end{bmatrix} + \begin{bmatrix} D_1^e \\ -D_2^e \end{bmatrix}, \tag{A.12}$$

which is the matrix system for a single element, yielding the equations

$$K_{11}^e v_1^e + K_{12}^e v_2^e = f_1^e + D_1^e \tag{A.13}$$

$$K_{21}^e v_1^e + K_{22}^e v_2^e = f_2^e + D_2^e. \tag{A.14}$$

Assembling the elements

The system of equations ending the previous section was for one element only. Now, we need to construct a global matrix K for all the elements and global vectors for the other terms. This is done by summing the second node of one element with the first node of the next one, as these nodes are one and the same (see Figure A.1),

$$\begin{bmatrix} K_{11}^{(1)} & K_{12}^{(1)} & & & & \\ K_{21}^{(1)} & (K_{22}^{(1)} + K_{11}^{(2)}) & K_{12}^{(2)} & & & \\ & K_{21}^{(2)} & (K_{22}^{(1)} + K_{11}^{(3)}) & K_{12}^{(3)} & & \\ \cdots & \cdots & \cdots & \cdots & \cdots & \cdots \\ & & K_{21}^{(N_e-1)} & (K_{22}^{(N_e-1)} + K_{11}^{(N_e)}) & K_{12}^{(N_e)} & \\ & & & K_{21}^{(N_e)} & K_{22}^{(N_e)} & \end{bmatrix} \begin{bmatrix} V_1 \\ V_2 \\ V_3 \\ \vdots \\ V_{N_e} \\ V_{N_e+1} \end{bmatrix}$$

$$= \begin{bmatrix} f_1^{(1)} \\ f_2^{(1)} + f_1^{(2)} \\ f_2^{(2)} + f_1^{(3)} \\ \vdots \\ f_2^{(N_e-1)} + f_1^{(N_e)} \\ f_2^{(N_e)} \end{bmatrix} + \begin{bmatrix} D_1^{(1)} \\ -D_2^{(1)} + D_1^{(2)} \\ -D_2^{(2)} + D_1^{(3)} \\ \vdots \\ -D_2^{(N_e-1)} + D_1^{(N_e)} \\ -D_2^{(N_e)} \end{bmatrix}.$$

As the electric field, which is the first derivative of V, is not always continuous across elements, the electric field would be a step function when solved by FEM. This is because we are approximating the potential, which is quadratic (when the charge density is constant in x), with linear elements. The derivative is therefore a constant, while the exact electric field would, here, be linear. To avoid this division into discrete steps, we can divide the domain into a large enough number of elements, such that the displacement field of the second node of an element 1 is approximately equal to that of the first node of element 2 next to it,

$$-D_2^{(1)} + D_1^{(2)} \approx 0.$$

Using this, we see from the matrix equation above, the vector of D's would reduce to

$$\mathbf{d} = \begin{bmatrix} D_1^{(1)} \\ 0 \\ 0 \\ \vdots \\ 0 \\ -D_2^{(N_e)} \end{bmatrix} \tag{A.15}$$

A.1.1 Boundary conditions

The Dirichlet boundary conditions for the Poisson problem in 1D are, as stated before,

$$V_1 = V_0 \tag{A.16}$$

$$V_N = 0. \tag{A.17}$$

Hence, of the N_e equations in the matrix equation in the previous sections, two V's are already known. We can then eliminate the first equation, which determines V_1, and the last one. Also, we subtract the first column, corresponding to V_1, from the right-hand side, and similarly, from the last column.

$$\begin{bmatrix} K_{22} & K_{23} & \dots & K_{2,N-1} \\ K_{32} & K_{33} & \dots & K_{3,N-1} \\ \dots & \dots & \dots & \dots \\ K_{N-1,2} & K_{N-1,3} & \dots & K_{N-1,N-1} \end{bmatrix} \begin{bmatrix} V_2 \\ V_3 \\ \vdots \\ V_{N-1} \end{bmatrix} = \begin{bmatrix} b_2 - K_{21}V_0 \\ b_3 - K_{31}V_0 \\ \vdots \\ b_{N-1} - K_{N-1,1}V_0 \end{bmatrix}, \tag{A.18}$$

where b is the sum of the f and D vectors in the previous section.

A different kind of boundary condition is of the form

$$\epsilon \frac{dV}{dx} + \alpha V = \beta, \tag{A.19}$$

where α and β are constants. The absorbing scattering condition is used to limit the problem to the space domain we are interested in. It is set by replacing the last element in the $\mathbf{d}$ vector in A.15 by

$$\epsilon^{(N_e)} \left. \frac{dV}{dx} \right|_{x=x_2^{(N_e)}} = \beta - \alpha V_N, \tag{A.20}$$

and then moving αV_N to the right-hand side, into the K matrix in Equation A.18.

The solution to the resulting system can be found by setting some initial parameters for the potential V_0, the dielectric constant, the distance and the charge density. The solved potentials can then be used to estimate the electric field between the end-nodes of an element as

$$\mathbf{E} = \frac{V_1^e - V_2^e}{l^e} \hat{\mathbf{x}}, \tag{A.21}$$

where l^e, as before, is the length of an element. Figure A.4 shows the potential and electric field found by the FEM plotted against the analytical solutions.

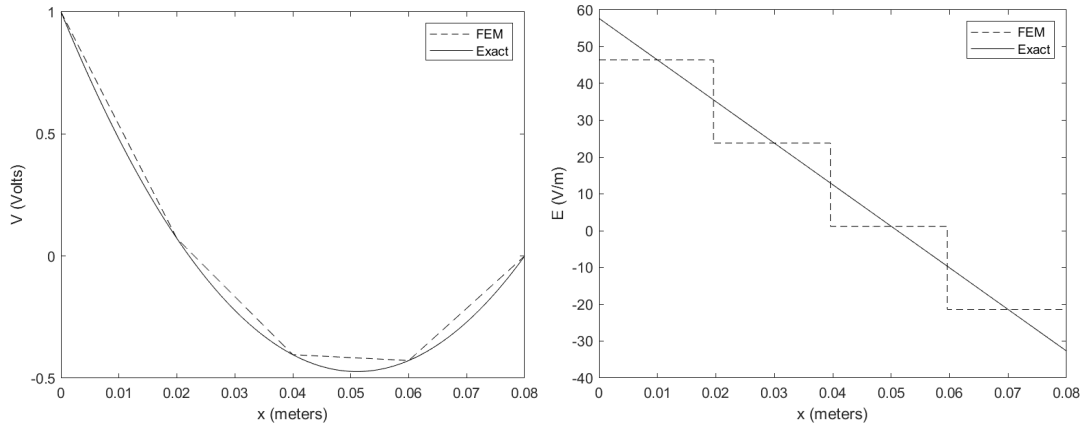

(a) **(b)**

Figure A.4: The electric (a) potential and (b) field found using FEM with 4 linear elements plotted against the exact solution. Plots based on Polycarpou [59, Ch. 1].

Error estimation

The error in the solution, compared to the analytical solution, is found from

$$\text{error } (\%) = \left(\frac{1}{|A_{exact}|} \sum_{e=1}^{N_e} \left| A_{exact}^{(e)} - A_{FET}^{(e)} \right| \right) \times 100 \ \%, \tag{A.22}$$

which is the difference between the areas covered by the functions plotted from the FEM and analytical solutions. It can be demonstrated that doubling the number of elements, decreases the error by a factor of 4. Another way to measure the numerical error is by finding the distance between the solutions in the orthogonal space, the L_2 norm,

$$||L_2|| = ||V_{exact} - V_{FEM}|| = \left(\sum_{e=1}^{N_e} \int_{\Omega^e} \left[V_{exact}^{(e)} - V_{FEM}^{(e)} \right]^2 dx \right)^{1/2} \tag{A.23}$$

For the FEM solution plotted in Figure A.4, the error was 36.70 % and the L_2 norm – 0.0117. Although this is a high error, it's interesting that in the end-points of the elements, the numerical solution is very close to the analytical. It's only when one starts interpolating it to other points inside an element that the error becomes significant. This can be mediated, as noted above, by increasing the number of elements: The L_2 norm, like the percent-wise error, also decreases by a factor of 4 for every doubling of the number of elements. Also, one can use higher-order elements and interpolation functions. If one takes the two end-nodes of a 1D element and also introduces the midpoint as a third node, the element becomes quadratic. Since the exact electric potential in this Poisson example was quadratic, we would see a one-to-one correspondence between the FEM solution and the analytical expression. Elements can also be cubic or of higher order.

A.2 2D and 3D FEM

The 1D discussion above illustrated the different steps involved in solving a boundary-value problem using FEM. However, 2D and 3D methods are more useful for practical applications. A 3D method is too complex to present in a short demonstration. However, the extension from a 2D problem to a 3D problem is similar to extending the problem from 1D to 2D, except for that it adds more computational complexity.

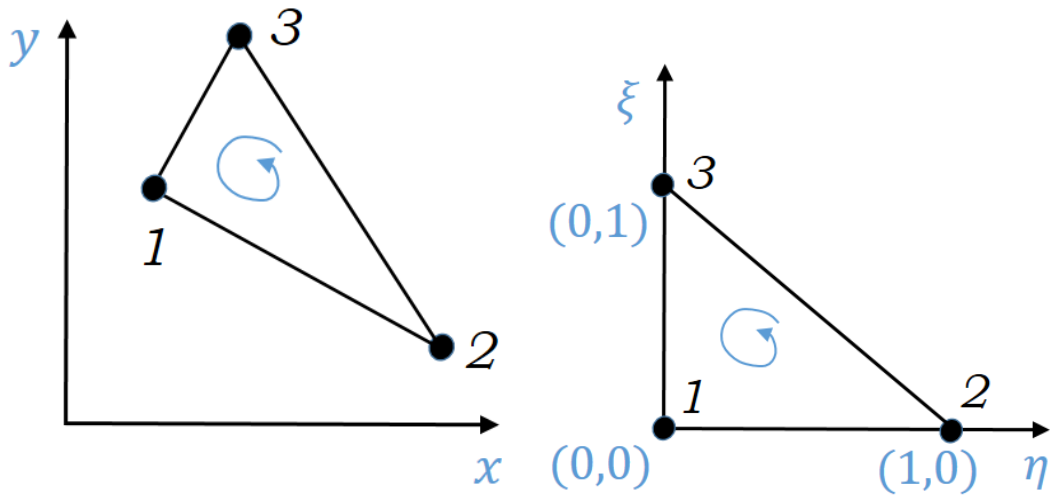

(a) (b)

Figure A.5: (a) Linear triangular element, showing direction of numeration and (b) the master element in the $\xi\eta$-plane.

A.2.1 Interpolation functions – linear triangular element

In a 2D problem, the domain needs to be divided into simple geometrical shapes, typically triangles or quadrilateral elements. We'll only focus on triangles.

A triangle consists of vertices, corresponding to the three nodes of an element, which are numbered counter-clockwise to avoid negative areas and a negative Jacobian as shown in Figure A.5. The linear interpolation function spanning a triangle has to be linear in two orthogonal directions to be mapped to the master triangle in Figure A.5b. The master triangle is the projection of the linear triangle onto the natural coordinate system, which was previously shown in the 1D problem.

The linear interpolation functions are defined so that function $N_i(\xi, \eta) = 1$ at node i and zero at all other nodes. The general form of the function is $N_i = c_1 + c_2\xi + c_3\eta$ and they satisfy $\sum_i N_i = 1$. It can be shown that

$$N_1(\xi, \eta) = 1 - N_2 - N_3 = 1 - \xi - \eta.$$

Inside an element e, the unknown variable, denoted u, is a weighted value

$$u = \sum_{i=1}^{3} u_i^e N_i \tag{A.24}$$

and the x, y-coordinates inside an element are expressed as $x = x_1^e + x_{21}\xi + x_{31}\eta$, and similarly for y. This allows the conversion from x, y-coordinates to ξ, η by

$$\begin{bmatrix} \frac{\partial N}{\partial \xi} \\ \frac{\partial N}{\partial \eta} \end{bmatrix} = J \begin{bmatrix} \frac{\partial N}{\partial x} \\ \frac{\partial N}{\partial y} \end{bmatrix}, \tag{A.25}$$

where J is the Jacobian

$$J = \begin{bmatrix} \frac{\partial x}{\partial \xi} & \frac{\partial y}{\partial \eta} \\ \frac{\partial x}{\partial \eta} & \frac{\partial y}{\partial \xi} \end{bmatrix} = \begin{bmatrix} x_{21} & y_{21} \\ x_{31} & y_{31} \end{bmatrix}. \tag{A.26}$$

The Galerkin method here, as in the 1D case, entails the construction of a weighted residual

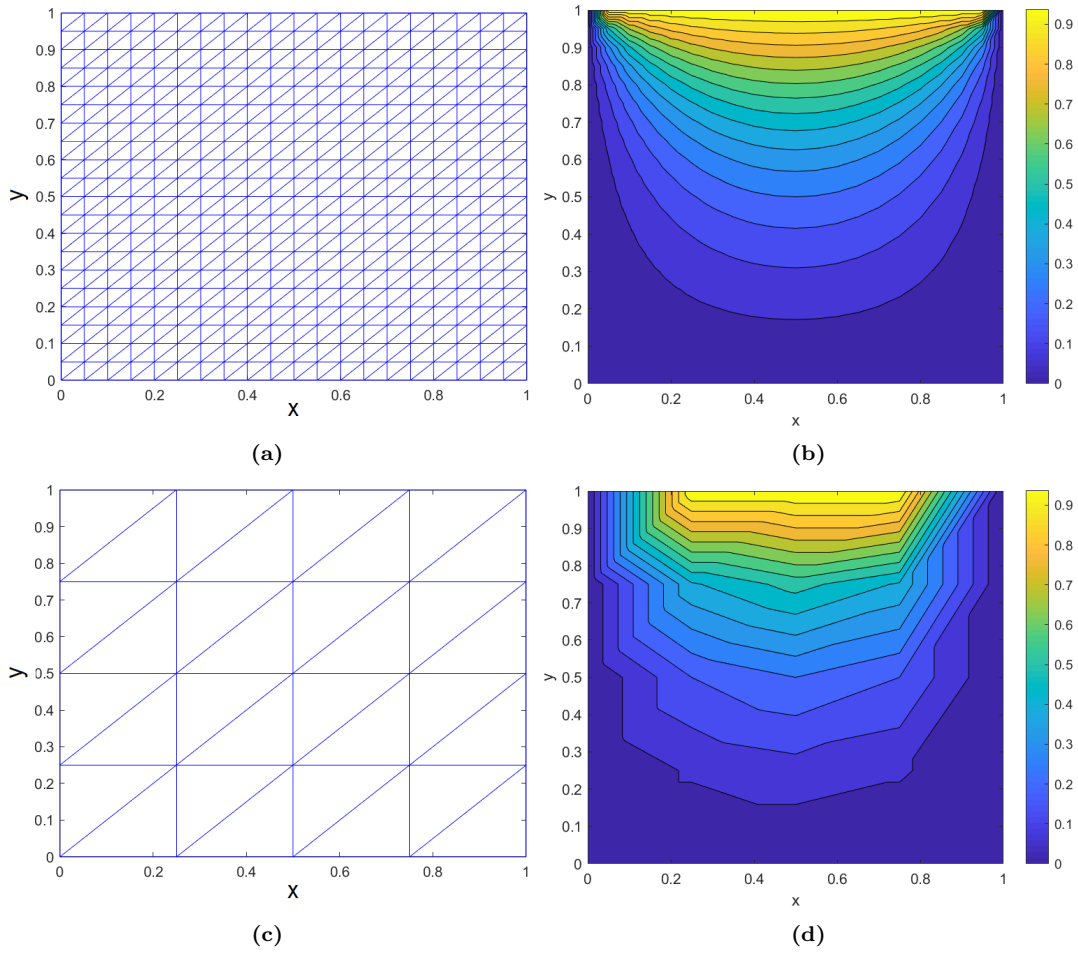

Figure A.6: FEM solution of a 2D Poisson problem. (a) Fine mesh consisting of linear triangles, b) fine mesh solution to the Poisson equation showing field norm distribution in the domain, c) coarse mesh, d) coarse mesh solution. Incident field amplitude is set to unity. The axes measure distances in number of excitation wavelengths. Plots based on Polycarpou [59, Ch.2].

out of the governing differential equation. The goal is to minimize this residual – if the numerical solution was equal to the exact one, the residual would be zero – by weighting it using the interpolation functions and integrating over the domain area of the element, setting the integral to zero. After constructing such expressions for every node, the problem for element e is formulated by the matrix equation

$$K^e u^e = b^e, \tag{A.27}$$

where the matrix K^e is, as in the 1D case, the element matrix. These matrix equations for every e are assembled into a global equation,

$$K\mathbf{u} = \mathbf{b}, \tag{A.28}$$

the same way as for the 1D case. Figure A.6 shows the mesh for a 2D Poisson problem, where the upper boundary is kept at a constant positive voltage, while all the other boundaries are grounded. The L_2 norm for the fine mesh is 0.0173, while for the coarse one, it is 0.0781.

Appendix B

Building the models in COMSOL Multiphysics

COMSOL Multiphysics has a graphical user interface for building the geometry and specifying boundary conditions. In general, construction of the models in this text relied on the example library available on `comsol.com`, specifically the example called *Optical Scattering Off of a Gold Nanosphere*[102]. COMSOL's support team assisted in the implementation of the periodic models.

B.1 COMSOL tutorial

This section demonstrates how to build the "top hat" AuFON model using COMSOL's graphical user interface, as it is the most complex of the models considered in the thesis.

Upon opening COMSOL, the user is presented with several model types. At the start screen, select **Model Wizard** and then **3D**. On the Select Physics screen, click the arrow next to *Optics*, then the arrow next to *Wave Optics* and then select *Electromagnetic Waves, Frequency Domain (ewfd)*. Click on **Add** and then **Study**. Select the *Wavelength Domain* study and then click **Done**.

In the Model Builder pane, under *Global Definitions*, select *Parameters 1*.

Input the data in Table B.1 into the fields under *Parameters*. These parameters are for a wavelength sweep, to find the optical cross sections. For a radius sweep, initial, final and step values for the radius should be input.

The geometry will be built as shown in Figure B.1, seen in the XY plane.

Table B.1: Model parameters.

Name	Expression	Description
au	100[nm]	Gold film thickness
poly	250[nm]	Polystyrene core radius
r0	poly + au/3	AuFON radius (XY plane)
height	2*(poly+au) + 100[nm]	Height of simulation space
space	5[nm]	particle spacing
width	r0*2 + space	Total cell width
R0	width/2	Half cell width
theta	60[deg]	
R	R0/(sin(theta))	
lambda	785[nm]	Light wavelength
t_pml	lambda_max/2	PML thickness
n_m	1.33	Refractive index, medium
P	0.15[W]	Incident light power
E0	sqrt(P/width^2*2*Z0_const)	Incident electric field norm
I_0	E0^2/(2*Z0_const)	Incident light intensity
cell_area	6*2*r0*tan(pi/6)*height	surface area of cell boundaries
geom_area	pi*r0^2	Geometric cross section of particle
lambda_min	450[nm]	Initial wavelength
lambda_max	850[nm]	Final wavelength
lambda_step	2[nm]	Wavelength increment

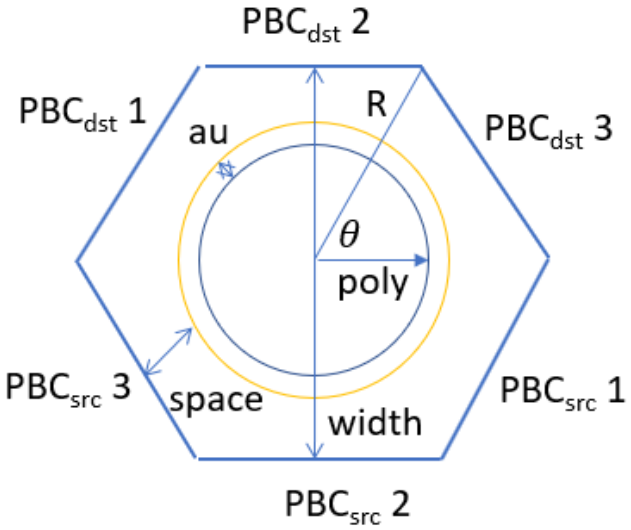

Figure B.1: Illustration of the hexagonal lattice Wigner-Seitz primitive cell, with some parameters from Table B.1 annotated and the boundaries where periodic conditions were applied marked.

B.1.1 Building the model geometry

Click the arrow next to *Component 1 (comp1)* and right-click *Definitions*. Select *Variables* and input the values in Table B.2 into the fields. Note that one can at any time look at how the various constants or variables are defined in COMSOL by using the *Equation View*. In the *Model Builder* on the left side of the COMSOL window, click the "eye" and select **Equation View**. This creates a new node in the model tree, where the relevant variables can be seen.

Right-click *Geometry 1* and select *Ellipsoid*. Under *Size and shape*, input `(poly+au/3)` into *a-semiaxis* and *b-semiaxis*. In the last semiaxis, input `poly+au`.

Table B.2: Model variables.

Name	Expression	Description
nrelPoav	nx*ewfd.relPoavx+ny*ewfd.relPoavy+nz*ewfd.relPoavz	**Poynting** $\cdot\, \hat{\mathbf{n}}$
eff_abs	intop_vol(ewfd.Qh)/I_0/geom_area	Abs. Efficiency
eff_sc	intop_surf(nrelPoav)/I_0/geom_area	Sca. Efficiency
eff_ext	eff_sc + eff_abs	Ext. Efficiency
sers	intop_bdrs(ewfd.normE^4/E0^4)/cell_area	surf area-avgd SERS EF

Right-click *Geometry 1* and select *Block*. Under *Size and shape*, type `2*(poly+au)` into all dimensions. Under *Position*, *Base:* select **Center**. Leave x and y as 0, but type `-(poly+au)` in z.

Create a sphere. Under *Size*, input `poly`.

Right-click *Geometry 1*, hover over *Booleans and partitions* and select *Difference*. Under *Objects to add*, select the ellipsoid and under *Objects to subtract* select the block.

Create a new block, set base to center and rotation to 90 deg. This block delimits the simulation space. Under *Size and shape*, set *Width* to `2*R`, *Depth* to `2*R0` and *Height* to `height+2*t_pml`. Click the arrow next to *Layers* and input `t_pml` in the column labeled *Thickness (m)*, next to Layer 1. In *Layer position*, check **Top** and **Bottom**.

Next we will create four blocks which will carve the shape of the hex lattice cell. In all of them, set *Width* and *Depth* to codewidth and *Height* to `height+2*t_pml`. In the first pair of blocks, set *Position* coordinates x, y, z to `0, R, -height/2-t_pml`. In the first block, set *Rotation* to `-30` deg and in the other one to `120` deg. In the second pair of blocks, set the coordinates to `0, -R, -height/2-t_pml`, and rotate them `-60` deg and `-210` deg, respectively.

Right-click *Geometry 1*, hover over *Booleans and partitions* and select *Compose*. Select all the block objects in the input box. To make it easier, use the Graphics Window and the toolbar in it to hide or view objects using the buttons in Figure B.2. One can also click on the Graphics Window and press Ctrl+A to select all objects, then delete the unneeded ones. In the *Set formula* text box, write `blk1-blk2-blk3-blk4-blk5`. Then click **Build All Objects** or press F8.

(a) **(b)**

Figure B.2: Graphics Window toolbar in COMSOL Multiphysics. (a) Buttons to hide and restore objects. (b) Buttons to change selection of object types.

B.1.2 Defining the model

Right-click on *Definitions*, hover mouse over *Selections* and click on **Explicit**. Label it as *Particle*. Set *Geometric entity level* to **Domain** and click-select domains 4, 5 and 6. Alternatively, click on **Paste Selection** and write `4,5,6`.

Right-click on *Definitions*, hover mouse over *Selections* and click on **Explicit**. Label it as *Surface*. Set *Geometric entity level* to **Boundary** and select domains 14, 15, 16, 17, 20, 25, 26, 28, 30.

Right-click on *Definitions*, hover mouse over *Component couplings* and click on *Integration*. Set *Operator name* to **intop_surf**. Under *Source Selection*, set *Geometric entity level* to **Boundary** and *Selection* to **Surface**.

Create another *Integration* comp. coupling, label it as **intop_vol**. Under *Source Selection*, set *Geometric entity level* to **Domain** and *Selection* to **Particle**.

Create a new *Integration* and label it **intop_bdrs**. Under *Source Selection*, set *Geometric entity level* to **Boundary** and select boundaries `4, 5, 12, 23, 32, 35`.

Right-click on *Definitions* and click on **Perfectly Matched Layer**. In *Domain Selection* click on **Paste Selection** and write `1,3`. Under *Geometry* (click on arrow to expand it), set *Type* to **Cartesian** and under *Scaling*, set **PML scaling factor** to 1 and **PML scaling curvature parameter** to 1.

Right-click on *Materials* under *Component 1* in the Model Builder pane. Select **Add Material from Library**. Click the arrow next to *Built-in* and double-click **Air**. Click on the newly-added material under *Materials*, label it as "Water", expand *Material Contents* and set **Refractive index, real part** to `n_m`, which was defined as a global parameter. Set *Geometric entity level* to **Domain**. Under *Selection*, select all the domains in the Graphics Window.

Going back to the materials library, expand *Optical*, *Inorganic Materials*, *Au - Gold*, *Models and simulations* and double-click on **Au (Gold) (Rakic et al. 1998: Lorentz-Drude model)**. Set *Geometric entity level* to **Domain**. Select domain 4 (the gold "hat").

Then, in the materials library, expand *Optical*, *Organic Materials*, *Polymers* and double-click on **(C8H8)n (Polystyrene, PS) (Sultanova et al. ...)**. Set *Geometric entity level* to **Domain**. Select domains 5 and 6 (the central sphere-halves).

Click on *Electromagnetic Waves, Frequency Domain (ewfd)*. Under *Settings*, set *Formulation* to **Scattered field**, *Background electric field* to **User defined** and input the values in Table B.3 under *Background electric field*.

Table B.3: Electric field component values, for input into the model

Field component	Value (V/m)
x	`E0*exp(-j*ewfd.k0*nm*(-z))`
y	0
z	0

Right-click on *Electromagnetic Waves, Frequency Domain (ewfd)* and select **Periodic Condition**. In *Periodic Condition 1*, under *Boundary Selection*, select boundaries 2, 5, 8, 31, 32, 33. Set *Type of periodicity* to **Continuity**.

Right-click Periodic Condition 1 and click **Duplicate**. Then select boundaries 1, 4, 7, 34, 35, 36.

Duplicate it once again and select boundaries 11, 12, 13, 22, 23, 24.

B.1.3 Meshing

The hex lattice model was not meshed manually. Select **User-controlled mesh** under *Settings*, *Sequence type*. Then set *Element size* to **Fine**.

See e.g. the COMSOL application *Scatterer on a Substrate* [1] for an example on how to mesh a geometry with parallel boundaries manually. This method was used on the square lattice models for this thesis.

Click **Build All** and you should see a mesh on your model.

B.1.4 Solving the model

Right-click on *Study 1* and select **Parametric Sweep**. Click on *Parametric Sweep* and under *Study Settings*, click on "+". Under *Parameter name* column header, select **au**. Input `range(10, 10, 200)` under *Parameter value list* and `nm` under *Wavelengths*. Under *Output While Solving*, check **Plot**.

Click on *Step 1: Wavelength Domain*. Under *Study Settings* set **Wavelengths** to `lda`.

Alternatively, to solve as a function of wavelength (not gold thickness), skip adding the Parametric Sweep and simply type `range(lambda_min, lambda_step, lambda_max)` in *Wavelengths* under *Step 1: Wavelength Domain*, *Study Settings*. Under *Results While Solving*, check **Plot**.

Under *Study 1*, click **Compute**.

B.1.5 Extracting data

Click the arrow next to *Results*, right-click *Data Sets* and select **Cut Line 2D**. Under *Data*, select data set **Cut Plane XY**. Under *Line Data*, select entry method **Two points**.

Set coordinates for the two points defining a cut line as in Table B.4. Click **Plot**.

Table B.4: COMSOL model cut line coordinates.

Point	x	y
Point 1	0	`r0 + t_air`
Point 2	0	`-(r0 + t_air)`

Right-click *Results*, select **2D Plot Group**. Right-click on *2D Plot Group* and select **Surface**. Under *Data*, make sure that *Data set* is set to **Cut Plane XY** and select a parameter value to generate the plot for. Set expression to `ewfd.normE/E0` to see field enhancement values at every point in the XY plane. Click on **Plot**.

Right-click *Derived Values*, select **Global Evaluation**. Enter the expressions in Table B.5 and click **Evaluate – New Table**. Expand *Tables* under *Results* and click on the newly-created table. Under the Graphics window, on the toolbar for *Table 1*, click on **Export** and save data as a csv file to process in Python or MATLAB.

Table B.5: COMSOL model global evaluation expressions.

Expression	Description
`eff_sc`	Scattering efficiency
`eff_abs`	Absorption efficiency
`eff_ext`	Extinction efficiency
`sers`	SERS EF

[1] https://www.comsol.no/model/scatterer-on-substrate-14699

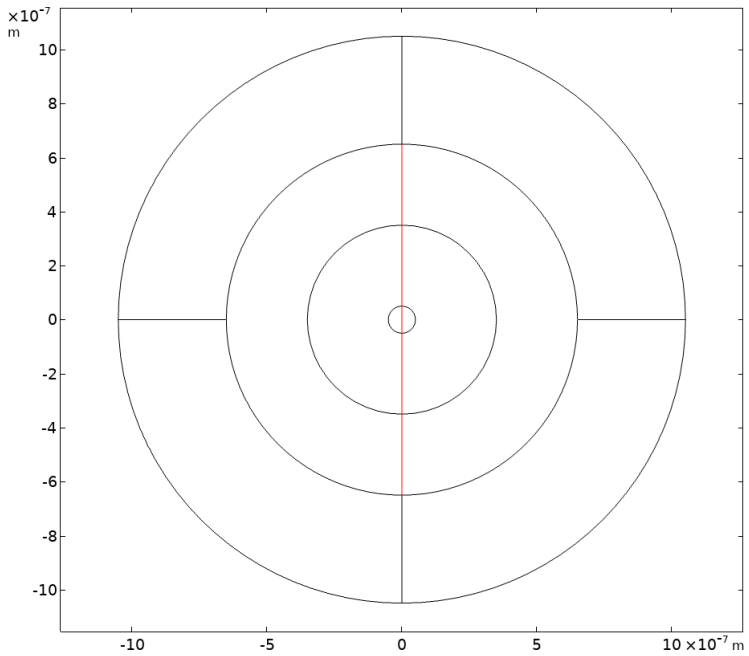

Figure B.3: Cut line plot.

Right-click *Results*, select **1D Plot Group**. Right-click on *1D Plot Group* and select **Table Graph**. Under *Data*, set *Table* to the newly-created table and choose the column for the *x-axis data*. Plot columns should be set to **Manual** and one can select one or multiple columns to plot.

The next and final step presented here was used in the single particle models in this thesis, to evaluate the field enhancement along a cutline. These models were built similarly to the COMSOL application *Optical Scattering Off a Gold Nanosphere* [2]. When the model is solved, click arrow next to *Results*, right-click *Data Sets* and select **Cut Plane XY**. Click *Cut Plane XY*. Under *Data*, select data set **Study 1/Parametric Solutions 1**. Under *Plane Data*, select plane type **Quick** and set *Plane* to **XY-planes**.

Right-click *Results*, select **1D Plot Group**. Right-click on *1D Plot Group* and select **Line Graph**. Click **Plot** to plot the data along the cut line defined previously. One can select the dataset to use from the Line Graph or from the Plot Group and select a specific parameter value. That is, one can plot the E field norm for all or any one of the simulated wavelengths solved for in the parameter sweep. It is also possible to export the Line plot data (only way to export the E field norms) by right-clicking the Line Graph under *1D Plot Group #* and select **Add Plot Data to Export**. Then click on the **Plot #** node under *Export* and select the settings for the exported data file. Click **Export** and look for the file on your hard drive.

Save the model as `tophat_aufon_500nm.mph`.

B.2 COMSOL with LiveLink for MATLAB

COMSOL can be run using MATLAB code by using the program shortcut `COMSOL Multiphysics 5.x with MATLAB`. If you've installed COMSOL with LiveLink for Matlab (Matlab must be installed before COMSOL, or reinstalled after Matlab is installed), then the user guides for LiveLink will be found at `C:\ProgramFiles\COMSOL\COMSOL54\Multiphysics\`

[2] www.comsol.com/model/optical-scattering-off-of-a-gold-nanosphere-14697

doc\pdf\LiveLink_for_MATLAB. Specifically, the file IntroductionToLiveLinkForMATLAB.pdf has a step-by-step guide on how to open, create and modify a COMSOL model using MATLAB scripting. Meanwhile, the file LiveLinkForMATLABUsersGuide.pdf is an extensive COMSOL API documentation, which should be used as a reference when you need some specific API function.

B.2.1 Modifying and running a COMSOL model using LiveLink

When you already have a model defined in a .mph file, you can access it by opening COMSOL through the shortcut COMSOL Multiphysics 5.x with MATLAB, navigating to the folder where you keep your models and execute the following MATLAB statement:

Load the model using
```
model = mphopen('tophat_aufon_500nm');
```

where 'tophat_aufon_500nm' is the string representing the model file tophat_aufon_500nm.mph. Make sure that the model file isn't opened in the COMSOL desktop application in addition to COMSOL with MATLAB. Otherwise, it will open as read-only in MATLAB and you will not be able to modify the model.

Next, open the MPH Navigator using command mphnavigator. This GUI window allows you to click on various properties of your model and copy the code needed to access them. For example, if you want to change the spacing of particles in the model, the MATLAB statement copied from Navigator would be e.g.
```
model.param.set('space', '10[nm]');
```

You can launch an instance of the COMSOL desktop application from MATLAB by typing mphlaunch. Whatever changes to the model you make in MATLAB, will be instantly visible in the COMSOL app launched this way.

To run the model from MATLAB, you can first type
```
ModelUtil.showProgress(true);
```
to see a stand-alone progress window while the model is being solved. Also, the following code line is useful, to make MATLAB wait for the COMSOL server to finish a process before sending the next command:
```
ModelUtil.setServerBusyHandler(ServerBusyHandler(1))
```

Run the model by typing
```
std.run;
```

The MATLAB command prompt will be busy and unresponsive while COMSOL is solving the model. When the model is solved, you should save the model with results by typing
```
mphsave(model, 'tophat_aufon_500nm_10nm_spacing');
```

You can also save the model as a Matlab script using
```
mphsave(model, 'tophat_aufon_500nm_10nm_spacing.m');
```

The results are evaluated by first creating a new table, here Table 1:
```
model.result.table.create('Table 1','Table');
model.result.numerical('gev1').set('table', 'Table 1');
```

Evaluate the global expression defined for finding the scattering, absorption and extinction efficiencies, and SERS EF:

```
model.result.numerical('gev1').setResult;
```

Save the table data as a csv

```
model.result.table('Table 1').save('tophat_aufon_500nm_10nm_spacing.csv');
```

Generate a surface plot of the electric field for a given parametric value. The exact names of properties for the parametric solutions have to be checked in mphnavigator. The following code lines give an example:

```
model.result('pg1').feature('surf1').set('looplevel', [1 29]);
model.result('pg1').run;
```

Plot the graphic in MATLAB

```
mphplot(model,'pg1')
```

Save the graphic as a PNG with a descriptive filename

```
saveas(gcf, 'tophat_aufon_500nm_10nm_spacing.png');
```

B.3 Technical considerations

Although COMSOL is quite user-friendly, it has limitations in its utilization of a computer's resources. The software adheres to Amdahl's law [101], but only larger models benefit from parallel computing, as the part of the problem that can be run in parallel becomes significant. COMSOL does, however, not utilize hyperthreading to its potential and it is recommended to set the CPU core number to the number of physical cores, not logical cores. Additionally, it is recommended to limit the core number on a given CPU to 10 cores to avoid bottle-neck issues.

Despite many requests from the user base asking for GPU-assisted computations over the past few years, as modern graphics adapters have many more cores than a general-purpose CPU, it is still not implemented. As the application is developed in Java, for cross-platform portability, it is understandable that tying the software to specific hardware implementations will require much reworking of the code base. However, cross-platform code for the Java runtime has its own performance limitations compared to low-level languages.

The memory requirements for the models are quite substantial, although COMSOL does implement some efficient methods to solve large systems of linear equations discussed in Chapter 4 and using sparse matrices. As a rule of thumb, the computer needs 16 GB of RAM for every 2 000 000 of finite element nodes, or degrees of freedom. For instance, a model of a one-micron sphere, with the mesh resolved to a few nanometers at the sphere's surface, can easily require 50 GB RAM to solve. The Parametric Sweep feature also uses more memory than using the alternative, Study, feature. However, the type of parametric sweep presented in this appendix could not be performed with the Study. It is possible to make the parametric sweep store only the last solution for a range of parameters, which saves memory.

Appendix C

Multipole models

Figure 5.4a in Section 5.1.3 presented gold sphere sizes which support only the dipole mode in water. Figure C.1 illustrates the emergence of multipole scattering resonance peaks for sphere diameters where new modes emerge. At large sphere size, the extinction efficiency is dominated by scattering, so only the scattering efficiency is calculated here.

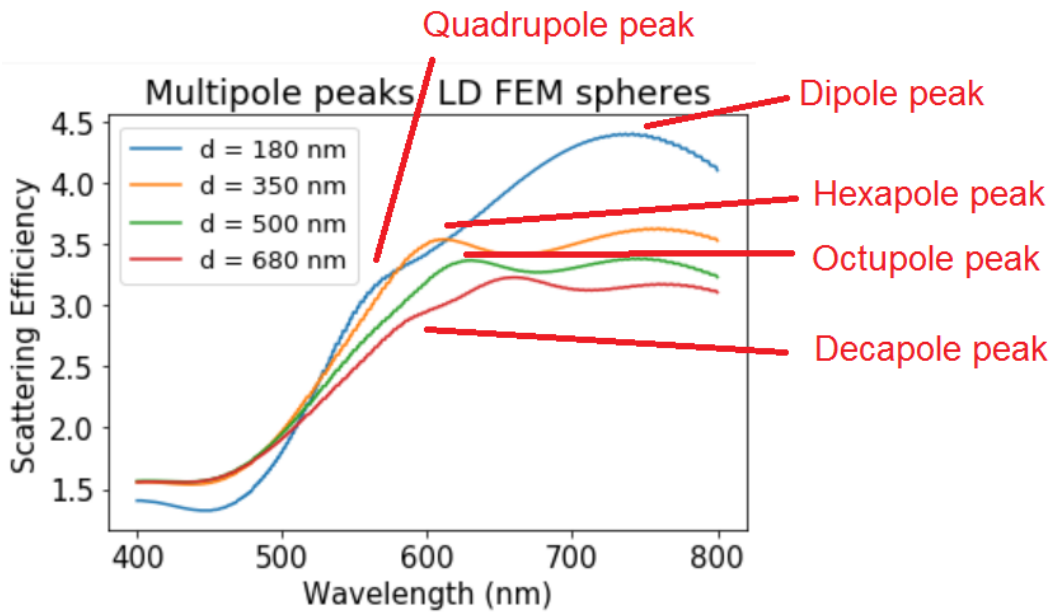

Figure C.1: Scattering efficiencies of large Lorentz-Drude (LD) gold spheres, showing where the multipole peaks emerge on the different spheres.

Figure C.2 displays the electric field amplitudes in the XY-plane, showing a quadrupole, hexapole, octupole and decapole excitation for 180 nm, 350 nm, 500 nm and 680 nm diameter spheres. From the scalebars it is seen that the field enhancement on the surfaces of such spheres is small. The incident field is 10^{-3} V/m. Between figures (a)-(d), the field enhancement is between a factor of 3 and 4. The oscillator strength of the dipole is decreased to accomodate quadrupole, hexapole and higher-order oscillators, each of which are weaker than the one dipole oscillator in smaller spheres.

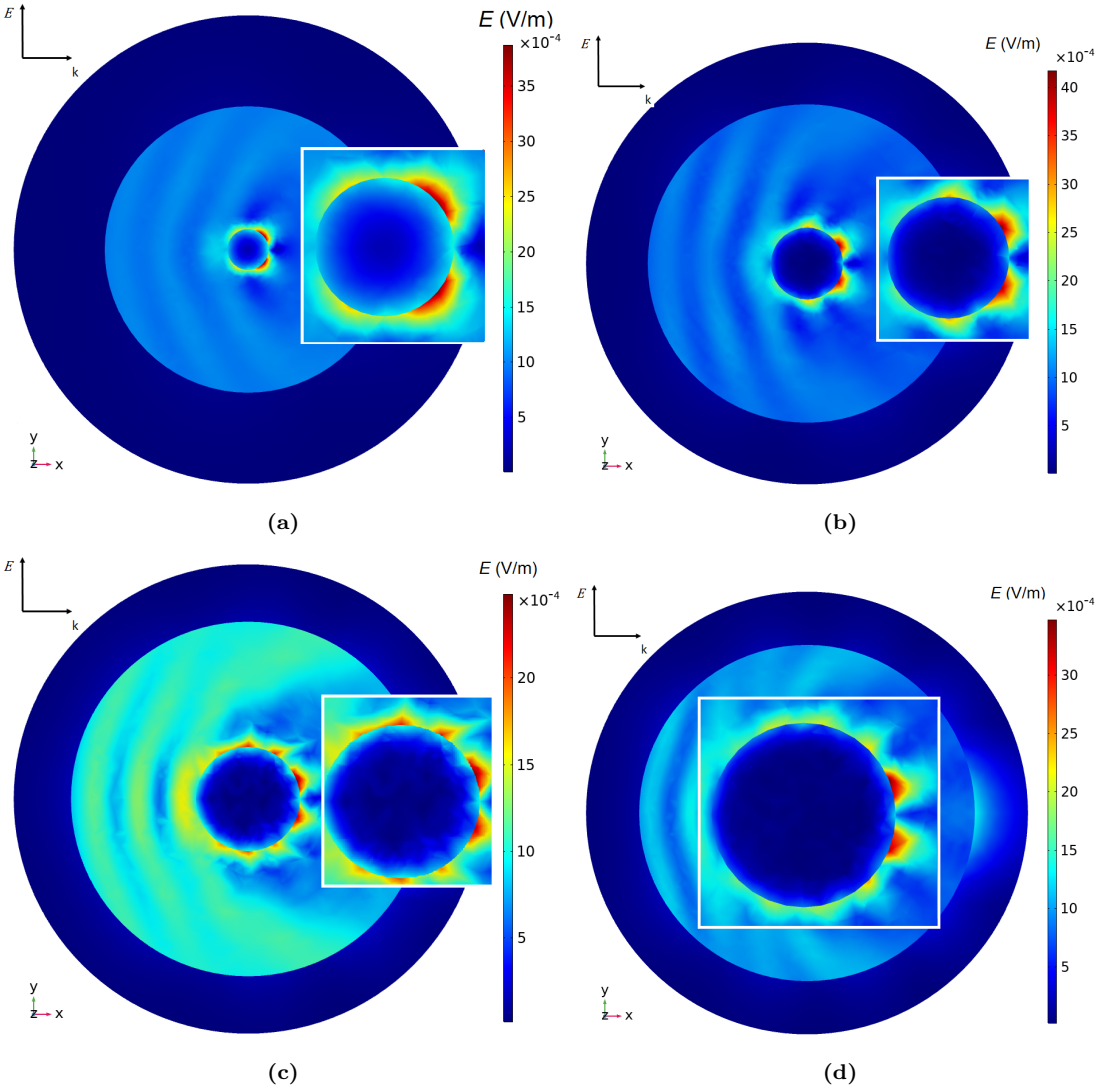

Figure C.2: Electric field amplitude distributions in XY-plane. (a) 180 nm diameter, showing a quadrupolar surface mode, (b) 350 nm diameter, hexapole, (c) 500 nm diameter, octupole and (d) 680 nm diameter, decapole.

Appendix D

Using DDSCAT

The DDA implementation in this text is DDSCAT version 7.3.3, by P. J. Flatau and B. T. Draine [51], [53]. The software is distributed at `http://ddscat.wikidot.com/` in the form of Fortran source code. DDSCAT is used as the DDA implementation of choice at nanoHUB.org, the US national computational infrastructure for nanoscience. The user guide distributed with the software has a detailed overview of the various compilation and installation options. The next section, however, presents a quick tutorial on installing the software and running it.

D.1 Compilation, setup and usage

Currently, the only way to use the software is to compile the source on a Linux system. The Windows binaries on the DDSCAT website are of an older version and no longer updated. Additionally, the available Windows binary is compiled with the most standard options, which do not support double-precision computations or support for multi-core CPUs. To compile the most recent version on Windows, you need to buy a Fortran 90 or 95 compiler. On Linux, the most popular compiler, gFortran, is free software. Mac OS doesn't have much support when it comes to open-source tools and the additional compilation options for multi-core support might not be available [99]. There are a number of ways a Linux environment can be installed:

- Install a Linux distribution such as Linux Mint, Ubuntu, etc. on your computer (e.g. alongside a system such as Microsoft Windows). The commands presented in this section assume that the Linux system is based on Debian (i.e. Debian, Mint, Ubuntu, etc.), but it shouldn't be difficult to apply them on a Red Hat Linux derivative (Red Hat, Fedora, OpenSUSE, etc.) either. In most cases, it is enough to replace the commands `sudo apt install` with `su` and then `yum install`, followed by package name. The calculations for the thesis were done using Linux Mint. The download page and installation instructions are found at `https://www.linuxmint.com/`. Note that installing a Linux system on your PC will replace the bootloader on your machine with the one used by Linux, with Linux set as the default system. This can be changed by modifying the bootloader settings from within Linux.
- Install a virtual Linux system on top of a Windows or Mac host machine. This is OK for testing the software and learning how to use it on simple simulations. Otherwise, with the host and guest OS sharing the CPU, RAM and HDD, the performance is not good for more complex simulations. A popular open-source virtualization platform

is VirtualBox, found at `virtualbox.org`. After installing, follow the installation instructions for your chosen Linux distribution. VirtualBox can install the system directly from the iso image file downloaded from the OS download page. So no need to create bootable USB sticks, etc.

- Install a virtual server on a cloud service, such as Microsoft Azure, Google Compute Platform or Amazon Web Services. All these services allow you to test their infrastructure for free for a limited time, Google being the most generous. They all install the chosen system automatically from an image file, after choosing the server configuration, and let you instantly access the server via SSH. PuTTY is a popular free SSH client for Windows. See `putty.org`.
- DDSCAT's user guide also suggests trying a Unix/Linux emulation environment for Windows, such as MinGW or CYGWIN. See the user guide for details. If you have not used such environments before, it may be easier to simply set up a complete Linux system, as suggested in the first bullet point above.
- One final option is using nanoHUB.org, where the whole software chain is set up. However, it was found to be rather inflexible and some of the software there seems to be outdated or error-prone. They do, however, offer the option to upload model files to solve on their infrastructure, which includes powerful cluster servers.

After installing the system, download the source and examples archives at
`http://ddscat.wikidot.com/downloads`
and unpack them in a directory called `ddscat` in your home directory. The commands below are typed and run from the Linux terminal.

First, run `sudo apt update` to get the latest packages for your system.

Install the GNU Fortran compiler with the command `sudo apt install gfortran`. Then navigate into the `src` directory and run the `make ddscat` command to compile DDSCAT. This will compile with the standard configuration. Edit the file `Makefile` to change this. The most relevant settings to change are:

- `PRECISION`: change this to `dp` for double-precision calculations.
- To enable multicore support, first install OpenMP by going back to the Linux terminal prompt and running command `sudo apt install libomp-dev`. Then edit the makefile and set `DOMP = -Dopenmp` and `OPENMP = -fopenmp`. These settings are valid when compiling using `gfortran`. After compilation, change the environment variable `OMP_NUM_THREADS` to the number of threads supported by your CPU (usually two per physical core). Type e.g.
  `export OMP_NUM_THREADS=2`
  at the terminal prompt if your CPU supports two threads. The commands `lscpu` or `hardinfo` can show the number of threads supported by your CPU(s). Note: It was revealed that DDSCAT has very limited multicore support and for the relevant calculations, it did not make any difference if OpenMP was enabled or not.

The user guide also suggests using Message Passing Interface (MPI) to run computations in parallel. It does, however, point out that this is primarily meant for models with several incident radiation polarizations and/or target orientations. If the intention is to simulate a target irradiated by a range of wavelengths, as in this thesis, then there is not benefit to using MPI [100].

Then run `make all` to compile all binaries. Alternatively, you can also compile the software

by entering the `examples_exp` directory and running the `runexamples` script by typing `./runexamples`.

The simplest way to start running simulations is by entering a directory in the examples folder and modifying the `ddscat.par` file to suit your model. For example, if you want to simulate light scattering from a spherical or ellipsoidal gold nanoparticle, you can use the example files in the `ELLIPSOID` directory. For near-field calculations in addition, use the `ELLIPSOID_NEARFIELD` examples as a starting point.

DDSCAT has a limited number of material dielectric functions in the `diel` folder under `examples_exp`. The code listing for calculating Lorentz-Drude gold model refractive indices, Appendix E.1 can be used to prepare an input file with Lorentz-Drude gold data for DDSCAT so that it looks like the included `Au_evap` file.

It's convenient to set up symbolic links to the executables in the src folder. Enter the directory of the examples you wish to use, e.g. `ELLIPSOID`, and create a symbolic link to the DDSCAT application by typing
`ln -s ../../src/ddscat ddscat`
Assuming that the examples directory lies in the same directory as `src`, it creates a symbolic link called `ddscat`. For calculating near-fields you will also need symbolic links to the `vtrconvert` and `ddpostprocess` executables, which are also in the source folder.
DDSCAT is then run by typing `./ddscat >& ddscat.log &`

The calculated optical cross sections are stored in the file `qtable`. Including the ampersand at the end of a command allows you to run the process in the background and run other commands in the meantime, such as `cat qtable` to view the calculated optical efficiencies as they are computed. Note that the software computes efficiencies directly, not cross sections. Background processes are terminated by typing `kill PID`, where `PID` is the process ID found by typing `ps -a` and looking for the line that says `ddscat`. Or simply `killall ddscat`.

Other software which will be useful for visualization of the results can be installed with the following commands:
`sudo apt install gnuplot-x11` installs GNUPlot, which can be used to plot the result data in `qtable`. Start gnuplot by typing `gnuplot`. Plot e.g. the (normalized) scattering cross section with the command
`plot "qtable" every ::13 using 2:5`.
This command is explained more closely in [98, p. 10].

DDSCAT's user guide also suggests using ParaView and MayaVi2 to visualize the simulated structures. Mayavi2 can be used to view the near-field amplitude, while ParaView can render the target geometry and can be invoked before calculation to help prepare the model. These are installed with the following commands:
`sudo apt install paraview`
`sudo apt install mayavi2`

The user guide, sections 31-32, explains how to use these for visualization of the data produced by DDSCAT.

D.2 Parameter file – ddscat.par

Every subdirectory under `examples_exp` contains its own `ddscat.par` file describing the simulation model. An example file for a single 100 nm gold sphere is included below:

```
1  ' ========== Parameter file for v7.3 ==================='
2  '**** Preliminaries ****'
3  'NOTORQ' = CMDTRQ*6 (DOTORQ, NOTORQ) -- either do or skip torque calculations
4  'PBCGS2' = CMDSOL*6 (PBCGS2, PBCGST, GPBICG, QMRCCG, PETRKP) -- CCG method
5  'GPFAFT' = CMETHD*6 (GPFAFT, FFTMKL) -- FFT method
6  'GKDLDR' = CALPHA*6 (GKDLDR, LATTDR, FLTRCD) -- DDA method
7  'NOTBIN' = CBINFLAG (NOTBIN, ORIBIN, ALLBIN) -- binary output?
8  '**** Initial Memory Allocation ****'
9  100 100 100 = dimensioning allowance for target generation
10 '**** Target Geometry and Composition ****'
11 'ELLIPSOID' = CSHAPE*9 shape directive
12 48.49 48.49 48.49 = shape parameters 1 - 3
13 1          = NCOMP = number of dielectric materials
14 '../diel/m0.96_1.01' = file with refractive index 1
15 '**** Additional Nearfield calculation? ****'
16 0 = NRFLD (=0 to skip nearfield calc., =1 to calculate nearfield E)
17 0.0 0.0 0.0 0.0 0.0 0.0 (fract. extens. of calc. vol. in -x,+x,-y,+y,-z,+z)
18 '**** Error Tolerance ****'
19 1.00e-5 = TOL = MAX ALLOWED (NORM OF |G>=AC|E>-ACA|X>)/(NORM OF AC|E>)
20 '**** Maximum number of iterations ****'
21 100      = MXITER
22 '**** Integration limiter for PBC calculations ****'
23 1.00e-2 = GAMMA (1e-2 is normal, 3e-3 for greater accuracy)
24 '**** Angular resolution for calculation of <cos>, etc. ****'
25 0.5 = ETASCA (number of angles is proportional to [(3+x)/ETASCA]^2 )
26 '**** Wavelengths (micron) ****'
27 0.5 0.5 1 'INV' = wavelengths (1st,last,howmany,how=LIN,INV,LOG,TAB)
28 '**** Refractive index of ambient medium ****'
29 1.0000 = NAMBIENT
30 '**** Effective Radii (micron) **** '
31 0.39789 0.39789 1 'LIN' = eff. radii (1st,last,howmany,how=LIN,INV,LOG,TAB)
32 '**** Define Incident Polarizations ****'
33 (0,0) (1.,0.) (0.,0.) = Polarization state e01 (k along x axis)
34 2 = IORTH   (=1 to do only pol. state e01; =2 to also do orth. pol. state)
35 '**** Specify which output files to write ****'
36 1 = IWRKSC (=0 to suppress, =1 to write ".sca" file for each target orient.
37 '**** Specify Target Rotations ****'
38 0.    0.   1  = BETAMI, BETAMX, NBETA  (beta=rotation around a1)
39 0.    0.   1  = THETMI, THETMX, NTHETA (theta=angle between a1 and k)
40 0.    0.   1  = PHIMIN, PHIMAX, NPHI (phi=rotation angle of a1 around k)
41 '**** Specify first IWAV, IRAD, IORI (normally 0 0 0) ****'
42 0   0   0    = first IWAV, first IRAD, first IORI (0 0 0 to begin fresh)
43 '**** Select Elements of S_ij Matrix to Print ****'
44 9 = NSMELTS = number of elements of S_ij to print (not more than 9)
45 11 12 21 22 31 33 44 34 43  = indices ij of elements to print
46 '**** Specify Scattered Directions ****'
47 'LFRAME' = CMDFRM (LFRAME, TFRAME for Lab Frame or Target Frame)
48 1 = NPLANES = number of scattering planes
49 0.  0. 180. 1 = phi, theta_min, theta_max (deg) for plane A
```

First, note that physical dimensions are denoted in microns.

Lines 2-7 define the solvers and methods used for the various calculation and post-processing steps. Line 4 specifies the iterative method used for solving the system of equations. The methods are all conjugate gradient methods.

Line 9 defines the amount of RAM in MB to use for the initial geometry creation, in every dimension in 3D.

Line 11 defines the type of geometric target to create. A file with coordinates can be included instead if the required geometry is not already defined in the software. For multi-particle models or non-spherical structures such files are a necessity.

Line 12 defines the target dimensions, using a number of dipoles for each of the x, y and z dimensions. For a spherical target, these parameters are equal. With d as the dipole spacing and $diam$ the target diameter, the shape parameter $SHPAR_1 = SHPAR_2 = SHPAR_3 = SHPAR$ is related to these via

$$SHPAR = \frac{diam}{d}. \tag{D.1}$$

Lines 13-14 allow setting the different materials used in the model and to set the locations of the files containing the refractive indices and dielectric functions of these materials. The calculations in this thesis are performed using a file called `Au_LD`, generated using the Lorentz-Drude model, which is then put into the `diel` directory under `examples_exp`. In fact, in the parallel computations approach further below, it is placed in the model directory directly.

Lines 16-17 specify whether near-field calculations will be done and by what fraction the target volume will be expanded for these calculations. If the x dimension of the target spans the space between x_1 =**-x** and x_2 =**x**, then the expanded volume will be bounded by $x_1 - L_x r_1$ and $x_2 + L_x r_2$. L_x is defined as $x_2 - x_1$ and $r_i \in [0, 1]$ are the fractions the user has to specify on line 17.

Line 20 sets the convergence criterion for the iterative method and line 21 sets the number of iterations to perform to try and reach the convergence criterion. If the solution does not converge, the calculation stops then and there, without continuing on to the next excitation wavelength, scattering angle, etc. For the calculations performed in this thesis, `MAXITER` should be set to 1000 or more. `TOL` can also be relaxed up to an order of magnitude. Otherwise the solution will not converge for higher wavelengths (this pertains to the noble metals used in this thesis, as they become more absorptive at higher wavelengths – takes more iterations to solve). However, it should be experimented will different numbers of iterations and tolerances to find the optimal trade-off between solution accuracy, computation time and making sure that the solution will in fact converge.

Line 27 sets the interval of excitation wavelengths to solve for, specifying the number of wavelengths in the interval and how the steps are computed.

Line 29 sets the refractive index of the surrounding medium.

Line 30 sets the effective radius, a_{eff}, of the target. Taking a unit cell containing the target, it is defined using unit cell volume V as $a_{eff} = (3V/4\pi)^{1/3}$. The volume of the unit cell is also defined as $V = Nd$, where N is the number of dipoles in the target unit cell and d is again the dipole spacing. One can approximate N, to predict the accuracy of the model (higher $N \rightarrow$ more accurate result). For a sphere, an estimate is obtained from

$$\hat{N} \approx \frac{4\pi}{3} \cdot \left(\frac{\text{SHPAR}}{2}\right)^3. \tag{D.2}$$

Table D.1 shows that this estimate becomes more accurate with higher SHPAR values.

Using this estimate and volume V from a_{eff}, d can be computed as $V/\hat{N}$. For spheres, an exact value is obtained from Eqn. (D.1). For a spherical target, effective radius is equal

Table D.1: Actual number of dipoles, N, in target and the estimate, $\hat{N}$, using (D.2), as a function of SHPAR. The estimation error is also shown.

SHPAR	N	$\hat{N}$	Error (%)
10	552	524	5.07
20	4224	4189	0.83
40	33552	33510	0.13
60	113104	113097	0.006

to the sphere radius. This was verified by checking the optical cross sections from the calculations, using a certain radius, and comparing with Mie solutions for a sphere of the same radius.

Line 33-34 define what polarizations to compute for. Line 33 indicates a y-polarized incident wave as the main excitation wave and line 34 specifies whether the model will also be solved for a z-polarized wave. It's enough for our purposes to calculate with one polarization only, setting `IORTH` to 1.

To keep the computation times low and the models comparable to the results from COMSOL, the remaining lines will be kept at their default values, with no target rotations with respect to target axes and only one scattering plane.

D.3 Near-field calculations

For calculations where `NRFLD` on line 16 in `ddscat.par` was set to 1, DDSCAT will produce binary files containing near-field solutions. These are the files called `w000r000k000.E1` and `w000r000k000.E2` (the latter, only if `IORTH` in parameters file was set to 2).

Make sure that the model directory contains a symbolic link to `ddpostprocess`. For every `w000r000k000.E#` file you will also need a `ddpostprocess.par` parameters file as input for the DDPOSTPROCESS application. See the `ELLIPSOID_NEARFIELD` directory under `examples_exp` for an example parameters file:

```
1 'w000r000k000.E1'            = name of file with E stored
2 'VTRoutput'                  = prefix for name of VTR output files
3 1   = IVTR (set to 1 to create VTR output)
4 1   = ILINE (set to 1 to evaluate E along a line)
5 -0.59684 0.0 0.0 0.59684 0.0 0.0 501  = XA,YA,ZA, XB,YB,ZB (phys units), NAB
```

Lines 1-3 should be self-explanatory. The VTR files are data files for visualization. Line 4 specifies whether DDPOSTPROCESS should compute the near-field intensity (relative to that of the incident radiation) along a line defined by the coordinates on line 5.

Line 5 is structured like so: coordinates of starting point A, (x_A, y_A, z_A), coordinates of end point B, (x_B, y_B, z_B) and the number of points linearly distributed along the line, including start and end points. Multiple line entries (on separate text lines in this file) can be defined to measure the field around and/or inside a target.

D.4 Parallel DDSCAT simulations

Calculating the scattering, absorption and extinction efficiencies for several wavelengths is a task that computer scientists call "embarassingly parallel problems" [97, p. 14], that is,

problems that can be easily divided into concurrent subproblems. Since all the computational steps for each wavelength are the same, solving the model for each wavelength can be distributed on multiple processors or processor cores/threads (logical cores).

Using Amdahl's law [97, p. 13-14], the speedup can be expressed as

$$S = \frac{1}{1 - p + \frac{p}{n}}, \tag{D.3}$$

where p is the fraction of the time it takes to solve the problem sequentially (without parallelization) that can be parallelized and n is the number of concurrent processes. If the sequential solution time is normalized to one, p/n represents the time fraction per concurrent process and $1-p$ represents the time fraction needed for the part of the problem that cannot be parallelized. Assuming the DDA problem is fully parallelizable (solving over a range of wavelengths should mean that one can solve for each wavelength independently), $1 - p \approx 0$, implying $p \approx 1$, and thus

$$S \approx \frac{1}{\frac{p}{n}} = \frac{n}{p} = n \tag{D.4}$$

Thus, using n cores or threads should make the computations go n times faster.

The idea for the parallelization used in this thesis came from Seeram [100], where it is suggested that although DDSCAT does not distribute the wavelength simulations onto several processes, it can be done by writing a script that subdivides the main model into several smaller DDSCAT models, each solving for a subinterval of the wavelength range defined in the main `ddscat.par` parameter file. This entails copying the main model directory n times, modifying the parameter file in each such that each submodel is assigned a subrange of wavelengths, with no overlap. Then, running the submodels concurrently and assembling the results into a single dataset for plotting and analysis. It should be noted that this trivial parallelization approach, which treats the DDSCAT code as a black box, not requiring rewriting any of it, is also used in the DDSCAT implementation called *nanoDDSCAT*, hosted at nanohub.org. Though in their implementation, it is not possible to choose over how many threads one wishes to parallelize, as the computing resources are shared. Once one learns how to prepare the input files of DDSCAT, it is also more comfortable to run the models on a machine you physically control, as the nanoDDSCAT interface oversimplifies the model setup steps, hiding some important details. Figure D.1 illustrates how the main model can be subdivided into many subproblems. For simplicity, there is a subproblem for every wavelength in the range defined in the main model. The boxes next to the main model tile are the files defining the main model: the parameter file, geometry data, dielectric response functions for materials used and a bash script that will run each subproblem.

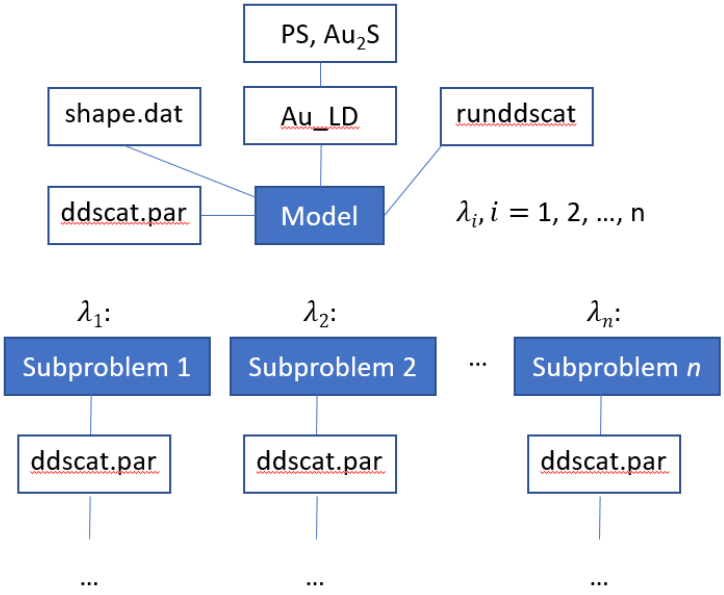

Figure D.1: Illustration of the parallelization approach. The main model is defined by files describing the parameters, geometry, dielectric constants and a script for executing the model. The subproblems are copies of it, tuned to solve only for a single wavelength or a subrange of the total range defined in the main model.

Figure D.2 illustrates the response of the system when running the model sequentially and using the parallelization method outlined above.

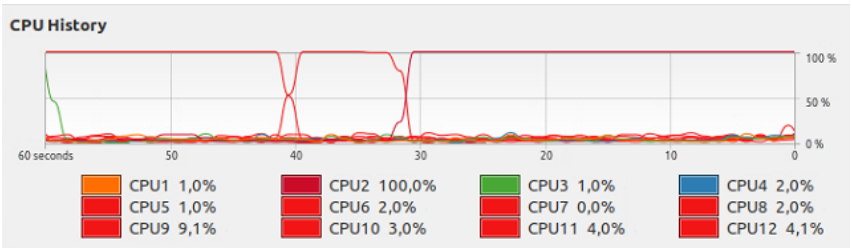

(a)

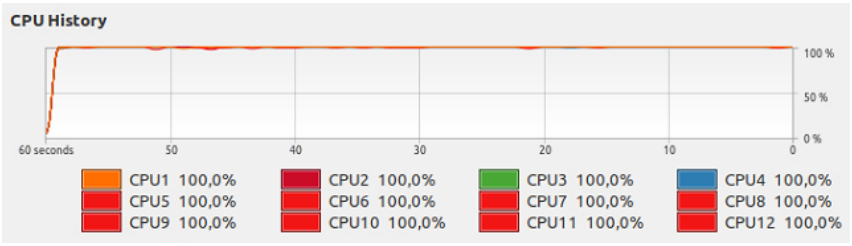

(b)

Figure D.2: GNOME System Monitor utility showing CPU threads in use. (a) Only one thread fully engaged (sequential processing), without the parallelization method, and (b) all threads fully engaged (parallel processing).

This approach alone yields a substantial increase in speed. A single-precision simulation with near-field calculation, using a single 100 nm Lorentz-Drude gold sphere target with shape parameter 50, an error tolerance of 10^{-5}, and running over the wavelength interval 400 nm - 800 nm, ran in 18 minutes, 11 seconds over 12 CPU threads. Meanwhile, a sequential calculation of the same model requires about 2.5 hours. That is, about 8 times slower. Note that this model is a fairly simple one, with only 65 000 dipoles making up the

target geometry, and simulated mostly over VIS wavelengths. The solution time becomes progressively longer for higher wavelengths. Spreading the full wavelength interval linearly over the threads makes those computing for shorter wavelengths finish much sooner than the threads computing solutions for longer wavelengths. The first thread, with the shortest wavelengths assigned to it, ran in 3 minutes, while the last thread finished after the 18 minutes, 11 seconds already mentioned. Such behavior is also seen in the simulations run by Seeram [100]. However, the supercomputer used by him had many physical processors, which made the communication lag between the CPUs rise with more processors. Hence, the time usage plots are not directly comparable.

It takes on average about 0.3-0.4 minutes to compute a solution for a wavelength around 400 nm, while solution for the wavelengths close to 800 nm take 2-3 minutes each to compute (with the model parameters above). Draine [52] illustrates that higher refractive indices can require many more iterations to solve the model. For longer wavelengths, the absorption coefficient of gold (the imaginary part of its refractive index) increases greatly, making the refractive index greater than unity. This explains the greater time needed to solve the longer-wavelength problems. An approach was devised where the CPU cores solving for longer wavelengths are given fewer wavelengths to solve for. Figure D.3 shows how a total of 201 wavelengths were distributed among 20 CPU cores. The solution time was not benchmarked, but there was a significant improvement, although the distribution was not always optimal. For larger wavelength ranges, other distributions were used, accommodating 301 or 401 wavelengths.

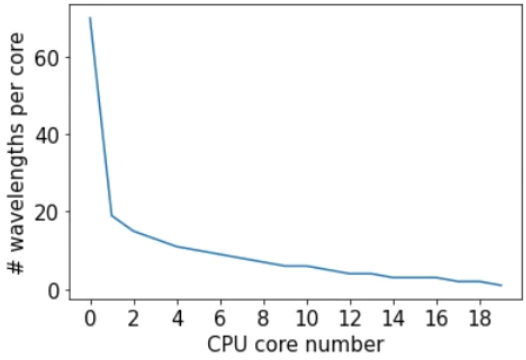

Figure D.3: Distribution of 201 wavelengths among 20 CPU cores, as a part of the parallelization approach for DDSCAT.

The code in Appendix E.6 implements the parallelization algorithm outlined here.

Appendix E

Code listings

This appendix contains the code for generating refractive indices using the Lorentz-Drude model, the Mie solutions to the scattering sphere problem, the CDA implementation and code for running DDSCAT on multiple CPU threads (parallel computations). The code for data processing and plotting is omitted for brevity.

Python 3 is installed with a 64-bit executable downloaded from `python.org`. Using Python 2 is incompatible with the included code, as there are some syntactical differences. The required Python libraries are installed locally using the command
`pip install numpy scipy matplotlib plotly jupyter pandas --user`.

E.1 Lorentz-Drude model of gold

```
1  ##########################################################################
2  #
3  # Lorentz-Drude model of the gold metal's dielectric function
4  # source file: ld_model_indices.py
5  # author: Roman Malyshev
6  #
7  ##########################################################################
8
9  import pandas as pd
10 import numpy as np
11 import matplotlib.pyplot as plt
12 from numpy import pi, sqrt, cos, sin, exp
13
14
15 def lambdaToEv(lda):
16     ''' Converts a wavelength value in nm to a value in electron volts '''
17     #lda = lda*1e-9 # in m
18     freq = c/lda # in s^-1
19     eV = h*freq/e0 # in eV
20     return np.round(eV,2)
21
22 def eps_r_f(w):
23     ''' Calculating the intraband contribution
24     to the dielectric function. '''
25     return 1 - Omega_p**2/(w*(w-1j*G0))
26
27 def eps_r_b(w):
28     ''' Calculating the interband contribution.
29         In Rakic (1998), the imag. part is negative by setting "- 1j*w*G_j[i]", rather than with a "+".
```

```
    This is changed to adhere to the definition of refr index as n + ik in Bohren and Huffman.'''
    val = 0
    for i in range(len(f_j)):
        val += f_j[i]*w_p**2/(w_j[i]**2 - w**2 + 1j*w*G_j[i])
    return val

def eps_r(w):
    ''' Summing to get the dielectric (Lorentz-Drude) function. '''
    return np.array(eps_r_f(w) + eps_r_b(w))


def eps_r_lda(lda):
    ev = lambdaToEv(lda)
    return eps_r(ev)


# constants
c = 3e8        # m/s
e0 = 1.6e-19   # C
h = 6.63e-34   # J*s
hbar = h/(2*pi)

# Plasma frequency -- Rakic (1998)
w_p = 9.03 # eV

# Rakic (1998) parameters (LD) -- all in eV
f0 = 0.760
G0 = 0.053
Omega_p = sqrt(f0)*w_p
f_j = [0.024, 0.010, 0.071, 0.601, 4.384]
G_j = [0.241, 0.345, 0.870, 2.494, 2.214]
w_j = [0.415, 0.830, 2.969, 4.304, 13.32]

# wavelengths in m
lda = np.arange(400,801,1)
# in eV
eV = lambdaToEv(lda*1e-9)
eps = eps_r(eV)
n = sqrt(eps).real
k = sqrt(eps).imag

# Write to file
df = pd.DataFrame({'n': n, 'k': k}).to_csv('n_ld.csv')

# Plot
plt.plot(lda, n, label="n")
plt.plot(lda, abs(k), label="abs(k)")
plt.xlabel('Wavelength (nm)')
plt.legend()
```

E.2 Analytical solution using Mie coefficients

```
#############################################################################
#
# Mie coefficients solution for a scattering nanosphere
# source file: mie_coefficients_solution.py
# author: Roman Malyshev
#
#############################################################################

import pandas as pd
```

```
10 import numpy as np
11 import plotly.graph_objs as go
12 import matplotlib.pyplot as plt
13 from numpy import pi, sqrt, cos, sin
14 from scipy.special import jv, yv
15 from scipy.optimize import curve_fit, leastsq
16
17
18 def plotSet(data, set_key, title_text):
19     ''' Plots a set of datasets '''
20
21     plt.rcParams.update({'font.size': 15})
22     for d in data.keys():
23         plt.plot(data[f'{d}']['wavelengths'], data[f'{d}'][set_key], label=f'{d}')
24     plt.ylabel(title_text)
25     plt.xlabel("Wavelength (nm)")
26     plt.title(f"Mie solution, LD model")
27     plt.rcParams.update({'font.size': 13})
28     plt.legend()
29     plt.show()
30
31
32 def MieCrossSects(lambda0, n_Au, r0, n_m):
33     '''Calculates optical cross sections using Mie coefficients
34
35     Code developed from the derivations in Bohren & Huffmann (1983)
36
37     params:
38
39     n_m                    # refr. index of the medium
40     n_Au = n - 1j*k        # refr. index of gold
41     r0                     # radius of the particle in meters
42     lambda0                # wavelength of incident light in meters
43     '''
44
45     m = n_Au/n_m                 # rel index of gold (to medium's)
46     lda = lambda0/n_m            # wavelength in medium
47     k=2*pi/lda                   # wavenumber
48     x=k*r0                       # size param: wavenr * radius
49     mx=m*x                       # size param, weighted by the relative index
50     N=int(round(2+x+4*x**(1/3))) # maximum n-pole (order)
51
52     n=np.arange(1,N+1)
53     order = n + 0.5
54     j_n = sqrt(0.5*pi/x)*jv(order, x)    # sph B fn, from 1st kind Bessel fn
55     y_n = sqrt(0.5*pi/x)*yv(order, x)    # sph B fn, from 2nd kind Bessel fn
56     h_n = j_n + 1j*y_n                 # spherical Hankel fn's
57     j_n_mx = sqrt(0.5*pi/mx)*jv(order, mx)
58
59     # First order functions
60     j_0 = sin(x)/x
61     y_0 = -cos(x)/x
62     j_0_mx = sin(mx)/mx
63
64     # Riccati-Bessel functions
65     phi_n = x*j_n
66     xi_n = x*h_n
67     chi_n = x*y_n
68     phi_mx = mx*j_n_mx
69
70     phi_0 = x*j_0
```

```
    chi_0 = x*y_0
    phi_0_mx = mx*j_0_mx

    phi_n_1 = np.append(phi_0, phi_n[np.arange(N-1)])
    phi_mx_1 = np.append(phi_0_mx, phi_mx[np.arange(N-1)])
    chi_n_1 = np.append(chi_0, chi_n[np.arange(N-1)])

    d_phi=(phi_n_1 - n/x * phi_n)
    d_phim=(phi_mx_1 - n/mx * phi_mx)
    d_xi=(phi_n_1 + 1j * chi_n_1) - n/x * (phi_n + 1j * chi_n)

    # Scattering coefficients
    a_n = (m * phi_mx * d_phi - phi_n * d_phim) / (m * phi_mx * d_xi - xi_n * d_phim)
    b_n = (phi_mx * d_phi - m * phi_n * d_phim)/(phi_mx * d_xi - m * xi_n * d_phim)

    # Cross sections
    Qsca=2*pi/(k**2)*sum((2*n+1)*(a_n**2 + b_n**2))
    Qext=2*pi/(k**2)*sum((2*n+1)*(a_n + b_n).real)
    Qabs=Qext-Qsca

    return Qsca, Qabs, Qext


# params
df = pd.read_csv(f'n_ld.csv', decimal='.', delimiter=",", header=0)
n = df['n']
k = df['k']
n_m = 1.33          # optical index of the medium
n_Au = n - 1j*k     # refr. indices of gold as function of wavelength
radii = np.array([25, 30, 35, 40, 45, 50])*1e-9  # radius of the particle in nm
crs_sects = {}
lda = np.arange(400,801,1)*1e-9

for r0 in radii:
    Qsca = []
    Qabs = []
    Qext = []
    area = pi*(r0)**2

    for i in range(len(lda)):
        result = MieCrossSects(lda[i], n_Au[i], r0, n_m)
        Qsca.append(result[0])
        Qabs.append(result[1])
        Qext.append(result[2])

    d = np.round(r0*2e9,0)
    crs_sects.update({f'{d}': {'wavelengths': lda/1e-9,
                               'sca': Qsca,
                               'norm_scatt': Qsca/area,
                               'abs': Qabs,
                               'norm_abs': Qabs/area,
                               'ext': Qext,
                               'norm_ext': Qext/area}})

plotSet(crs_sects, 'sca', 'Scattering Cross Section ($m^2$)')
plotSet(crs_sects, 'norm_scatt', 'Scattering efficiency')
```

E.3 Coupled-dipole approximation - 1D array

Parameters such as the plasmon frequency ω_p and the half-width (`gamma` in the code below) were calculated using the Lorentz-Drude optical constants and Mie coefficients using the code above.

```
1  ##########################################################################
2  #
3  # Coupled-dipole approximation model of far field coupling of plasmonic
4  # particles ordered in a 1D array.
5  # source file: cda.py
6  # author: Roman Malyshev
7  #
8  ##########################################################################
9
10 import numpy as np
11 import matplotlib.pyplot as plt
12 from numpy import pi, sqrt, round, exp, where
13 import pandas as pd
14
15 def ldaToEv(lda):
16     '''Converts a wavelength in meters to electron volts
17
18     Arguments
19     ============
20     lda - wavelength (scalar or vector) in meters
21
22     Returns
23     ============
24     eV - the equivalent electron-volt value'''
25     c = 3e8 # m/s
26     h = 6.63e-34 # Js
27     e0 = 1.6e-19 # C
28     eV = h*c/lda/e0 # eV
29     return round(eV,2)
30
31
32 # particle radius, meters
33 R = 50e-9
34
35 # surface plasmon resonance frequency for a 100 nm Ag sphere, from Mie solution
36 wp = ldaToEv(415e-9)                  # for Ag. For Au, replace with 515e-9
37
38 # wavelengths
39 ldas = np.arange(300,801,1)*1e-9
40 w = ldaToEv(ldas)
41
42 # wavevectors
43 k = 2*pi/ldas
44
45 # particles in array
46 N = 1001
47
48 # lattice const
49 latconsts = np.array([470, 500, 550, 600, 650, 700, 750])*1e-9
50 latresonances = np.array([])
51 polarizabilities = {}
52 for r in latconsts:
53
54     # dipole sum
55     S = 0 # m^-3
```

```
56      if N > 1:
57          # 's' polarisation
58          for i in range(1,int(N/2) + 1):
59              S += 2*exp(1j*k*i*r)*((1j*k*i*r - 1)/(i*r)**3 + k**2/(i*r))
60
61      # Drude half-width - HWHM
62      gamma = 0.41 # eV                  # for Ag. For Au, replace with 0.7 eV
63      # polarizability
64      A = 0.5*wp*R**3
65      a_small = -A/(w - wp + 1j*gamma + A*S)
66      a = a_small/(1 - a_small * S)
67      # extinction cross section
68      Cext = 4*pi*k*a.imag # m^2
69      Qext = Cext/(pi*R**2) # Extinction efficiency
70      plt.plot(ldas*1e9, Qext, label=f'{int(r*1e9)} nm')
71      plt.legend()
72      # wavelength corresponding to lattice constant
73      lc_lda = where(ldas == r)[0][0]
74      # wavelength of lattice resonance
75      lattice_peak_eff = np.max(Qext[np.arange(lc_lda - 50, lc_lda + 50, 1)])
76      latresonances = np.append(latresonances, ldas[np.where(Qext == lattice_peak_eff)[0]][0])
77      polarizabilities.update({r: a})
78
79
80  # Plot lattice peak locations vs lattice constant
81  plt.plot(latconsts*1e9, latresonances*1e9)
82  plt.plot(latconsts*1e9, latconsts*1e9, 'r--')
83  plt.xlabel('Lattice const (nm)')
84  plt.ylabel('Lattice peak location (nm)')
85
86  # Display the data
87  pd.DataFrame({'Lattice const (nm)': latconsts*1e9, 'Peak location (nm)': latresonances*1e9})
```

Adding random periodicities. Replace lines 39-50 with the following:

```
1  # lattice const
2  latconsts = np.array([470, 500, 550, 600, 650, 700])*1e-9 # meters
3  epsilon = 10 # nanometers
4  latresonances = np.array([])
5  polarizabilities = {}
6
7  for r in latconsts:
8      # dipole sum
9      S = 0 # m^-3
10     if N > 1:
11         # 's' polarisation
12         for i in range(1,int(N/2) + 1):
13             rd = np.random.randint(r*1e9 - epsilon, r*1e9 + epsilon)*1e-9
14             S += (exp(1j*k*i*rd)*((1j*k*i*rd - 1)/(i*rd)**3 + k**2/(i*rd)))*2
```

E.4 Coupled-dipole approximation - 2D square array

Replace lines 36-50 in code listing E.3 with the following:

```
1  from numpy import pi, sqrt, round, exp, where, cos, sin, sqrt, arctan
2
3  def distance(x,y):
4    ''' Calculates the norm of the r vector from origin to a point P
5    in a square lattice array, given the coordinates of the point.
6
7    Arguments
```

```
  ============
  x,y - coordinates of point P as real scalar values.

  Returns
  ===========
  The norm of the vector'''
    return r*sqrt(x**2 + y**2)

# particles in array
Nx = Ny = 1001
N = Nx*Ny

latconsts = np.array([470, 500, 550, 600, 650, 700, 750])*1e-9
latresonances = np.array([])
for r in latconsts:

    # dipole sum
    S = 0 # m^-3

    if N > 1:
        # 's' polarisation
        for x in range(0,int(Nx/2) + 1):
            for y in range(0, int(Ny/2) + 1):
                if x == 0 and y == 0:
                    next

                elif x == 0 and y > 0:
                    S += 2*exp(1j*k*y*r)*((1j*k*y*r - 1)/(y*r)**3 + k**2/(y*r))

                elif y == 0 and x > 0:
                    next # no contribution along x axis when orthogonal polarization

                else:
                    S += 4*exp(1j*k*distance(x,y))*((1-1j*k*distance(x,y))*(3*(cos(arctan(y/x)))**2 - 1)
                        + k**2*(sin(arctan(y/x)))**2/distance(x,y))
```

E.5 Coupled-dipole approximation - 2D hexagonal array

```
#########################################################################
#
# Coupled-dipole approximation model of far field coupling of plasmonic
# particles ordered in a 2D hexagonal lattice array.
# source file: cda2d_hx.py
# author: Roman Malyshev
#
#########################################################################

import numpy as np
import matplotlib.pyplot as plt
from numpy import pi, sqrt, round, exp, where, cos, sin, sqrt, arctan, dot
from numpy.linalg import norm
import pandas as pd

def ldaToEv(lda):
    '''Converts a wavelength in meters to electron volts

    Arguments
    ============
```

```
21      lda - wavelength (scalar or vector) in meters
22
23      Returns
24      =============
25      eV - the equivalent electron-volt value'''
26      c = 3e8 # m/s
27      h = 6.63e-34 # Js
28      e0 = 1.6e-19 # C
29      eV = h*c/lda/e0 # eV
30      return round(eV,2)
31
32  def pnormangle(m,n):
33      ''' Returns the norm and angle (with x-axis) of a 2D vector
34      representing a the distance from the origin to a point 'p'
35      in a hexagonal lattice.
36      Assumes that the angle between each lattice vectors and the
37      x-axis is 60 degrees.
38
39      Arguments
40      ==========
41      m - scalar value to represent a coordinate in terms of a1 lattice vector
42      n - represents a coordinate in terms of a2 vector
43
44      Returns
45      ==========
46      Array consisting of the norm of constructed vector p and the angle
47      between p and the x-axis.
48      '''
49
50      # Lattice vectors
51      a1 = np.array([0.5, -0.5*sqrt(3)])
52      a2 = np.array([0.5, 0.5*sqrt(3)])
53
54      # Point in terms of lattice vectors
55      p = m*a1 + n*a2
56
57      return [norm(p), np.angle(p[0]+1j*p[1])]
58
59  def dipoleSum(Nx, Ny, r):
60    '''Computes the dipole sum, given the array period r and dimensions Nx and Ny.
61
62    Arguments
63    ===========
64    Nx - scalar value that gives the dimension of array in the direction of vector a1, positive integer.
65    Ny - Dimension of array in the direction of vector a2, positive integer
66    r  - array period in hexagonal lattice, real scalar
67
68    Returns
69    ==========
70    S - the dipole sum as a floating point value
71    '''
72
73      # dipole sum
74      S = 0 # m^-3
75
76      for m in range(0,int(Nx/2) + 1):
77          for n in range(0, int(Ny/2) + 1):
78              if m == 0 and n == 0:
79                  next
80              elif m == n:
81                  S += 4*exp(1j*k*m*r)*(1 - 1j*k*m*r)/(m*r)**3
```

```
            elif m == 0 and n > 0:
                S += 0.5*exp(1j*k*n*r)*((1j*k*n*r - 1)/(n*r)**3 + 3*k**2/(n*r))
            elif n == 0 and m > 0:
                S += 0.5*exp(1j*k*m*r)*((1j*k*m*r - 1)/(m*r)**3 + 3*k**2/(m*r))
            else:
                [pnorm, pang] = pnormangle(m,n)
                S += 4*exp(1j*k*pnorm*r)*((1-1j*k*pnorm*r)*(3*(cos(pang))**2 - 1)/(pnorm*r)**3 \
                + k**2*(sin(pang))**2/(pnorm*r))

    return S

# particle radius, meters
R = 50e-9
# surface plasmon resonance frequency for a 100 nm Ag sphere, from Mie solution
wp = ldaToEv(415e-9)                    # for Ag. 515e-9 for Au.

# wavelengths
ldas = np.arange(350,801,1)*1e-9
w = ldaToEv(ldas)
# wavevectors
k = 2*pi/ldas

# Array dimensions
Nx = Ny = 1001
# Total particle count
N = Nx*Ny

latconsts = np.array([470, 500, 550, 600, 650, 700, 750])*1e-9

plt.rcParams.update({'font.size': 15})
for r in latconsts:
    # Drude half-width - HWHM
    gamma = 0.43 # eV                  # for Ag. 0.7 eV for Au
    # polarizability
    A = 0.5*wp*R**3
    S = dipoleSum(Nx, Ny, r)
    a_small = -A/(w - wp + 1j*gamma + A*S)
    a = a_small/(1 - a_small * S)
    # extinction cross section
    Cext = 4*pi*k*a.imag # m^2
    Qext = Cext/(pi*R**2) # Extinction efficiency

  # plots the extinction efficiencies
    plt.plot(ldas*1e9, Qext, label=f'{int(r*1e9)} nm')

plt.xlabel('Wavelength (nm)')
plt.ylabel('$Q_{ext}$')
plt.rcParams.update({'font.size': 13})
plt.legend()
```

E.6 Parallelization of DDSCAT model - paraddscat.py

Note: The shell commands integrated into the Python code assume a Linux environment or similar. Before running this, make sure that all the files listed in Figure D.1 are present in the main model folder. *runddscat* can be empty, as it will be written by the code below.

```
##############################################
#
# paraddscat.py - parallelizes DDSCAT model.
# author: Roman Malyshev
#
```

```
6  ##############################################
7
8  import subprocess as sp
9  import numpy as np
10 import os
11 import pandas as pd
12 import matplotlib.pyplot as plt
13
14 ######################################################################
15 # retrieve the number of "CPUs" on current pc (threads, in reality)
16 ######################################################################
17 sp.run('lscpu > cpuout', shell=True)
18 f = open('cpuout', 'r')
19 lines = f.readlines()
20
21 for line in lines:
22     if 'CPU(s):' in line:
23         str = line
24         break
25
26 cpus = [int(i) for i in str.split() if i.isdigit()][0]
27 cmd = sp.run('rm cpuout', shell=True)
28 cpus = int(cpus)
29 print(f'Will use {cpus} CPUs')
30 print('Working directory: ' + os.getcwd())
31
32 # Parameters to modify in ddscat.par
33
34 ldas = [450, 650]  # nm  # specifies start and end of wavelength range
35 step = 1 # nm
36 nrsteps = len(np.arange(ldas[0], ldas[1] + step/2, step))
37 print(nrsteps) # range of wavelengths to solve for
38
39 # read ddscat.par of main model and print contents
40 backupdir = 'nanoshell_au2s_au_2_4' # This is the main model directory
41 f = open(f'{backupdir}/ddscat.par', 'r')
42 lines = f.readlines()
43 f.close()
44
45 ################################################################
46 # Copy main model the number of times defined in 'cpus' above
47 ################################################################
48 dirnm = f'nanoshell_au2s_au_2_4_155075N' # all submodel directories are kept in this dir
49
50 cmd = sp.run(f'mkdir {dirnm}', shell=True)
51 cmd = sp.run(f'cp -r runddscat.py {dirnm}', shell=True) # This script will run all other ones.
52
53 # Update main python script for running the processes
54 f = open(f'{dirnm}/runddscat.py', 'r')
55 lines = f.readlines()
56 f.close()
57
58 dirs = []
59 # creates submodel dirs and writes the main python file to run all submodels at once.
60 for cpu in range(cpus):
61     subdir = f'{dirnm}/{cpu}'
62     cmd = sp.run(f'cp -r {backupdir} {subdir}', shell=True)
63     print(f'cp -r {backupdir} {subdir}: {cmd.returncode}')
64     os.chdir(f'{subdir}')
65     cmd = sp.run(f'ln -s ../../../src/ddscat ddscat', shell=True)
66     os.chdir('../../')
```

```
    if cpu < cpus - 1:
        lines.append(f"            run('{cpu}/runddscat'),\n")
    else:
        lines.append(f"            run('{cpu}/runddscat'))\n")
    dirs.append(f'{subdir}')
lines.append('\n\n')
lines.append(f'asyncio.run(main())\n')
lines.append('\n')
f = open(f'{dirnm}/runddscat.py', 'w')
f.writelines((lines))
f.close()


# read ddscat.par in each submodel dir and modify it to distribute the parameter range on CPUs
# modify bash script 'runddscat' in each process directory to run ddscat from that directory

paramstr = "'LIN' = wavelengths (first,last,how many,how=LIN,INV,LOG)\n"
param = ldas[0]
stps = nrsteps

x = np.arange(0,cpus,1)
ldascpu = -51.1*x**(1/10) + 70
ldascpu = np.round(ldascpu).astype('int')
print(ldascpu)
print(sum(ldascpu))
plt.plot(x,ldascpu)

for i in range(cpus):
    subdir = f'{dirnm}/{i}'
    n = ldascpu[i]
    f = open(f'{subdir}/ddscat.par', 'r')
    lines = f.readlines()
    f.close()

    f = open(f'{subdir}/runddscat', 'r')
    runlines = f.readlines()
    f.close()

    for j in range(len(lines)):
        if paramstr in lines[j]:
            print("old line: " + lines[j])
            lines[j] = f"{param/1000} {(param + step*(n-1))/1000} {n} {paramstr}"
            param += step*n
            print("new line: " + lines[j])
            break

    for j in range(len(runlines)):
        if "cd " in runlines[j]:
            print("old line: " + runlines[j])
            runlines[j] = f"cd {i}\n"
            print("new line: " + runlines[j])
            break

    # write params to ddscat.par
    f = open(f'{subdir}/ddscat.par', 'w')
    r = f.writelines((lines))
    f.close()

    # write lines to runddscat
    f = open(f'{subdir}/runddscat', 'w')
    r = f.writelines((runlines))
```

```
    f.close()


# Write file to run the simulation
f = open('ddscatrun', 'w')
f.writelines([runlines[0], f'cd {dirnm}\n', 'python3 runddscat.py &\n']))
f.close()
sp.run('chmod a+x ddscatrun', shell=True)

# Run it from terminal by typing './ddscatrun'

# Run this after the simulation ends (or during to look at incoming data)
# Extracts data from all 'qtable' files in all submodel dirs.

radii= []
ldas = []
Qext = []
Qabs = []
Qsca = []

for i in range(cpus):
    subdir = f'{dirnm}/{i}'
    f = open(f'{subdir}/qtable', 'r')
    lines = f.readlines()
    f.close()

    for l in range(15, len(lines)):
        line = lines[l].split()
        if 'NaN' not in line:
            radii.append(line[0])
            ldas.append(line[1])
            Qext.append(line[2])
            Qabs.append(line[3])
            Qsca.append(line[4])

radii = np.array(radii).astype(float)*1000
ldas = np.array(ldas).astype(float)*1000
Qext = np.array(Qext).astype(float)
Qabs = np.array(Qabs).astype(float)
Qsca = np.array(Qsca).astype(float)
print(ldas)
print(len(ldas))

# Plots the extinction efficiency data
plt.plot(ldas, Qext)
plt.xlabel('Wavelength (nm)')
plt.ylabel('$Q_{ext}$')

print(f'Max ext = {max(Qext)}, at {int(ldas[np.where(Qext == max(Qext))[0]][0])} nm')
```

R. Malyshev

FEM model of plasmonic particle arrays for glucose sensing

NTNU
Norwegian University of
Science and Technology